STUDY OF PHASE-MATCHING GEOMETRIES IN BULK AND PERIODICALLY-POLED LITHIUM NIOBATE AND THEIR USE IN TERAHERTZ OPTICAL PARAMETRIC OSCILLATORS

Caroline L. Thomson

A Thesis Submitted for the Degree of PhD
at the
University of St Andrews

2012

Study of phase-matching geometries in bulk and periodically-poled lithium niobate and their use in intracavity terahertz optical parametric oscillators

Caroline L. Thomson

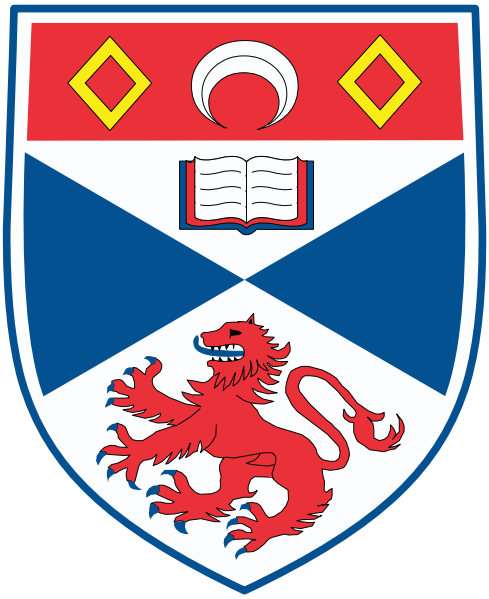

University
of
St Andrews

Thesis submitted for the degree of

Doctor of Philosophy

April 2012

Declarations

I, Caroline Louise Thomson, hereby certify that this thesis, which is approximately 44,000 words in length, has been written by me, that it is the record of work carried out by me and that it has not been submitted in any previous application for a higher degree. I was admitted as a research student in September 2007 and as a candidate for the degree of Doctor in Philosophy in September 2008; the higher study for which this is a record was carried out in the University of St Andrews between 2007 and 2011.

Caroline L Thomson Date

I hereby certify that the candidate has fulfilled the conditions of the Resolution and Regulations appropriate for the degree of Doctor in Philosophy in the University of St Andrews and that the candidate is qualified to submit this thesis in application for that degree.

Malcolm H Dunn Date

Copyright Declaration

In submitting this thesis to the University of St Andrews I understand that I am giving permission for it to be made available for use in accordance with the regulations of the University Library for the time being in force, subject to any copyright vested in the work not being affected thereby. I also understand that the title and the abstract will be published, and that a copy of the work may be made and supplied to any bona fide library or research worker, that my thesis will be electronically accessible for personal or research use unless exempt by award of an embargo as requested below, and that the library has the right to migrate my thesis into new electronic forms as required to ensure continued access to the thesis. I have obtained any third-party copyright permissions that may be required in order to allow such access and migration, or have requested the appropriate embargo below.

The following is an agreed request by candidate and supervisor regarding the electronic publication of this thesis:

Access to all of printed copy but embargo of all of electronic publication of thesis for a period of 1 year on the following ground:

Publication would preclude future publication.

Caroline L Thomson Malcolm H Dunn Date

Acknowledgements

Firstly, I must thank Prof. Malcolm Dunn for giving me the opportunity to complete my PhD studies in the nonlinear optics group. Without his continued guidance and support I would surely not have achieved so much, even if, at times, his enthusiasm for the research was hard to keep up with! I must also express my gratitude for the many helpful and insightful discussions that took place between us.

My sincere thanks go also to Dr. David Walsh, Dr. David Stothard and Dr. Tom Edwards. Their advice and assistance in the lab was invaluable and their experience was a very useful resource. They also contributed to the creation of a fun working environment. I must also thank Dr. Cameron Rae for his continued willingness to loan lab equipment.

Writing this thesis has taught me the importance of my friends. Particular thanks go to Mhairi, Paul, Jane, Lucy and Dave Bolton - I know that I couldn't have made it through without your support and kindness.

Without my family, I would not be where I am today. They have always encouraged and inspired me to strive for perfection in every aspect of life.

Finally I must thank Rob for his love, support and proof-reading.

Dedication

To my family, especially to those whose inspiration and love is no longer felt.

Abstract

This thesis describes the experimental implementation of novel intersecting cavity terahertz optical parametric oscillators based on bulk and periodically-poled magnesium oxide-doped lithium niobate. Both collinear and non-collinear phase-matching geometries have been demonstrated and injection-seeding has been implemented in devices using periodically-poled material to reduce threshold and increase the down-conversion efficiency.

A comprehensive characterisation of the original intracavity terahertz OPO was undertaken, which revealed the parameters having the greatest impact on OPO efficiency (idler mirror reflectivity and cavity length) and led to a better understanding of the losses in the system. During the characterisation process, generation of further terahertz radiation at the same frequency as that generated by the parametric process was observed and identified as being a result of difference frequency generation (DFG) between the parametrically-generated idler and terahertz waves. This phenomenon had previously only been observed when periodically-poled materials were employed in the system. The effect of this additional DFG process has been analysed in terms of the enhancement of the terahertz field on the basis of the coupled wave equations and physically measured quantities.

The use of periodically-poled lithium niobate has been a major part of the research presented in this thesis. A comprehensive study of the modified

phase-matching conditions was carried out and both collinear and novel hybrid non-collinear phase-matching geometries were identified. Several computer models were developed to assess the performance of any given grating design in these different geometries and the effects of temperature tuning and pump wavelength variation were also investigated using the models. Experimental studies confirmed the viability of the modelling approach but material limitations (particularly the early onset of crystal damage) limited the outcomes of the experiments. A detailed comparison of the poled and bulk materials was made to highlight the present drawbacks of the poled material.

Finally, injection seeding was used to improve the efficiency of the collinear phase-matched PPLN OPOs. When seeding was used the depletion of the pump pulse was increased to the point of being measurable, reaching an upper level of 10%. Coupling constraints placed on the seed laser limited the amount of depletion attained. The potential for injection seeding to be used in the hybrid non-collinear phase-matching scheme was also identified but not realised during the course of this work. Were this technique successful, the tuning range of the intersecting cavity terahertz OPO could be extended to encompass the sub-1THz region, something that has previously been limited by the available idler cavity angles.

Publications and Conference Attendances

Publications

M. Naftaly, R. A. Dudley, J. R. Fletcher, F. Bernard, C. Thomson and Z. Tian, *Frequency calibration of terahertz time-domain spectrometers*, J. Opt. Soc. Am. B, **26**, No. 7, 2009

D. J. M. Stothard, T. J. Edwards, D. Walsh, C. L. Thomson, C. F. Rae, M. H. Dunn and P. G. Browne, *Line-narrowed, compact, and coherent source of widely tunable terahertz radiation*, App. Phys. Lett. **92**, 141105, 2008

Conferences and workshops attended

Photon12, Durham University, September 2012, "Periodically-Poled Materials for the Parametric Generation of THz Radiation" (accepted for oral presentation)

EMMA interest group meeting, National Physical Laboratory, February 2010

"2nd UK/Europe-China Workshop on Millimetre Waves and Terahertz Technologies", Rutherford Appleton Laboratory, October 2009 (poster)

European Summer School on "New Trends in Terahertz Imaging", UPMC Paris Universitas, July 2009 (poster)

EKTN THz meeting, Royal Society, London, 25 February 2009 (poster)

Contents

1 Introduction

1.1 Background

The terahertz region of the electromagnetic spectrum is generally accepted to occupy the approximate frequency range 500GHz-10THz. The region is bounded on the high frequency side by the far-infrared and on the low frequency side by the sub-millimetre region. Spectral features associated with physical processes including rotational transitions of molecules, lattice vibrations in solids and intraband transitions in semiconductors populate the terahertz region [1]. Terahertz radiation is non-ionising and has the ability to penetrate a wide variety of non-conducting materials including clothing, paper, cardboard, wood, plastics and ceramics. These properties mean that terahertz can be used in applications which exploit the unique spectral fingerprints of materials in this region. The range of terahertz applications is wide and includes, but is not limited to, the non-destructive testing of pharmaceuticals [2], label-free analysis of biomolecules [3], medical imaging [4] and security applications [5].

Until relatively recently (around the 1990s), the terahertz region had been inaccessible due to a lack of suitable sources of terahertz radiation, commonly referred to as "the terahertz gap" [6]. Difficulties in extending the operating frequencies of electronic devices far beyond several hundred GHz prevented access to the terahertz region from the sub-millimetre region, whereas a lack of suitable semiconductor materials prevented the extension of interband diode

lasers to terahertz frequencies [7].

The desire for convenient and widely-tunable terahertz sources for use in applications has driven research into a range of source technologies, which are the topic of several recent reviews [6, 8]. These can be broadly divided into those that operate in the time domain and those that operate in the frequency domain.

Time-domain devices include photoconductive antennas and devices based on optical rectification, both of which utilise femtosecond lasers [7]. These devices produce broad-band terahertz radiation and the conversion of time-domain data to a conventional spectrum in the frequency domain requires the use of the fast Fourier transform algorithm, a process that can be complicated by measurement uncertainties [9].

Free electron lasers (FELs) and quantum cascade lasers (QCLs) operate in the frequency domain. Although FELs provide high power terahertz radiation (up to $\approx$5kW) that is tunable over the frequency range 120GHz-4.8THz [10], they are not accessible to many researchers owing to their large (facility-sized) scale. On the other hand, QCLs are not widely tunable, the quality of devices is compromised due to complex manufacturing, the beam quality is generally poor and they have yet to reach room-temperature operation [11].

A multiplied sub-millimetre source covering the frequency range (1.1-1.7)THz is now commercially available from Virginia Diodes, Inc. (VDI) [12]. The source provides tens of μW power across the output band. An input power of several mW at (367-567)GHz is frequency-tripled to achieve output in the terahertz region [13]. VDI are currently developing similar sources for the production of 1.9 THz, 2.5THz and 2.7THz radiation, primarily for use in radio astronomy applications [14].

A class of device that is tunable, displays high spatial beam quality, operates at room temperature and exhibits a wide tuning range within a single device, is the terahertz optical parametric oscillator. The science and technology of this class of

device is the subject of this thesis, and an introductory review is presented in the following sections.

1.2 Parametric generation of terahertz radiation

Optical parametric oscilators (OPOs) exploit the second-order ($\chi^{(2)}$) nonlinear effect that exists in many non-centrosymmetric materials to split incident "pump" photons into two new photons called the "signal" and "idler", the frequencies of which must add up to that of the initial photons. The ratio of the split is determined by the phase-matching conditions which must be adhered to for the process to be efficient. The phase-matching conditions ensure that the photons of the desired frequency and direction of propagation add up together in phase, expressed in mathematical terms as:

$$\frac{2\pi n_p}{\lambda_p}\hat{p} = \frac{2\pi n_i}{\lambda_i}\hat{i} + \frac{2\pi n_s}{\lambda_s}\hat{s}$$

which can also be expressed as

$$\underline{k}_p = \underline{k}_i + \underline{k}_s$$

where $\underline{k}_m$ represents the wave-vector (defined as $\frac{2\pi n_m \nu_m}{c}$), n_m indicates the refractive index and λ_m is the wavelength corresponding to the wave denoted by m. The subscripts p, i and s denote the pump, idler and signal waves respectively. $\hat{p}$, $\hat{i}$ and $\hat{s}$ are unit vectors describing the propagation directions of the three waves. Phase-matching can be achieved either collinearly or non-collinearly as shown in figure 1.1, and tuning of the signal and idler waves is achieved, in the case of non-collinear phase-matching, by varying the angle ϕ.

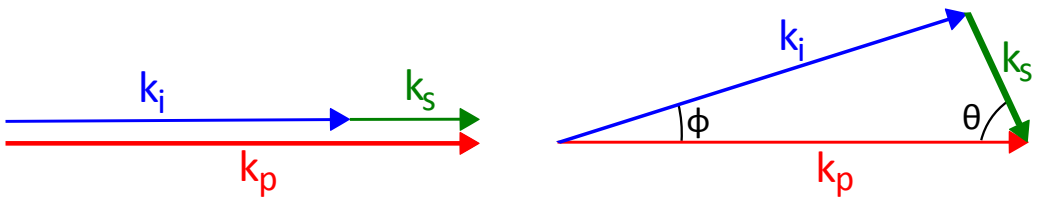

(a) Collinear phase-matching (b) Non-collinear phase-matching

Figure 1.1: Illustration of collinear and non-collinear phase-matching geometries.

Since the first demonstrations of OPOs by Giordmaine and Miller in 1965 [15] and Byer [16] and Smith [17] in 1968, OPOs have been widely used to access areas of the electromagnetic spectrum that are otherwise inaccessible using lasers alone [18]. Even in 1969, Harris [19] optimistically predicted that within a few years of his writing, the entire spectral region from 0.2μm to >100μm would be accessible through narrow-band, tunable sources.

Of particular interest here is the production of terahertz radiation due to the 248cm^{-1} (7.4THz) polariton mode in lithium niobate, which was first demonstrated by Gelbwachs and co-workers in 1969 [20]. The pump laser used was a Q-switched ruby laser and the nonlinear crystal was inserted into an optical resonator that was resonant for the Stokes wave (the Stokes wave corresponds to what is referred to as the idler wave in this thesis); tuning of the Stokes wave was effected by changing the angle of incidence of the pump laser with respect to the axis of the Stokes resonator. The purpose of this experiment was to confirm the effect of stimulated Raman emission, which had been proposed by Henry and Garrett in 1968 [21] so no attempt was made to measure the terahertz radiation directly; however, the presence of the terahertz wave was inferred by the measurement of the Stokes wave.

Yarborough *et al.* also obtained tunable radiation by the same means in 1969 [22]. In this experiment, there was no resonator for the Stokes wave but the end faces of the $LiNbO_3$ crystal were polished flat and parallel, forming a lossy cavity. The experiment served mainly as a extension of the Gelbwachs *et al.* experiment but in this case the terahertz radiation was both extracted and measured for the first time. Tuning of the output wavelength over the range (50-238)μm was achieved by rotating the crystal itself, with the experimentally-observed results being shown alongside a plot of the dispersion of the A_1 symmetry polariton mode in figure 1.2. The vertical lines on the dispersion curve indicate the angular separation of the pump and idler (labelled θ in the figure) which is necessary for the phase-matching condition to be met. Inset in the figure is the phase-matching diagram which shows the directions of propagation of the three interacting waves. The THz powers measured were uncertain due to detector

calibration problems but it was estimated that, for 1MW of pump power, 5W of terahertz radiation was measured. There is also a discussion of the losses associated with the generation process, specifically the losses due to surface reflections (estimated to be ≈50%) and absorption within the crystal.

Following further work by Johnson *et al.* in 1971 [23], which was similar in execution to that of Yarborough described above, Piestrup and co-workers made further progress in the generation of terahertz waves on the basis of polariton enhancement of parametric generation in lithium niobate in 1975 [24]. The pump laser used was a Nd:YAG laser and by using longer nonlinear crystals, an extended tuning range of (150-700)μm was observed. The terahertz radiation was not directly measured, but generated powers of up to 4kW at 330μm were reported, which was reduced to 500W generated at 250μm because of the

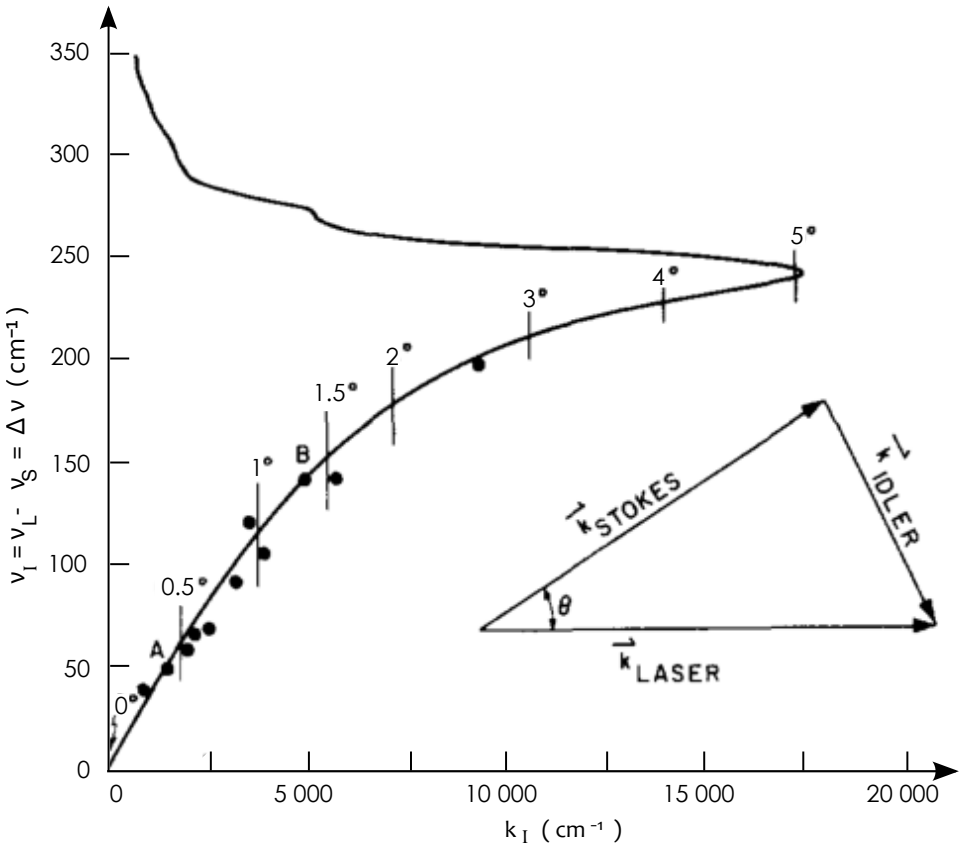

Figure 1.2: Dispersion curve of $LiNbO_3$ in the vicinity of the A_1 symmetry 248cm^{-1} polariton mode. The dots correspond to the points experimentally observed by Yarborough and co-workers. Reprinted with permission from [22]. © 1969 American Institute of Physics.

terahertz absorption, which is also increased in the terahertz region by the presence of the polariton resonance.

The use of OPOs for the generation of terahertz radiation then lay dormant for around 20 years until the Kawase group in Japan restarted research in this area in 1996, with the aim of advancing the previous work [25]. This recent work utilised Q-switched Nd:YAG lasers operating at 1064nm as the pump source rather than the Q-switched ruby laser used in the earlier work. A non-collinear phase-matching scheme was again adopted, with the twin advantages of providing a means for tuning the device as well as enabling the terahertz wave to be extracted rapidly before being absorbed within the lithium niobate crystal. The wavelengths of the pump and idler waves are very close in this system, with the pump at 1064nm and the idler wavelength tunable across the range $\approx$(1068-1071)nm. Immediately it is apparent that the large difference in frequency between the pump and terahertz will result in a low quantum defect - each photon at the pump frequency that is involved in the parametric process is converted into an idler photon and a terahertz photon, the maximum conversion efficiency, η, being determined by the ratio of the terahertz frequency to the pump frequency. Thus the optical-to-terahertz conversion efficiency is limited to $\approx 1\%$. The nonlinear device and the pump laser were separate, with oscillation threshold being reduced by placing the nonlinear medium in an external cavity that is resonant for the idler wave as shown in figure 1.3. Tuning of the idler and terahertz frequencies was achieved by rotating the idler cavity mirrors and a variety of techniques were used to extract the terahertz radiation, including a monolithic grating coupler and an array of silicon prisms mounted

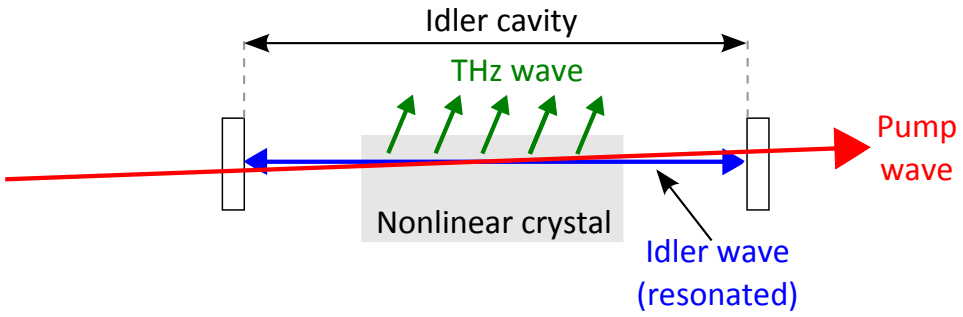

Figure 1.3: Schematic of an extracavity OPO system of the kind used by the Kawase group.

on the surface of the $LiNbO_3$ crystal.

1.3 Intracavity terahertz parametric oscillators

The nonlinear optics group at the University of St Andrews has extensive experience in developing OPOs, with particular expertise and interest in the implementation of OPOs within laser cavities to increase their efficiency, versatility and simplicity [26–28]. In that regard the group identified the opportunity to improve upon the aforementioned terahertz OPO by removing some of the problems associated with the extracavity device.

The intracavity terahertz OPO has been developed into a robust device capable of producing terahertz radiation continuously tunable across the frequency range ≈(0.9-3)THz with a free-running linewidth of ≈50GHz [29]. The layout of the device is shown in figure 1.4a. The laser gain medium is Nd:YAG, which is end-pumped by a fibre-coupled, quasi-cw laser diode operating at 808nm. The nonlinear crystal is placed within the cavity of the pump laser so that it is subject to the high intracavity pump field, a direct effect of which is a reduction in the threshold of the OPO. As with the extracavity system, tuning is achieved by

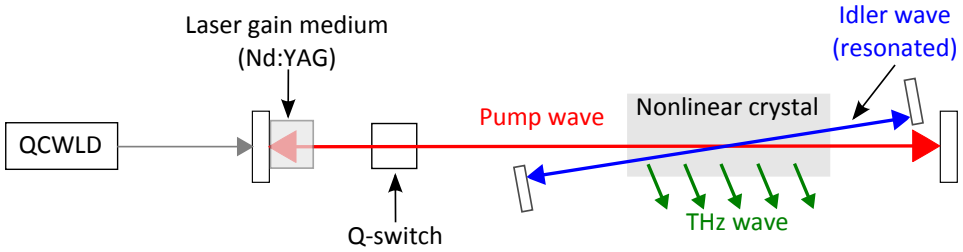

(a) Schematic of the intracavity terahertz OPO developed at the University of St Andrews.

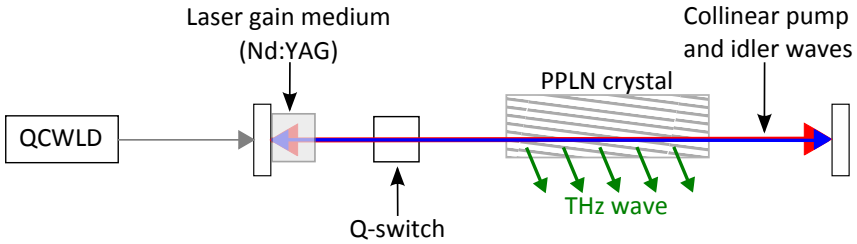

(b) Schematic of an intracavity terahertz OPO based on PPLN.

Figure 1.4: Two terahertz OPO configurations that have been realised by the St Andrews nonlinear optics group.

changing the angle of the idler cavity. The linewidth of the device can be reduced by using étalons within the pump and idler cavities [30], when the linewidth is reduced to $\lessapprox$1GHz, or by use of injection seeding, which results in a linewidth of $<$100MHz [31]. The development of the original intracavity terahertz OPO was the subject of an earlier thesis [32]. Further developments included the use of novel periodically-poled lithium niobate (PPLN) crystals to collinearise the pump and idler whilst maintaining the rapid exit of the terahertz through the side of the crystal, as shown in figure 1.4b. Phase-matching diagrams appropriate to the non-collinear system based on bulk lithium niobate and the collinear system based on PPLN are shown in figure 1.5. The introduction of a periodic structure within the lithium niobate can be regarded as the addition of a grating wave vector, G at an angle α to the optic axis [33]. However this grating vector is bi-directional, which results in two solutions to the phase-matching conditions, as illustrated in the figure. The consequences of this must be fully understood in order to produce useful devices. In collinearising the pump and

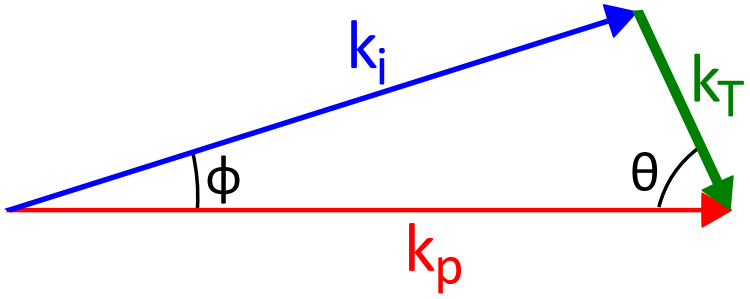

(a) A wave vector diagram illustrating the non-collinear phase-matching condition used in lithium niobate.

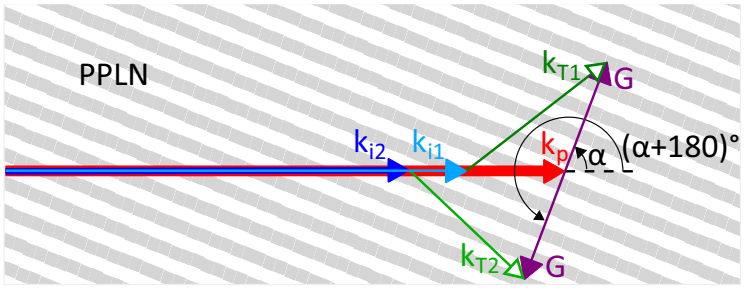

(b) A wave vector diagram illustrating collinear phase-matching using PPLN and the two possible phase-matching solutions.

Figure 1.5: Phase-matching diagrams representing the non-collinear and collinear phase-matching geometries.

idler waves, the ability to tune the terahertz OPO has been lost, although some amount of tuning is possible by changing the crystal temperature, as will be demonstrated later in this thesis. Since the gratings are custom-designable, however, PPLN crystals can be engineered to produce whatever terahertz frequency is desired by the end-user. PPLN-based devices may lead to the production of more compact and efficient terahertz sources, the discussion of which topic will follow in subsequent chapters.

This thesis seeks to advance the level of understanding of the basic intracavity terahertz OPO in terms of the factors affecting its efficiency. The use of novel periodically-poled lithium niobate (PPLN) crystals and alternative phase-matching configurations are also investigated with the aim of further extending the operation of the terahertz OPO.

1.4 Thesis summary

Chapter 2 of this thesis examines the original intracavity terahertz OPO in detail with regard to the factors affecting its efficiency. The parasitic loss of the pump cavity is measured using several methods and the idler cavity parameters are assessed with regard to optimising the down-conversion efficiency of the OPO. The chapter concludes by demonstrating the operation of the system as a computer-controlled terahertz spectrometer.

In chapter 3 the characterisation of difference frequency generation between the terahertz and idler waves is presented. This phenomenon, to our knowledge, is reported here for the first time, having previously only been observed in systems based on periodically-poled lithium niobate. Comprehensive investigations of temporal and spectral profiles, phase-matching and angle of emission were undertaken to confirm the difference frequency generation process. A model has been developed to predict the enhancement of the terahertz field by the difference frequency generation process, and the implications for improving down-conversion efficiencies are explored.

Chapters 4 and 5 present the methods used to design PPLN crystals and the characterisation of several devices based on these materials. Comparisons are made between these devices and the original device based on the bulk material. A particular issue explored is the role of the grating vector, which is a bipolar vector, and its impact on device performance. A novel hybrid phase-matching scheme is proposed and analysed, leading to computer modelling for device optimisation. The work presented in these chapters is being prepared for submission as journal articles.

The use of injection seeding to improve the operation of the terahertz OPOs, both in terms of a reduction in threshold and improved down-conversion efficiency, is reported in chapter 6. The terahertz OPO utilising a collinear phase-matching geometry with PPLN exhibited a large improvement in its efficiency, being brought to the point of showing measurable pump depletion, something which had not been possible in the absence of injection seeding. This work will aid the development of more efficient PPLN-based devices and is also being prepared for inclusion in a publication.

Finally, chapter 7 concludes the thesis by reflecting on the work presented and highlighting the possible direction for future experiments.

The following papers are being prepared for submission on the basis of the work described in this thesis:

1. "*The development of a terahertz spectrometer based on parametric generation using MgO:LiNbO$_3$*" (see chapter 2)
2. "*Difference frequency generation in lithium niobate and its potential to enhance the parametric generation of terahertz radiation*" (see chapter 3)
3. "*The design and experimental characterisation of PPLN crystals for the parametric generation of terahertz radiation*" (see chapters 4, 5 and 6)
4. "*A comparative study of intracavity terahertz OPOs based on bulk and periodically-poled MgO:LiNbO$_3$*" (see chapters 5 and 6)

References

[1] Y.-S. Lee. *Principles of Terahertz Science and Technology*. Springer US, 2009.

[2] A. J. Fitzgerald, B. E. Cole, and P. F. Taday. Nondestructive analysis of tablet coating thicknesses using terahertz pulsed imaging. *Journal of Pharmaceutical Sciences*, 94(1):177–183, 2005.

[3] M. Nagel, P. Haring Bolivar, M. Brucherseifer, H. Kurz, A. Bosserhoff, and R. Buttner. Integrated thz technology for label-free genetic diagnostics. *Applied Physics Letters*, 80(1):154–156, 2002.

[4] B. B. Hu and M. C Nuss. Imaging with terahertz waves. *Optics Letters*, 20:1716–1718, 1995.

[5] A. Dobroiu, Y. Sasaki, T. Shibuya, C. Otani, and K. Kawase. THz-Wave Spectroscopy Applied to the Detection of Illicit Drugs in Mail. *Proceedings of the IEEE*, 95(8):1566–1575, 2007.

[6] J. M. Chamberlain. Where optics meets electronics: recent progress in decreasing the terahertz gap. *Phil. Trans. R. Soc. Lond. A*, 362:199–213, 2004.

[7] A. G. Davies, E. H. Linfield, and M. B. Johnston. The development of terahertz sources and their applications. *Physics in Medicine and Biology*, 47(21):3679, 2002.

[8] G. Kh. Kitaeva. Terahertz generation by means of optical lasers. *Laser Physics Letters*, 5(8):559–576, 2008.

[9] M. Naftaly, R. A. Dudley, J. R. Fletcher, F. Bernard, C. Thomson, and Z. Tian. Frequency calibration of terahertz time-domain spectrometers. *J. Opt. Soc. Am. B*, 26:1357–1362, 2009.

[10] G. Ramian. The new UCSB free-electron lasers. *Nuclear Instruments and Methods in Physics Research Section A: Accelerators, Spectrometers, Detectors and Associated Equipment*, 318(13):225 – 229, 1992.

[11] M. A. Belkin, Q. I. Wang, C. Pflügl, A. Belyanin, S. P. Khanna, A. G. Davies, E. H. Linfield, and F. Capasso. High-Temperature Operation of Terahertz

Quantum Cascade Laser Sources. *IEEE Journal of Selected Topics in Quantum Electronics*, 15:952–969, 2009.

[12] Virginia Diodes, Inc. Millimeter-Wave & THz Systems. http://vadiodes.com/index.php?option=com_content&view=article&id=180:systems&catid=21&Itemid=16 (Accessed 31/03/2012).

[13] J. L. Hesler, D. Porterfield, W. Bishop, T. Crowe, A. Baryshev, R. Hesper, and J. Baelmans. Development and Characterisation of an Easy-to-Use THz Source. In *16th International Symposium on Space Terahertz Technology*, 2005.

[14] T. W. Crowe, J. L. Hesler, S. A. Retzloff, C. Pouzou, and G. S. Schoenthal. Solid-State LO Sources for Greater than 2THz. In *22nd International Symposium on Space Terahertz Technology*, 2011.

[15] J. A. Giordmaine and R. C. Miller. Tunable Coherent Parametric Oscillation in $LiNbO_3$ at Optical Frequencies. *Phys. Rev. Lett.*, 14:973–976, 1965.

[16] R. L. Byer, M. K. Oshman, J. F. Young, and S. E. Harris. Visible CW parametric oscillator. *Applied Physics Letters*, 13:109–111, 1968.

[17] R. G. Smith, J. E. Geusic, H. J. Levinstein, S. Singh, and L. G. Van Uitert. Low-Threshold Optical Parametric Oscillator using $Ba_2NaNb_5O_{15}$. *J. Appl. Phys.*, 39:4030–4032, 1968.

[18] M. H. Dunn and M. Ebrahimzadeh. Parametric Generation of Tunable Light from Continuous-Wave to Femtosecond Pulses. *SCIENCE*, 286:1513–1517, 1999.

[19] S. E. Harris. Tunable Optical Parametric Oscillators. *Proceedings of the IEEE*, 57(12):2096–2113, 1969.

[20] J. Gelbwachs, R. H. Pantell, H. E. Purhoff, and J. M. Yarborough. A tunable stimulated Raman oscillator. *Applied Physics Letters*, 14:258–262, 1969.

[21] C. H. Henry and C. G. B. Garrett. Theory of Parametric Gain near a Lattice Resonance. *Phyiscal Review*, 171:1058–1064, 1968.

[22] J. M. Yarborough, S. S. Sussman, H. E. Purhoff, R. H. Pantell, and B. C. Johnson. Efficient, tunable optical emission from $LiNbO_3$ without a resonator. *Applied Physics Letters*, 15(3):102–105, 1969.

[23] B. C. Johnson, H. E. Puthoff, J. SooHoo, and S. S. Sussman. Power and linewidth of tunable stimulated far-infrared emission in $LiNbO_3$. *Applied Physics Letters*, 18:181–183, 1971.

[24] M. A Piestrup, R. N. Fleming, and R. H. Pantell. Continuously-tunable submillimeter wave source. *Applied Physics Letters*, 25:418–420, 1975.

[25] K. Kawase, M. Sato, T. Taniuchi, and H. Ito. Coherent tunable THz-wave generation from $LiNbO_3$ with monolithic grating coupler. *Applied Physics Letters*, 68:2483–2485, 1996.

[26] M. Ebrahimzadeh, G. A. Turnbull, T. J. Edwards, D. J. M. Stothard, I. D. Lindsay, and M. H. Dunn. Intracavity continuous-wave singly resonant optical parametric oscillators. *J. Opt. Soc. Am. B*, 16:1499–1511, 1999.

[27] D. J. M. Stothard, P. Y. Fortin, A. Carleton, M. Ebrahimzadeh, and M. H. Dunn. Comparison of continuous-wave optical parametric oscillators based on periodically poled $LiNbO_3$ and periodically poled $RbTiOAsO_4$. *J. Opt. Soc. Am. B*, 20:2102–2108, 2003.

[28] D. Stothard, C. F. Rae, and M. H. Dunn. An Intracavity Optical Parametric Oscillator With Very High Repetition Rate and Broad Tunability Based Upon Room Temperature Periodically Poled $MgO:LiNbO_3$ With Fanned Grating Design. *IEEE Journal of Quantum Electronics*, 45:256–263, 2009.

[29] T. J. Edwards, D. Walsh, M. B. Spurr, C. F. Rae, M. H. Dunn, and P. G. Browne. Compact source of continuously and widely-tunable terahertz radiation. *Optics Express*, 14(4):1582–1589, 2006.

[30] D. J. M. Stothard, T. J. Edwards, D. Walsh, C. L. Thomson, C. F. Rae, M. H. Dunn, and P. G. Browne. Line-narrowed, compact and coherent source of widely tunable terahertz radiation. *Applied Physics Letters*, 92:141105, 2008.

[31] D. Walsh, D. J. M. Stothard, T. J. Edwards, P. G. Browne, C. F. Rae, and M. H. Dunn. Injection-seeded intracavity terahertz optical parametric oscillator. *J. Opt. Soc. Am. B*, 26:1196–1202, 2009.

[32] D. A. Walsh. *Intracavity Terahertz Optical Parametric Oscillators.* PhD thesis, University of St Andrews, 2010.

[33] W. Koechner. *Solid-State Laser Engineering (6^{th} ed.).* Springer, 2006.

2

The intersecting cavity terahertz OPO

In this chapter a detailed characterisation of the intersecting cavity terahertz OPO is presented. Through careful measurement and analysis of the operational characteristics of the pump laser and the OPO we trace the flow of energy through the various processes that take place, quantify the losses of the pump and idler cavities and investigate the effect of several cavity parameters on the performance of the OPO in relation to its optimisation. The attainment of this new level of understanding of the system has also proved invaluable to increasing our understanding of systems based on periodically-poled lithium niobate (see chapters 4 and 5) in relation to comparing the suitability of poled and non-poled materials for the generation of terahertz radiation using optical methods. The development of a computer-controlled terahertz spectrometer, based on a terahertz OPO reported elsewhere [1, 2], is also reported. The spectrometer can be tuned across a user-specified spectral region and exhibits excellent repeatability of tuning; it has also been used by several collaborators from outwith the University of St Andrews for spectroscopic studies of various materials, the results of some of which studies will be presented here.

The terahertz OPOs described in this thesis all share a single pump laser source. It is therefore imperative to understand the behaviour of the pump laser so as to make meaningful and quantitative comparisons between the different systems. The original intersecting cavity terahertz OPO was designed and constructed in collaboration with Drs David Walsh, Tom Edwards and David Stothard and has

been presented in [1, 2]. The in-depth characterisation of this device, leading to new insights and further refinements, is the subject of this chapter. This device is also the basis of several new terahertz OPO systems that will be discussed in later chapters.

2.1 System overview

The basic layout of our intersecting cavity terahertz OPO is shown in figure 2.1. This original device, which underpins all of the subsequent terahertz OPOs presented here, was strongly influenced by the extracavity terahertz OPO developed by Kawase and co-workers [3]. The innovative step of placing the nonlinear crystal within the pump laser cavity serves to reduce the oscillation threshold by an order of magnitude[1], increases efficiency and thereby results in more compact devices.

Mirrors M1 (R>98% at 1064nm, high transmission at 808nm) and M2 (R=98% at 1064nm) form the cavity for the Q-switched pump laser; M1 was deposited directly onto the laser gain medium (LG) - a Nd:YAG crystal (1.3% doping, Northrop Grumman), 7mm long and 4mm in diameter. The cavity length was approximately 38cm. Although the use of a 100% reflectivity mirror for M2 would result in higher intracavity intensities and therefore lower thresholds it is necessary to have some transmission of the pump field in order to observe its down-conversion. The Q-switch ('QS' in the diagram) is comprised of a quarter-wave plate (QW), a Pockels cell (PC) and an air-spaced polarising beam cube (PC). A quasi-continuous wave laser diode (QCWLD) purchased from LIMO Littsoschenko provides the 808nm pump light, which is imaged in a 1:1 ratio from the end of an optical fibre into the laser gain medium via a pair of aspheric lenses. The nonlinear crystal (MgO:$LiNbO_3$) has dimensions (5×5×30)mm and has its crystallographic z axis parallel to the polarisation of the laser. The ends of the crystal are anti-reflection coated at 1064nm and the (5×30)mm side faces, through which the terahertz wave is extracted, have a high-quality optical polish. An array of four high-resistivity (>10kΩcm) silicon prisms (SP) is used for

index-matching to couple the terahertz radiation out of the crystal. Good optical contact between the prisms and the nonlinear crystal is maintained using a specially designed crystal mount.

Mirrors M3-M5 form the OPO idler cavity (note that we adopt the convention that the generated infrared light is called the "idler" and the lowest frequency the "THz" wave, rather than the standard labelling of the "pump", "signal" and "idler" in order of decreasing frequency.). M3 has a reflectivity of 94%, M4 is a high reflector at 45° and M5 is a high reflector. The coatings of all the mirrors are the same as the pump wavelength (1064nm), one of the advantages of the pump and idler wavelengths being so close to each other. The "dog-leg" cavity arrangement shown in figure 2.1 allows for various cavity parameters including the length and and output reflectivity to be explored easily by changing M3 alone. These effects will be discussed later in this chapter.

2.2 The pump laser

A quasi-continuous wave LIMO fibre-coupled diode laser was purchased for the purpose of end pumping the intracavity terahertz OPO. This laser is capable of producing up to 100W of continuous wave radiation in pulses up to 500μs duration at repetition rates of up to 400Hz. The light was coupled into an 800μm core optical fibre via a pair of aspheric lenses. The pulse characteristics of this laser allow pumping the Nd:YAG for ≈2 fluorescence lifetimes (τ ≈250μs), allowing a significant build up of population inversion for later extraction via Q-Switching, whilst maintaining a lower average power than continuous

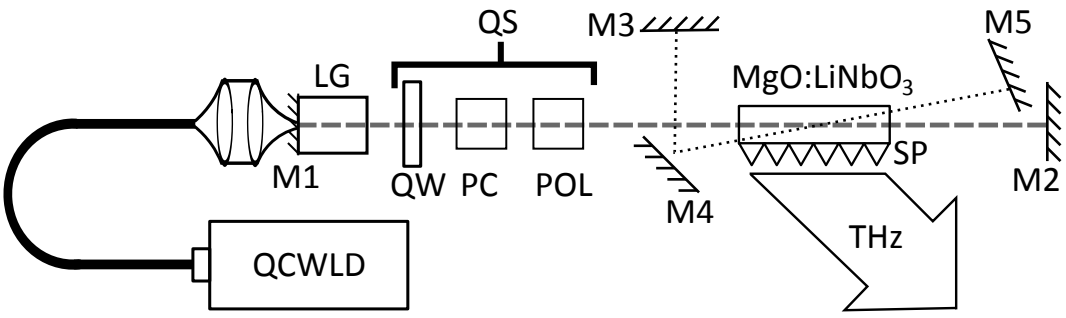

Figure 2.1: The design of the basic intersecting cavity terahertz OPO. The dashed and dotted lines respectively indicate the paths of the Q-switched pump and idler waves.

pumping would require for the same result. Laser diodes are prone to temperature tuning effects, so to ensure optimal efficiency the laser diode was temperature stabilised via a thermo-electric cooler at 25°C, where minimum transmission through the Nd:YAG was observed, and hence maximum energy absorption.

The pump volume was measured by placing a 100mm focal length lens at a distance 2f from both the mirrored end of the laser gain medium and a CCD camera used to acquire beam profile data via the BeamPro software package. The inclusion of an RG1000 absorption filter in the experimental setup allowed the fluoresence volume to be measured. Both the fluoresence and pump volumes are shown in figure 2.2; the pump volume was confirmed as ≈800μm and had some localised peaks in intensity whereas the fluoresence volume profile does not exhibit these. The fluorescence volume is Gaussian-like and has a diameter of ≈1mm.

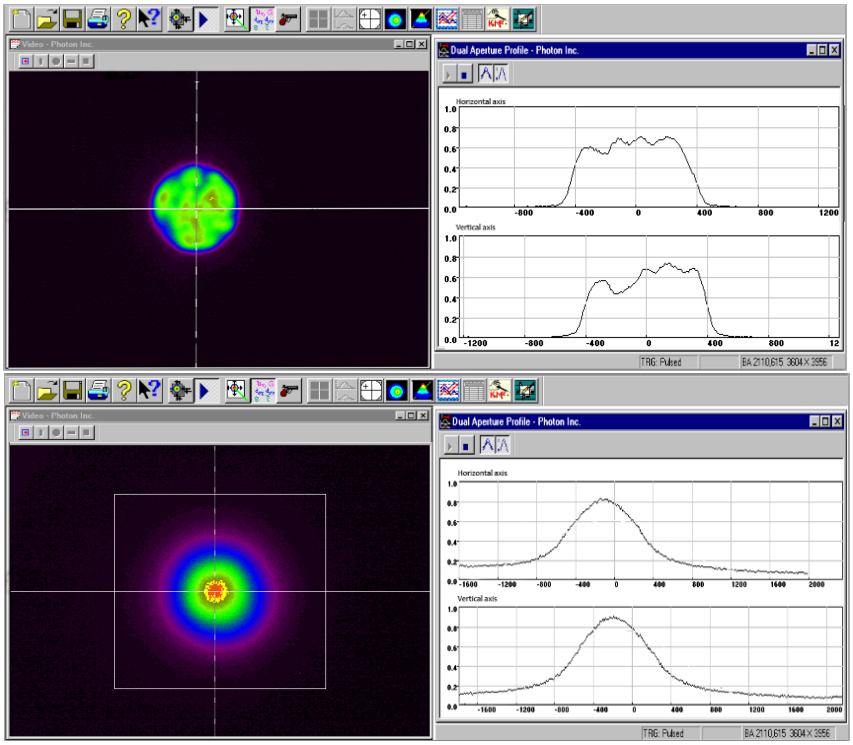

Figure 2.2: The upper images show the pump beam profile within the Nd:YAG crystal. The lower images show the fluoresence volume (1064nm), obtained by using a filter to block the residual 808nm light.

2.2.1 Output power as a function of drive current

The analysis outlined in this chapter of the thesis assesses the performance of the OPO in relation to the available power produced by the laser diode. Measurements of the laser diode power output were made as a function of increasing drive current so that absolute pump energies could be established.

Measurements of average power were made using a Melles Griot broadband power meter comprising a 10mm diameter thermopile. The average power is converted to pulse energies using the relation:

$$E_{pulse}(J) = \frac{\text{mean power (W)}}{\text{repetition rate (Hz)}} \tag{2.1}$$

The energy-current characteristic for the laser diode is shown in figure 2.3 and displays the anticipated linear dependence of energy on drive current when operating above laser threshold (19.6A).

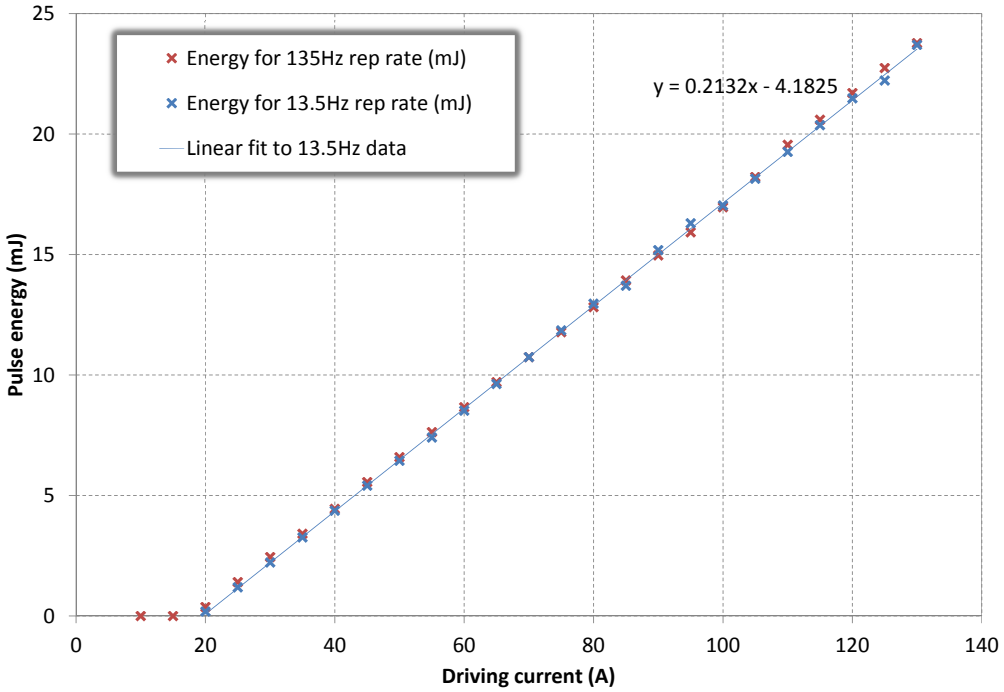

Figure 2.3: Energy-current characteristic of the LIMO pump laser output measured from the coupling fibre. The pulse duration was 250μs.

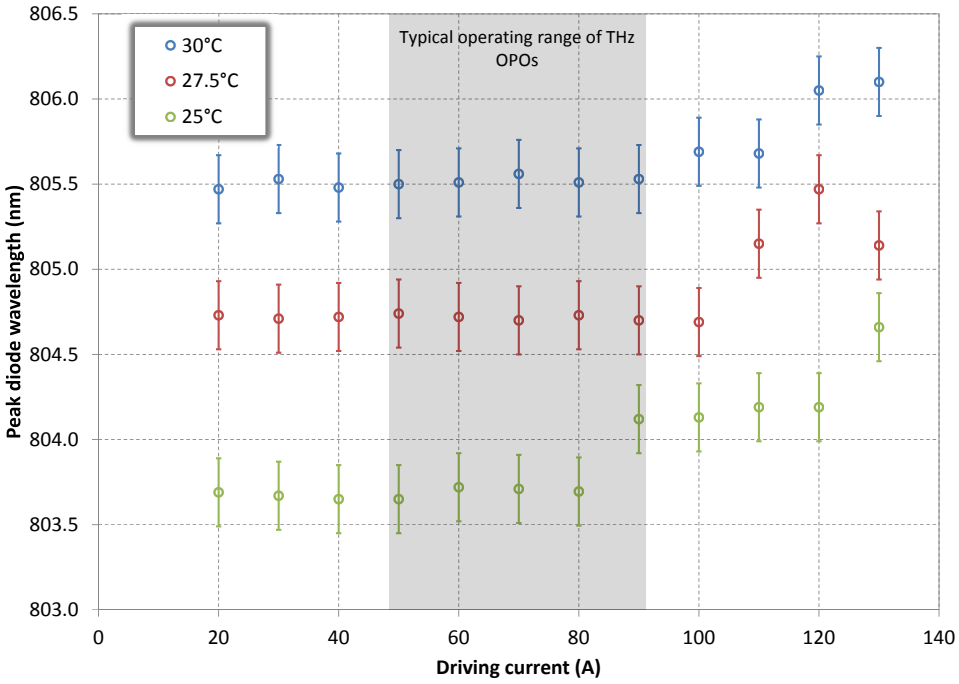

Figure 2.4: The variation of the output wavelength of the laser diode as a function of operating temperature and driving current. The typical range of OPO operation is indicated by the shaded grey area.

2.2.2 Wavelength variation with respect to current and temperature

The temperature tuning effects of the laser diode were characterised by measuring the spectral peak of the diode output using an optical spectrum analyser (OSA) as a function of laser diode temperature and driving current. Figure 2.4 shows the outcome of this investigation. A thermo-electric cooler was used to temperature stabilise the laser diode at 25°C, at which point there was minimum transmission through the Nd:YAG crystal, implying a maximum in energy absorption.

2.2.3 Parasitic loss of the 1064nm pump laser

To make an accurate assessment of the efficiency of the pump laser and, subsequently, the intersecting cavity terahertz OPO, it is imperative to know the parasitic losses of the system so that measured pulse energies can be translated into intracavity energies. Here two methods for quantifying the parasitic losses of the pump laser are utilised and compared.

The first method used to determine the losses of the pump laser was that of Findlay and Clay [4]. This analysis makes use of the fact that the higher the losses due to diffraction and output coupling are, the higher the threshold pump power will be. The relationship between the small-signal gain and the losses at threshold can be described by the following condition [5]:

$$e^{g_0 l}\sqrt{R}V_D V_S = 1 \tag{2.2}$$

where $g_0 l = \Delta N \sigma l$ is the small-signal gain, ΔN is the inversion density between the upper and lower laser levels, σ is the stimulated emission cross-section, l is the length of the active medium, R is the reflectivity of the output coupler, V_D and V_S are the diffraction and scattering loss factors per transit, respectively. The pump power and the small-signal gain are related by:

$$P_{pump} = \frac{AI_S}{\eta_{excite}} g_0 l \tag{2.3}$$

where A is the cross-sectional area of the active medium, I_S is the saturation intensity and η_{excite} is the excitation efficiency (the ratio of the available power in terms of inversion to the pump power). Equations 2.2 and 2.3 can be combined to describe the pump power at threshold:

$$P_{pump,thresh} = \frac{AI_S}{\eta_{excite}} \left(\ln\left(\sqrt{R}\right) + \ln(V_D V_S) \right) \tag{2.4}$$

The threshold of the laser is measured for different output couplers by reducing the pump power until laser oscillation is barely visible. Then the threshold pump power is plotted as a function of the output coupler's reflectivity; the straight-line fit describing the data has an x-axis intercept equal to $\frac{AI_S}{\eta_{excite}} \ln(V_D V_S)$. Thus knowing the gradient and intercept of the best-fit line the round-trip loss factor $(V_D V_S)$ can be determined.

The threshold pump power was measured for five different plane output couplers, having reflectivities of 99.9%(high-reflector), 98%, 94%, 80%, 70% and 60%. The pump laser losses were characterised as more optical components were added, from the situation of an empty cavity up to the point where all the elements (including the nonlinear medium) were inserted and the pulse was Q-switched. Figures 2.5a and 2.5b provide the data for these two cases. The

Cavity setup	Gradient of fit	y-intercept	Loss	Loss due to error in fit	Loss from parallelogram
Empty	-90.681±5.267	2.661±0.738	2.89%	2.23-3.48	1.15-5.37
Polariser	-88.251±2.863	4.085±0.401	4.52%	4.42-4.80	3.62-5.93
Polariser+waveplate	-84.471±2.336	4.062±0.327	4.70%	4.45-4.93	3.68-5.94
Q-switched	-79.481±4.664	7.091±0.653	8.54%	8.25-8.77	6.38-11.71
Q-switched+crystal	-60.905±1.893	12.682±0.265	18.79%	18.63-18.97	15.63-22.94

Table 2.1: The resonator losses measured using the method of Findlay and Clay [4]. The losses are quoted in percent per round-trip and have been established using the error in the straight line fit and by constructing a parallelogram of errors.

mean value for the resonator losses was calculated as described earlier and by using least-squares fitting to determine the best-fit line. In order to estimate the errors in this loss value two strategies may be used:

Firstly, the errors in the gradient and intercept derived from the least-squares analysis can be used to create two other fits - one having the steepest gradient and highest intercept value and the other having the shallowest gradient and the lowest intercept value. The former leads to a higher loss value and the latter a lower loss value. Typically the errors from this approach are less than 1%. Secondly, a parallelogram of errors may be created. This analysis yields much higher errors, of the order 2%. Table 2.1 provides the numerical values of the round-trip losses under various conditions along with the errors in these values, calculated as described in the text.

An alternative approach to quantifying the losses of the pump laser is to utilise the characteristics of the relaxation oscillations that are observable when the laser is not Q-switched. The technique is described and demonstrated in a publication by Böhm and co-authors [6] and will be explained briefly here.

Transient solutions to the rate equations exhibit damped relaxation oscillations as they evolve towards the steady-state. As a result, small variations in pump power cause damped oscillations of the laser power at a frequency ω and damping rate Γ. In an ideal four-level laser the frequency and damping rate are described as

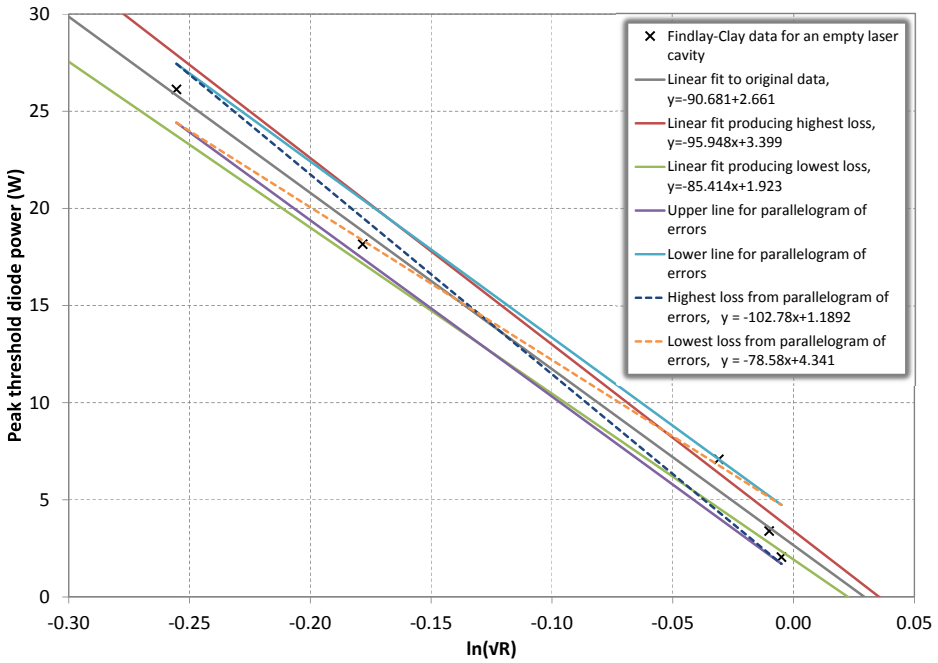

(a) A Findlay-Clay plot relating to the 1064nm pump laser with no other optical elements present in the cavity. The additional lines indicate the highest and lowest loss values (see text for details)

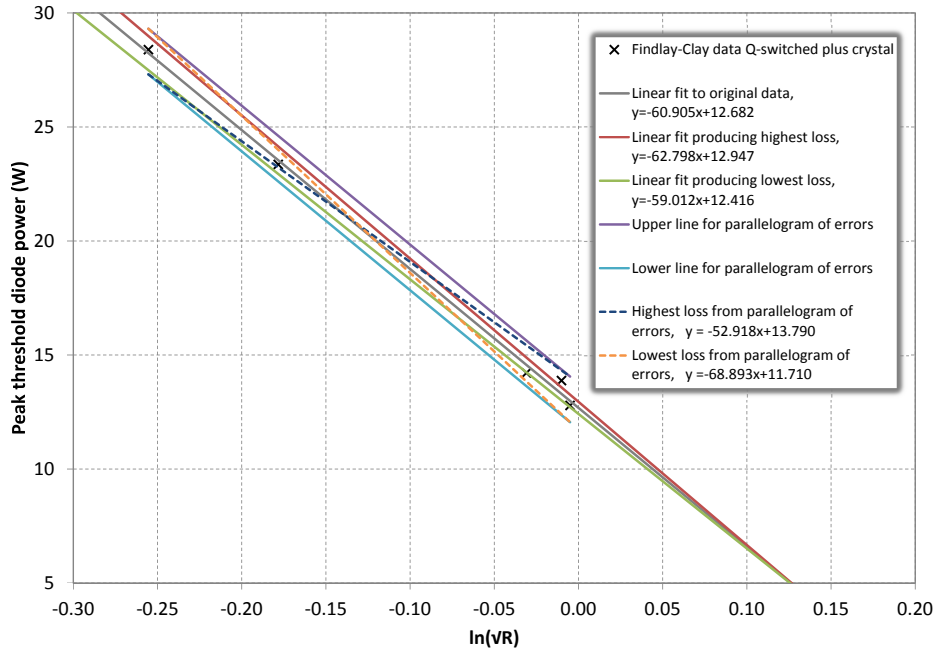

(b) A Findlay-Clay plot relating to the Q-switched 1064nm pump laser with all optical element present in the cavity.

Figure 2.5: Outcomes of the Findlay-Clay analysis of the pump cavity loss at different stages of its development.

follows:

$$\omega = \sqrt{\gamma\, A_3(\eta-1) - (\eta\, A_3/2)^2} \approx \sqrt{\gamma\, A_3(\eta-1)} \tag{2.5}$$

$$\Gamma = A_3\eta/2 \tag{2.6}$$

where η is the relative pump rate, A_3 is the atomic decay rate of the upper laser level (units of s^{-1} per atom) and γ is the cavity loss rate (units of s^{-1}). By squaring ω and rearranging the terms the following expression can be obtained for the cavity loss rate:

$$\gamma = \frac{\omega^2}{A_3(\eta-1)} \tag{2.7}$$

The expression for ω in equation 2.6 can be re-written in terms of the cavity lifetime, τ_c and the upper-state lifetime, τ:

$$\omega = \sqrt{\frac{(X-1)}{\tau_c\tau} - (\frac{X}{2\tau})^2} \approx \sqrt{\frac{(X-1)}{\tau_c\tau}}$$

which is equivalent to

$$\omega = \sqrt{\frac{(X-1)\beta\, c}{2L\tau}} \tag{2.8}$$

where X is equivalent to η, β is the fractional loss per round trip (parasitic loss plus output loss), L is the length of the optical cavity and τ, the upper-state lifetime, is given by $1/A_3$.The damping rate can also be expressed using the new terms as:

$$\Gamma = \frac{X}{2\tau} \tag{2.9}$$

As before, the expression for ω can be rearranged to yield a description of β:

$$\omega^2 = \frac{(X-1)\beta\, c}{2L\tau}$$

$$\beta(X-1) = \omega^2\left(\frac{2L}{c}\right)\tau \tag{2.10}$$

In equation 2.10 we now have an expression for the cavity losses that is dependent on measurable or experimentally-determinable quantities only! By constructing a graph of ω^2 against (X-1) a straight-line fit can be obtained, the gradient of which is equal to $\frac{\beta\, c}{2L\tau}$. Although the value of τ is well-documented and takes a value of approximately 230μs, its value can be obtained by examining a particular set of relaxation oscillations (at a known pumping level X) - by fitting an exponential decay of the form $y = Ae^{-\Gamma\, t}$ the value of τ can be

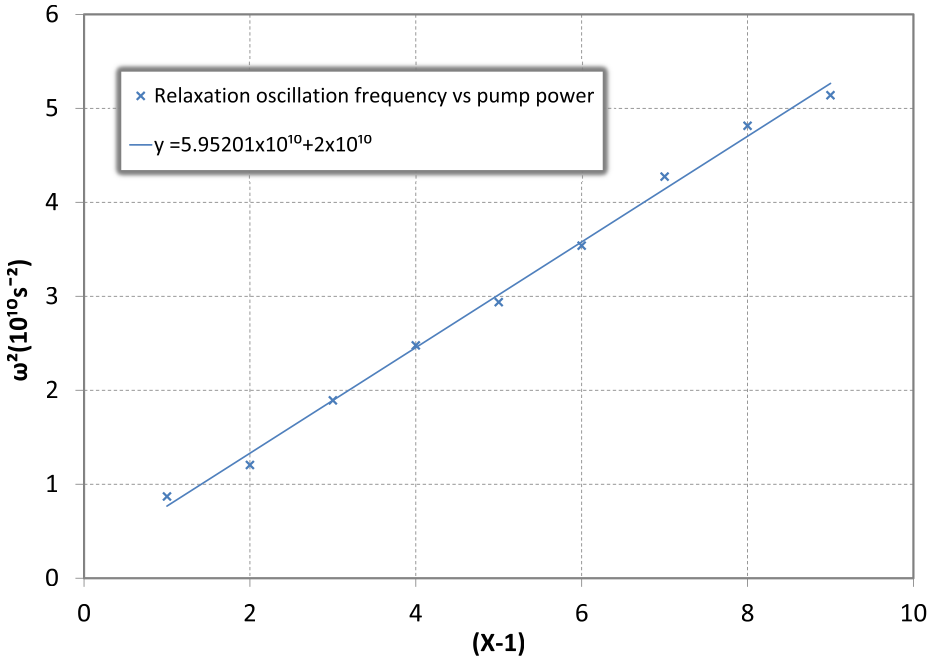

Figure 2.6: The relaxation oscillation frequency plotted as a function of pump power, where X is the number of times above threshold. The linear fit to the data yields a value for the parasitic loss of the resonator as described in the text.

extracted using the relationship in equation 2.9.

Figure 2.6 shows the plot of ω^2 against (X-1) for the 1064nm pump laser that is the subject of this chapter of the thesis. Present in the laser cavity are the $\lambda/4$ waveplate and the polarising beam cube, because the laser light must be polarised in order to achieve reliable measurements. In this case, the output coupler was made highly reflecting (R≈99.9%) since the parasitic loss was expected to be small. The total loss value implied by the gradient of the graph is 3.45%-3.53%, so the parasitic loss is in the region 3.35%-3.43%; these values agree reasonably with those in table 2.1.

2.2.4 Beam profiling

The pump laser cavity is formed from two plane mirrors and is, as such, unstable. Thermal lensing in the Nd:YAG gain medium introduces a curvature to stabilise the cavity, however the focal power of the thermal lens changes under different pumping conditions. The pump beam dimensions were characterised as a function of diode power with the measurements being performed using

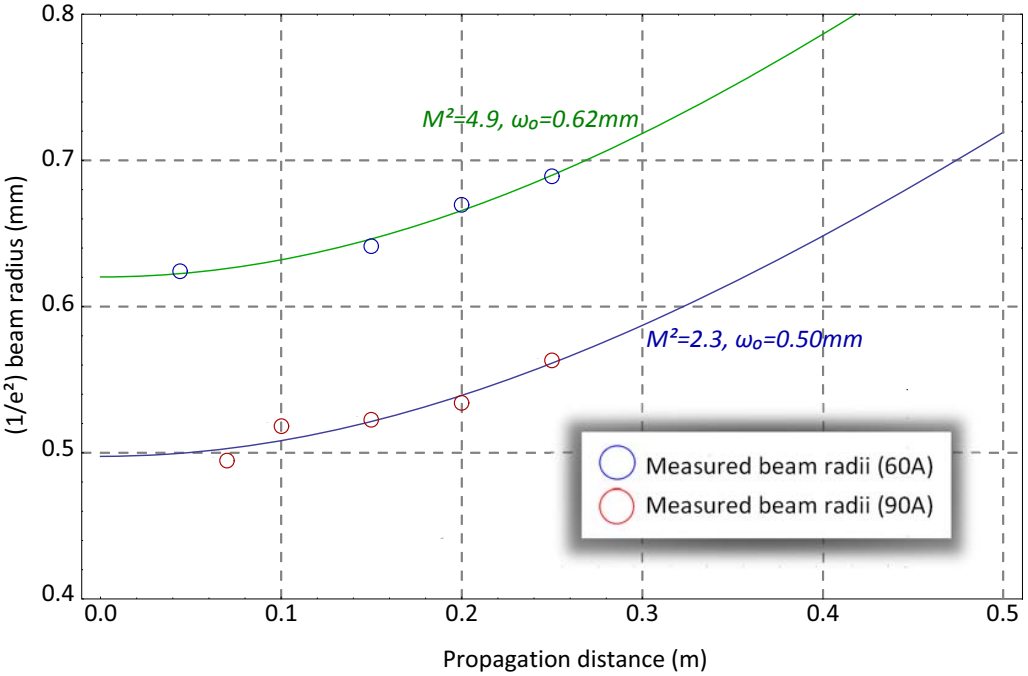

Figure 2.7: Graph showing the measured beam profiles at the two drive currents that broadly encompass the operating range of the terahertz OPOs. The circles indicate the measured data and the solid lines show the beam radii expected based on the beam waists and M^2 factors identified in the figure.

either a BeamPRO CCD-based beam profiling system or a knife-edge plus power meter arrangement.

Beam profile measurements at different operating levels (i.e. different diode powers) in a system operating at a repetition rate of 135Hz show that the dimensions of the $(1/e^2)$ beam radius decrease with increasing current (figure 2.7). This particular characteristic of the laser is undesirable, since it could lead to damage in the MgO:$LiNbO_3$ crystals due to the increase in intensity. By making comparisons between the measured $(1/e^2)$ beam radii and those predicted using the laser cavity modelling software *Psst!* [7] the relationship between the laser diode operating conditions and the focal length of the resulting thermal lens was established.

In *Psst!* the radius of curvature of the mirror corresponding to that deposited on the Nd:YAG crystal was changed incrementally and the effect on the beam radius at 10cm from the output coupler was noted. The radius of curvature is equal to

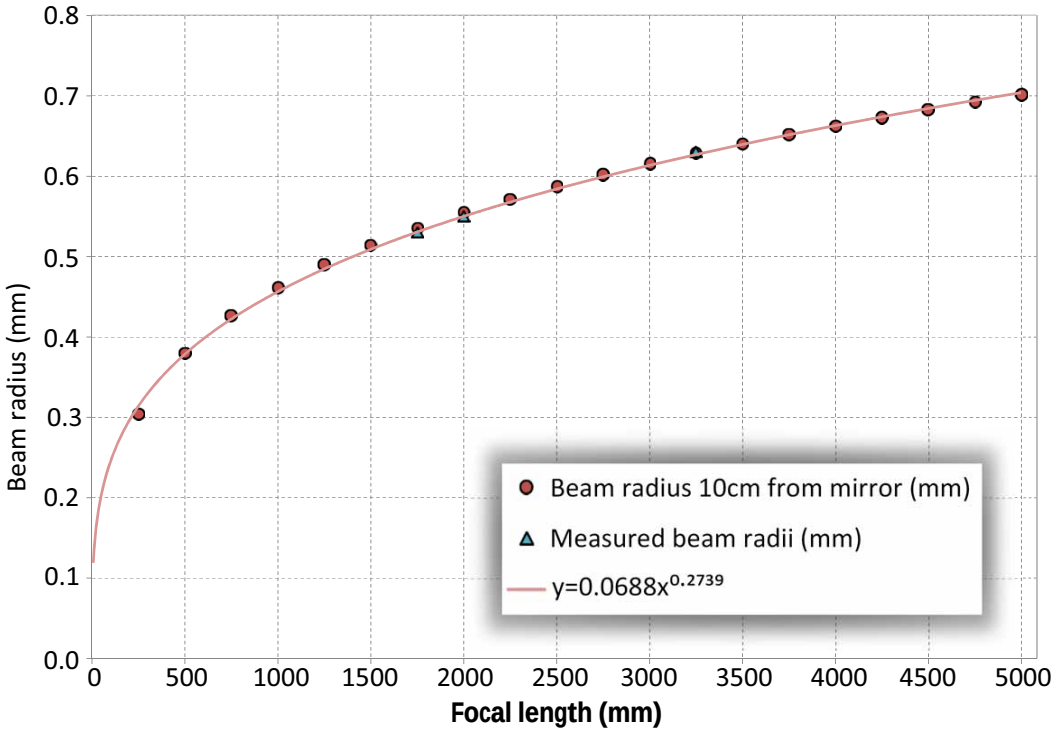

Figure 2.8: The measured and anticipated beam radii at a position 10cm from the output coupler. The measured radii are in excellent agreement with those predicted.

twice the focal length of the equivalent thermal lens. Measurement of a spot size at this position is equivalent to measurement of the spot size at 10cm inside the laser cavity because the beam waist is formed on the output coupler. The beam radius at this fixed point changes according to the following relation, which was determined using a least-squares fit:

$$(1/e^2)\text{beam radius (mm)} = 0.0688 \times (\text{focal length (mm)})^{0.2759} \tag{2.11}$$

as shown in figure 2.8, which shows the relationship between the beam radius and the focal length of the thermal lens.

Making use of the measured beam radii at certain known pumping levels and the relationship described by equation 2.11 the relationship between the focal length of the thermal lens and the laser diode peak power was determined as the follows:

$$\text{focal length (mm)} = (3 \times 10^6) \times (\text{diode peak power (W)})^{-2.102} \tag{2.12}$$

as shown in figure 2.9. By substituting equation 2.12 into equation 2.11 the variation of the beam radius with the diode peak power was derived. Hence

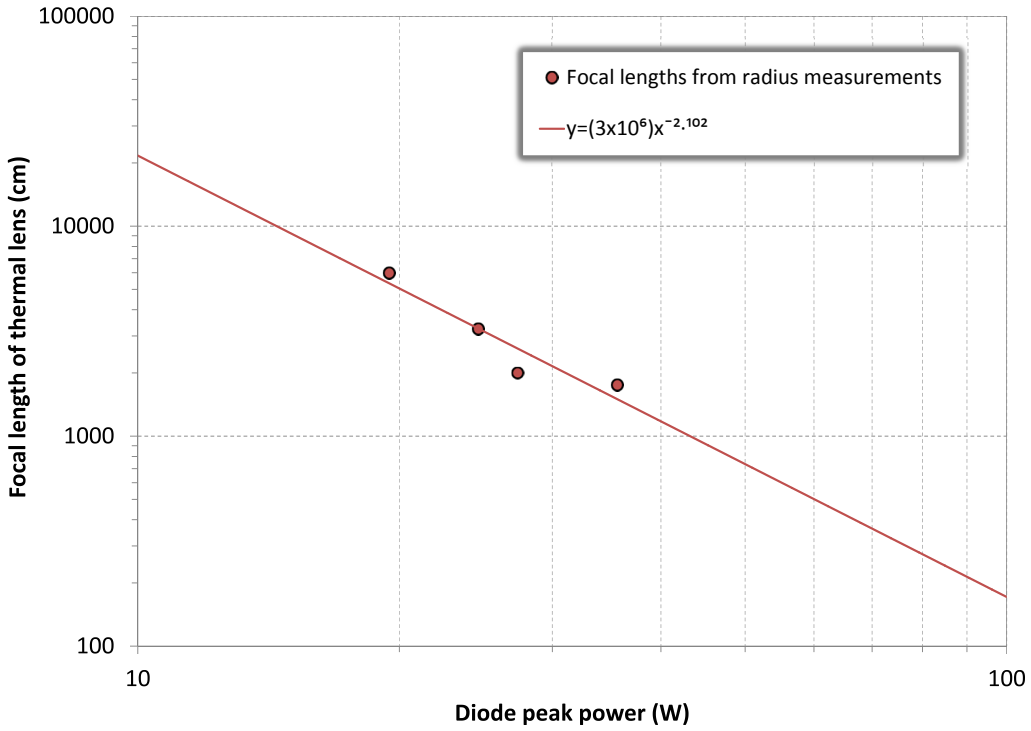

Figure 2.9: The dependence of the focal length (mm) of the thermal lens upon the diode peak power (W). The beam radii were measured at diode levels spanning the normal operating range. The graph is plotted on a log-log scale for clarity.

under similar pumping conditions (i.e. similar repetition rate, pump pulse duration etc.) an approximate value for the beam radius in the nonlinear medium could be obtained at any diode power level. This allowed pump intensities to be calculated relatively easily. Under other operating conditions the beam radius had to be measured separately.

The reduction in the beam size with increasing diode power highlighted by figures 2.7 and 2.8 could lead to damage in the $LiNbO_3$ crystal - the data shows that the beam radius can reduce by a factor of two across the operating range of the device, which in turn implies a factor of 4 increase in the intensity; hence it is desirable to keep the beam size as constant as possible. To that end, the use of intracavity lenses to stabilise the spot size was investigated.

The presence of even a weak, 1m focal length lens serves to minimise the change in spot size. The use of a 200mm focal length lens was also characterised in

relation to terahertz OPOs based on periodically-poled lithium niobate (PPLN) because the crystal dimensions available in this material are reduced relative to the bulk lithium niobate crystals, putting tighter constraints on the beam sizes needed. This investigation was carried out using the *Psst*! simulation package as before. All of the cavity parameters were kept constant and a lens of the appropriate focal length was incorporated into the cavity calculations, as shown in 2.10. Again, the radius of curvature of the Nd:YAG mirror was changed systematically to represent the changing thermal lens. Figure 2.11 shows the calculated effect of the thermal lens on the beam radius at a fixed position outside of the cavity under these conditions. A distance of 10cm beyond the plane output coupler was chosen since the location of the centre of the crystal is located 10cm from this mirror but inside the cavity, and the beam profile is symmetric about the outpur coupler. The intracavity lenses greatly reduce the impact of the thermal lens on the beam size as well as reducing the beam size itself. Figure 2.12 illustrates the measured difference in beam propagation for the situations with and without a lens inside the cavity.

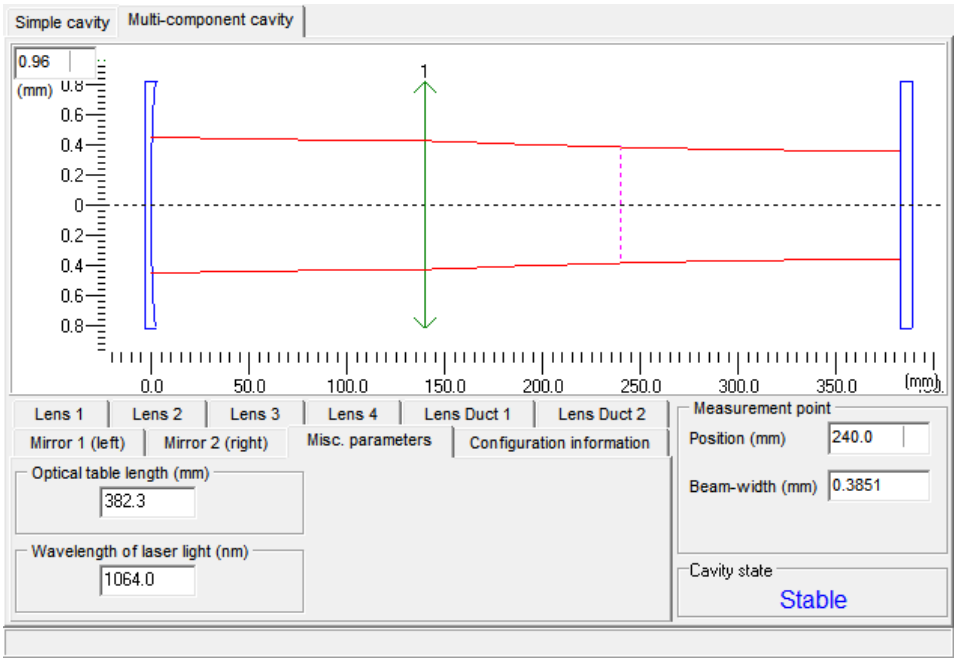

Figure 2.10: The *Psst*! model of the pump laser cavity with a 1m focal length lens inserted at a distance of 14cm from the mirror coated onto the Nd:YAG crystal. The position of the lenses was kept constant across the various experiments in which they were used.

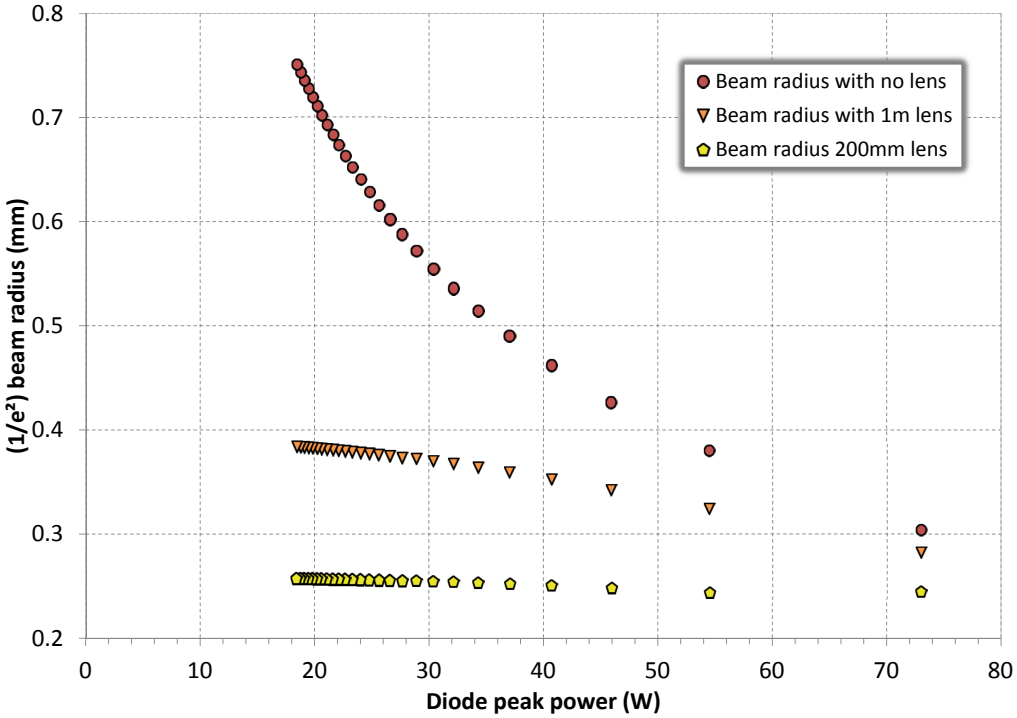

Figure 2.11: The beam radii calculated at a fixed position of 10cm outside the cavity and corresponding to the insertion of various lenses into the cavity.

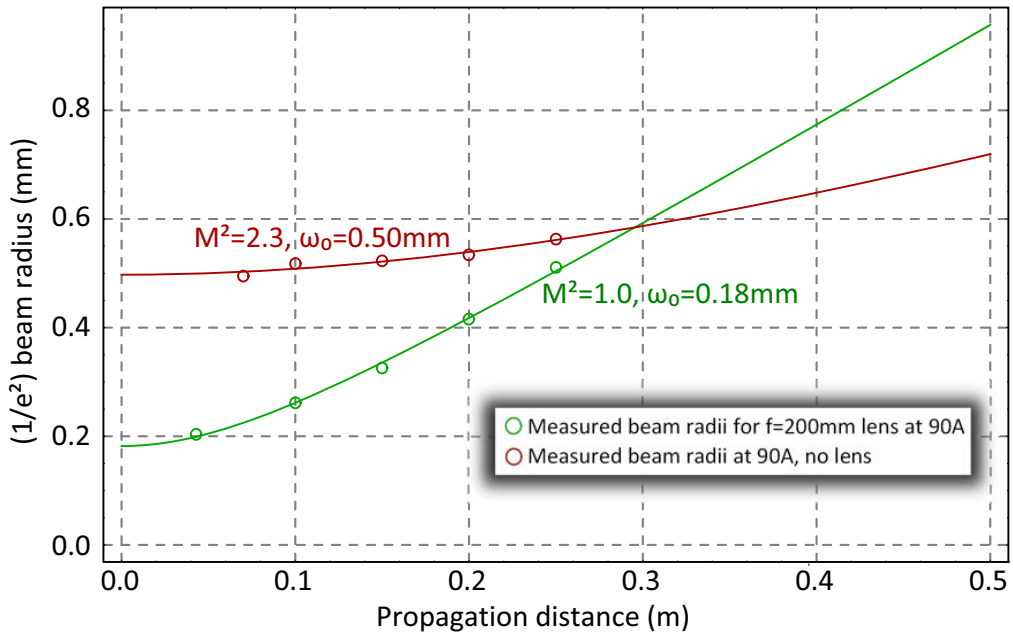

Figure 2.12: The beam profiles measured under identical pumping conditions for cavities with and without an intracavity lens. The lens both reduces the spot size by more than a factor of two in the region of the cavity where the nonlinear crystal is present and improves the beam quality.

2.2.5 Pump pulse duration

Crucial to the evaluation of intracavity pump intensities is the measurement of the temporal profile of the pulse. The full-width at half-maximum (FWHM) pulse duration of the undepleted pump pulse is used both in calculating the pump intensity and in gain calculations. The pump pulse was measured by focussing the output of the pump onto a fast (<1ns rise-time) photodiode connected to an oscilloscope from which the temporal data could be extracted. A typical set of depleted and undepleted pump pulse temporal profiles are shown in figure 2.13, in this case corresponding to a pump depletion of 53%. The undepleted pulse was measured by physically blocking the idler cavity to prevent down-conversion from occurring. The trigger point common to all temporal measurements is the point where a voltage is applied to the Q-switch and the background ringing on the traces is due to the Q-switch electronics. Mode beating of multiple longitudinal modes of the laser cavity cause the deep modulations seen in the pump pulse, which introduces an uncertainty in the measured pulse duration.

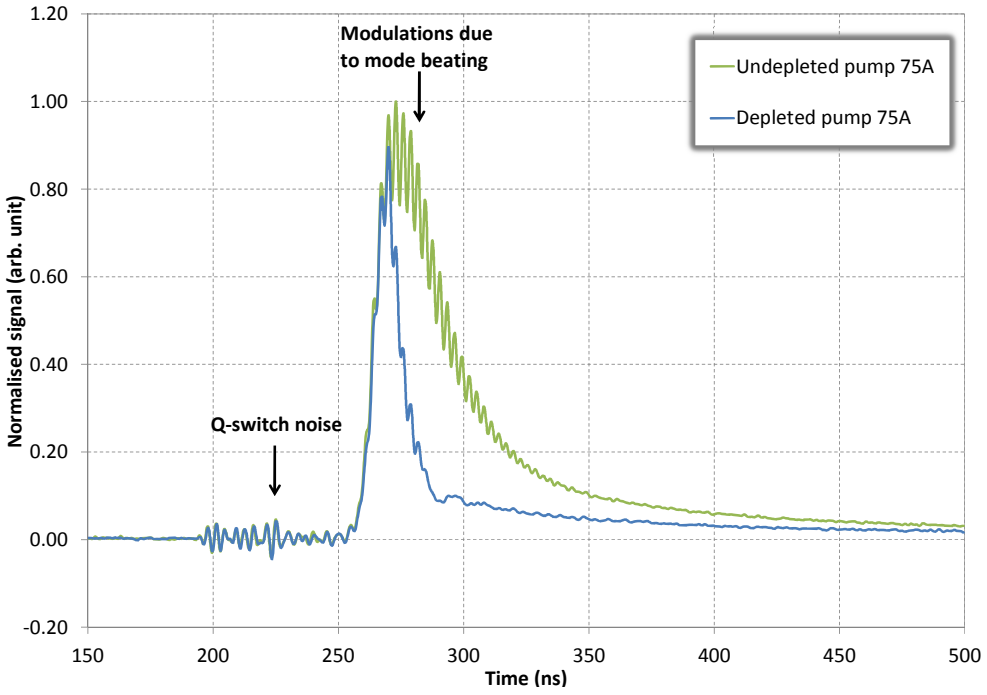

Figure 2.13: An example of a typical pump pulse with and without the down-conversion process taking place. Mode beating due to the multi-mode operation of the pump laser introduces uncertainties into the measurement of the pulse duration.

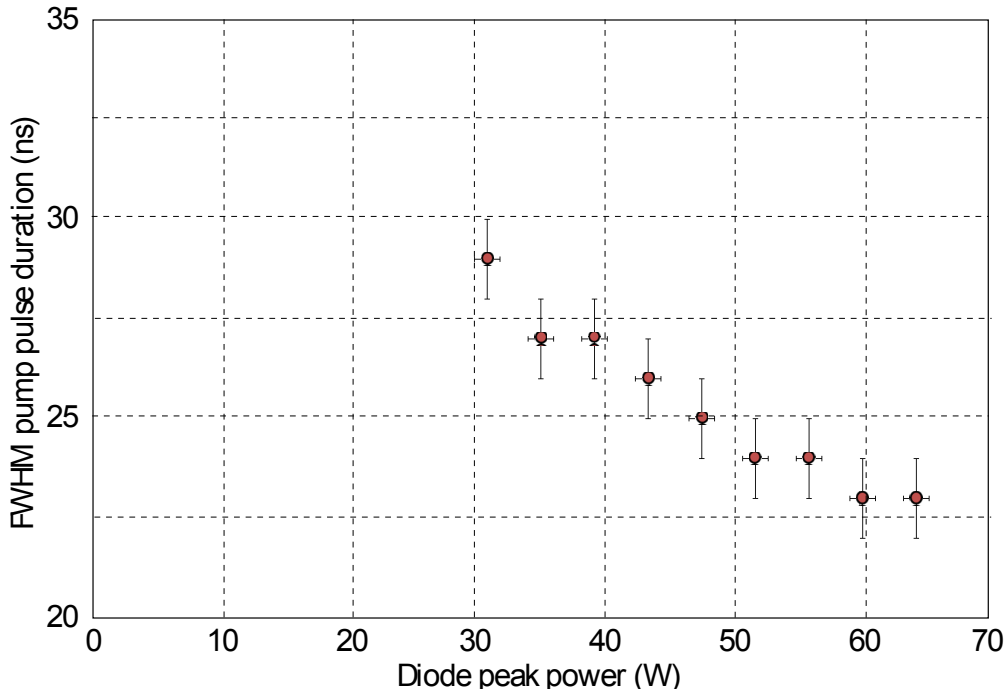

Figure 2.14: FWHM pump pulse durations corresponding to the OPO being above threshold but with the down-conversion process prevented by physically blocking the idler cavity.

Figure 2.14 shows the effect of increasing the diode peak power on the pump pulse duration for a system with a repetition rate of 135Hz. The data in the graph corresponds to the OPO operating above threshold and the error bars indicate the uncertainty in the pump pulse duration due to the mode-beating present in the profiles. It is seen that under these conditions the pump pulse duration is reduced from ≈30ns to ≈22ns across the range of diode powers for which the OPO is above threshold.

2.2.6 Determination of intracavity intensity

The pump intensity can be determined using the following relations:

$$\text{peak pump power (W)} = \frac{\frac{\text{mean undepleted pump power (W)}}{\text{repetition rate (Hz)}}}{\text{FWHM pulse duration (ns)}} \tag{2.13}$$

the intracavity power is given by

$$\text{intracavity pump power (W)} = \text{peak pump power (W)} \times \frac{1}{(1-R)} \tag{2.14}$$

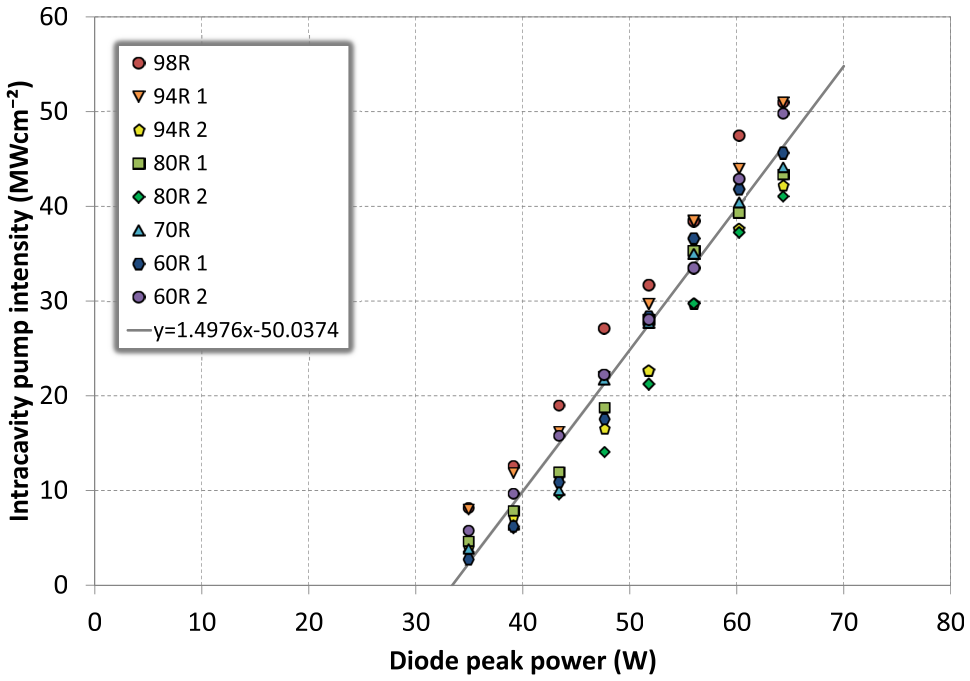

Figure 2.15: Operational characteristics of the pump laser corresponding to several different OPO idler cavities, measured with the idler cavity blocked so as to prevent the downconversion process from taking place. The data sets are labelled according to the reflectivity of the idler cavity output coupler.

and finally

$$\text{intracavity pump intensity (Wcm}^{-2}) = \frac{\text{intracavity pump power (W)}}{\pi((\frac{1}{e^2})\,\text{beam radius (cm)})^2} \tag{2.15}$$

where the beam radius can be calculated on the basis of the diode peak power, from equations 2.11 and 2.12.

By measuring the mean pump power and its duration (as shown in figure 2.13) across a range of idler cavity configurations, and making use of the relationships describing the pump beam radius as a function of diode power (equations 2.11 and 2.12) the intracavity pump pulse intensity was calculated for each data set. Figure 2.15 shows that all of the data sets describing the intracavity intensity of the pump laser can be represented by a single straight line fit having the equation $y = 1.4976x - 50.0374$. On that basis, any difference in the magnitude of the energy downconverted by the parametric process must be due to differences in the idler cavity.

2.3 The nonlinear material

The nonlinear material used in the intracavity terahertz OPO is magnesium oxide-doped lithium niobate (MgO:$LiNbO_3$), which shares many of the physical properties of lithium niobate ($LiNbO_3$) except that the photorefraction is reduced to the extent that devices based on MgO:$LiNbO_3$ can be operated at room temperature with a doping level of 5 mol$\%$ [8]. Since it is a well-established material there are several reviews describing the properties of lithium niobate [9–11].

In the ferroelectric phase (below the Curie temperature of 1210° C), lithium niobate possesses trigonal crystal symmetry with 3m point group symmetry about the optic ("c") axis. Lithium niobate is a negative uniaxial crystal with ordinary refractive index n_o and extraordinary refractive index n_e as indicated in figure 2.16. These refractive indices have been extensively characterised across the wide transparency range of ≈(0.4-5)μm [12, 13] for different levels of MgO-doping, Li content and operating temperatures.

The physical tensor properties of lithium niobate are described by a Cartesian coordinate system (x,y,z), with the x axis chosen to be parallel to the optic axis. The parametric gain coefficient, Γ, depends on the effective nonlinear coefficient, d_{eff}, according to the following relation:

$$\Gamma^2 L^2 = \frac{8\pi^2 d_{eff}^2 L^2}{c\epsilon_0 n_p n_i n_T \lambda_i \lambda_T} I_p \tag{2.16}$$

where d_{eff} is the effective nonlinear coefficient expressed in mV^{-1}; L is the crystal length expressed in metres; I_p is the pump intensity expressed in Wm^{-2}; $n_{p,i,T}$ are the refractive indices of MgO:$LiNbO_3$ at the pump, idler and terahertz wavelengths and λ_i and λ_T are the free-space wavelengths of the idler and terahertz waves expressed in metres. In the case of collinear gain, which is where all three waves propagate along the same direction, the interaction length, L, is equal to the crystal length.

It is evident that in order to increase the efficiency of the nonlinear process (by increasing the parametric gain coefficient) the magnitude of d_{eff} should be

maximised. The value of d_{eff} is dependent on the nonlinear tensor components and on the phase-matching configuration. The nonlinear tensor for lithium niobate is:

$$\tilde{d} = \begin{pmatrix} 0 & 0 & 0 & 0 & d_{31} & -d_{22} \\ -d_{22} & d_{22} & 0 & d_{31} & 0 & 0 \\ d_{31} & d_{31} & d_{33} & 0 & 0 & 0 \end{pmatrix}$$

where d_{22}, d_{31} and d_{33} are reported as being 2.1,-4.3 and -27pmV^{-1} respectively in the work of Roberts [14] and d_{31} and d_{33} are reported to take values of -4.6 and 25.4 pmV^{-1} in the work of Shoji [15]. These values were measured at a wavelength of 1064nm. The notation used for d_{ijk} is:

i:	x=1	jk:	xx=1	zy=yz=4
	y=2		yy=2	xz=zx=5
	z=3		zz=3	xy=yx=6

So to access the d_{33} component all three fields must have extraordinary polarisation. Such a situation cannot be exploited using birefringent phase-matching but can be exploited using non-collinear phase-matching, in which the generated terahertz frequency can be tuned by altering the phase-matching angle between the pump and idler waves.

In materials such as $LiNbO_3$ and MgO:$LiNbO_3$, which are both infrared- and

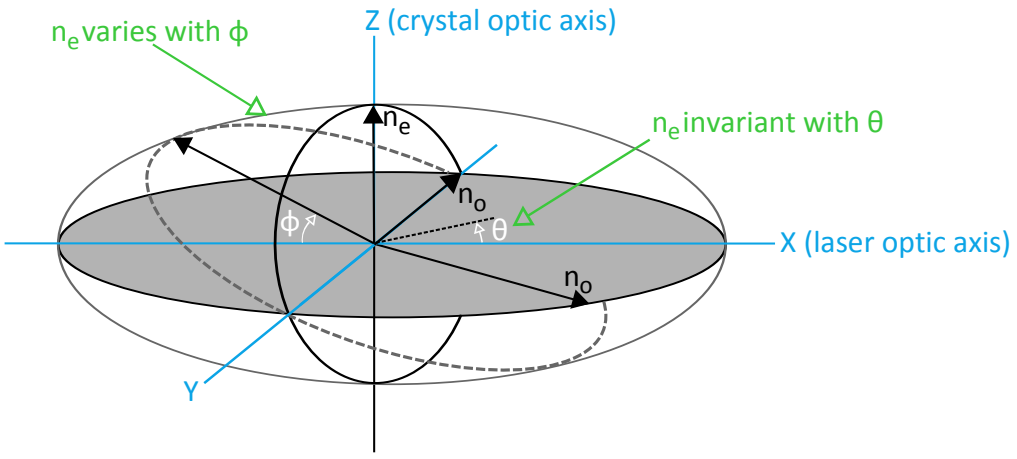

Figure 2.16: Optical ellipsoid for a negative uniaxial material. n_e does not vary with angle θ so walk-off is not a problem when eee-type phase-matching is employed.

Raman-active, the effective nonlinear coefficient d_{eff} can be enhanced by polariton resonances at the A_1-symmetry modes, due to coupling (energy transfer) between the electron cloud and the ions, causing ionic vibrations [16]. The effective nonlinear coefficient then becomes the sum of the electronic nonlinear coefficient, d_E, and the ionic nonlinear coefficient, d_Q, taking the form:

$$d_{eff} = d_E + d_Q = d_E + \sum_j \frac{\Omega_{Pj}^2 d' Q_j}{\omega_{0j}^2 - \omega_s^2} \tag{2.17}$$

where d_E is the usual electronic nonlinear coefficient (at optical frequencies), ω_s is the signal frequency, ω_{0j} is the resonant frequency of the j^{th} lattice vibration mode, Ω_{Pj} is the ionic plasma frequency for the j^{th} mode and $d'Q_j$ is the ionic coupling coefficient for mode j.

When ω_s is far from the lattice vibration frequency, the value of d_{eff} is dominated by d_E only. As ω_s approaches ω_{0j} the ionic contribution to d_{eff} increases. The lowest A_1-symmetry mode in $LiNbO_3$ is at 248cm^{-1} (≈7.4THz) [16] and it has been observed that the ionic nonlinearity can account for 80% of d_{eff} when ω_s is in the terahertz region [17]. This enhancement increases d_{eff} from ≈25pmV^{-1} at optical frequencies to ≈125pmv^{-1}, which results in a large parametric gain coefficient (see equation 2.16).

The absorption coefficient at terahertz frequencies is similarly affected by ionic vibrations and is described by:

$$\alpha_T = \frac{2\omega_T}{c} Im \left(\epsilon_\infty + \sum_j \frac{S_j \omega_{0j}^2}{\omega_{0j}^2 - \omega_T^2 - i\omega_T \Gamma_j} \right)^{1/2}$$

where ω_{0j}, S_j and Γ_j respectively denote the eigenfrequency, oscillator strength and bandwidth of the j^{th} A_1-symmetry mode and ϵ_∞ is the dielectric constant on the high frequency side of the vibration. The value of α_T lies in the range (10-100)cm^{-1} for the frequency range (0.5-2.0)THz. Such high absorption coefficients preclude collinear phase-matching. Instead, the non-collinear phase-matching geometry utilised in the present system ensures that the terahertz wave exits the MgO:$LiNbO_3$ crystal before suffering complete

absorption. The effect of absorption on the parametric gain will be discussed more extensively in the next section.

2.4 Parametric gain

In a singly-resonant OPO (SRO), the gain medium is placed within an optical cavity that resonates either the signal wave or the idler wave. The gain exhibited by the nonlinear medium must exceed the losses of that cavity within the duration of the pump pulse to the extent that significant pump pulse depletion, and thus down-conversion, can take place. It is due to the fact that the nonlinear medium itself has no inherent energy storage mechanism that the process must occur within the duration of the pump pulse.

On the assumption that the pump intensity is constant throughout the length of the nonlinear medium, the coupled wave equations can be solved to determine the single-pass gain, G, experienced by one or other of the down-converted waves (i.e. the idler or the terahertz wave):

$$G = \frac{I_{out}}{I_{in}} = \cosh^2[\Gamma\, L] \tag{2.18}$$

where I_{in} is the input intensity of the wave, I_{out} is its output intensity, L is the length of the nonlinear medium and Γ is the parametric gain coefficient, defined as in equation 2.16.

Example gain calculation for the case of collinear propagation

Here a typical case of terahertz wave generation is analysed, where:

$$\begin{aligned} L &= 30\text{mm}(= 0.03\text{m}); \\ d_{eff} &= 125\text{pmV}^{-1}(= 125 \times 10^{-12}\text{mV}^{-1}); \\ \lambda_i &= 1.07\mu\text{m}(= 1.07 \times 10^{-6}\text{m}); \\ \lambda_T &= 186.79\mu\text{m}(= 1.87 \times 10^{-4}\text{m}); \\ n_i &= 2.1; \\ n_T &= 5.05; \end{aligned}$$

then using equation 2.18 we obtain:

$$\Gamma^2 L^2 = (9.057 \times 10^{-11}) \times I_p(\mathrm{Wm}^{-2})$$

Taking a typical pump intensity of 40MWcm^{-2} (=4$\times$10^{11}Wm^{-2}), then:

$$G = \cosh^2[6.02] \approx 4.2 \times 10^4$$

For $LiNbO_3$ and MgO:$LiNbO_3$ however, the resonant enhancement effects due to polaritons that lead to a five-fold increase in the value of d_{eff} also result in strong absorption of the generated terahertz wave, meaning that it must be extracted from the nonlinear medium as rapidly as possible. This necessitates the use of a non-collinear phase-matching geometry.

The interaction length is thus limited either due to the rapid walk-off of the generated terahertz wave from the pump and idler waves which is necessary to avoid strong absorption losses, or it is limited by the absorption of the terahertz wave itself. The impact of these two possibilities on the interaction length is explored below.

2.4.1 The influence of the walk-off of the terahertz wave on the interaction length

The terahertz wave is now allowed to exit through the side face of the MgO:$LiNbO_3$ in order to minimize the absorption losses experienced by the terahertz wave, as shown in figure 2.17. A non-collinear phase-matching

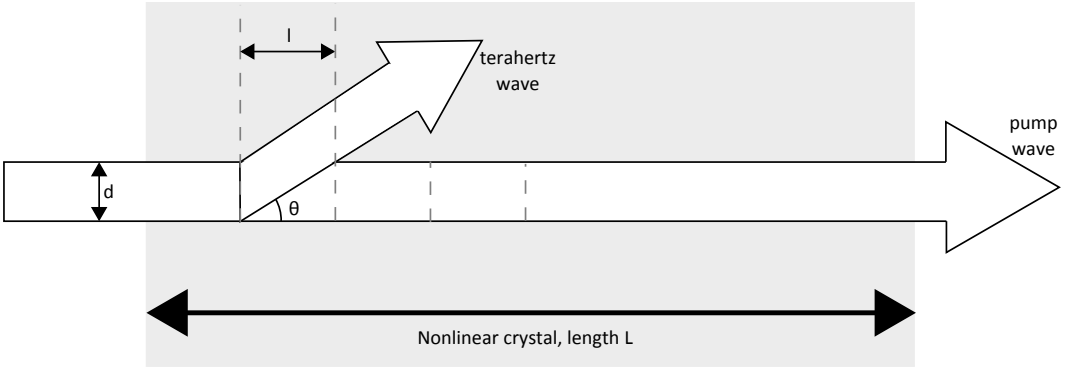

Figure 2.17: Illustration of the reduction in the interaction length caused by the large terahertz wave propagation angle.

geometry is thus required, with the terahertz wave propagating at an angle (typically $\geq$60°) to the pump and idler waves, which themselves remain almost collinear.

In this case the single-pass gain can be estimated by considering the nonlinear medium as being made up of segments, which are equal in length, over which the three waves can be regarded as overlapping such that equation 2.18 can be used to calculate the gain due to each of the segments separately. The total gain is then determined by the multiplication of the gains from the individual segments. The number of segments is given by:

$$N = \frac{L}{l}$$

where L is the length of the nonlinear medium and l is the segment length, described by:

$$l = \frac{d}{\tan\theta}$$

where θ is the walk-off angle of the terahertz wave.

The gain due to the i^{th} segment is (from equation 2.18):

$$g_i = \frac{I_{out}(i)}{I_{in}(i)} = \frac{I_{out}(i)}{I_{out}(i-1)} = \cosh^2[\Gamma_i l] \tag{2.19}$$

Assuming that the gain exhibited by one segment is the same for every segment, the overall gain experienced by the idler wave after having propagated through the entire length of the nonlinear medium is:

$$G_{single-pass} = \frac{I_{out}}{I_{in}} = g_1 g_2 ... g_{N-1} g_N = \cosh^{2N}[\Gamma_i l] \tag{2.20}$$

Example gain calculation including the effect of walk-off

Examining the situation where the parameters are the same as were used for the collinear case, except for the fact the terahertz wave propagates at an angle of 64° to the pump wave and assuming beam diameters of $\approx$1mm, then the segment length is:

$$l = \frac{1}{\tan 64°} = 0.49\text{mm};$$

and the number of gain segments is:

$$N = \frac{30}{0.49} = 61$$

Using equation 2.20 the single-pass gain is found to be:

$$G = \cosh^{122}[0.1] = (1.005)^{122} \approx 1.84$$

When compared with the collinear single-pass gain (4.2×10^4) the penalty suffered due to the walk-off of the terahertz wave becomes very clear.

2.4.2 The influence of terahertz absorption on the interaction length

The approach used to assess the effect of absorption of the terahertz wave on the interaction length is similar to that which was used to assess the effect of walk-off, except that the length, l, is now determined by the effective absorption length associated with the terahertz wave.

If the condition where only 5% of the initial terahertz field has not been absorbed at the end of a segment is adopted, then:

$$\frac{I}{I_0} = e^{-\alpha_T l} = 0.05$$

so

$$-\alpha_T l = \ln(0.05)$$

and

$$l = \frac{3}{\alpha_T} \tag{2.21}$$

where α_T is the absorption coefficient at the terahertz wavelength of interest.

Values of the terahertz absorption coefficient in both stoichiometric and congruent $LiNbO_3$ and MgO:$LiNbO_3$ have been obtained through various measurement techniques, including terahertz time-domain spectroscopy (THz-TDS) and Fourier transform infrared spectroscopy (FTIR) [17–20]. The absorption coefficient has also been calculated using the following relation:

$$\alpha_T = \frac{2\omega_T}{c}\mathrm{Im}\left(\epsilon_\infty + \sum_j \frac{S_j\omega_{0j}^2}{\omega_{0j}^2 - \omega_T^2 - i\omega_T\Gamma_j}\right)^{1/2} \tag{2.22}$$

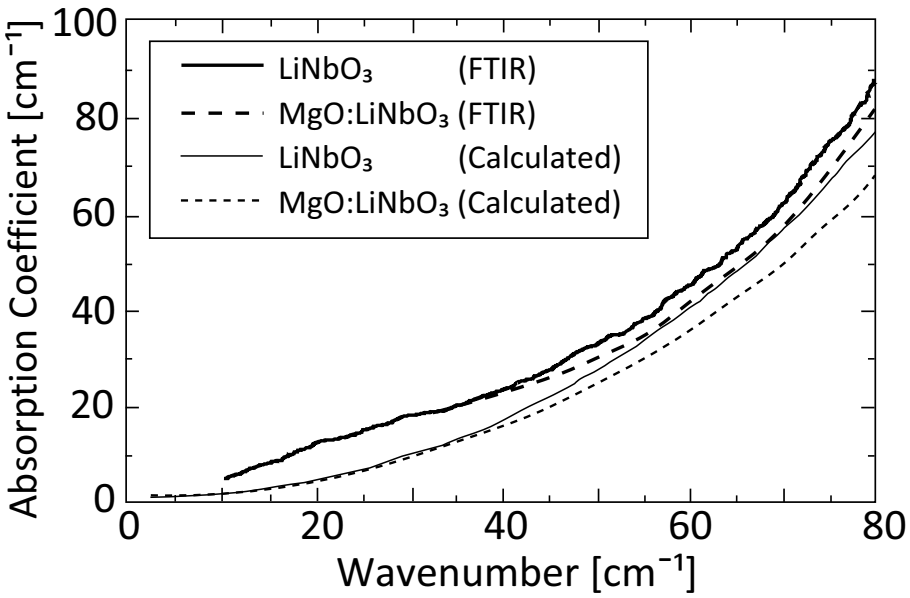

Figure 2.18: Plot reproduced from [17] showing the terahertz absorption coefficients of $LiNbO_3$ and MgO:$LiNbO_3$ from FTIR measurements and values calculated from the complex polariton wave vector. © 2000 IEEE.

where ω_{0j}, S_j and Γ_j respectively denote the eigenfrequency, oscillator strength and bandwidth of the j^{th} A_1-symmetry mode. For the frequency region (0.5-2)THz the absorption coefficient is found to take values in the range (10-100)cm^{-1} (approximately). Figure 2.18 shows the terahertz absorption coefficient for $LiNbO_3$ and MgO:$LiNbO_3$ derived from experimental data and theoretical calculations by Shikata [17]. MgO:$LiNbO_3$ has a lower absorption coefficient than $LiNbO_3$ because the dopant introduces a perturbation to the A_1-symmetry phonon modes, causing a reduction in the phonon linewidth and an increase in the nonlinear susceptibility.

Example gain calculation including the effect of terahertz absorption

If figure 2.18 is used to obtain a suitable absorption coefficient for the wavelength under consideration, then $\alpha_T \approx 30\text{cm}^{-1}$ and, from equation 2.21, $l = 1\text{mm}$, so that $N = \frac{30}{1} = 30$. The single-pass gain is then:

$$G = \cosh^{60}[0.2] = [1.02]^{60} \approx 3.3$$

Again the single-pass gain suffers a dramatic reduction due to the terahertz absorption.

2.4.3 Gain and threshold in an optical parametric oscillator

In the case of an SRO in which the idler wave is resonated in an optical cavity and the terahertz wave is extracted on a single pass of the nonlinear medium, oscillation builds up from noise/parametric fluorescence associated with the idler wave. For the oscillator to be above threshold the noise must experience gain such that it is amplified to the level of a coherent signal. The threshold power-to-noise ratio has been established (based on a threshold signal energy of 100μJ) in the work of Brosnan and Byer [21] as being:

$$\ln\left(\frac{\text{signal power}}{\text{noise power}}\right) = 33$$

and since the gain is equal to

$$10 \times \log_{10}(e^{33})$$

this implies a gain of ≈140dB.

Since the idler is reflected back and forth through the nonlinear medium by the cavity mirrors, this amplification must reach the required level over the number of idler cavity round-trips that can be made within the duration of the pump pulse, which is assumed to have a Gaussian temporal profile and a $(1/e^2)$ intensity half-width, τ. The importance of minimising the cavity length is apparent in the context of maximising the number of round-trips that can be made during the pump pulse.

The total gain (not including losses) over the duration of the pump pulse is then given as:

$$G_{total} = [G_{single-pass}]^{2N_{RT}} \tag{2.23}$$

where N_{RT} is the number of round-trips of the idler cavity taking place during the pump pulse, expressed as:

$$N_{RT} = \frac{\text{pulse duration}}{\text{cavity round-trip time}}$$

where the factor of two accounts for the fact that there is gain on both passes of the idler cavity owing to the fact that the pump wave is resonant.

Making a substitution for $G_{single-pass}$ from equation 2.20, equation 2.23 becomes:

$$G_{total} = [\cosh^{2N}[\Gamma_i l]]^{2N_{RT}}$$

which is equivalent to

$$G_{total} = \cosh^{4NN_{RT}}[\Gamma_i l] \tag{2.24}$$

and the threshold condition can be expressed as

$$\cosh^{4NN_{RT}}[\Gamma_i l] \geq 10^{14} \tag{2.25}$$

Example total gain calculation

If a pulse duration of ≈30ns is assumed, then for an idler cavity length of 20cm there are 22 round-trips of the idler cavity within the pump pulse. Using the same values for the terahertz walk-off angle and absorption coefficient as previously, the total gain is:

$$G_{total} = \cosh^{44\times122}[0.1] = (1.005)^{44\times122} = 4.2\times10^{11} \approx 116\text{dB}$$

on the basis of a terahertz walk-off length, and

$$G_{total} = \cosh^{44\times60}[0.2] = (1.02)^{44\times60} = 5.0\times10^{22} \approx 227\text{dB}$$

on the basis of a terahertz absorption length.

2.4.4 Alternative representation of loss due to absorption

Another way in which the absorption loss of the terahertz can be accounted for is by considering it as axial absorption. A loss term is added into the coupled wave equations which, when solved, yield the following expression (see appendix A):

$$E_{10}(z=L) = E_{10}(z=0)\times e^{\frac{-\gamma_2 L}{2}} \times \frac{1}{2}[(1-\frac{\gamma_2}{\tilde{\Gamma}})e^{-\frac{\tilde{\Gamma}L}{2}} + (1+\frac{\gamma_2}{\tilde{\Gamma}})e^{\frac{\tilde{\Gamma}L}{2}} \tag{2.26}$$

where

$$\tilde{\Gamma} = 2\left(\left(\frac{\gamma_2}{2}\right)^2 + \Gamma^2\right)^{\frac{1}{2}} \tag{2.27}$$

and γ_2 is the field amplitude absorption coefficient rather than the intensity absorption coefficient (given by $\frac{\alpha_T}{2}$). L is the length of the nonlinear medium. Since the single-pass gain is equal to $(\frac{E_{10}(z=L)}{E_{10}(z=0)})^2$ (to go from an amplitude gain to an intensity gain), it is represented by the expression:

$$G_{\text{single-pass}} = (e^{\frac{-\gamma_2 L}{2}} \times \frac{1}{2}[(1 - \frac{\gamma_2}{\tilde{\Gamma}})e^{-\frac{\tilde{\Gamma} L}{2}} + (1 + \frac{\gamma_2}{\tilde{\Gamma}})e^{\frac{\tilde{\Gamma} L}{2}})^2 \tag{2.28}$$

and the total gain over the duration of the pump pulse is then given by equation 2.23 as before.

Example total gain calculation including absorption

Maintaining the same idler cavity and pump pulse parameters and using a field amplitude absorption coefficient of 15cm^{-1}, the single-pass gain is:

$$G_{single-pass} = 2.17$$

So for the total gain we have

$$G_{total} = 2.17^{22} = 2.51 \times 10^7 \approx 74dB.$$

2.5 Operational characteristics of the OPO

Figure 2.19 shows the output power of the laser and OPO as a function of the input diode energy for a typical OPO construction. In this case, the idler cavity has a 94% mirror as its output coupler and the idler cavity length is ≈24cm. The output power of the pump laser clamps at the OPO threshold value despite the diode energy increasing linearly. Increased pump power is then transferred from the laser gain medium population inversion, through the circulating field and into increased power in the signal and idler waves. In the absence of down-conversion, which is effected by blocking the idler cavity, the pump power grows linearly. The pump laser reaches threshold at 6.3mJ of diode pumping and the OPO reaches threshold at 11.4mJ.

In order to optimise the OPO performance, several parameters of the idler cavity were adjusted, namely the reflectivity of the output coupler and the cavity length. These parameters were changed simply by altering mirror M3, shown in figure

2.1. The pump laser cavity was kept the same throughout the characterisation of the idler cavity.

2.5.1 Variation of down-conversion energy with idler cavity mirrors

As stated previously the reflectivity of mirror M3, which acts as the output coupler for the idler cavity (see figure 2.1) was altered to establish the effect it had on the efficiency of the OPO. The amount of energy that is down-converted from the pump field to the idler and terahertz fields can be calculated using either mean power measurements of the pump field or by examining the temporal profiles of the pump pulse when depletion of the pulse is allowed to take place and then prevented. In the first method, the mean power of the pump is measured with and without the parametric process occurring; the process is prevented from happening by physically blocking the idler cavity. The mean powers can be converted to pulse energies using the following approach:

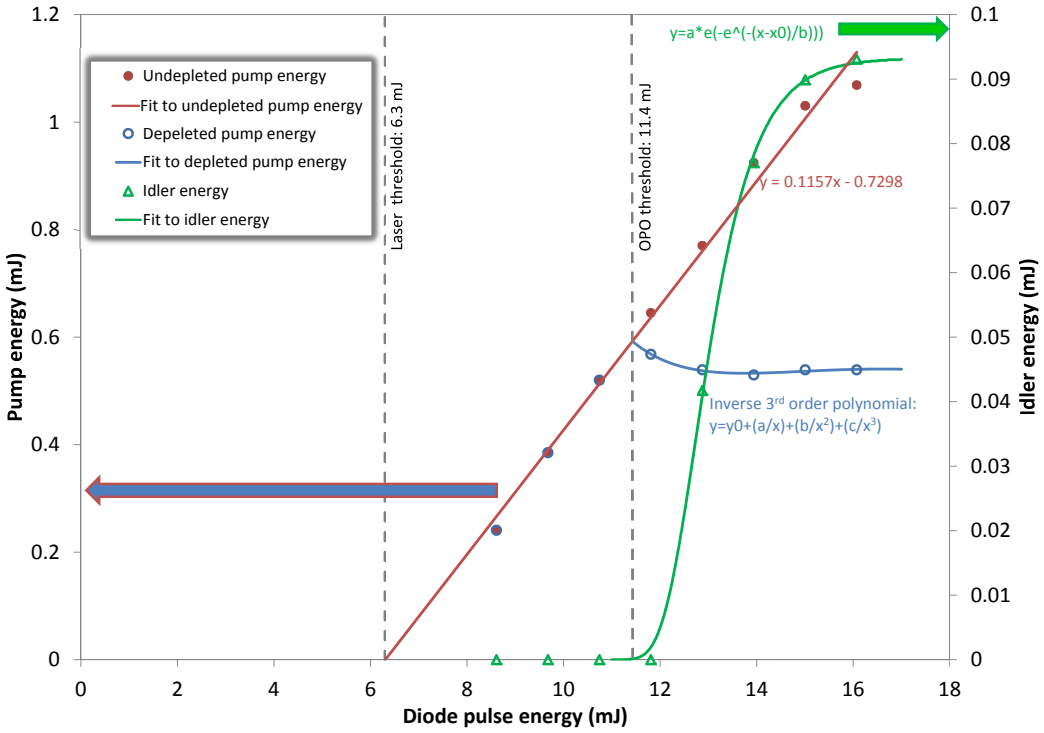

Figure 2.19: The output power characteristics of a typical OPO. The pump grows linearly below OPO threshold and when downconversion is prevented from occurring but is clamped when the OPO is allowed to operate.

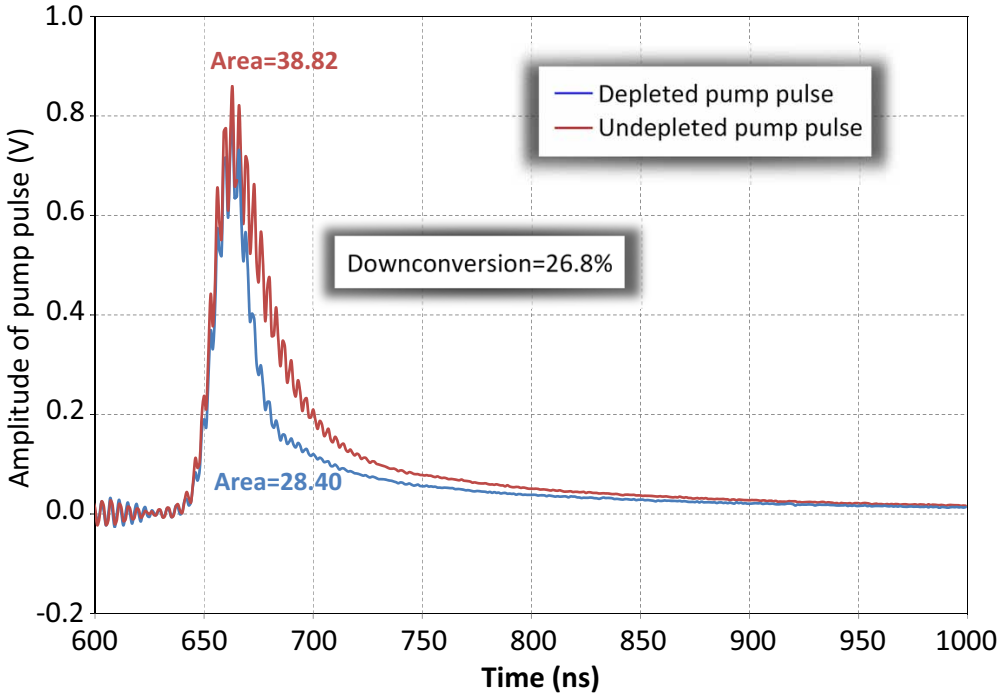

Figure 2.20: Analysis of pump pulse temporal profiles to establish the amount of down-conversion taking place.

The energy in the pump that is measured through the output coupler is given by

$$E_p(\text{mJ}) = \frac{P_m(\text{mW})}{\text{repetition rate (Hz)}} \tag{2.29}$$

where P_m is the measured mean power.

The total energy in the pulse, accounting for the output coupling and parasitic losses is then

$$E_T(\text{mJ}) = \frac{E_p(\text{mJ})(\beta_o + \beta_p)}{\beta_o} \tag{2.30}$$

where β_o is the output coupling loss and β_p is the parasitic loss of the cavity. The total energies are calculated for the cases where the parametric process is allowed and then prevented by blocking the path of the idler beam. The difference between the two energies has been down-converted through the parametric process and is divided between the idler and terahertz fields according to the ratio of their frequencies.

The second means of establishing the amount of energy that has gone into the down-conversion process is by calculating the difference in area between the

temporal profiles of the pump pulse in its depleted and undepleted state, as shown in figure 2.20. If the difference in areas is expressed as a percentage of the undepleted pump pulse area then the energy that has gone into the process is the same percentage of the undepleted pump energy, calculated using equation 2.30 and taking the value of β_p to be in the range $\approx$(10-20)% depending on the idler cavity length (see section 2.5.3 for details on how this figure was reached).

The amount of energy in the down-conversion process is shown as a function of the pump intensity in figure 2.21. Looking at figure 2.21 it is apparent that, generally speaking, the higher the reflectivity of the output coupler is, the greater is the amount of energy in the down-conversion process. A further benefit from using mirrors of higher reflectivity is that the OPO threshold is reduced with respect to lower reflectivities, as shown in figure 2.22. The data in these figures corresponds to a fixed pump cavity, i.e. only the idler cavity mirror has been altered. In changing the reflectivity of the output coupler the OPO threshold intracavity intensity can be reduced by almost 10MWcm^{-2}. Although it may seem appealing to increase the reflectivity of the mirror even further, it is necessary to maintain some output for the purpose of monitoring the

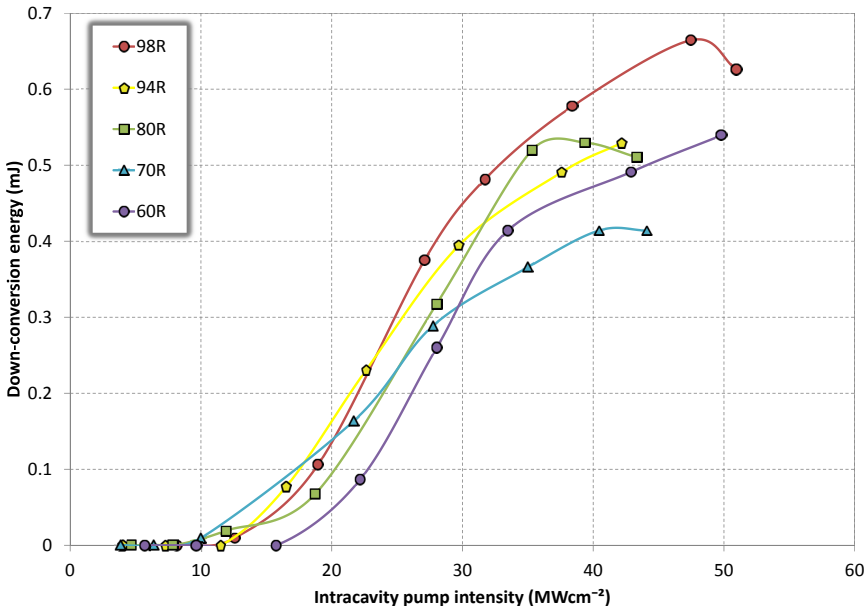

Figure 2.21: The amount of energy in the down-conversion process as a function of the intracavity intensity, plotted for a range of idler cavity output couplers. The threshold of the OPO can be reduced by almost 10MWcm^{-2} by increasing the output coupler's reflectivity.

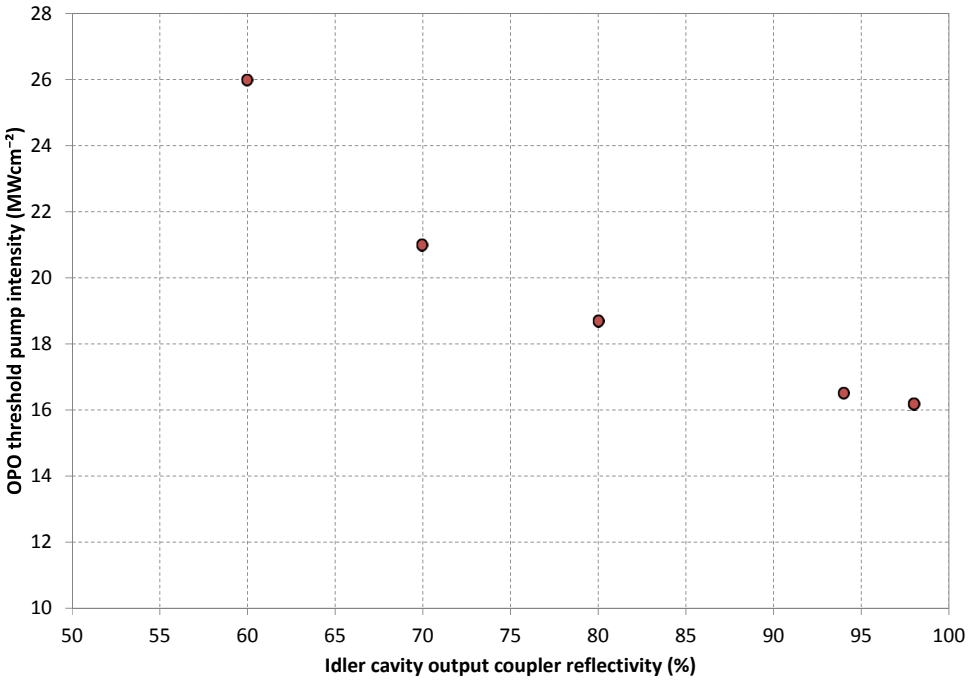

Figure 2.22: The required intracavity intensity to reach OPO threshold in relation to the reflectivity of the idler cavity output coupler. The use of higher reflectivity mirrors leads to lower OPO thresholds.

parametric process through power, temporal and spectral measurements of the idler pulse. It should be noted, however, that in using the approach described here to calculate the energy going in to the down-conversion process, the assumption is made that all of the depleted pump energy is being used by the parametric process before the onset of parasitic and output coupling losses, that is, the process happens at the peak of the pump pulse. Far above threshold this is a valid approximation, but in the case where the OPO is only just above threshold it may result in artificially large down-conversion energies since the idler pulse may be delayed with respect to the peak of the pump pulse.

If the amount of energy in the down-conversion process is instead analysed in relation to the pump pulse energy (calculated using equations 2.29 and 2.30) then it is possible to evaluate the efficiency of the process under various pump conditions. Figure 2.23a shows several data sets corresponding to the use of different idler cavity mirrors (as labelled) and has reference lines at the 25%, 40% and 50% levels. The data in this graph has been extracted from the pump mean

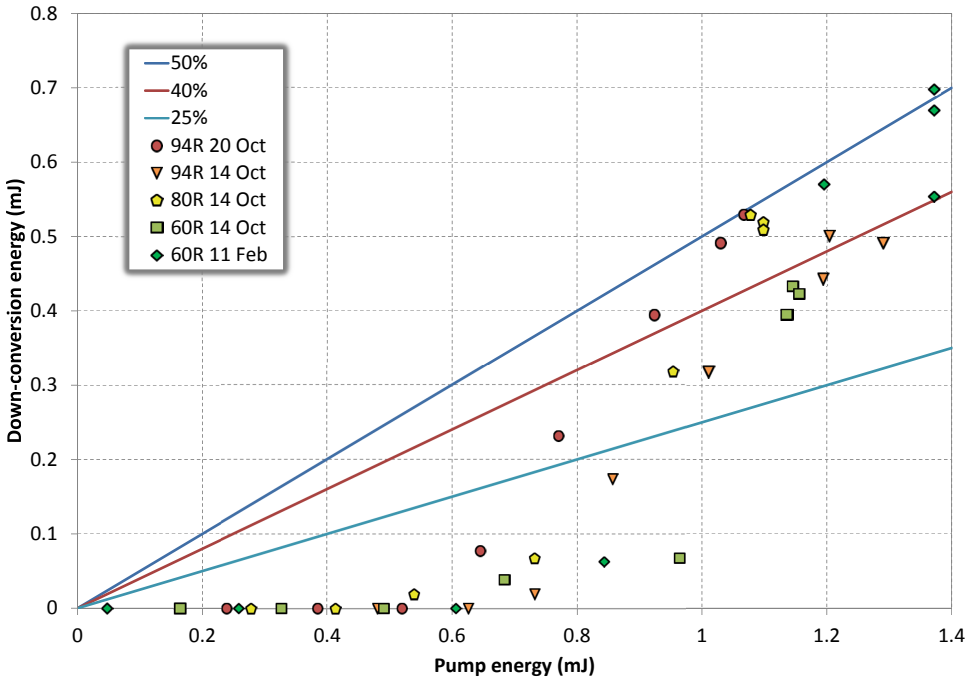

(a) Down-conversion energies derived from mean power measurements.

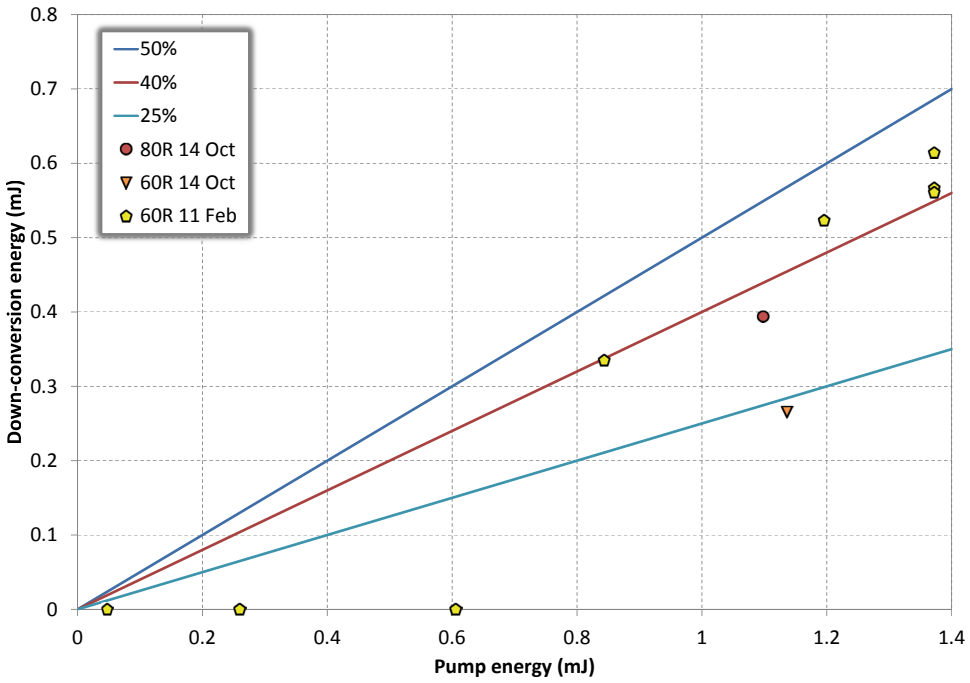

(b) Down-conversion energies derived from pump pulse temporal profiles.

Figure 2.23: Comparison of down-conversion energies (and depletion percentages) obtained using both possible methods.

power. As before, there is a general trend that as the idler cavity output coupler is made more reflective, greater amounts of pump depletion are then achieved. However looking at the data sets which used the same idler cavity configuration (94%R and 60%R) it is clear that there is also an amount of variability in the output, due to the precise alignment of the cavity mirrors for example, meaning that the data may not be exactly reproducible from one experiment to the next.

Figure 2.23b shows the down-conversion energy measured when using the percentage area difference between the depleted and undepleted pump pulses. Comparing the measured down-conversion energy for the data set labelled "60R 11 Feb" it is clear that there is not always total agreement between the two methods of measuring the down-conversion energy - in the first case (figure 2.23a) the pump depletion struggles to reach 25% whereas the temporal data (figure 2.23b) implies an almost constant 40% depletion of the pump once the device has exceeded threshold.

2.5.2 Variation of down-conversion energy with idler cavity length

The other cavity parameter that could be varied easily was the cavity length. Using a fixed pump laser system as before, the characteristics of the OPO were recorded as the cavity length was set to 24cm, 21cm and 13cm by moving the output coupler, which had a reflectivity of 90%. No intracavity lens was employed in this configuration. Figure 2.24a shows the down-conversion energy as a function of the intracavity intensity; the energy in the down-conversion was calculated on the basis of the mean power measured in the depleted and undepleted pump beams, as described previously. The data shows that the greatest amount of energy is put into the down-conversion process for the shortest idler cavity, with the longest cavity having the least energy available to the process; the OPO threshold also scales with the cavity length. That this is the case is evident from the arguments put forward in section 2.4, where it can be appreciated that the greater the number of round-trips of the idler cavity that are made, the lower the threshold intensity can be.

Figure 2.24b shows the measured idler energies, which were calculated from

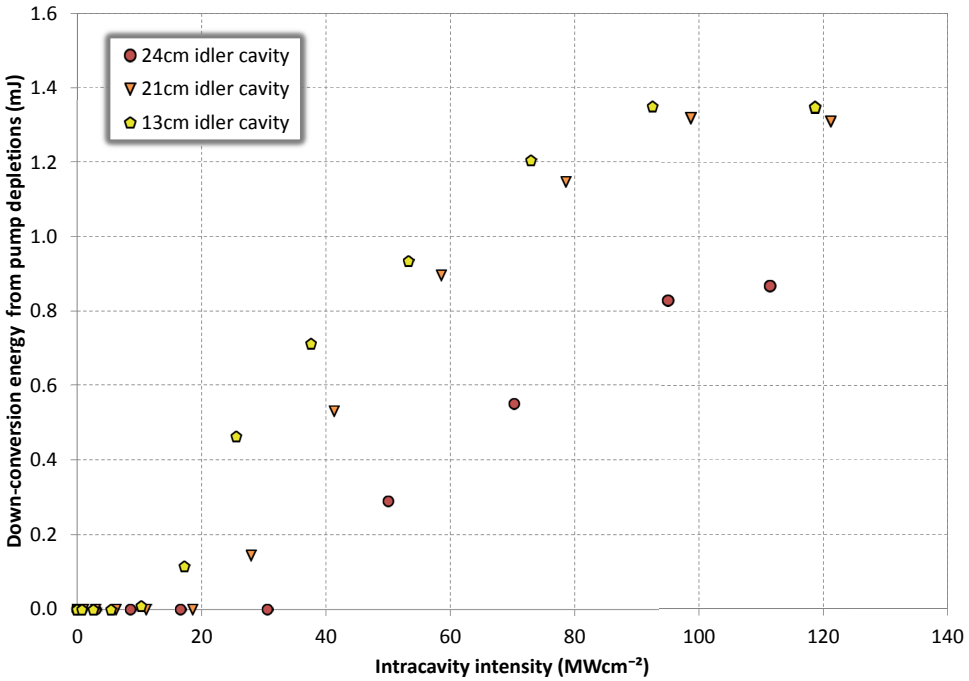

(a) Down-conversion energies derived from mean power measurements.

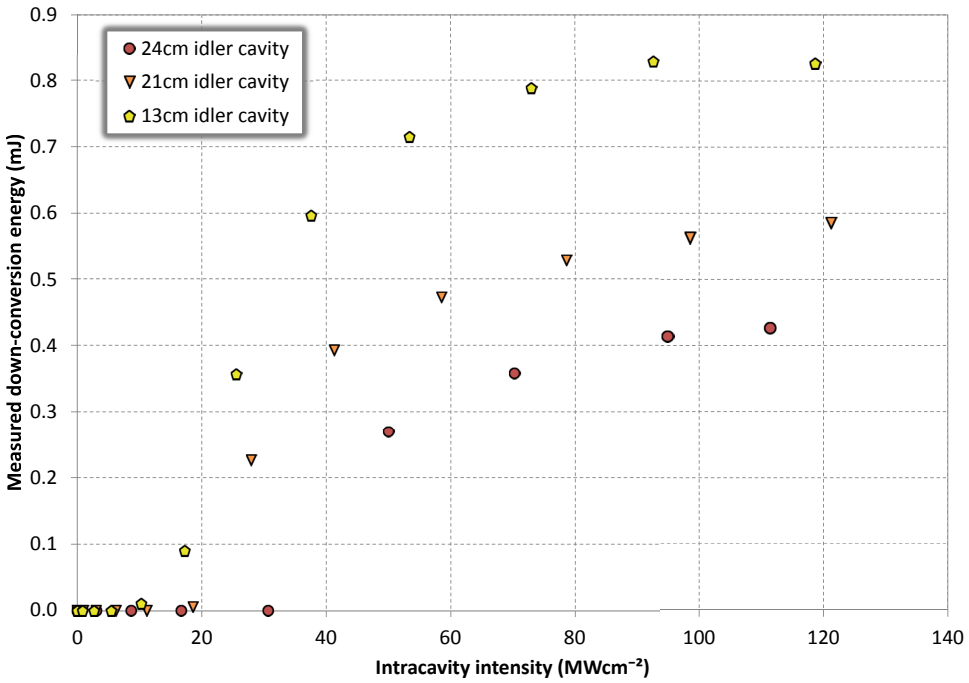

(b) Down-conversion energies derived from measured idler mean powers.

Figure 2.24: Comparison of down-conversion energies obtained from calculations and measurements.

idler mean power measurements using the same method as was used for the pump beam. The measured idler energies follow the same trend as a function of cavity length as do the energies expected from the measured pump depletions. The discrepancy between the measured idler energies and those inferred from the amount of pump depletion is, however, largely inconsequential when the fundamental operational characteristics of the OPO are being considered. This is because the calculated values represent the idler energy that is actually being generated within the nonlinear medium rather than that which is subsequently extracted, where extraction losses and the uncertainties therein may make the device seem less efficient than it actually is.

2.5.3 Idler cavity losses

The magnitude of the idler cavity losses can be assessed through comparison of the energy that is calculated to have gone into the down-conversion process and the energy that is actually measured in the idler pulse. Since no additional optical components other than the nonlinear material are contained within the idler cavity, the parasitic loss results from diffraction of the intracavity beam. Fox and Li [22] developed a method for quantifying the round-trip loss due to diffraction in relation to the Fresnel number, N, of the cavity, given by:

$$N = \frac{a^2}{b\lambda} \tag{2.31}$$

where a is the $(1/e^2)$ beam radius (≈0.5mm), b is the length of the idler cavity (≈240mm) and λ is the idler wavelength (≈1.07×10^{-6}m). Using the values indicated results in a Fresnel numbers of 0.97, 1.16 and 1.79 for the different cavity lengths (long to short), which from consultation of figure 8 in the work of Fox and Li [22] yields a round-trip loss of ≈18% for the 24cm cavity, ≈15% for the 21cm cavity and ≈8% for the 13cm cavity.

These losses were used to produce the energy data shown in figure 2.24b from the measured idler powers. The discrepancy between the energy in the down-conversion and the measured idler energy is indicative that the parasitic loss values used are too low. Such an error may have been introduced by assuming too large a $(1/e^2)$ beam radius for the idler. To establish what value of

beam radius would result in better agreement between the measured idler energies and the down-conversion energies, the parasitic loss factor in the power-to-total energy loss conversion calculation (equation 2.30 was modified so that the agreement was improved. Figure 2.25 shows the results of this investigation.

In all cases a higher parasitic loss is required to match the idler energies corresponding to four or five times OPO threshold; lower losses better represent the energies closer to threshold. Since no intracavity lens was made use of to stabilise the pump beam radius, the radius varied as shown in figure 2.11. The dimensions of the pump beam define the dimensions of the idler beam, so because the pump beam dimensions decrease with increasing diode power so too do the idler beam dimensions. The $(1/e^2)$ radius of the idler beam is included in the calculation of the Fresnel number (equation 2.31) and it can be seen from examination of equation 2.31 that a smaller $(1/e^2)$ radius leads to lower Fresnel numbers and consequently higher losses.

2.5.4 Effect of changing cavity parameters on the generated terahertz radiation

It should be noted that the effect of changing various cavity parameters on the device efficiency has been characterised in terms of the measured idler powers (energies) because of the inherent difficulties in relation to the measurement of the corresponding terahertz energies. Since the degree of absorption suffered by the terahertz wave depends on the terahertz frequency being generated and the distance over which the terahertz wave must propagate through the material, followed by additional absorption loss due to the presence of water vapour in the atmosphere, it is difficult to precisely relate the measured terahertz energy to that generated inside the nonlinear material. In terms of optimising the efficiency of the device it is far easier to measure the idler wave energies and relate those quantities to the generated energies through knowledge of the parasitic loss, or to simply measure the amount of pump depletion under particular operating conditions. The total down-conversion energy is partitioned into the idler and terahertz fields according to the Manley-Rowe relations such

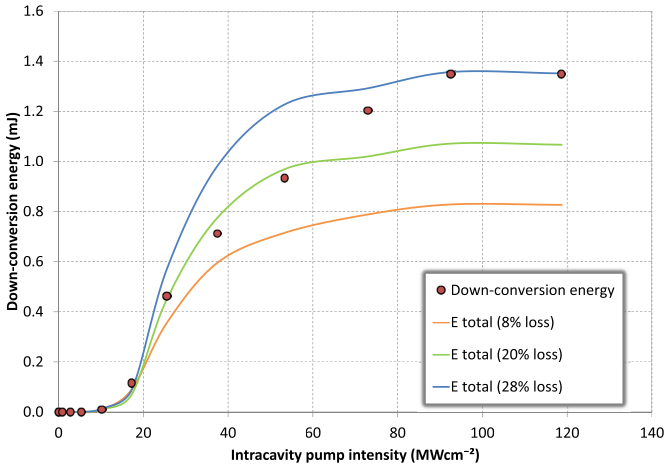

(a) 13cm idler cavity

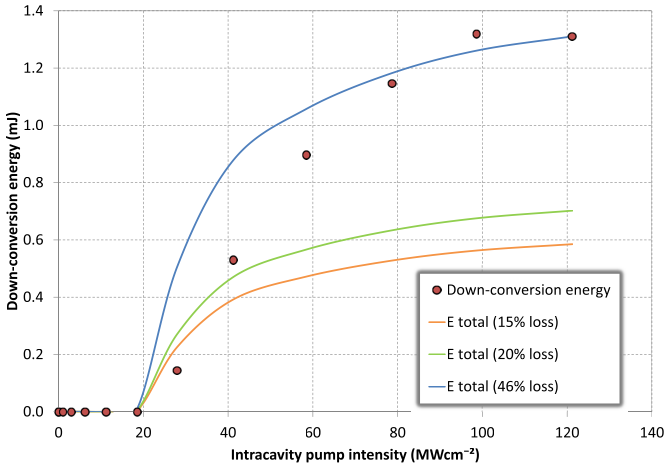

(b) 21cm idler cavity

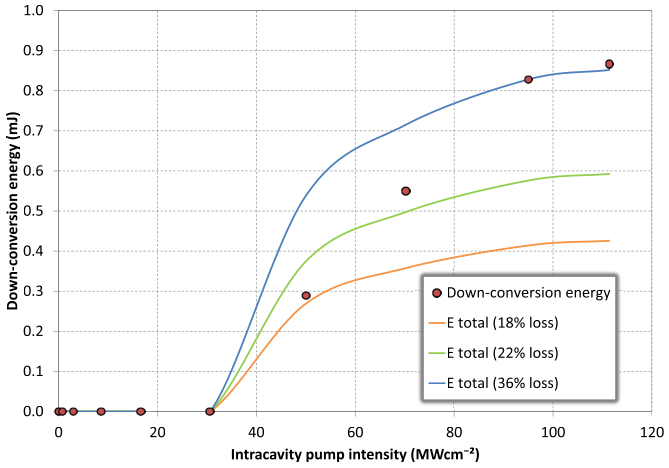

(c) 24cm idler cavity

Figure 2.25: Attempts to reconcile the measured idler energies with those anticipated from the pump depletion by changing the parasitic loss of the idler cavity.

that only 0.35% of the available energy goes into the terahertz wave at a frequency of 1THz, rising to 1.06% at 3THz. Typically this results in generated terahertz energies in the range (3-14)μJ, though only about one thousandth of this is extracted and measured due to absorption losses/interface losses, i.e. approximately (3-14)nJ. For example, in the case of the data presented in figure 2.24a, using a 13cm-long idler cavity instead of a 24cm-long one produces an increase in the terahertz produced within the crystal from 4.9μJ to 7.6μJ, of which typically 0.1% is then coupled out (i.e. an increase from ≈5nJ to ≈8nJ). Similar analyses apply throughout the thesis.

2.6 Calculation of gain at threshold

Following on from the description of the appropriate gain calculations earlier in this chapter, the gain corresponding to the measured threshold conditions in several OPO configurations that have been implemented shall be evaluated here. All three methods of calculating the gain (i.e. using the walk-off length, an effective absorption length or including the effect of absorption in the coupled wave equations) have been used and this section also serves as a comparison between them.

Table 2.2 presents experimentally-determined threshold data for a range of OPO configurations that were characterised along with the results of the gain calculations described earlier in this chapter. The table is split into sections according to whether the data was known (i.e. set by the researcher), measured or calculated.

I_p is the intracavity pump intensity calculated on the basis of a $(1/e^2)$ beam radius appropriate to the particular configuration; τ_p is the FWHM pump pulse duration, measured in ns and γ_2 is the field amplitude absorption coefficient in units of m^{-1}. The two γ_2 values listed for each data set correspond to the calculated or measured value of α_T, taken from figure 2.18.

The trends seen in the data are that:

(a) threshold is lower for lower terahertz frequencies, due to α_T taking lower values;

(b) threshold is lower for shorter idler cavities since more round-trips of the idler cavity can be made during the pump pulse;

(c) threshold is lower when longer nonlinear crystals are used because of the increased total interaction length;

(d) threshold is lower for higher reflectivity idler cavity output couplers as a result of greater field enhancement (as shown earlier in the chapter).

There is a large spread in the gains calculated, however the two analyses based on absorption being the dominant effect agree relatively well from the point of view that 140dB gain is only an approximate figure describing the threshold point. The treatment of the terahertz walk-off length is rather severe in its effect on the resulting gain, due partly to the fact that it assumes that the terahertz ceases to be generated once part of the wave has walked off as shown in figure 2.17. In fact the terahertz generation persists since there is still interaction between the pump and idler waves. As well as an uncertainty in the terahertz

System parameters				Measured data		Total gain (dB)		
Crystal (mm)	Idler cavity	ν_T (THz)	γ_2 (m^{-1})	τ_p (ns)	$I_p(\times 10^{10}$ $Wm^{-2})$	Walk-off analysis	Absorption length	Axial absorption
30	0.1336m 90%R	1.9	2330 1995	45	7.98	67.759	81.868 95.017	106.568 124.084
30	0.1336m 90%R	1.6	1630 1380	40	7.27	46.114	79.896 94.539	102.917 120.978
30	0.218m 90%R	1.6	1630 1380	30	19.92	58.930	101.978 120.583	130.997 153.719
70	0.218m 90%R	1.6	1630 1380	35	6.30	49.479	85.053 99.889	112.345 132.364
70	0.218m 90%R	1.6	1630 1380	32	7.06	48.528	83.4136 97.960	110.161 129.776
70	0.218m 80%R	1.6	1630 1380	32	7.27	52.336	89.957 105.643	118.796 139.945

Table 2.2: Outcome of gain calculations for different OPO configurations.

absorption coefficient (accounted for in the table and producing ≈15% variation in the total gain), other uncertainties in the pump intensity (≈10%), the idler cavity length (≈1cm) and the pump pulse duration (≈1ns) also contribute to the variability of the derived gain, with the intensity having a direct effect on the gain through Γ and the uncertainty in cavity length and in the pump pulse duration affecting the number of round-trips of the idler cavity that are made within the duration of the pump pulse. These factors combined can contribute to at least 20% variation in the total gain value.

2.7 A frequency-domain terahertz spectrometer

The intracavity terahertz OPO characterised in this chapter forms the basis of a spectrometer system for the analysis of solids, liquids and gases. Transmission spectroscopy, evanescent wave spectroscopy and terahertz imaging studies have all been undertaken and the terahertz spectrometer has been used on behalf of collaborators from other research institutions. The initial implementation and characterisation of the system was undertaken by a colleague, Dr David Walsh. Some of the key results from his work are included here along with work pertaining to this thesis to provide valuable contextual information, for which due acknowledgement is given. The intracavity terahertz OPO has been licensed to a company who have commercialised the technology (M Squared Lasers, Glasgow).

2.7.1 Spectrometer layout

The construction of the spectrometer is shown schematically in figure 2.26. The footprint of the terahertz OPO itself is ≈(30×40)cm, excluding the laser diode driver and diagnostic components. The terahertz radiation exits the crystal through a letterbox aperture because it is generated within the overlap region of the pump and idler beams. Consequently, there is little divergence along the overlap region since the beam width is large with respect to the terahertz wavelength. In the perpendicular direction however, the terahertz generation region is limited by the diameters of the pump and idler beams (≈1mm) so the divergence angle is correspondingly large - as much as (6-8)° acorss the tuning

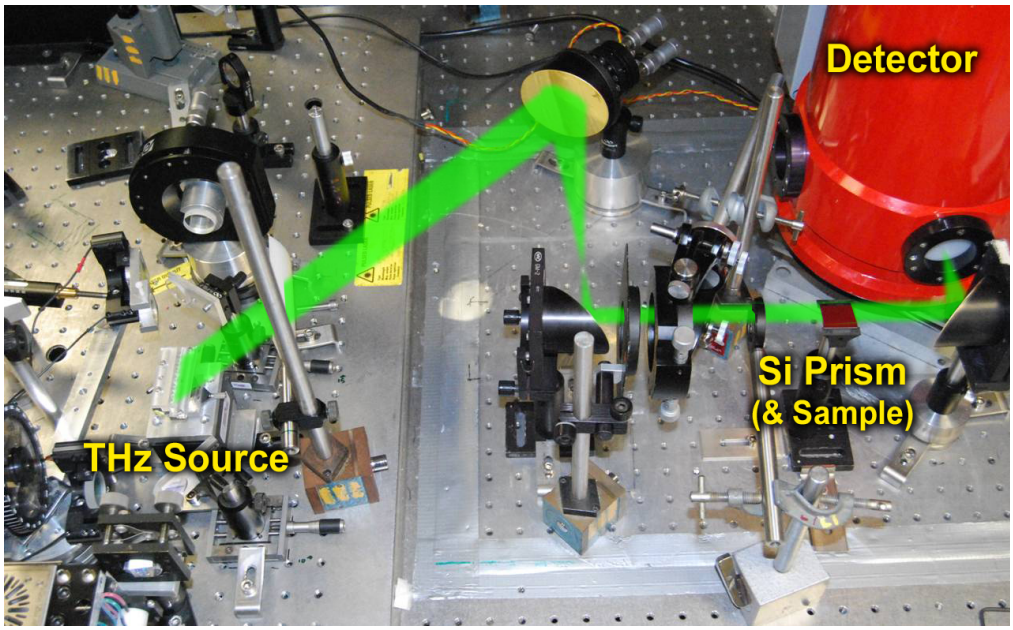

(a) Photograph of the terahertz spectrometer.

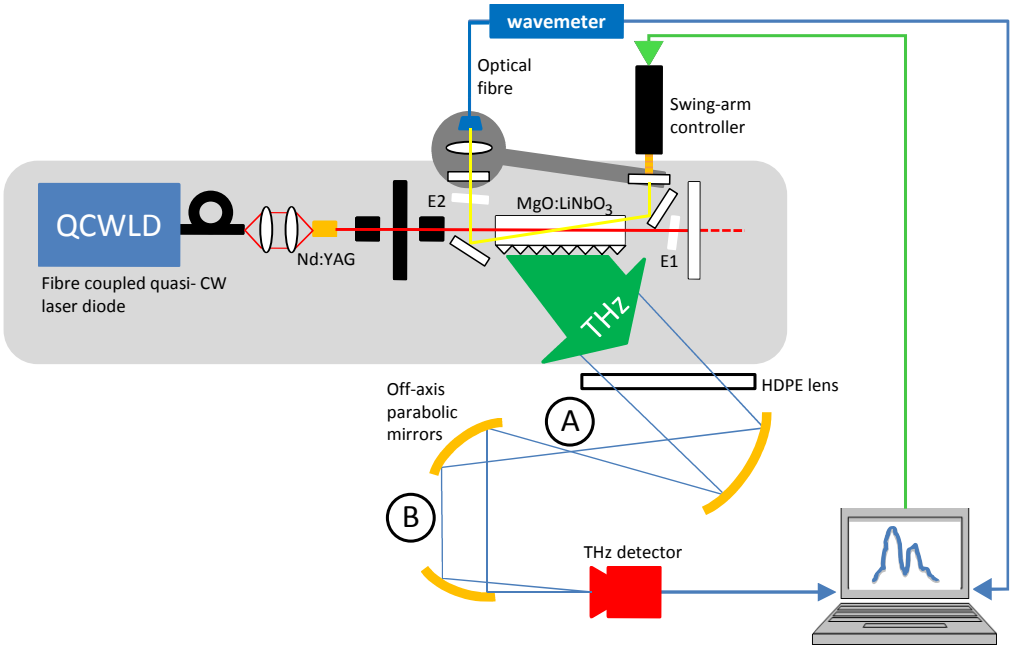

(b) Schematic of the terahertz spectrometer.

Figure 2.26: Annotated photograph and schematic of the terahertz spectrometer layout, indicating the key features.

range of the device. For that reason, an HDPE cylindrical lens was used to collect and collimate the terahertz beam and to compensate for astigmatism. Off-axis parabolic mirrors (Janostech) were then used to manipulate the beam as shown in figure 2.26b.

In region "A" of figure 2.26b the first parabolic mirror was used to focus the terahertz beam to a nearly-circular waist of $\approx 800\mu m$. Calculations of the beam waist dimensions for a diffraction-limited beam implied that the measured beam was ≈2.3 times the diffraction limit [23].

The second parabolic mirror served to collimate the beam with diameter ≈2cm in region "B" so that transmission experiments could be carried out, before then being focussed onto the input of an appropriate detector - in the case of figure 2.26, a cryogenically-cooled bolometer purchased from QMC Instruments.

2.7.2 Tuning range and linewidth

The terahertz frequency generated by the intracavity OPO is tuned by changing the angle of the idler cavity with respect to the propagation direction of the pump beam, as indicated in figure 2.27a. The maximum extent of tuning achieved to date is (0.9-3.0)THz.

At low terahertz frequencies the tuning range is limited by the small angular separation between the pump and idler beams ($\leq 1^\circ$ external to the crystal for terahertz frequencies less than 1THz and approximately 0.5° inside the crystal for the same condition), which means that the idler cavity must be extended when accessing the lowest frequencies in order to avoid clipping the pump beam and preventing laser oscillation from taking place. Increasing the length of the idler cavity has its limitations however, since the build-up time of the OPO will increase and its performance will be reduced. The tuning range is limited at the high frequency end by the crystal aperture clipping the idler cavity. Figure 2.27b illustrates the energy output across the typical tuning range of the terahertz frequency, measured through a nitrogen-purged path of ≈1m in length. The terahertz frequency is ascertained by measuring the pump and idler frequencies

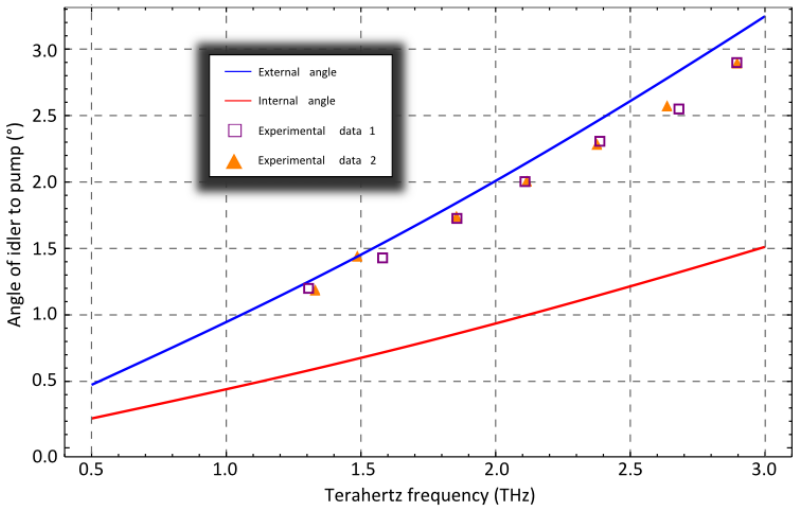

(a) A graph showing the calculated values of the angular separation of the pump and idler, internal and external to the crystal, as a function of the terahertz frequency. Measured external angle data is also included.

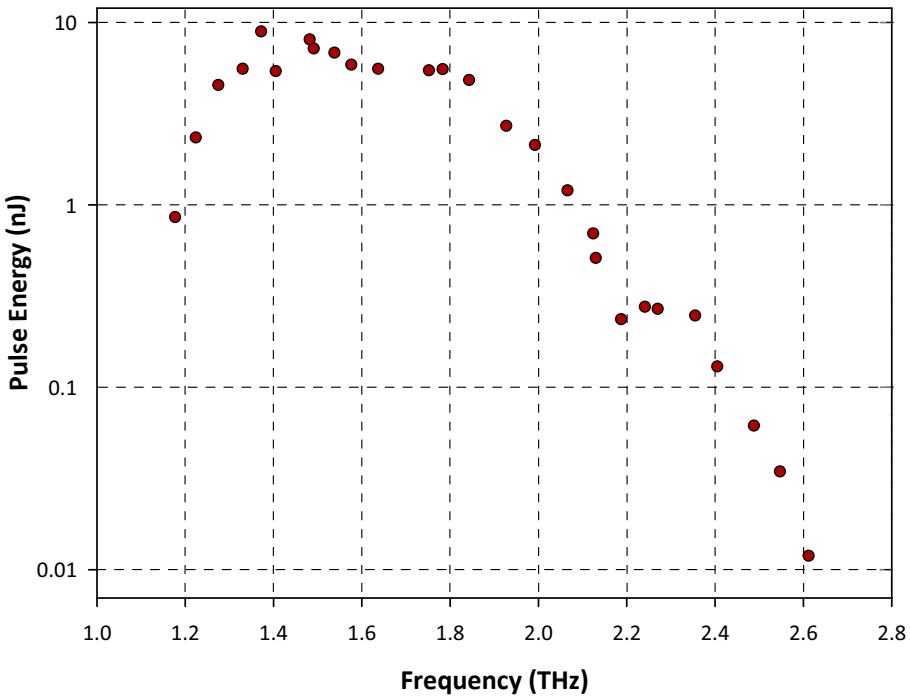

(b) The pulse energy output across the typical tuning range of the terahertz frequency generated using the intracavity terahertz OPO.

Figure 2.27: The tuning characteristics of the intracavity terahertz OPO.

using a wavemeter (Angstrom WL-7 [24]) as indicated in figure 2.26, the terahertz frequency being equal to the difference between those two frequencies.

The linewidth of the terahertz radiation is restricted due the conservation of energy by the linewidths of the pump and idler waves; therefore by measurements of these linewidths the approximate linewidth of the terahertz wave can then be inferred. In the absence of frequency control elements the linewidth of the terahertz radiation is ≈50GHz. The use of étalons in the pump and idler cavities results in a factor of ten reduction in the original linewidth, to <5GHz when the data acquisition is averaged over multiple pulses [25]. The terahertz frequency can then be tuned continuously over a band >50GHz by rotating the étalon in the idler cavity, settable anywhere within the coarse tuning range of the device. By grouping single pulse data into frequency bins of 250MHz width, sub-GHz resolution can be achieved.

Another means of narrowing the linewidth of the source that has been successfully implemented is injection seeding [23]. In this way the terahertz linewidth was reduced to <100MHz, this having been verified through the measurement of a ≈9MHz absorption feature at 1.4969THz in the spectrum of carbon monoxide. The reasons behind the selection of that particular absorption feature were that, firstly, it lies in the region where the terahertz energy extracted from the MgO:$LiNbO_3$ crystal is greatest, and secondly it does not coincide with any water absorption features, which otherwise plague free-space spectroscopic measurements. Measured terahertz spectra corresponding to 1m propagation through either a nitrogen-purged or air path (red and orange traces, respectively) are compared in figure 2.28. The purple data corresponds to the absorption spectrum of water, which was measured previously by the author at the National Physical Laboratory. The only real window where spectroscopic measurements can be made without water absorption features is in the range ≈(1.4-1.6)THz. There are also regions at ≈(1.2-1.4)THz and at ≈(1.9-2.1)THz where there are relatively few water absorption features, however the terahertz power produced by the source drops off rapidly in these regions, so the region at ≈(1.4-1.6)THz is the best to utilise.

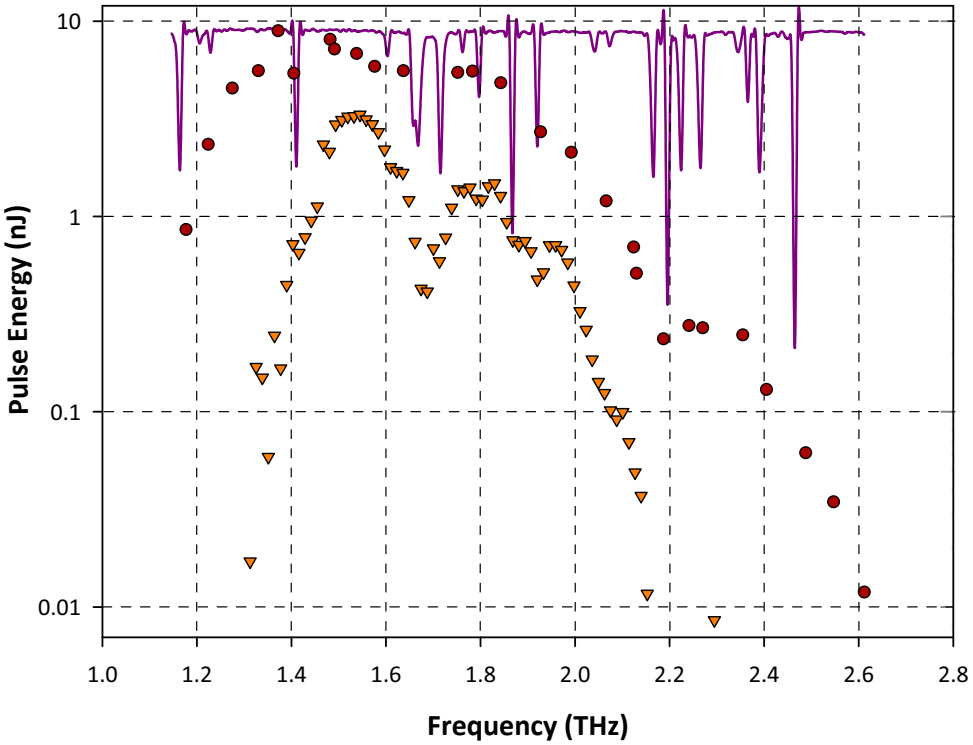

Figure 2.28: This figure illustrates the problem caused by the presence of atmospheric water vapour when making spectroscopic measurements in the terahertz region. The orange trace corresponds to the terahertz measured after propagation through 1m of air and the red trace is the terahertz measured after travelling along the same path purged with dry nitrogen gas. The purple trace shows the measured water absorption features (not on the same vertical scale).

2.7.3 Terahertz detection

Initial terahertz energy measurements were made using a composite silicon bolometer (model QSIB/2) purchased from QMC Instruments Ltd. Although the bolometer was the most sensitive detector available, a significant disadvantage in using it is the need to maintain the detector element at a temperature of 4.2K, which encumbers an otherwise room-temperature terahertz source.

The bolometer has a dynamic range better than 1:10^4 on a single pulse basis. It is capable of measuring energies of $<$1pJ without the need for pulse averaging, although typical pulse energies are on a scale of (10-20)nJ [1, 25]. The measured energies, though representing an improvement of more than an order of magnitude on the energies measured in an extracavity system [1], are disappointingly low given that the terahertz energy actually generated within the

nonlinear medium is in the region of several μJ (splitting the total down-conversion energy according to the ratio of the idler and terahertz frequencies to the pump frequency). That such a small amount of terahertz energy is extracted is indicative of the penalty suffered due to the high terahertz absorption coefficient, along with contributing factors such as the length of the optical path through free space.

Other means of measuring the terahertz output of the intersecting cavity OPO have been investigated (by several colleagues) through a "Proof of Concept" grant, funded by Scottish Enterprise. These technologies include Golay cells and pyroelectric detectors as well as the development of a novel electro-optic detector that would allow the temporal profiles of the terahertz pulses to be resolved, although this has not yet been realised. Table 2.3 summarises the key features of each of the detector technologies available.

Both the Golay cell and pyroelectric detector have longer response times and lower dynamic ranges than does the bolometer. These features limit the maximum repetition rate of the OPO since the pulses would run into each other at the point of detection (this is especially the case when using the Golay cell) and mean that in the case of the pyroelectric detector, data must be averaged over multiple pulses to improve the signal-to-noise ratio - typically $\approx$16 averages. Nonetheless these detector technologies are promising in that they provide the means for developing a fully-portable, completely room temperature terahertz spectrometer.

Detector	Time response	Minimum detectable energy	Dynamic range	Other characteristics
Bolometer	2ms	0.3pJ	35 000	Cryogenic, high running costs
Pyroelectric	10ms	100pJ	100	Cheap, low sensitivity
Golay cell	25ms	4pJ	2 500	Fragile, limited availability

Table 2.3: A comparison of terahertz detectors (data courtesy of DAW and MHD).

2.7.4 Automation of tuning using LabVIEW

Previously, tuning of the terahertz frequency was effected by manual adjustment of the idler cavity mirrors, both a time-consuming and relatively inaccurate method. To facilitate the rapid acquisition of data, the end mirrors of the idler cavity were mounted onto a swing-arm, as shown in figure 2.26b, allowing tuning by the movement of the swing-arm alone. The latest aspect of system development has been to implement computer control of the swing-arm position using a linear actuator and single-axis motion controller [26], as shown in figure 2.29. The terahertz frequency is inferred from the measured pump and idler frequencies and the result of five separate scans is shown in figure 2.30. The excellent repeatability of data across the full tuning range means that synchronous logging of the idler wavelength is no longer necessary since a given terahertz frequency is generated at only one actuator position. Therefore all that is required is an initial measurement of the pump and idler frequencies for calibration purposes. As a result of the spectrometer being put under computer control, the user has a far greater degree of control over the data that is acquired, having free choice of the frequency range to be traversed, the degree of averaging

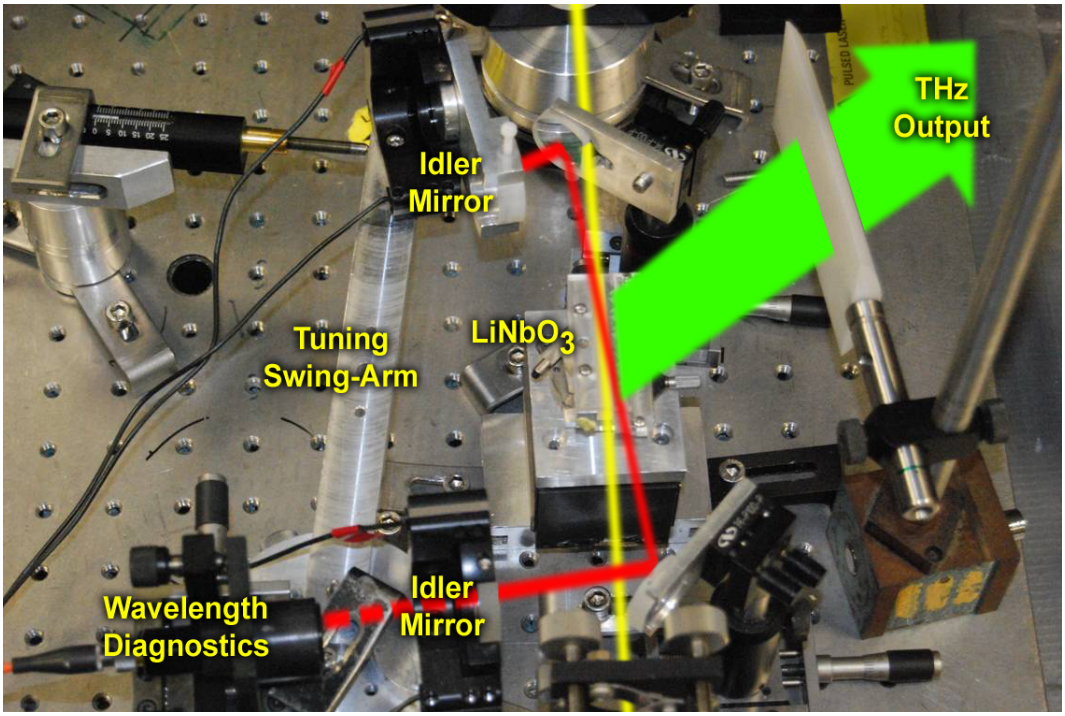

Figure 2.29: A top-down view of the swing-arm control mechanism.

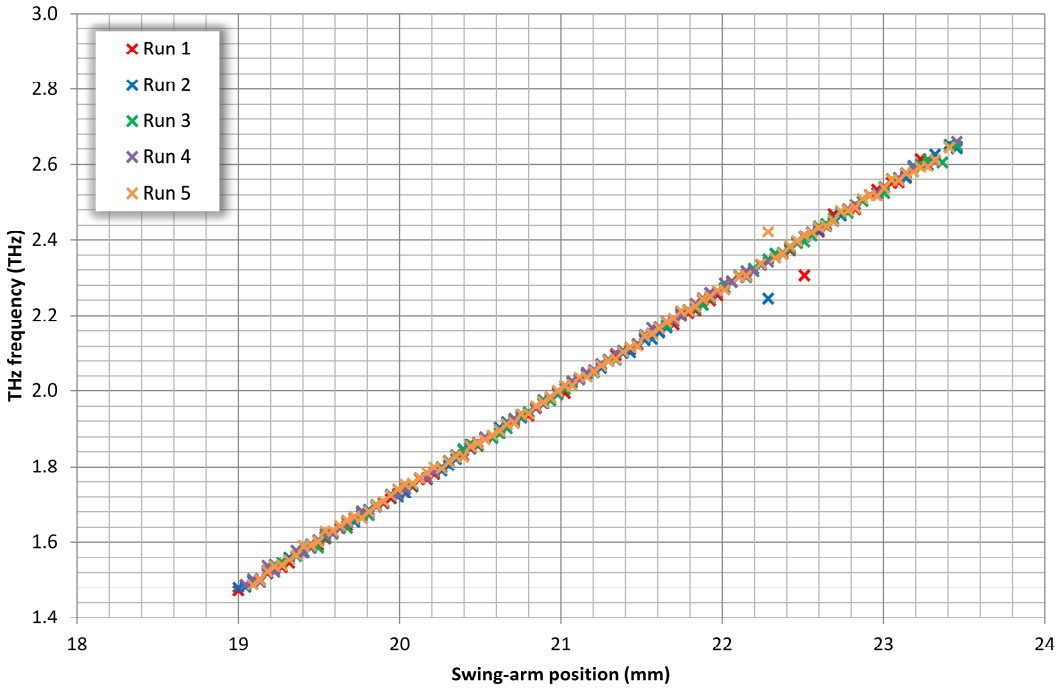

Figure 2.30: Graph indicating the excellent repeatability of tuning using the automated swing-arm control mechanism described in the text.

required and the number of scans to be made. A further development yet to be made is the addition of computer controlled étalon tuning, which would facilitate automated tuning across the entire tuning range but with a sub-GHz terahertz linewidth.

2.7.5 Results of spectroscopic measurements

During 2011, measurements of several ceramic samples were made on behalf of the Optical Diagnostics Group at Heriot-Watt University. The motivation behind this was to establish whether terahertz radiation was a suitable means of assessing these materials in terms of the presence of defects, with the purpose of the spectroscopy being purely to investigate whether the samples transmitted sufficient terahertz to make meaningful measurements.

These measurements were carried out using the spectrometer system described in this section. Tuning of the terahertz frequency was achieved using the automated tuning mechanism described earlier. The measurement procedure was to acquire a reference spectrum corresponding to nothing in the path of the terahertz beam and then to acquire one with the sample in the terahertz beam

path. In this manner the effects of the water vapour absorption could be normalised out, assuming that the atmospheric conditions had not changed significantly in the intervening time between taking these spectra.

Figure 2.31 shows an example of the spectra measured in this way. Any water vapour manifests itself as the dips present in the reference spectrum and the spectrum of the sample is similar but with much reduced transmission across the entire tuning range, indicating that the terahertz is being broadly absorbed by the ceramic material. To extract more meaningful data from the spectra the ratio of the reference and sample spectra must be taken according to the Beer-Lambert law, stated as:

$$\frac{I}{I_0} = e^{-\alpha L} \tag{2.32}$$

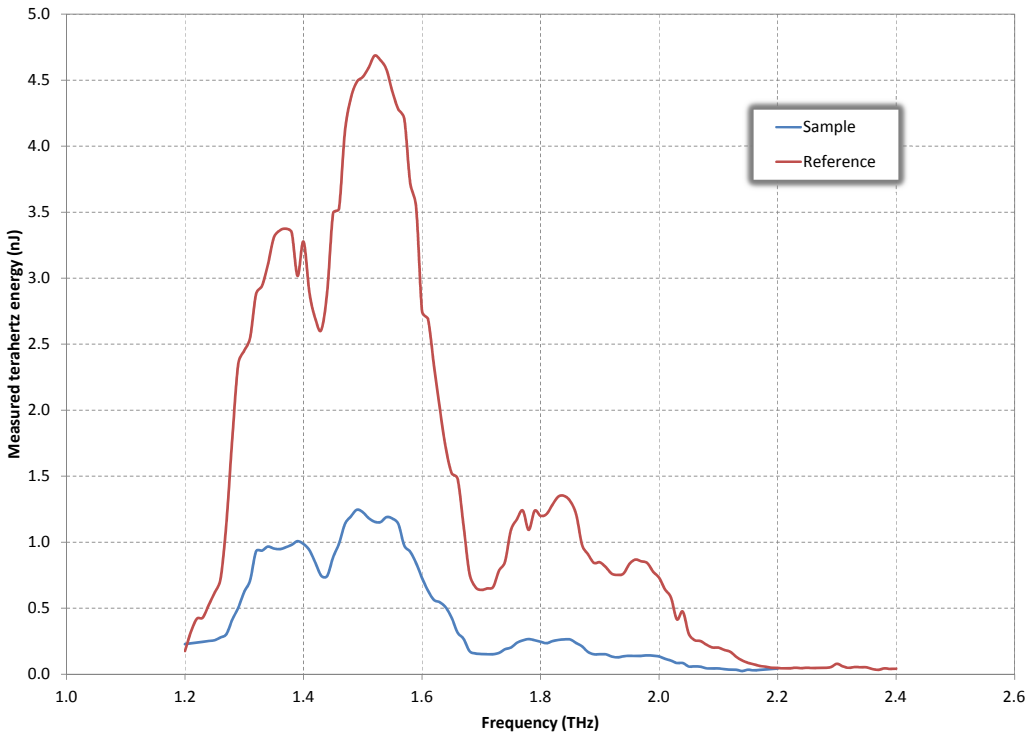

Figure 2.31: An example of the reference and sample spectra acquired in the manner described in the text.

where I is the intensity transmitted by the sample; I_0 is the reference intensity; α is the absorption coefficient and L is the propagation length through the sample. By taking the natural logarithm of both sides and solving for α the following expression is obtained:

$$\alpha L = \ln\left(\frac{I_0}{I}\right) \tag{2.33}$$

Referencing the spectra in this manner effectively removes the water vapour spectral features from the sample data since the path length through air only differs by the thickness of the sample, which in this case amounts to no more than a one percent change in the path length - the total path was ≈1m long and the samples were less than 1cm thick. As a result any spectral features due to the sample can be seen in the processed data.

Figures 2.32 and 2.33 show the processed spectra of two ceramic samples. The samplesexhibit approximately the same absorption trend across the terahertz tuning range except that sample 2 is more strongly absorbing than sample 3, most probably due to sample 2 being thicker than sample 3. It should be noted that the graphs showing the measured absorption of each sample are plotted over a limited range due to the fact that at the ends of the tuning range the measured signal drops to zero because of the strong water absorption at these points in the tuning range (see figure 2.28).

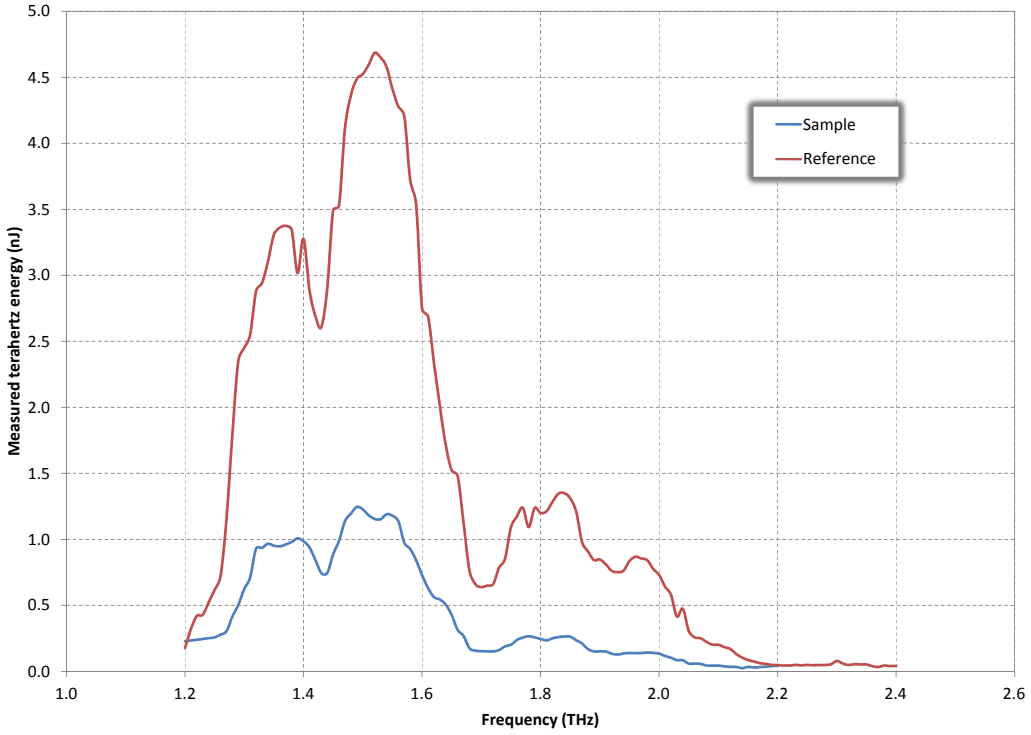

(a) Reference and trace corresponding to sample 2.

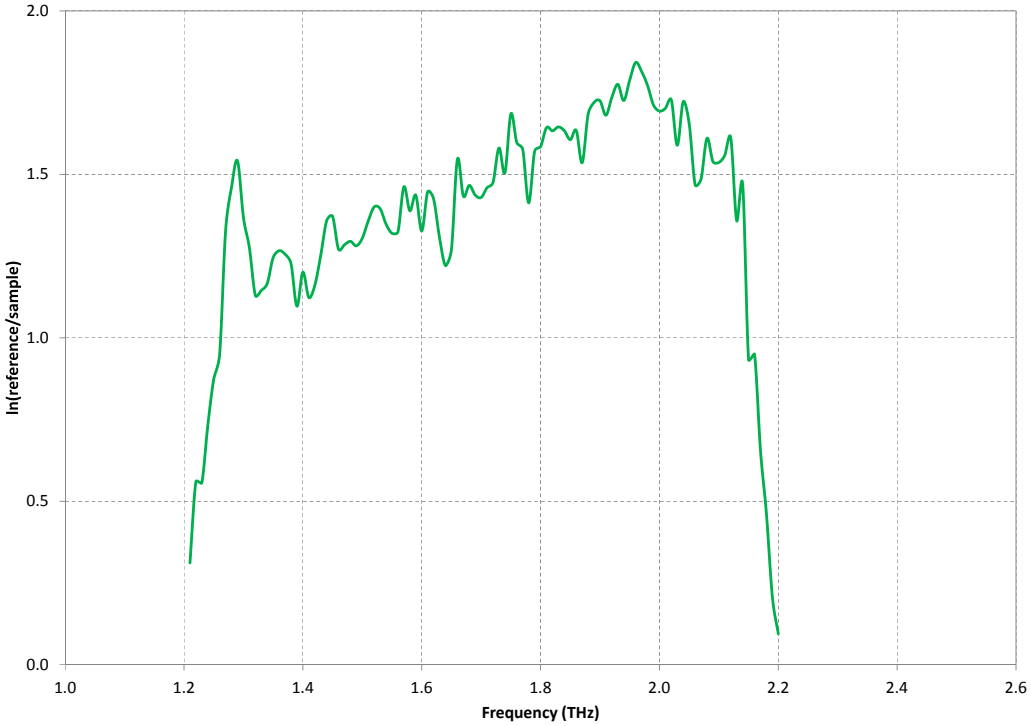

(b) Terahertz absorption spectrum of sample 2.

Figure 2.32: The processed spectra of ceramic sample 2.

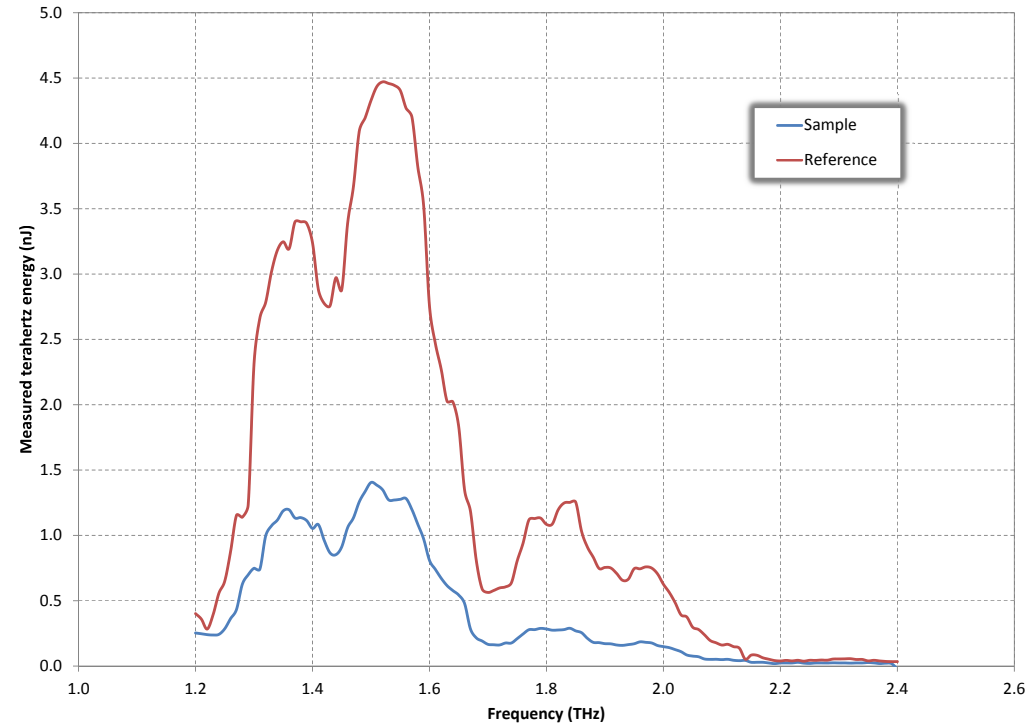

(a) Reference and trace corresponding to sample 3.

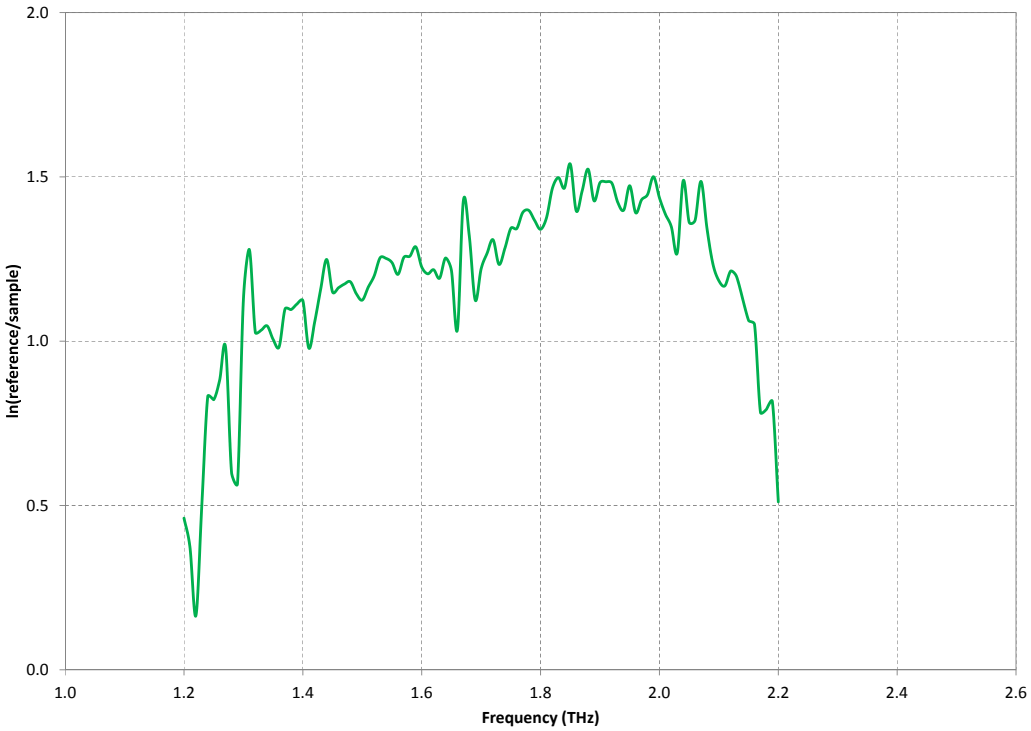

(b) Terahertz absorption spectrum of sample 3.

Figure 2.33: The processed spectra of ceramic sample 3.

2.8 Conclusions

The work presented in this chapter includes the characterisation of the intracavity terahertz OPO on a far more comprehensive scale than has been carried out previously. The cavity parameters which most affect the OPO threshold and the down-conversion efficiency have been identified and the parasitic losses of the pump and idler cavities have been calculated and reconciled with measured quantities. In light of the knowledge of the parasitic losses, it has been possible to perform calculations of threshold gain, which show good agreement between the experimental data and the threshold gain requirements.

The development of a compact, room-temperature and frequency-agile terahertz spectrometer has been described. The implementation of computer control of the idler cavity mirrors has resulted in a spectrometer which allows for the rapid collection of spectra and which is both easy to use and provides reproducible spectral data. The problem of absorption due to water vapour in the atmosphere is evident in the measured spectra, unless suitable steps are taken to purge the terahertz path with nitrogen. However, meaningful spectral information can still be extracted from free-space spectra if a reference spectrum is measured or if the spectral region of interest is confined to a region where there are no water absorption features.

The applicability of the device could be increased by the implementation of computer control for the intracavity étalons. This would allow higher resolution spectroscopy to be carried out. The further development of terahertz detectors, including the novel electro-optic detector, would make the spectrometer a completely room-temperature device.

References

[1] T. J. Edwards, D. Walsh, M. B. Spurr, C. F. Rae, M. H. Dunn, and P. G. Browne. Compact source of continuously and widely-tunable terahertz radiation. *Optics Express*, 14(4):1582–1589, 2006.

[2] D. A. Walsh. *Intracavity Terahertz Optical Parametric Oscillators*. PhD thesis, University of St Andrews, 2010.

[3] K. Kawase, J. Shikata, K. Imai, and H. Ito. Transform-limited, narrow-linewidth, terahertz-wave parametric generator. *Applied Physics Letters*, 78(19):2819–2821, 2001.

[4] D. Findlay and R. A. Clay. The measurement of internal losses in 4-level lasers. *Physics Letters*, 20(3):277–278, 1966.

[5] N. Hodgson and H. Weber. *Laser Resonators and Beam Propagation: Fundamentals, Advanced Concepts and Applications*. Springer, 2005.

[6] R Böhm, V. M. Baev, and P. E. Toschek. Measurements of operation parameters and nonlinearity of a Nd^{3+}-doped fibre laser by relaxation oscillations. *Optics Communications*, 134:537–546, 1996.

[7] M. Dunn, B. Sinclair, P. Lindsay, and A. Gillies. Photonics simulation software for teaching (Psst!). http://www.st-andrews.ac.uk/~psst/ (accessed 17/02/2012).

[8] O. Paul, A. Quosig, T. Bauer, M. Nittmann, J. Bartschke, G. Anstett, and J.A. L'huillier. Temperature-dependent Sellmeier equation in the MIR for the extraordinary refractive index of 5% MgO doped congruent $LiNbO_3$. *Applied Physics B: Lasers and Optics*, 86:111–115, 2007. 10.1007/s00340-006-2414-8.

[9] M. E. Lines and A. M. Glass. *Principles and applications of ferroelectric and related materials*. Clarendon Press, 1997.

[10] A. Rauber. *"Chemistry and physics of lithium niobate" in "Current topics in material science vol. 1"*. North-Holland, Amsterdam, 1978.

[11] R. S. Weis and T. K. Gaylord. Lithium niobate: Summary of physical properties and crystal structure. *Applied Physics A*, 37:191, 1985.

[12] U. Schlarb and K. Betzler. Influence of the defect structure on the refractive indices of undoped and Mg-doped lithium niobate. *Phys. Rev. B*, 50:751–757, Jul 1994.

[13] D. E. Zelmon, D. L. Small, and D. Jundt. Infrared corrected sellmeier coefficients for congruently grown lithium niobate and 5 mol.% magnesium oxide –doped lithium niobate. *J. Opt. Soc. Am. B*, 14(12):3319–3322, Dec 1997.

[14] D. A. Roberts. Simplified characterization of uniaxial and biaxial nonlinear optical crystals: a plea for standardization of nomenclature and conventions. *IEEE Journal of Quantum Electronics*, 28(10):2057–2074, 1992.

[15] I. Shoji, T. Kondo, A. Kitamoto, M. Shirane, and R. Ito. Absolute scale of second-order nonlinear-optical coefficients. *J. Opt. Soc. Am. B*, 14(9):2268–2294, Sep 1997.

[16] S. S. Sussman. Tunable light scattering from transverse optical modes in lithium niobate. Technical report, Stanford Univ., Stanford, CA, Microwave Lab. Rep. 1851, 1970.

[17] J. Shikata, K. Kawase, K. Karino, T. Taniuchi, and H. Ito. Tunable terahertz-wave parametric oscillators using $LiNbO_3$ and MgO:$LiNbO_3$ crystals. *IEEE Transactions on Microwave Theory and Techniques*, 48:653–661, 2000.

[18] M. Schall, H. Helm, and S. R. Keiding. Far infrared properties of electro-optic crystals measured by THz time-domain spectroscopy. *International Journal of Infrared and Millimeter Waves*, 20:595–604, 1999. 10.1023/A:1022636421426.

[19] D. R. Bosomworth. The far infrared optical properties of $LiNbO_3$. *Applied Physics Letters*, 9(9):330–331, 1966.

[20] L. Pálfalvi, J. Hebling, J. Kuhl, A. Péter, and K. Polgár. Temperature dependence of the absorption and refraction of Mg-doped congruent and stoichiometric $LiNbO_3$ in the THz range. *J. Appl. Phys.*, 97:123505, 2005.

[21] S. Brosnan and R. Byer. Optical parametric oscillator threshold and linewidth studies. 15(6):415–431, 1979.

[22] A. G Fox and T. Li. Resonant modes in a maser interferometer. *Bell Sys. Tech. J.*, 40:453–458, 1961.

[23] D. Walsh, D. J. M. Stothard, T. J. Edwards, P. G. Browne, C. F. Rae, and M. H. Dunn. Injection-seeded intracavity terahertz optical parametric oscillator. *J. Opt. Soc. Am. B*, 26:1196–1202, 2009.

[24] Angstrom WS7-L MC Wavelength Meter, HighFinesse GmbH, Tübingen, Germany.

[25] D. J. M. Stothard, T. J. Edwards, D. Walsh, C. L. Thomson, C. F. Rae, M. H. Dunn, and P. G. Browne. Line-narrowed, compact, and coherent source of widely tunable terahertz radiation. *Applied Physics Letters*, 92(14):141105, 2008.

[26] Newport compact motorised actuator cma-25pp and single-axis motor controller/driver smc100. http://www.newport.com/CMA-Series-Compact-Motorized-Actuators/140186/1033/info.aspx (Accessed 17/02/2012).

3

Difference frequency generation in $LiNbO_3$

3.1 Introduction

When the performance of the pump laser and OPO were being characterised (chapter 2), the generation of a second idler wavelength was observed. This second idler manifested itself as an additional, spatially separated beam. This chapter describes the procedures used to fully establish the origin of the second idler.

Through a rigorous series of measurements, the second idler has been attributed to a difference frequency generation process occurring between the terahertz and idler waves that are produced in the original parametric process. To our knowledge, such an effect has previously only been observed in systems based on periodically-poled lithium niobate [1, 2], where the "cascaded" idlers are also resonated in the shared pump and idler cavity; in the present system, the second idler is not resonated within the non-collinear idler cavity because it propagates along a separate path from the first idler.

A simple mathematical model has been devised to estimate the amount of enhancement experienced by the terahertz field due to the difference frequency process. The output of this model agrees well with the measured data.

3.2 Experimental setup

The system under consideration is shown in figure 3.1. The pump laser gain medium, LG, is a Nd:YAG crystal, 7mm in length and 4mm wide with a doping level of Nd at 1.3%. A fibre-coupled AlGaAs pulsed laser diode delivering pulses of 250μs duration and having peak powers up to 100W at a repetition rate of 135Hz and at a wavelength of 803.7nm (as described in chapter 2) is used to optically excite the gain medium. A standard electro-optic configuration based on a Pockels cell, quarter-wave plate and linear polariser is incorporated into the cavity for the purpose of Q-switching. Mirrors M1 and M2 form the pump laser cavity, with M1 having >99% reflectivity and M2 having 98% reflectivity. M3 - M5 are the mirrors that form the intersecting idler cavity. They have reflectivities >99.9%, >99.9% and 60% respectively. In this case the nonlinear medium is an MgO-doped $LiNbO_3$ crystal of length 70mm and width 5mm, with a doping level of 5 mol.%. The idler wavelength can be tuned by changing the angles of M3 and M5 in order to alter the phase-matching condition. The multiple idler beams become spatially distinct several centimetres after being output from M5, allowing their individual spectral and temporal characteristics to be measured. It should be noted that due to the angular separation between the two idlers, only the first idler (produced by the parametric process) is resonated in the idler cavity since the second idler beam is not incident on the mirror surfaces at 90°.

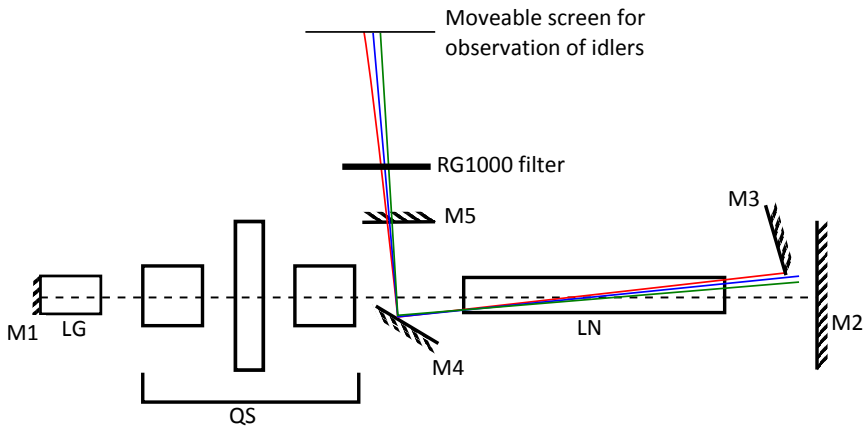

Figure 3.1: Schematic diagram of the intracavity terahertz OPO in which difference frequency generation was observed. The screen was used to display the idler beams so that photographs could be taken of them.

The powers measured in the second idler are therefore associated with only a single pass of the cavity.

3.3 Determination of the nature of the additional spots

A series of measurements of the features newly-observed in the proximity of the idler beam was undertaken so as to determine their nature. These included spectral, temporal and power measurements at several points across the OPO tuning range, the details of which are provided here.

3.3.1 Interpretation of the measured spectral data

An optical fibre was translated across the three spots emerging from the idler cavity so that the spectral content of each could be measured using an optical spectrum analyser (model HP86140A). The wavelength of the first idler wave, which is the brightest and leftmost observed beam (as shown in figure 3.1, was tuned to five points across the tuning range of the OPO (approximately 1068nm to 1073nm) by altering the angles of mirrors M3 and M5. The spectrum analyser returned the signal in dBm over a specified range of vacuum wavelengths. The resolution bandwidth of the spectrum analyser is 0.2nm and the video bandwidth used was 135Hz, to match the repetition rate of the laser. When converted to a frequency, the resolution bandwidth takes a value of 53GHz, which is comparable to the linewidth of the OPO (see chapter 2), meaning that linewidth and bandwidth effects are indistinguishable. The spectrum analyser recorded the maximum signal received across the wavelength range over a given length of time so that a value could be obtained for the linewidths of the various observed wavelengths.

As an example, the initial measurement of the first idler at a wavelength of 1070.30nm and a second idler at 1076.30nm is shown in figure 3.2. This OSA trace represents a single measurement of all three wavelengths, at a position close enough to the idler cavity output coupler that all three beams overlap spatially. In frequency terms, the separation of the pump and first idler is

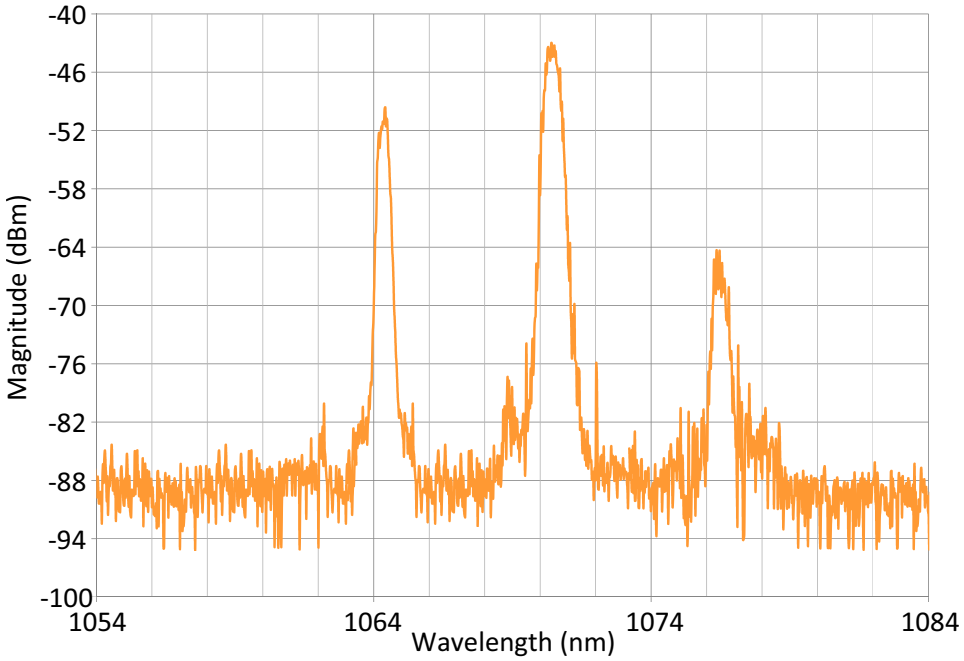

Figure 3.2: The initial OSA trace showing the presence of more than one spectral feature in the output of the idler cavity. The pump is at a wavelength of 1064.31nm, the first idler at 1070.30nm and the second idler at 1076.30nm.

1.568THz and the separation of the two idlers is 1.562THz. Since the frequency spacings are equal (to within the measurement capabilities), difference frequency generation resulting from the interaction of the terahertz wave with the first idler may be the mechanism behind the production of the second idler. The phase-matching scheme that would describe such an occurrence is depicted in figure 3.3. The relationship between the pump, idler and terahertz frequencies in the original parametric process is:

$$\nu_p = \nu_{i1} + \nu_T \tag{3.1}$$

where the subscripts p, $i1$ and T denote the pump, first idler and terahertz waves respectively. The corresponding wave vectors are calculated using the following equation:

$$k_j = \frac{2\pi n_j \nu_j}{c} \tag{3.2}$$

where the subscript j indicates the wave of interest, ν_j is the frequency of the wave expressed in Hz and n_j is the appropriate refractive index. Here the pump and idler waves are assumed to experience the same refractive index (calculated using the Sellmeier by Zelmon and colleagues [3]) denoted by n_0, and the

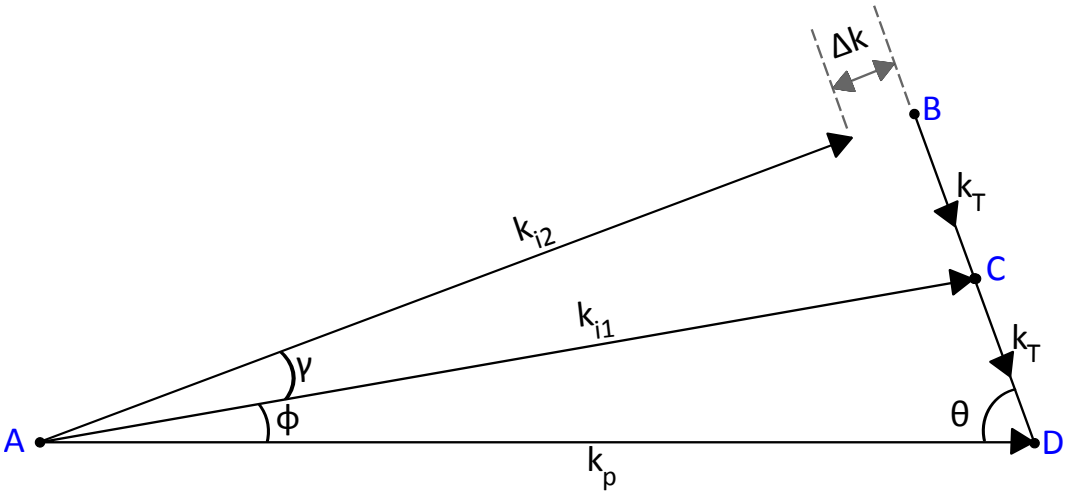

Figure 3.3: Phase-matching condition corresponding to parametric generation of the first idler and terahertz waves along with difference frequency generation of the second idler by the mixing of the terahertz with the first idler.

refractive index for the terahertz wave is n_T, calculated using the Sellmeier equation developed by Pálfalvi [4].

Using equations 3.1 and 3.2 we find that the wave vector of the first idler is related to those of the pump and terahertz waves as follows:

$$k_{i1} = (k_p - \frac{n_0}{n_T} k_T) \tag{3.3}$$

If difference frequency generation due to injection seeding with the terahertz wave arising from the original parametric process were behind the generation of the third wavelength present in the OSA traces then the angle ϕ is determined by the phase-matching conditions corresponding to the parametric process. Due to the terahertz injection seeding the difference frequency generation process, BC and CD must be collinear and equal in length. The relationship between the wave vectors corresponding to the pump, second idler and terahertz waves is then:

$$k_{i2} = k_p - \frac{2n_0}{n_T} k_T \tag{3.4}$$

where k_{i2} denotes the wave vector of the second idler.

A phase mismatch, Δk arises in the context of difference frequency generation from k_{i2} not being equal in length to AB. The degree of this mismatch can be

determined if θ, the length AB and the value of k_{i2} (either from measurements or from equation 3.4) are known. The procedure to calculate Δk is as follows:

Using the cosine rule, the value of θ can be determined:

$$k_{i1}^2 = k_p^2 + k_T^2 - 2k_p k_T \cos\theta$$

Thus

$$\left(k_p - \frac{n_0}{n_T}k_T\right)^2 = k_p^2 + k_T^2 - 2k_p k_T \cos\theta$$

and

$$\left(\frac{n_0}{n_T}\right)^2 k_T^2 - \frac{2n_0}{n_T}k_T k_p = k_T^2 - 2k_p k_T \cos\theta$$

Rearranging for $\cos\theta$

$$\cos\theta = \frac{n_0}{n_T} - \frac{1}{2}\left(\frac{n_0^2}{n_T^2} - 1\right)\left(\frac{k_T}{k_p}\right) \tag{3.5}$$

Knowing θ, length AB can be calculated, again using the cosine rule:

$$\begin{aligned}(AB)^2 &= k_p^2 + (2k_T)^2 - 4k_p k_T \cos\theta \\ (AB)^2 &= k_p^2 + 4k_T^2 - 4k_p k_T\left(\frac{n_0}{n_T} - \frac{1}{2}\left(\frac{n_0^2}{n_T^2} - 1\right)\frac{k_T}{k_p}\right)\end{aligned} \tag{3.6}$$

The frequency constraints on the second idler dictate that its wave vector is described by equation 3.4. Squaring this we find that:

$$k_{i2}^2 = k_p^2 + \frac{4n_0^2}{n_T^2}k_T^2 - \frac{4n_0}{n_T}k_T k_p$$

Thus (after rearranging)

$$(AB)^2 - k_{i2}^2 = 2k_T^2\left(1 - \frac{n_0^2}{n_T^2}\right)$$

The term on the left can be expanded as

$$(AB)^2 - k_{i2}^2 = (AB - k_{i2})(AB + k_{i2})$$

where $(AB - k_{i2}) = \Delta k$ and $(AB + k_{i2}) \approx 2k_p$ (since Δk is small and $k_p \approx k_{i1} \approx k_{i2}$)

Hence

$$\Delta k \approx k_T \left(\frac{k_T}{k_p}\right)\left(1 - \frac{n_0^2}{n_T^2}\right) \tag{3.7}$$

Or alternatively

$$\frac{\Delta k}{k_T} = \frac{\nu_T}{\nu_p}\frac{n_T}{n_0}\left(1 - \frac{n_0^2}{n_T^2}\right) \tag{3.8}$$

Considering a typical situation where a frequency of 2THz is generated ($n_T \approx 5.11, n_0 = 2.147$), then $\frac{\Delta k}{k_T} = 0.014$, so Δk is very small in relation to the size of the terahertz wave vector.

In order to quantify the extent of the phase-mismatch at the different points in the OPO tuning range, Gaussian profiles of the form $y = ae^{(-0.5(\frac{(x-x0)}{b})^2)}$ were fitted to the peaks in the spectral data in order to find the central wavelengths and widths of the wavelengths present. The graphs shown in figure 3.4 show the fitted peaks corresponding to the first idler being tuned to approximately 1072nm. The wavelengths were then converted into frequencies for use in subsequent calculations. Table 3.1 lists the measured frequencies and corresponding Δk values for the acquired data set. The first three columns list the spectral data that was acquired experimentally and the remaining data has been calculated on the basis of the experimental data. The terahertz frequency is calculated from equation 3.1 and the value of ν_{i2} corresponding to perfect phase-matching ($\Delta k = 0$) is then obtained using equations 3.4 and 3.2. Equation 3.8 is then used to evaluate $\frac{\Delta k}{k_T}$. Alternatively, as shown in the sixth column of the

Measured data			Calculated data			
ν_p (THz)	ν_{i1} (THz)	ν_{i2} (THz)	ν_T (THz) (equation 3.1)	ν_{i2} (THz) (equation 3.4)	$\frac{\Delta k}{k_T}$ (m^{-1}) (from data)	$\frac{\Delta k}{k_T}$ (m^{-1}) (calculated)
281.675	280.549	279.478	1.126	279.465	-0.005	0.008
281.677	280.109	278.547	1.568	278.587	0.011	0.011
281.680	279.974	278.339	1.706	278.321	-0.004	0.012
281.656	279.665	277.608	1.991	277.679	0.014	0.015
281.665	279.434	277.515	2.231	277.225	-0.051	0.017

Table 3.1: Summary of results from OSA measurements of the different wavelengths visible through the output of the idler cavity.

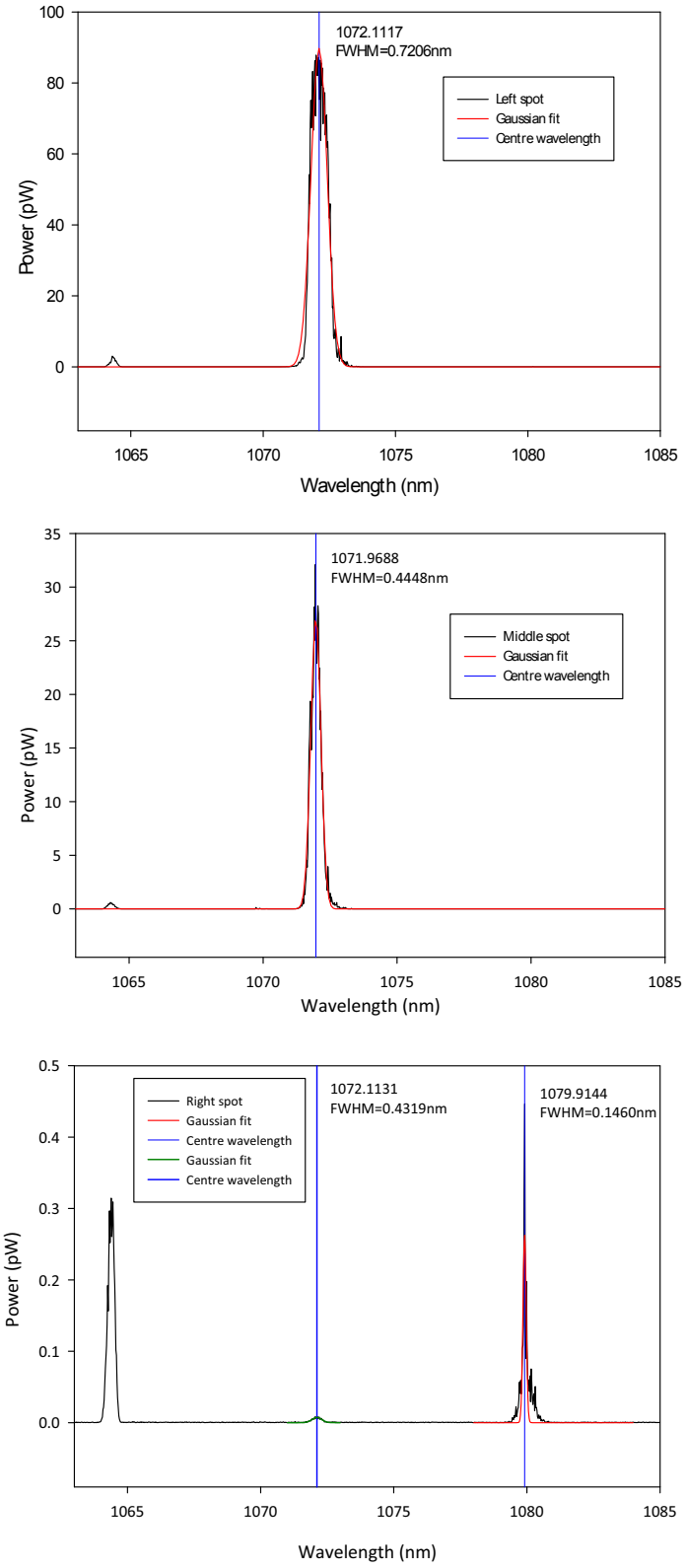

Figure 3.4: Gaussian fits applied to the data corresponding to the three visible spots emerging from the idler cavity.

table, $\frac{\Delta k}{k_T}$ can be found from the measurements and is given by the difference between k_{i2} from equation 3.4 and the measured value of k_{i2}, divided by the measured value of k_T. Although there is some discrepancy between the value of Δk derived from measurements and calculations the measured pump and idler linewidths of (50-70)GHz readily account for the difference between the values obtained via those two methods.

3.3.2 Recording the idler positions

In order to determine the separation of the three idler waves accurately a digital camera was used to record the position of the idler spots at several distances from one of the idler cavity mirrors. Using a Nikon D40x DSLR camera the infrared spots could be viewed on a sheet of card used to interrupt the beam path. Direct imaging of the idler beams was the only practical means of establishing their locations due to the intermittent nature of the third spot emerging from the idler cavity, which meant that finding the positions of peak intensity for each spot with a photodetector was prone to very large uncertainties and no meaningful information could be obtained using that method.

The camera was placed on a tripod in order to keep its position constant during the image capture process. An exposure length of 6 seconds was used so as to clearly observe the individual spots but to avoid saturating the image. Pictures were taken of the screen and a steel rule, acting as a length scale, at five points at equal intervals between 28 and 50cm away from the 60% mirror. An RG1000 filter was placed along the path of the idler beams external to the OPO cavity to eliminate the parasitic green light (produced by doubling of the pump light) from the photographs. For each distance of the screen from M5 two photographs were taken - one in which the steel rule was visible and a second in which the background lighting has been turned off to make the idler spots visible. Since the area covered by the two images is exactly the same the two can be overlaid to obtain a length scale for determining the spot separation.

The top image in figure 3.5 is an example of an image obtained in the manner

described above. Once merged the images were imported into *ImageJ*, an image processing and analysis program. This program was used to plot a profile across the idler spots, as shown in the lower part of figure 3.5, the physical extent of which was calibrated using the steel rule present in the image. The data from these plots was then imported into *SigmaPlot* where gaussian profiles were fitted to the peaks to identify the centre of the spots more accurately.

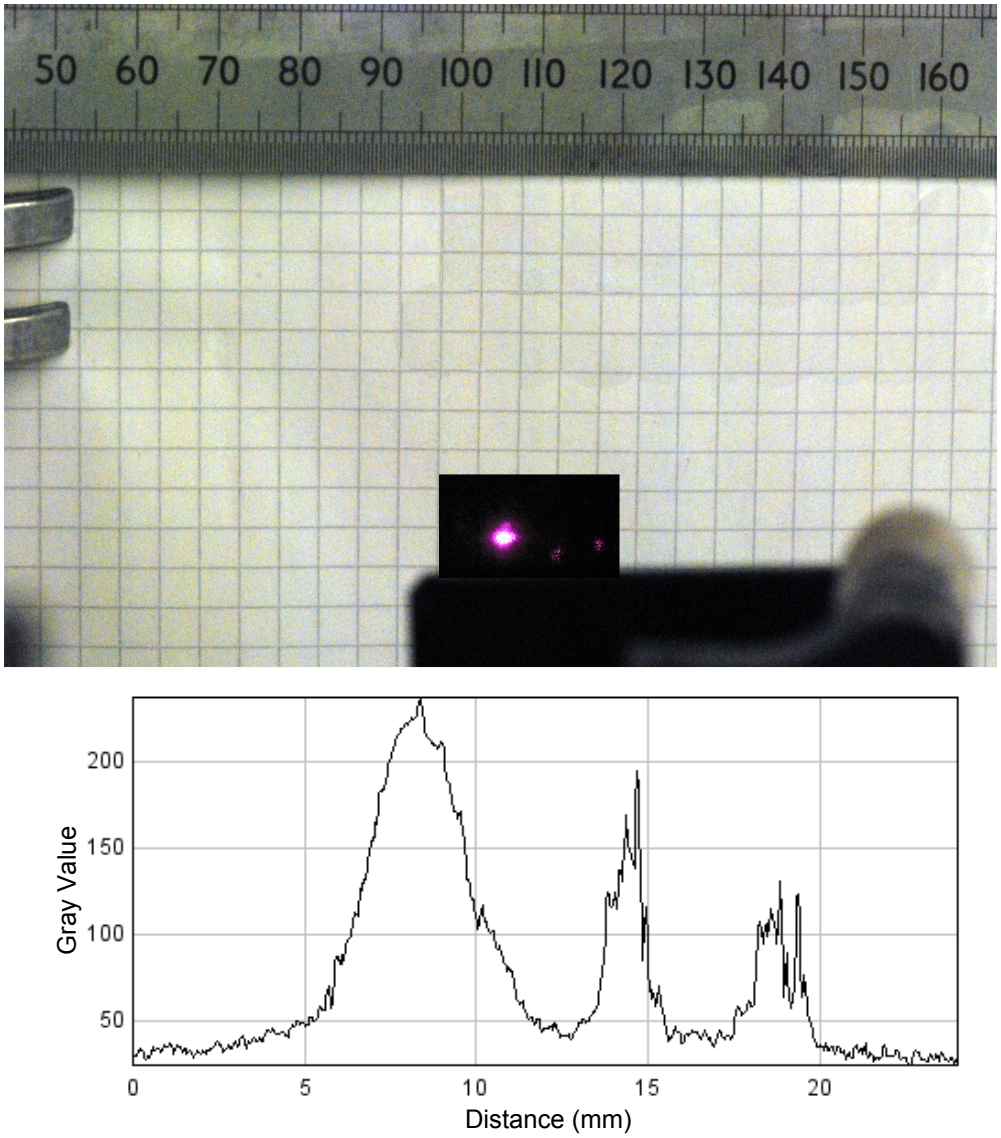

Figure 3.5: The upper image shows the combination of visible and infrared pictures captured using the digital SLR camera. The lower image is a profile plot corresponding to a line drawn through the three spots visible in the upper image. The distance in mm has been calibrated using the length scale from the top image.

3.3.3 Determining the angular separation of the idlers

Once the precise locations of the idler spots had been identified graphs showing the separation of the two additional spots from the first idler (the brightest one in the images) were constructed. An example of this is shown in figure 3.6. The vertical axis of this plot indicates the separation from the first idler, which corresponds to a constant value of zero on that axis. By fitting straight lines to the data sets the distance relative to the idler cavity output coupler that corresponds to the additional spot of interest overlapping with the first idler can be determined. The angular separation of the other spots from the first idler can also be determined using the relationship:

$$\tan(\text{angle of separation}(^\circ)) = \frac{\text{horizontal separation}}{\text{distance from mirror}} = \text{gradient}$$

The data shown in figure 3.6 corresponds to the first idler being tuned to 1070.79nm. The straight-line fit describing the position of the second feature relative to the first idler has a negligible gradient and thus implies that the

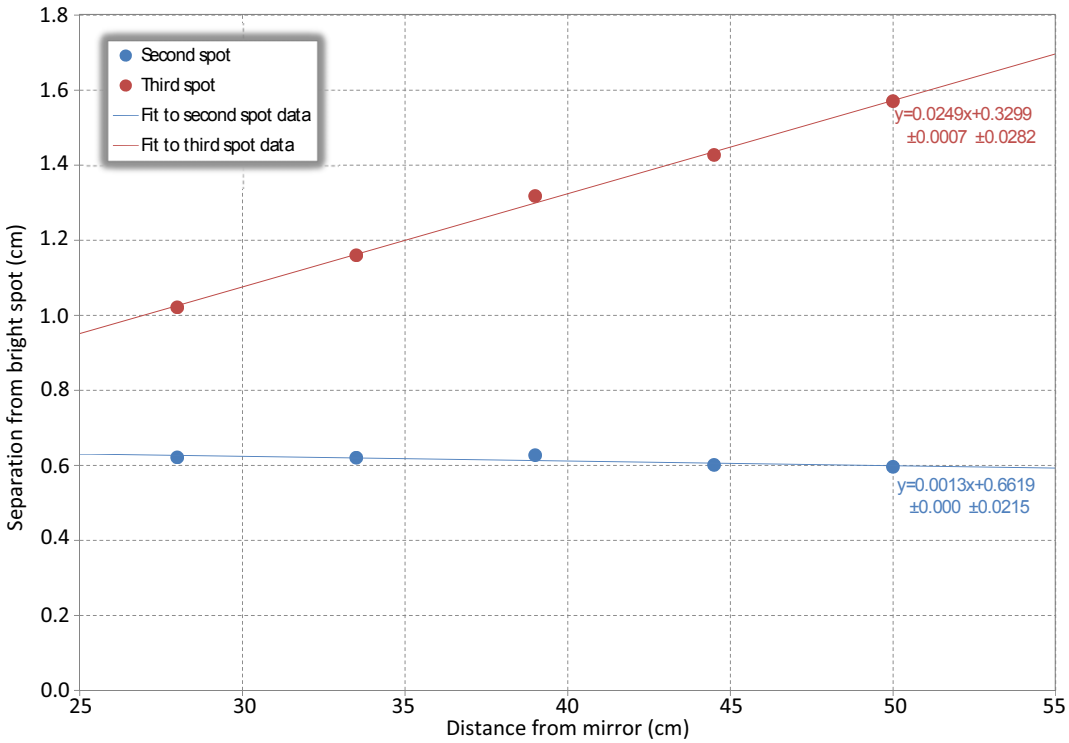

Figure 3.6: The graph shows the horizontal displacement of the second and third spots from the first idler for the situation where the first idler has been tuned to 1070.79nm. The equations of the straight lines correspond to solutions established using a least-squares fitting procedure.

second spot is parallel to the first idler in terms of its propagation direction. The third spot propagates at an angle of 1.43° to the first idler and the two beams intersect at approximately 13.25cm from the idler cavity output mirror (i.e. inside the cavity), which corresponds to a generation point within the crystal, 1.65cm from its end. Similar measurements were made for an initial idler wavelength of 1071.79nm. In this case the angular separation between the first first idler and the third spot was found to be 2.11°, whilst that of the first idler and the second spot was again found to be negligible. Following a similar approach as was used to reach equation 3.5 to describe the angle θ in figure 3.3, the second idler phase-matching angle γ can be calculated using the cosine rule:

$$k_T^2 = k_{i1}^2 + k_{i2}^2 - 2k_i k_{i2}\cos\gamma \tag{3.9}$$

where k_{i2} is given by

$$k_{i2} = k_p - \frac{2n_0}{n_T}k_T$$

Hence substituting for k_{i1} we have

$$k_T^2 = 2k_{i1}^2 + (k_p - \frac{2n_0}{n_T}k_T)^2 + 2k_{i1}(k_p - \frac{2n_0}{n_T}k_T)\cos\gamma$$

and by rearranging for $\cos\gamma$

$$\cos\gamma = \frac{k_{i1}^2 + k_p^2 + \frac{4n_0^2}{n_T^2}k_T^2 - k_T^2 - \frac{4n_0}{n_T}k_p k_T}{2(k_p - \frac{2n_0}{n_T}k_T)k_{i1}}$$

which can simplified to yield the final expression

$$\cos\gamma = \frac{k_p - \frac{2n_0}{n_T}k_T}{2k_{i1}} + \frac{k_{i1}^2 - k_T^2}{2(k_p - \frac{2n_0}{n_T}k_T)k_{i1}} \tag{3.10}$$

Of course, knowing the wavelength of the second idler from measurements, the value of $\cos\gamma$ can be calculated directly from equation 3.9 without the need to use equation 3.10, but it is a useful exercise to see just how good the agreement between the two routes is. Table 3.2 compares the values of γ obtained using the two equations (converted to angles outside the crystal) and, where possible, physically measured angles (from data such as that in figure 3.6). The two measured angles agree well with the calculated values of γ and the difference between them is easily accounted for by the uncertainties in the spatial separation measurements derived from the photographs of the idler spots.

Terahertz frequency (THz)	$\gamma(^\circ)$ from equation 3.9	$\gamma(^\circ)$ from equation 3.10	$\gamma(^\circ)$ measured
1.32	1.07	1.06	
1.76	1.53	1.48	1.42
1.90	1.68	1.63	
2.19	2.01	1.90	2.11
2.42	2.30	2.23	

Table 3.2: The values of the angular separation, γ between the first and second idlers. The values in the table are derived from the spatial separation measurements described previously and equations 3.9 and 3.10. The values refer to external angles, which were calculated using Snell's law.

3.3.4 Temporal relationship between the pump and idlers

Two fast (0.2ns rise-time) InGaAs photodiodes were used to obtain simultaneous measurements of the pump and idlers and to measure the emergence of the second idler relative to the first - the absence of any delay between them would also be indicative that difference frequency generation was the mechansim behind the creation of the second idler.

The detector circuit used is shown in figure 3.7. V_R is the reverse bias voltage (6V was used) applied to the photodiode; R is a series resistor of value 6.8kΩ; C is a bypass capacitor having a value of 100nF and is used to eliminate unwanted

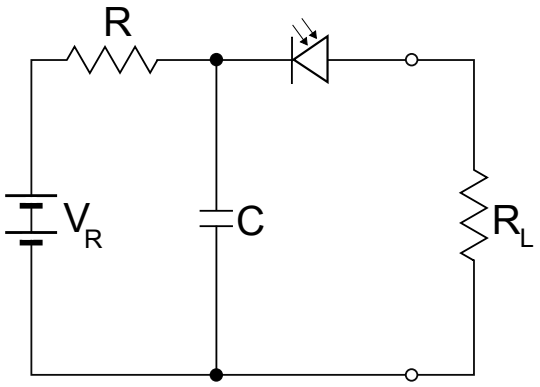

Figure 3.7: The circuit diagram of the detectors used to make simultaneous measurements of the pump and idler beams.

perturbations on the power supply and R_L is a 50Ω load resistor used for impedance matching to the 50Ω input terminal of an oscilloscope. A reverse bias is used to improve the speed and response of the photodiode by increasing the width of the depletion region and decreasing the junction capacitance.

In order to measure the various combinations of the pump and idler beams the beams of interest were focused onto the detectors and suitable attenuating filters were used to avoid damaging the detector elements. Cable lengths and propagation distances were matched for the two detectors. In the case of the beams exiting the idler cavity a pinhole was employed to avoid accidental measurement of the other beam.

Figure 3.8 presents the data acquired from simultaneous measurements of, firstly, the primary idler and the pump. The degree of pump depletion was observed by temporarily blocking the idler cavity using, for example, a small piece of card. The second plot illustrates that the two beams exiting the idler cavity have no temporal delay separating them, supporting the view that difference frequency generation is the source of the second beam. This plot also highlights the effect of using different attenuation values at the oscilloscope end of the detection system; the attenuators were necessary to suppress a ringing that was visible on the traces, meaning that extracting accurate pulse durations was difficult. Regardless of the choice of attenuator the idler beams all emerge at the same point in time so a 6dB attenuator was chosen for use in further measurements. It should be noted that although the vertical axis is in units of mV of signal measured by the photodiodes, differences in the optical attenuators used and the level of optimisation of the detector positions meant that the relative amplitudes of the beams are not indicative of their relative powers. Independent power measurements were made and will be discussed in the next section.

3.3.5 Conclusions made on the basis of experimental data

The measurements described in this section were taken in order to establish the nature and origin of the additional features observed through the output of the

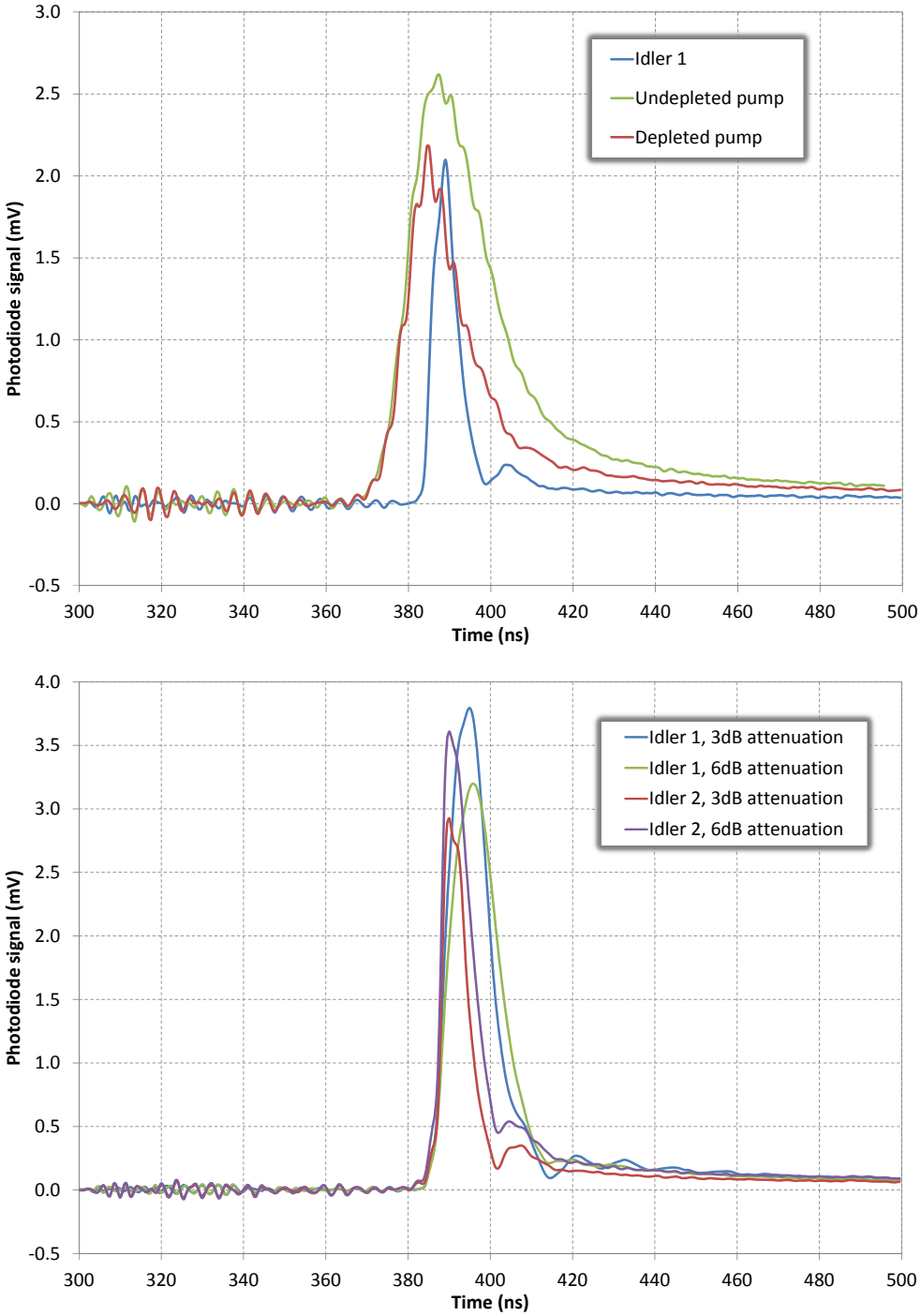

Figure 3.8: The upper plot shows the simultaneous measurements of the pump and first idler, with a delay of ≈12ns between the rising edge of the pump and the idler. The second graph shows the results of simultaneous measurements of the two idler beams, which appear at the same instant in time.

idler cavity. The spectral data corresponding to the additional beams indicated that the so-called "middle spot" was spectrally identical (considering the accuracy of the measurements) to the first idler and that the third beam contained different spectral features, which were explicable by difference frequency generation between the terahertz and first idler (see table 3.1). Measurements of the angular separation of the additional beams relative to the first idler showed that the second spot was in fact parallel to the first idler, leading us to explain its presence as resulting from a stray reflection somewhere within the idler cavity. The angle between the third beam and the first idler varied as the OPO was tuned but the angular separations measured were consistent with those expected for the case of difference frequency generation. Finally, temporal measurements of the third spot relative to the first idler revealed that there was no time delay between the generation of the two beams, unlike the case for the parametric generation of the idler and the terahertz beams, which exhibit a build-up time of typically 12ns. This data leads to the conclusion that the additional beam emergent form the idler cavity is produced through difference frequency generation. What follows next is an analysis of the effect this difference frequency generation has on the total amount of terahertz produced.

3.3.6 Idler power and threshold measurements

To assess the magnitude of the difference frequency generation process the power in the pump and idler beams were measured at one point in the tuning range of the OPO corresponding to a primary idler wavelength of 1070.8nm. Figure 3.9 illustrates the experimental setup used to achieve this. Three measurement points (labelled in the figure) were used to obtain sequential power measurements of the three fields using a large-area thermal power meter. A pinhole that was moveable using a translation stage (MP) was used to isolate the idler beam of interest. Owing to the close proximity of the two idlers a pick-off mirror, M6, was used to steer the first idler to measurement point "2". For each set of power measurements a spectral measurement was also acquired using the OSA; this allowed the measured powers to be corrected for the small amount of pump radiation that is present in these two beams (see figure 3.4) and

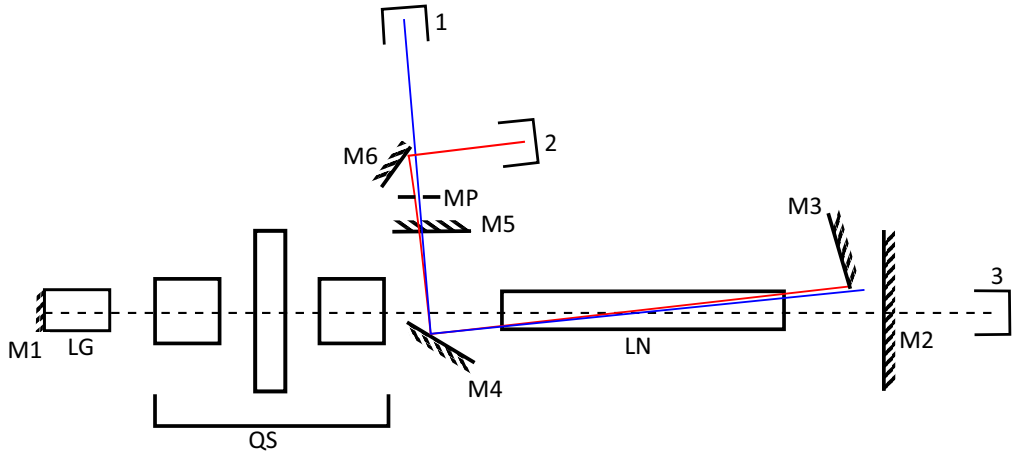

Figure 3.9: Schematic diagram of the measurement approach used to characterise the idler powers.

which results from the pump beam being clipped slightly by mirrors M3 and M4, which form part of the off-axis idler cavity. As well as increasing the measured idler power slightly the residual pump also obscures the threshold of idler generation so it is important to scale the power appropriately.

Figure 3.10 shows an OSA trace of the first idler when the OPO was operating just above threshold. To correct for the pump wavelength contribution to the measured mean power, the power value was adjusted according to the ratio of the peak heights at the pump and idler wavelengths. So for the case shown in figure 3.10, the measured power was scaled by a factor of (1-$\frac{0.25}{10}$). Following the idler power correction using the OSA traces the mean powers were converted to pulse energies using the following relation:

$$E_T = \frac{P_{mean}}{\text{repetition rate (Hz)}} \frac{\beta_o + \beta_p}{\beta_o} \tag{3.11}$$

where β_o and β_p are the output and parasitic losses of the cavity, respectively. In the case of the pump cavity, $\beta_p = 0.25$ and $\beta_o = 0.02$. For the idler cavity, $\beta_o = 0.4$ and the value of β_p is considered to be negligible with respect to β_o. Figure 3.11 shows the behaviour of the pump and idler fields with increasing laser diode energy. The pump laser is seen to clamp above OPO threshold while the laser output grows linearly in the absence of the parametric down-conversion process. The first and second idlers reach threshold at the same pumping level (≈8-8.5mJ), which is again indicative of the generation process responsible for

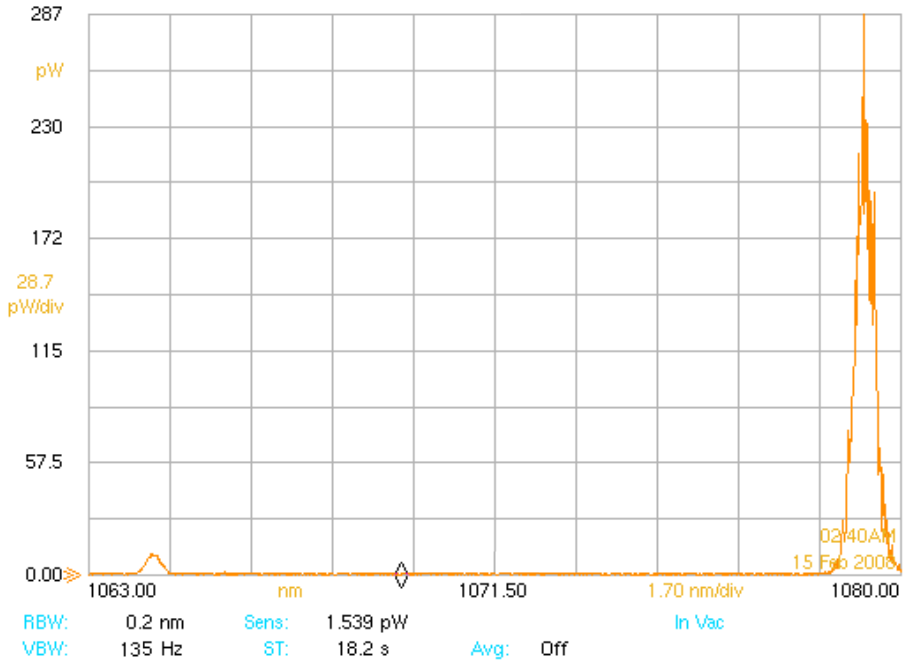

Figure 3.10: OSA trace collected at measurement point "1" when the OPO was not far above threshold, showing the contribution of the pump wavelength to the overall power.

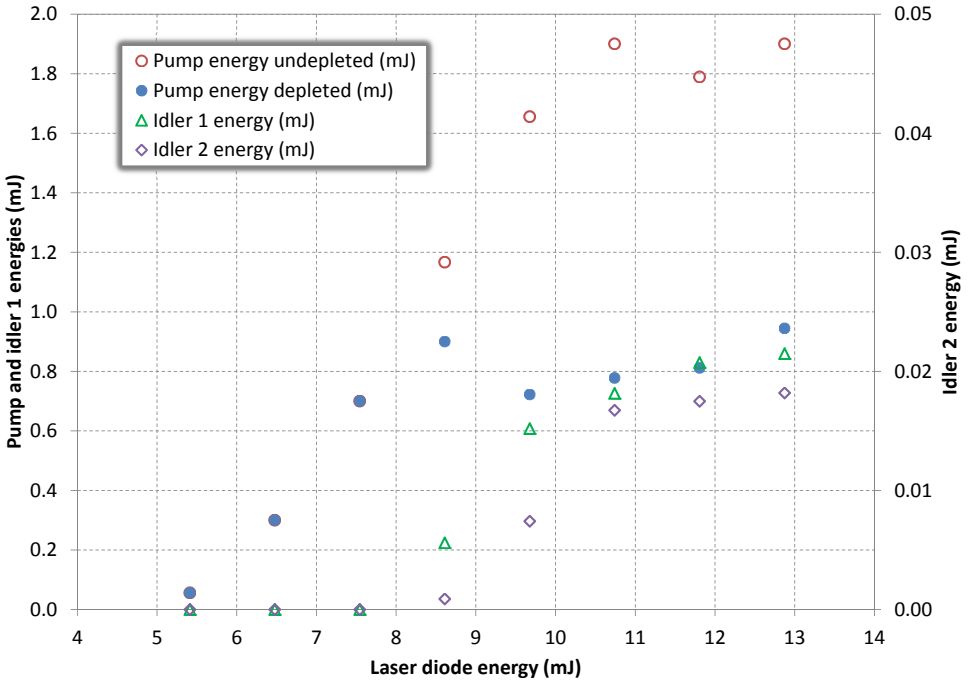

Figure 3.11: The energy characteristic of the laser with and without parametric down-conversion (achieved by physically blocking the off-axis idler cavity). Above the OPO threshold point the characteristic clamping of the laser power by down-conversion is clearly visible. The second idler is seen to reach approximately 2% of the first idler energy.

the appearance of the second idler being difference frequency generation between the terahertz and the first idler. The second idler energy reaches approximately 2% of the energy in the first idler pulses.

3.4 Enhancement of the terahertz field due to the presence of the second idler

We now consider the effect of the difference frequency generation process that occurs between the first and second idler and the terahertz waves in more detail.

The difference frequency at $\omega_2 = (\omega_3 - \omega_1)$ is generated by a strong pump wave at frequency ω_3 and a signal wave at frequency ω_1, which is also amplified through the difference frequency process. ω_1 to ω_3 correspond to the terahertz, second idler and first idler waves, respectively.

As shown in appendix B the expressions describing the evolution of the terahertz and second idler fields (E_T and E_2 respectively) with increasing segment number, n, are:

$$E_T(n) = \eta_{TT} E_T(0) + \eta_{T2} E_2^*(n-1) \tag{3.12}$$

$$E_2(n) = \eta_{2T} E_T^*(0) + \eta_{22} E_2(n-1) \tag{3.13}$$

where $E_T(0)$ and $E_T^*(0)$ are constant and n is the segment number. The coefficients $\eta_{TT}, \eta_{T2}, \eta_{2T}$ and η_{22} are related to quantities including the phase mismatch Δk and the parametric gain coefficient Γ and are defined in appendix B.

The pump field E_3, which corresponds to the first idler, is assumed to be strong and undepleted. This is consistent with the measured ratio of second idler to first idler of $\approx 2\%$. The electric fields are related to intensities through the expression:

$$I = \frac{1}{2} c \epsilon_0 E_i^2 n_i \tag{3.14}$$

where I is the intensity in Wm^{-2}; c is the speed of light in ms^{-2}; ϵ_0 is the permittivity of free space in Fm^{-1}; E_i is the electric field corresponding to a

particular wave in Vm^{-1} and n_i is the refractive index appropriate to the frequency under consideration. Hence by plotting the real part of $EE^*(n)$ as a function of the segment number, n, for the terahertz and second idler, their relative growth can be seen.

A simplistic graphical interpretation of the growth of the second idler and terahertz waves is shown in figure 3.12. The nonlinear crystal is split into N segments, each having a length equal to the walk-off length of the terahertz wave ($\approx$1mm) because the terahertz exits the crystal at a large angle to the optic axis, which limits the interaction length over which the terahertz experiences growth to the difference frequency process. Since the terahertz is generated along the entire length of the nonlinear crystal each segment has its own terahertz source that seeds the difference frequency generation, which has been generated by the original parametric process. The amount of terahertz seed is taken to be constant for each segment along the length of the nonlinear crystal.

Since the second idler is almost collinear with the first idler (with an angular separation of $\approx$(1-2)$^\circ$ measured outside the crystal) it experiences a cumulative increase along the crystal. The terahertz on the other hand walks off rapidly to exit the crystal before it can suffer strong absorption, hence its increase is

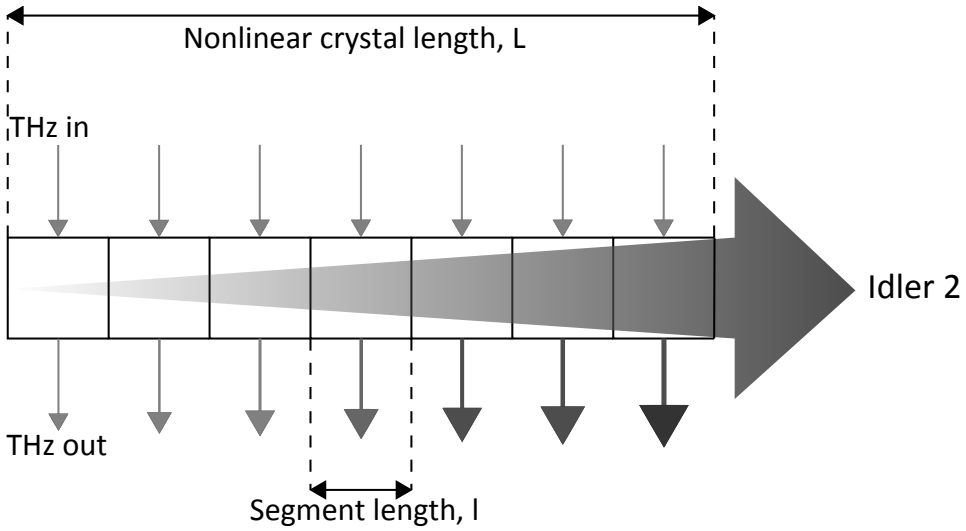

Figure 3.12: Schematic of the growth of the terahertz and second idler waves as they propagate through the nonlinear crystal.

smaller but still in the proportion with the increase in the second idler.

Figures 3.13a and 3.13b show how $E_i E_i^*(n)$ (which is proportional to the intensity) increases with segment number for the terahertz and second idler when $E_T(0)$ takes the value $e^{i\psi}$, where ψ represents the initial phase of the terahertz wave. The graphs show how the value of the phase mismatch, Δk, influences the growth of the intensities. From the outcomes of the modelling it is apparent that the starting value of ψ does not affect the evolution of the intensities so the graphs do not include a variation in ψ.

From equations 3.12 and 3.13 it is seen that the additional terahertz field generated in any segment is produced by second idler field from the previous segment. To compare the additional terahertz intensity with the second idler intensity from the previous segment, the second idler intensity must be scaled to reflect the relative intensity in the terahertz. To do this the second idler intensity must be multiplied by the ratio $\frac{\nu_2}{\nu_T}$. Figure 3.14 shows the result of this comparison. The red line shows the value of $(E_T(n)E_T^*(n) - E_T(0)E_T^*(0)) \times n_T$, which is proportional to the additional terahertz intensity generated in segment n. The blue line shows the value of $(E_2(n)E_2^*(n) - E_2(n-1)E_2^*(n-1)) \times n_2 \times \frac{\nu_2}{\nu_T}$, which is proportional to the additional second idler intensity in segment n scaled by the ratio of the second idler and terahertz frequencies, to account for the difference in photon energies. The graph shows that all of the additional energy (intensity) provided by the second idler is turned into additional terahertz energy (intensity).

Next the question of how much the terahertz intensity can be increased by this process must be addressed. Although no direct measurements of the terahertz were made during the investigation of this phenomenon, the energies of the first and second idlers were measured. Figure 3.15 describes the steps in the calculation process.

From the energy of the first idler and knowing the parasitic losses of the idler cavity, the corresponding terahertz energy can be calculated. Thus the starter

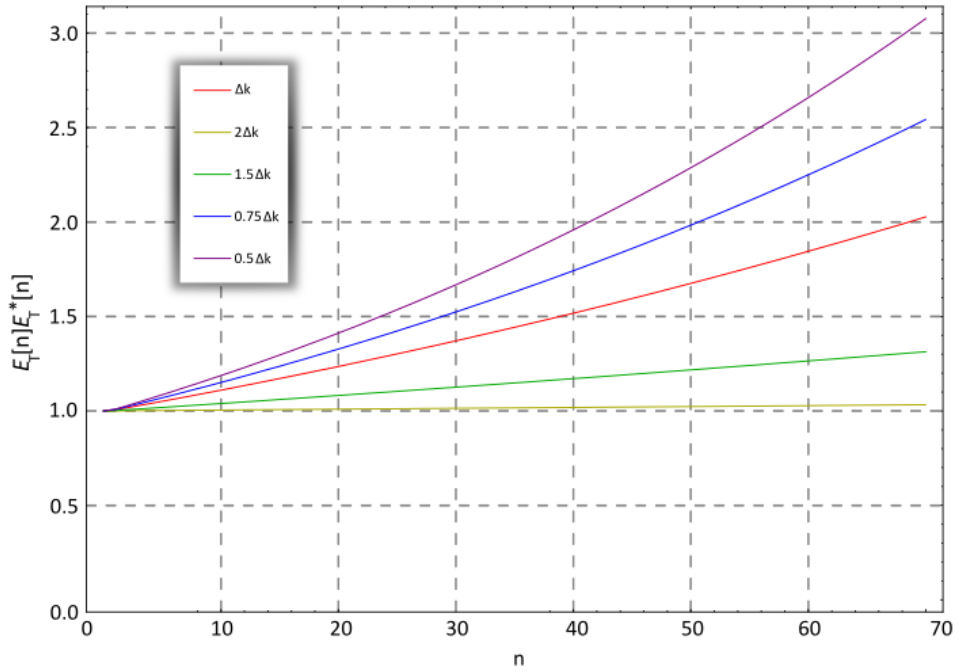

(a) The increase in $E_T E_T^*(n)$ with distance through the crystal.

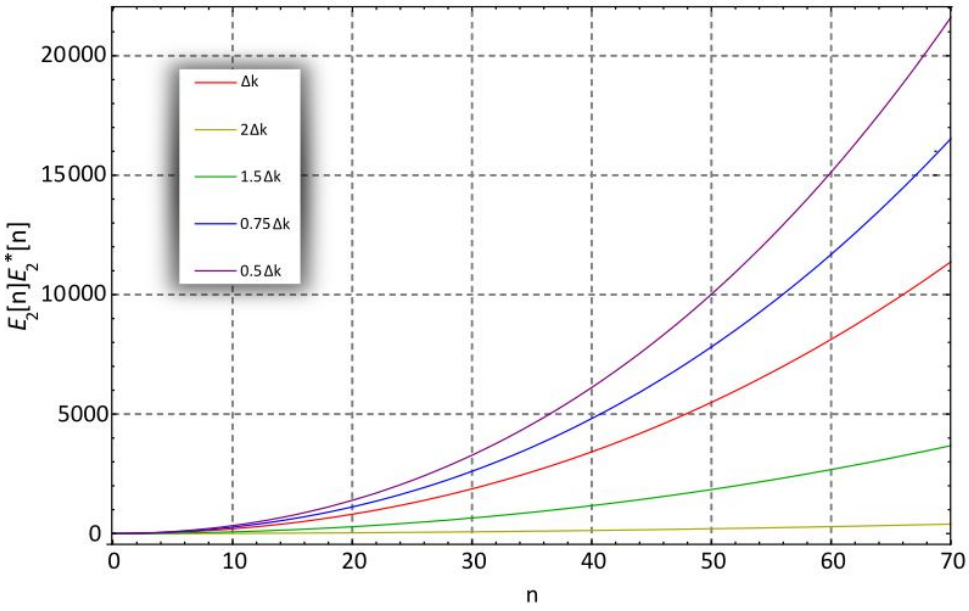

(b) The increase in $E_2 E_2^*(n)$ with distance through the crystal.

Figure 3.13: The growth of the second idler and terahertz intensities increase with propagation through the nonlinear crystal.

value of $E_T(0)$ can be established. The total additional terahertz intensity can then be extracted from the model, which can then be manipulated to yield the corresponding increase in the generated terahertz energy for comparison with the initial value. A similar process can be carried out for the second idler, the intensity of which is determined by calculating the value of $E_2E_2^*(n = N)$, i.e. at the end of the nonlinear crystal. With knowledge of the second idler pulse duration and beam size the energy of the second idler can be extracted. The value obtained should be consistent with that from the relative powers measured in the first and second idlers.

Under a typical operating regime where the terahertz frequency is ≈1.9THz and the generated energy of the first idler is 0.85mJ (equivalent to 50% pump depletion), the corresponding generated terahertz energy is ≈6μJ. This terahertz energy is equivalent to an input electric field of 0.016Vm^{-1} per mm-long segment. Following the procedure described in figure 3.15 yields an additional 2.76μJ of terahertz energy - an increase of 46% on the input terahertz energy. The process also produces an energy of ≈0.4mJ in the second idler. This result does not agree with the measured ratio of the second idler to the first idler, which was found to be 2%, however the model does not take into account the absorption of

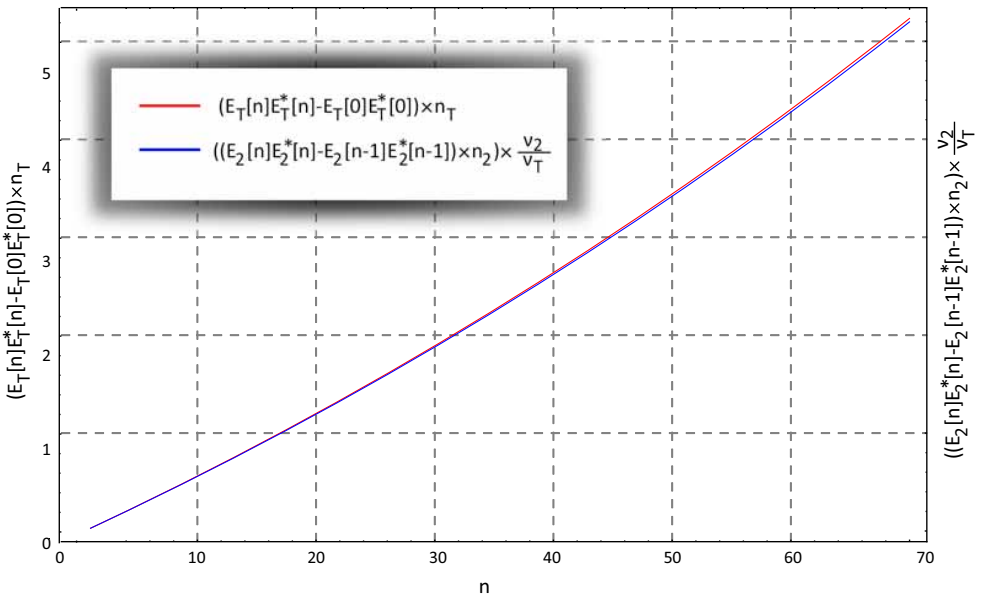

Figure 3.14: Graph showing how the generated terahertz intensity scales with the available second idler intensity.

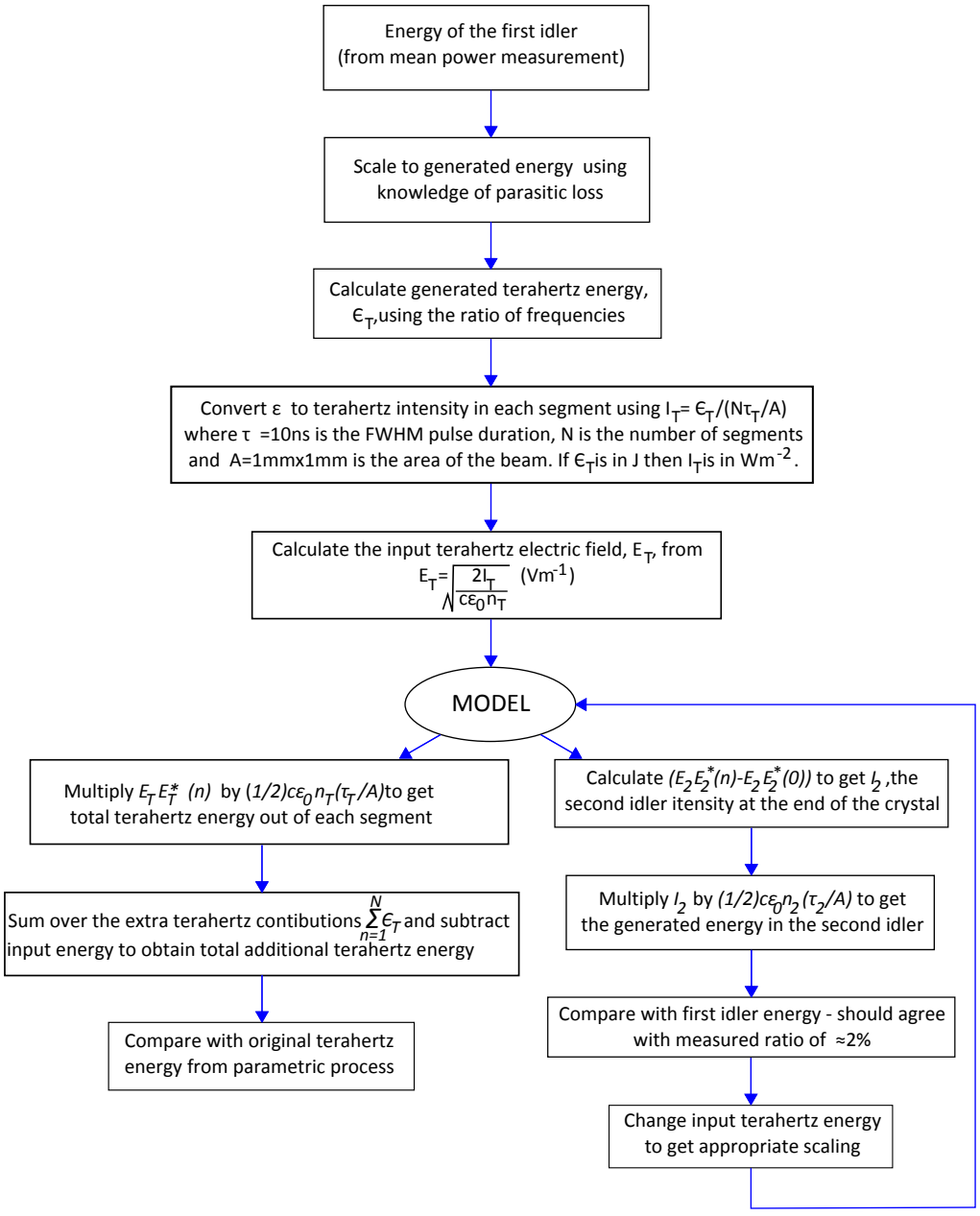

Figure 3.15: Flow chart describing the procedure to obtain physical values for the amount of second idler generated and for the terahertz enhancement.

the terahertz as it moves through the MgO:$LiNbO_3$ crystal. A simple way of doing so is to scale the input terahertz by a factor representing the absorption.

To get agreement between the model and the measured second idler energy, the total energy in the second idler at n=70 must equal 17μJ, around 5% of the initially calculated value. Accepting the values of Δk and Γ, which are derived from measured quantities, the generated second idler energy can be reduced to the match the measured value by scaling the input terahertz energy to 5% of its initial value to account for the terahertz absorption, i.e. it is reduced to 0.3μJ. This input terahertz energy yields 17μJ of energy in the second idler as required and produces an additional 0.138μJ of terahertz energy, which again represents an increase of 46% on the input terahertz energy and a 2% increase in the terahertz energy generated in the original parametric process. A reduction of the input terahertz energy to only 5% of its initial value is consistent with an absorption coefficient at 1.9THz, $\alpha_T \approx$ 40cm^{-1}, and a path length of 0.75mm which is a reasonable propagation length for the terahertz to reach the crystal face.

3.5 Conclusions

This chapter has characterised the phenomenon of difference frequency generation that was observed when a 70mm-long MgO:$LiNbO_3$ crystal was used as the nonlinear medium within the intracavity terahertz OPO. The presence of additional idlers in the output of the OPO was extensively characterised and shown to be explicable by difference frequency generation.

The effect has been modelled in terms of its ability to enhance the terahertz generated, with a 2% increase in terahertz energy anticipated (corresponding to a 50% increase in the input terahertz energy). Measurements of the terahertz wave will have to be made in order to confirm this result, however there is clear potential to further improve the efficiency of the device. In its present form, the model is only intended to provide a rough idea of the possible enhancement effect since it does not rigorously consider the effect of terahertz absorption,

which occurs simultaneously to the amplification process. The enhancement of 2% is based on the second idler making only a single pass of the crystal since it is not resonated in the idler cavity. It is possible that a means of resonating both idlers could be established to increase the terahertz enhancement, for example by selecting cavity mirrors having appropriate radii of curvature.

References

[1] D. Molter, M. Theuer, and R. Beigang. THz-OPO with a novel QPM-scheme. In *Proc. 34th Int. Conf. Infrared, Millimeter, and Terahertz Waves IRMMW-THz 2009*, pages 1–2, 2009.

[2] D. A. Walsh. *Intracavity Terahertz Optical Parametric Oscillators*. PhD thesis, University of St Andrews, 2010.

[3] D. E. Zelmon, D. L. Small, and D. Jundt. Infrared corrected Sellmeier coefficients for congruently grown lithium niobate and 5 mol.% magnesium oxide –doped lithium niobate. *J. Opt. Soc. Am. B*, 14(12):3319–3322, Dec 1997.

[4] L. Pálfalvi, J. Hebling, J. Kuhl, A. Péter, and K. Polgár. Temperature dependence of the absorption and refraction of Mg-doped congruent and stoichiometric $LiNbO_3$ in the THz range. *J. Appl. Phys.*, 97:123505, 2005.

4

Periodically-poled materials for THz generation

4.1 Introduction

Thus far the devices used to generate terahertz radiation described in the thesis have utilised bulk lithium niobate crystals as the nonlinear media. In this chapter we will explore the use of periodically-poled lithium niobate (PPLN) as an alternative means of satisfying the phase-matching conditions.

Various models will be developed to assess the nature of the terahertz radiation generated when a PPLN crystal is used as the nonlinear medium in a variety of phase-matching configurations. Due to the bipolarity of the grating vector a series of solutions are obtained for any particular phase-matching geometry. To be able to take advantage of the ability to custom-design gratings for any phase-matched geometry, it is essential to be able to identify these solutions in order to anticipate what the outcome of phase-matching will be.

As well as examining the use of PPLN in collinear phase-matching geometries including the tuning characteristic of such an arrangement, we will also explore its use in a novel "hybrid" phase-matching scheme. This is where the grating parameters are chosen so as to extend the tuning range of the terahertz intracavity optical parametric oscillator with respect to the system based on bulk

lithium niobate.

This chapter provides the theoretical details necessary to understand the results presented in the experimental chapters that follow. Chapter 5 will present the outcomes of experimental investigations of quasi-phase-matching using several different grating designs, both in collinear and non-collinear phase-matching geometries.

4.2 Overview of possible phase-matching schemes

4.2.1 Non-collinear phase-matching using bulk materials

The frequency and propagation direction of the photons involved in a parametric process must add up together with the same phase in order to experience gain. This phase-matching condition can be expressed as:

$$\underline{k}_p = \underline{k}_i + \underline{k}_T \tag{4.1}$$

which is equivalent to

$$\frac{2\pi n_p}{\lambda_p}\hat{p} = \frac{2\pi n_i}{\lambda_i}\hat{i} + \frac{2\pi n_T}{\lambda_T}\hat{T} \tag{4.2}$$

where $\underline{k}$ represents the wave-vector, n indicates the refractive index and λ is the wavelength. The subscripts p, i and T denote the pump, idler and terahertz waves respectively. $\hat{p}$, $\hat{i}$ and $\hat{T}$ are unit vectors describing the propagation directions of the three waves. Additionally, the allowed combinations of downconverted waves can be determined in terms of the conservation of energy using the following expression:

$$\frac{hc}{\lambda_p} = \frac{hc}{\lambda_i} + \frac{hc}{\lambda_T} \tag{4.3}$$

Looking at equation 4.2 it is clear that to be able to calculate whether or not phase-matching occurs we must have knowledge of the nonlinear material's refractive indices for each of the wavelengths. In the infrared region, where the pump and idler wavelengths lie, the refractive indices of lithium niobate and MgO-doped lithium niobate have been extensively characterised [1, 2]. In the terahertz optical parametric oscillator described in earlier chapters of the thesis all three waves are

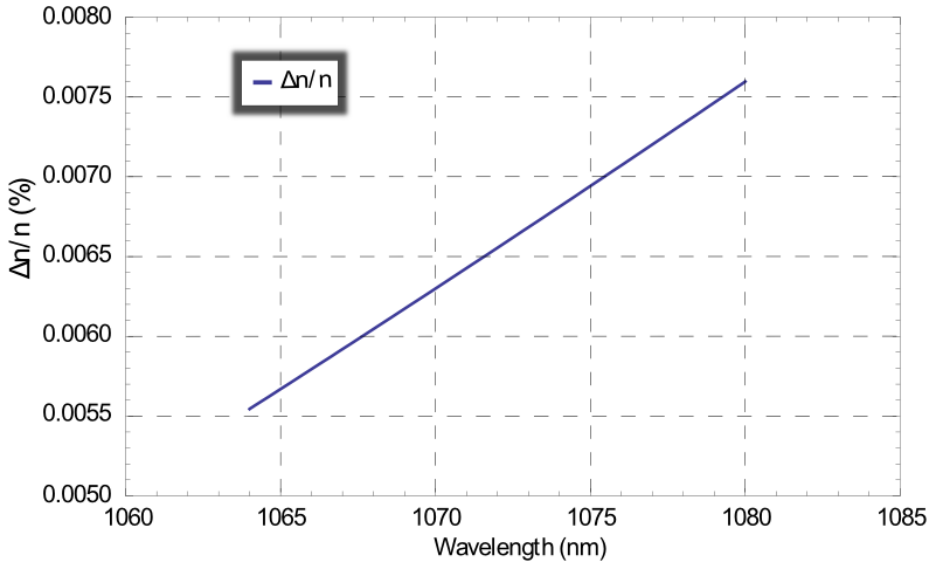

Figure 4.1: The difference between the values of n_e in percentage terms as calculated using the Zelmon and Schlarb Sellmeier equations across the wavelength range that encompasses the pump and idler appropriate for terahertz generation over 0.5-3 THz. The agreement between the two is excellent.

polarised along the extraordinary crystal axis and propagate in the x-y plane. For all calculations involving the refractive index at the pump and idler wavelengths the Sellmeier equation used is that of Zelmon et al. [1] who characterised the refractive indices of undoped and 5-mol.% MgO-doped lithium niobate at 21°C. An alternative Sellmeier is presented by Schlarb et al. [2], which characterises the refractive indices of doped and undoped lithium niobate as a function of Li and MgO content as well as temperature. The data in [2] was used to construct a Sellmeier equation appropriate to the crystal parameters in terms of temperature, Li and MgO content of that used in [1]. The result of this comparison is shown in figure 4.1. The two agree to within 0.01% across the entire wavelength range of the pump and idler.

In the terahertz region the refractive index of MgO-doped lithium niobate is not so well characterised and for this reason an expression describing the extraordinary refractive index was created on the basis of the data in [3]. A function of the form $n_T = Ae^{-\frac{\lambda_T - \lambda_0}{t_0}} + z$, where the wavelengths are measured in μm, was fitted to the aforementioned data to obtain the values of n_T across the terahertz range and is

shown in figure 4.2. The coefficients used in the fit are as follows:

$$\begin{aligned} A &= 3.8123 \\ \lambda_0 &= -14.90 \\ t_0 &= 65 \\ z &= 5.07 \end{aligned}$$

The magnitudes of the wave vectors for allowed idler and terahertz photon combinations can be calculated on the basis of the refractive index data.

It is desirable to be able to phase-match with all three waves propagating collinearly from the point of view of minimising the walk-off losses and producing a system with high gain. Unfortunately lithium niobate exhibits a strong absorption in the terahertz region due to the polariton resonance, making collinear propagation infeasible. The terahertz wave must instead be extracted through the side of the crystal to avoid its complete absorption, something that can be achieved by using the method of non-collinear phase-matching. In this case, the wave vectors form a triangle rather than a straight line, as shown in figure 4.3.

Tuning of the terahertz frequency in the non-collinear geometry is accomplished by altering the angle, ϕ, separating the pump and idler wave vectors. Either a two-mirror swing arm or a three-mirror cavity such as that shown in figure 3.1 can be

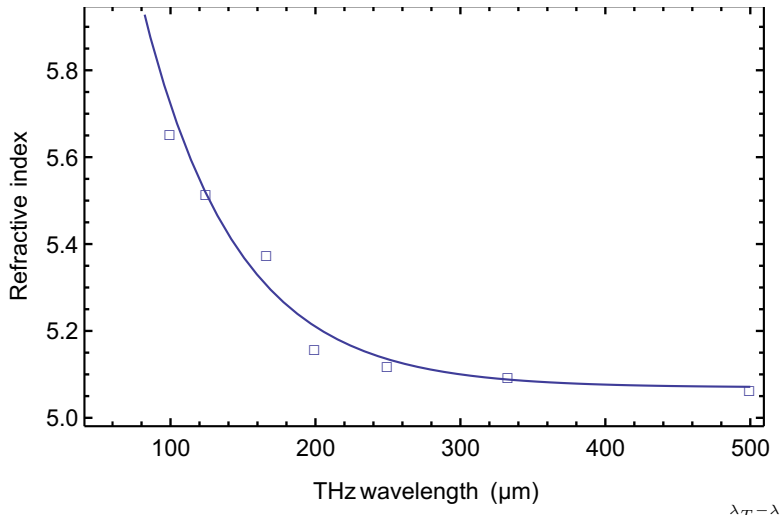

Figure 4.2: The refractive index data from [3] and the fit of form $n_T = Ae^{-\frac{\lambda_T - \lambda_0}{t_0}} + z$.

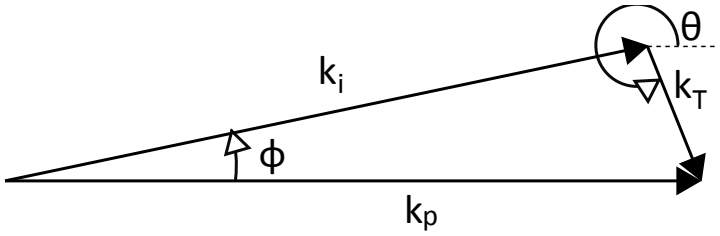

Figure 4.3: A wave vector diagram illustrating the non-collinear phase-matching condition used in MgO-doped lithium niobate.

used to form an optical cavity for the purpose of resonating the idler wave.

4.2.2 Collinear phase-matching via periodically-poled materials

Periodically-poled materials, which feature a periodic grating structure, allow the pump and idler waves to be collinearised by the introduction of a grating vector. This is referred to as *quasi-phase-matching* (QPM). In contrast to non-collinear phase-matching, QPM corrects the relative phase of the interacting waves via a structural periodicity incorporated into the nonlinear medium. The technique, first proposed by Armstrong in 1962 [4], overcomes the problem of destructive interference due to phase changes of the interacting waves by altering the phasing at the point of maximum amplitude of the generated wave (occurring after a distance known as the coherence length) so that the next component of it is added with a phase difference of π compared to the immediately preceding component. This means that constructive addition continues and the generated wave continues to grow.

One technique for abruptly altering the phasing of the generated wave is to produce a domain inversion in the nonlinear crystal after a distance equal to the coherence length and to continue with the process in a periodic fashion, a technique known as periodic poling. This poling can be implemented using a number of different techniques, either during the growth procedure or after it [5–7]. Though the concept of QPM was developed shortly after the first nonlinear optical experiment [4, 8], difficulties relating to the production of micron-scale structures delayed the implementation of the technique by almost thirty years [7]. Since then the use of engineered nonlinear optical materials, including PPLN, has resulted in the development of devices spanning the technologically

important mid-infrared spectral range (1-5μm) [9–11]. Recently there have been several publications relating to the use of PPLN for the generation of terahertz frequencies, mainly by difference frequency generation between two lasers [12, 13]. Other than the publication based on the work of Walsh [14], we are aware of only one other work relating to the use of PPLN in an optical parametric oscillator [15].

Much of the theory associated with conventional birefringent and non-collinear phase-matched optical parametric oscillators can be carried over to the description of quasi-phase-matching requiring only a few simple substitutions. These are derived from a Fourier series representation of the periodically modulated nonlinear coefficient:

$$d(z) = d_{eff} \sum_{m=-\infty}^{\infty} G_m \exp(-ik_m z)$$

where d_{eff} is the effective nonlinear coefficient of the same process in a single-domain bulk material, k_m=2$\pi m\Lambda$ is the grating vector of the m^{th} Fourier component and Λ is the grating period. From the Fourier expansion, the effective nonlinear coefficient for QPM is

$$d_Q = d_{eff} G_m \tag{4.4}$$

where

$$G_m = \frac{2}{m\pi} \sin(m\pi\, D) \tag{4.5}$$

where $D = l/\Lambda$ is the duty factor given by the length of a domain divided by the period of structure. The effective nonlinear coefficient for QPM is largest for the first-order process (where $m = 1$) with a 50% duty factor and takes the value

$$d_Q = \frac{2}{\pi} d_{eff} \tag{4.6}$$

The phase-matching condition for the first-order QPM process is

$$\underline{k}_p - \underline{k}_i + \underline{G} - \underline{k}_T = 0 \tag{4.7}$$

where $G = \frac{2\pi}{\Lambda}$ is the magnitude of the grating vector, which is at an angle, α, to the optic axis.

Herein lie two of the drawbacks associated with using periodically-poled lithium niobate (PPLN) in a terahertz optical parametric oscillator:

Firstly, the process already makes use of the highest d_{eff} (d_{33}) since all the waves have an extraordinary polarisation, meaning that although the overlap between the interacting waves may be increased by collinearising the pump and idler (the terahertz must still be extracted through the side of the crystal), the effective nonlinear coefficient is now reduced by at least a factor of $\frac{2}{\pi}$ as shown in equations 4.4-4.6. Secondly, the grating vector is a bipolar vector so there exist two solutions for each of the down-converted waves associated with any particular grating geometry. In the case where the grating vector is orthogonal to the optic axis these two solutions become degenerate in terms of the terahertz frequency and angle of propagation; otherwise the phase-matching conditions must be carefully considered so that the outcome of a particular phase-matching geometry can be properly anticipated - the solution exhibiting the greater spatial overlap between the three waves would generally be expected to reach oscillation threshold first.

In the intracavity optical parametric oscillator utilising PPLN the pump and idler waves share an optical cavity. This has the benefit of much reduced oscillation thresholds due to the nonlinear medium being subjected to the high intensity pump field as well as not requiring a single-frequency pump source, injection seeding and inter-cavity frequency locking schemes necessary in the pump-enhanced geometry reported in [15]. Figure 4.4 illustrates the phase-matching geometry for this case.

Tuning of the terahertz frequency across a wide range is no longer possible under this phase-matching scheme because the idler wave propagates collinearly with the pump wave. Some tuning is possible by altering the temperature and hence the grating period of the PPLN. This will be explored for a particular grating later on in this chapter.

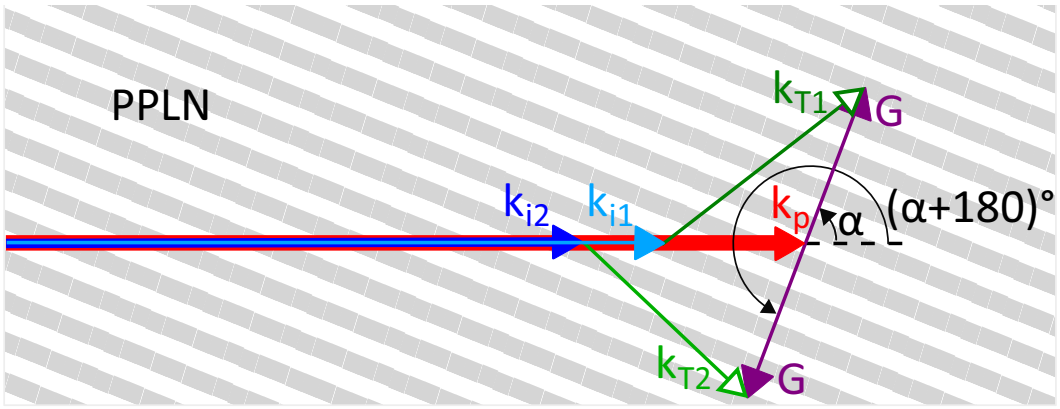

Figure 4.4: A wave vector diagram illustrating collinear phase-matching using PPLN and the two possible solutions that arise from the bipolar nature of the grating vector.

4.2.3 A hybrid non-collinear system using periodically-poled materials

An additional means in which the presence of a grating vector could be exploited is to combine the properties of both the non-collinear and collinear phase-matching schemes into a hybrid approach in which the pump and idler are again separated by an angle ϕ, as illustrated in figure 4.5. One of the limitations placed on the tuning range of our conventional non-collinear terahertz intracavity optical parametric oscillator is that frequencies below 1THz are inaccessible due to the idler cavity geometry. The mirrors forming the resonator for the idler encroach upon the pump beam since the angular separation of the pump and idler beams is less than 0.5° in this frequency range. The grating vector could be designed so as to increase the angular separation of the pump and idler required for phase-matching to take place at these lower frequencies.

A further complication created by the non-colinearity of the pump and idler waves is that there are now four solutions to the phase-matching conditions for any given terahertz frequency. Even once the idler angle has been fixed by virtue of the mirrors forming its resonator there exists an additional solution that phase matches with the opposite direction of the grating vector, producing another terahertz frequency!

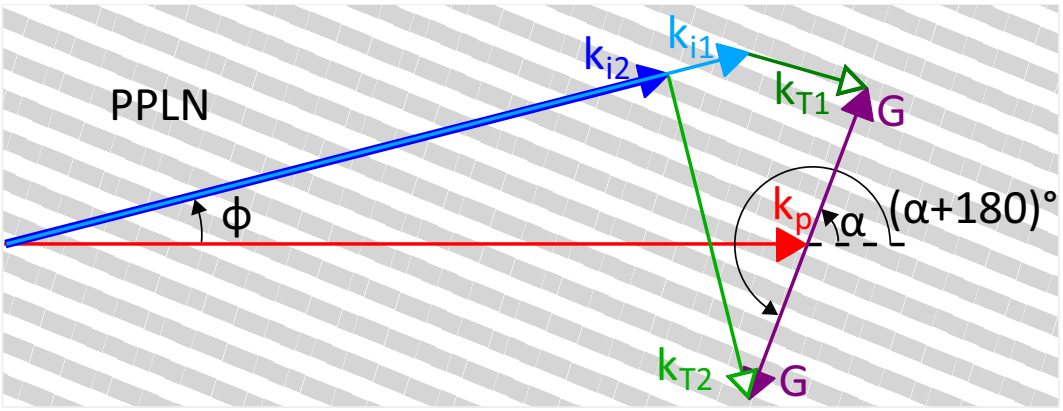

Figure 4.5: A wave vector diagram illustrating the hybrid phase-matching scheme and the two possible solutions that arise from a fixed idler propagation angle due to the bipolar nature of the grating vector.

Figure 4.6 shows one of the ways in which the phase-matching conditions in the presence of a grating vector may be interpreted. For a particular grating with known parameters G and α, a desired terahertz frequency is chosen. Using the realtionship $\nu_p = \nu_i + \nu_T$ the corresponding idler frequency is immediately determinable. The angles necessary for the phase-matching conditions to be satisfied are still unknown, however a scale diagram such as figure 4.6 can be used to identify the solutions. Circles of radius equal to the magnitudes of the idler and terahertz wave vectors are drawn, centred on the starting point of the idler and the end point of the grating vector. The phase-matching conditions are satisfied at points where the circles intersect.

In the case illustrated in figure 4.6 there are four solutions, each corresponding to the same idler/terahertz combination but with the idler and terahertz beams propagating at different angles. The laser designer has the ability to choose between these solutions by placing the idler cavity mirrors appropriately. However it must also be borne in mind that once a particular solution has been selected in this manner, there may be an additional solution arising from the idler propagating at the same angle but having a different wavelength (and consequently a different wave vector magnitude), resulting in another intersection between the new idler and a terahertz wave vector (of unknown magnitude) phase-matching as a result of the grating vector pointing in the opposite direction. Since this competing solution occurs at a higher terahertz

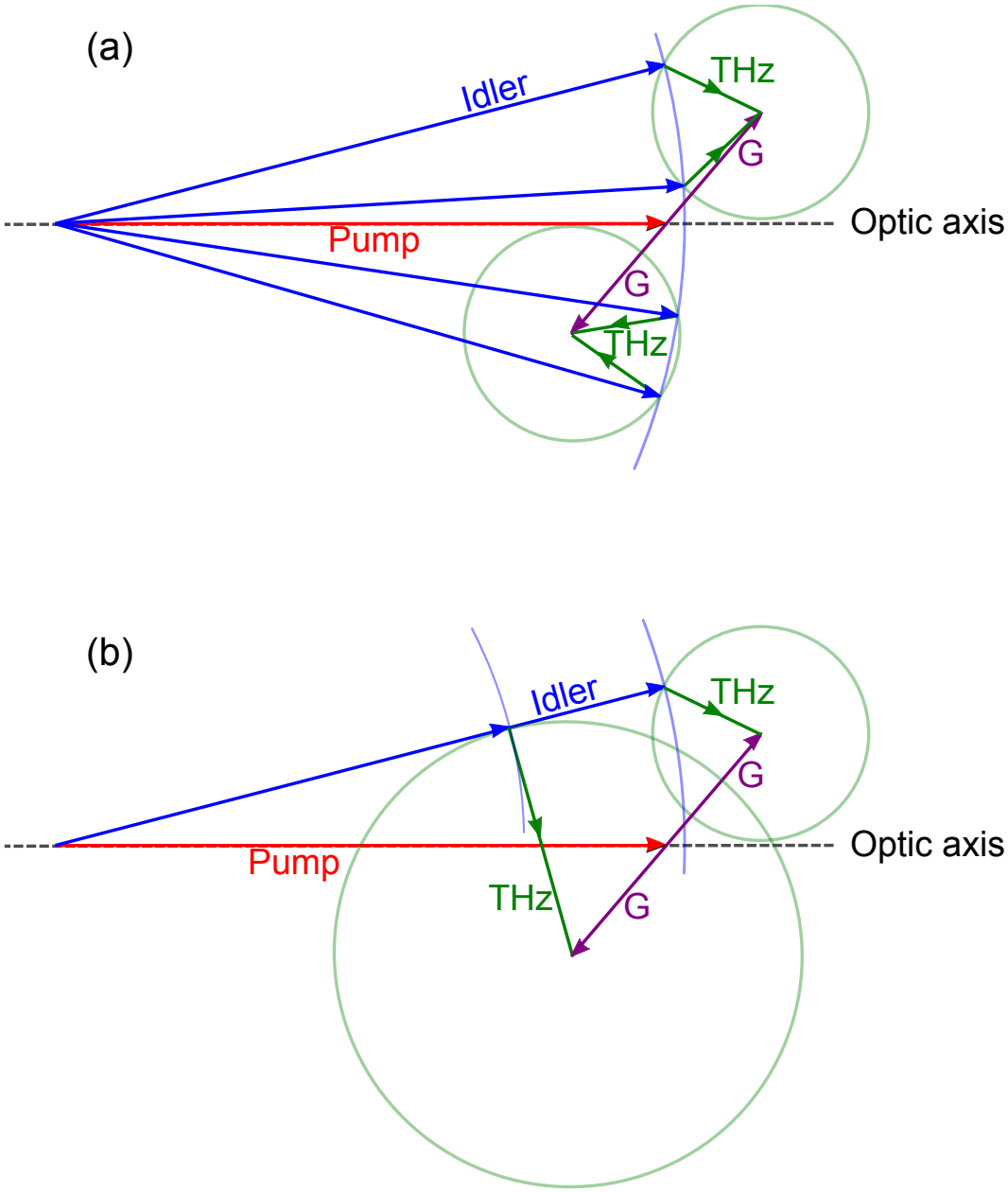

Figure 4.6: An example of how the phase-matching solutions may be identified by using a scale diagram to find the intersection points of the idler and terahertz wave vectors. Diagram (a) shows how the initial solutions are identified and (b) demonstrates how a competing solution may arise once a particular idler propagation angle has been selected. *Note that these diagrams are not drawn to scale and are merely for illustrative purposes.*

frequency than that of the desired solution it will experience greater gain and may also have a greater degree of overlap between the three waves. As a result of these factors the competing solution may be generated preferentially to the one for which the system was designed.

It is therefore necessary to possess a complete understanding of the nature of all possible solutions in order to anticipate the outcome of choosing a particular idler cavity angle. This can be achieved through a number of different methods, which will be discussed in the following sections.

4.3 PPLN grating design and use in collinear phase-matching schemes

Following the same convention adopted in [14], we can relate the grating characteristics $\left(\text{period } \Lambda = \frac{2\pi}{G} \text{ and angle } \alpha\right)$ to the terahertz radiation of frequency ν_T propagating at angle θ to the optical axis. Using figure 4.7 we can establish the following equations:

$$AD = \frac{2\pi n_{p,i}(\nu_p - \nu_i)}{c} = \frac{2\pi n_{p,i}\nu_T}{c} \tag{4.8}$$

$$AC = \frac{2\pi n_T \nu_T}{c} \tag{4.9}$$

$$DB = G\cos\alpha_G \tag{4.10}$$

$$BC = G\sin\alpha_G \tag{4.11}$$

$$\theta = \frac{\pi}{2} - \phi \tag{4.12}$$

where $\nu_{p,i,T}$ are the frequencies of the pump, idler and terahertz waves; $n_{p,i}$ and n_T are the refractive indices of the pump and idler (assumed to have the same value) and the terahertz wave, respectively; G is the grating vector magnitude and α the angle of the grating vector to the optic axis.

By considering the geometry of the right-angled triangles ABC and DBC we can express α in terms of θ through expressions describing the length BC:

$$\cos\theta = \frac{AB}{AC} = \frac{(AD + DB)}{AC} = \frac{(2\pi n_0 \nu_T/c) + G\cos\alpha}{2\pi n_T \nu_T/c} \tag{4.13}$$

$$\sin\theta = \frac{BC}{AC} = \frac{cG\sin\alpha}{2\pi n_T \nu_T} \tag{4.14}$$

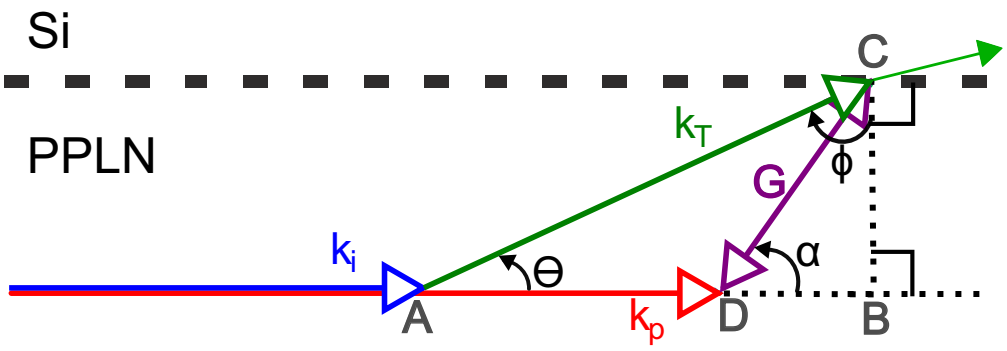

Figure 4.7: Diagram indicating the phase-matching scheme employed when a PPLN crystal is used. The pump and idler beams are co-linearised but the grating direction ensures that the terahertz propagates non-collinearly so that it exits the crystal rapidly.

Rearranging equations 4.13 and 4.14 for $G\sin\alpha$ and $G\cos\alpha$ we can recover the following expressions describing $\tan\alpha$ and G:

$$\tan\alpha = \frac{\sin\theta}{\cos\theta - \frac{n_{p,i}}{n_T}} \tag{4.15}$$

$$G = \frac{2\pi n_T \nu_T \sin\theta}{c\sin\alpha} \tag{4.16}$$

We can thus establish the grating parameters that are necessary for the production of a particular terahertz frequency propagating at a defined angle to the optic axis, meaning that we can engineer the grating such that the terahertz radiation is not trapped inside the PPLN crystal as a result of total internal reflection at the interface between the PPLN and the silicon prisms, which are in contact with the crystal side face - $\theta_{critical}$ varies between 42° and 36° across the range (0.5–3)THz.

4.3.1 The nature of the alternative solution

The consequences of the bi-directionality of the grating vector must now be considered in order to assess the likelihood that the crystal will produce the expected terahertz output. In this case the magnitude of the grating vector, G, remains unchanged but the angle of the vector to the optic axis becomes (180-α)°. In order to establish the propagation angle of the terahertz for the second solution, equation 4.15 must be expanded, at which point it takes the form of a quadratic equation - the solutions of which can be extracted using the

quadratic formula $x = \frac{-b \pm \sqrt{b^2-4ac}}{2a}$, x being $\cos\theta$ in this case. The following expressions are obtained for the coefficients of the quadratic formula:

$$a = tan^2\alpha + 1 \tag{4.17}$$

$$b = -2\frac{n_{p,i}}{n_T}tan^2\alpha \tag{4.18}$$

$$c = \left(\frac{n_{p,i}^2}{n_T^2}tan^2\alpha\right) - 1 \tag{4.19}$$

One of the solutions corresponds to the terahertz angle chosen by the crystal designer for the original solution and the other is the propagation angle of the second solution. The frequency of the second solution can then be found using equation 4.16 but only on the assumption that n_T remains unchanged. Since n_T is a function of the terahertz frequency, an iterative procedure must be introduced to identify that particular combination of terahertz frequency and refractive index that is consistent with the known relationship of refractive index as a function of terahertz frequency. These steps have been implemented in a *Mathematica* program that was subsequently used in the grating design process. Figure 4.8 outlines the procedure carried out via the program and the programming code itself is included in appendix C along with notes detailing its operation.

An example of the program's output is given in figure 4.9. In the particular case depicted in figure 4.9 the second solution propagates at an angle of 78.4° to the optic axis. Since this is greater than the angle for the primary solution there is less overlap between the three interacting waves (ie pump, idler and terahertz), hence the threshold is higher for this solution and the grating will produce the terahertz frequency for which it was designed. It should however be noted that this is not always the case and as such the *Mathematica* program provides an important check.

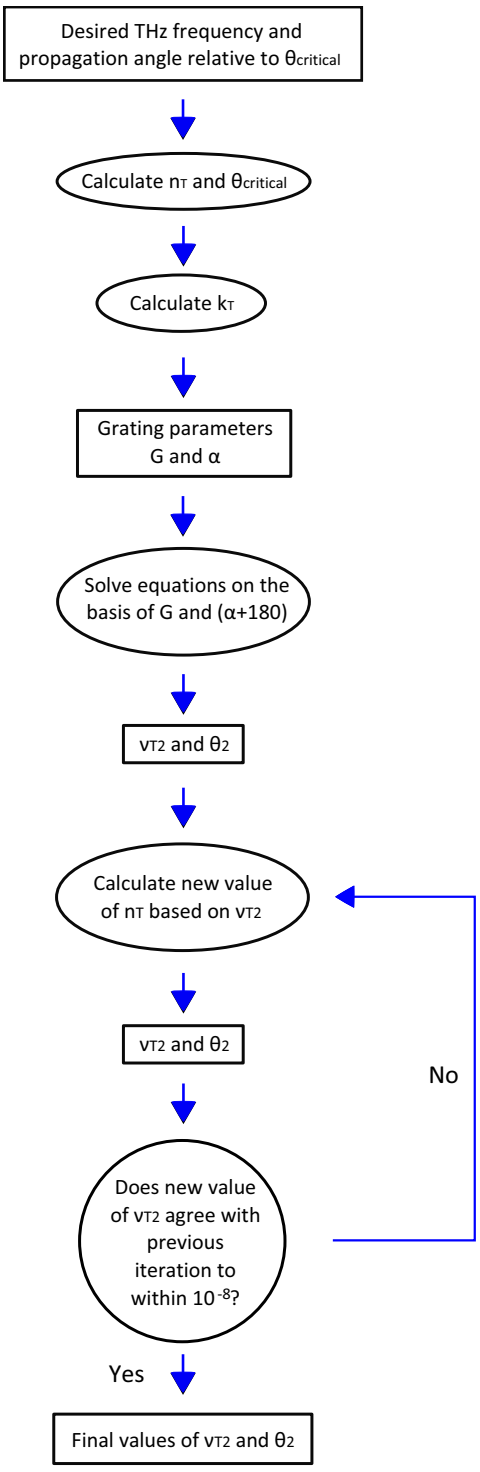

Figure 4.8: A flowchart indicating the steps carried out in the *Mathematica* program.

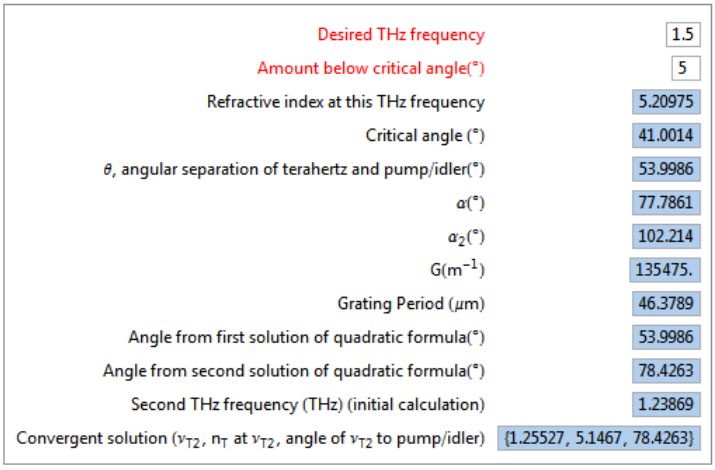

Figure 4.9: An example of the output of the *Mathematica* program showing the grating design required to produce 1.5THz incident on the PPLN:Si interface at 5° below the critical angle.

4.4 Use of PPLN crystals in hybrid phase-matching schemes

An additional way in which the presence of a grating vector could be exploited is to extend the tuning range of the original non-collinear phase-matching system. For example, one of the factors limiting the tuning range of the original device based on non-collinear phase-matching is that at low terahertz frequencies the mirrors forming the idler cavity begin to encroach upon the pump beam before eventually blocking it altogether. Figure 4.10 shows calculated and measured data for the angular separation of the pump and idler as a function of the terahertz frequency. The required effect of the grating vector in such a situation would be to increase the pump-idler angular separation, thus making it possible to reach frequencies below one terahertz. Taking as an example a frequency of 0.5THz, figure 4.10 indicates that an external angle of ≈0.5° is required between the pump and idler beams.

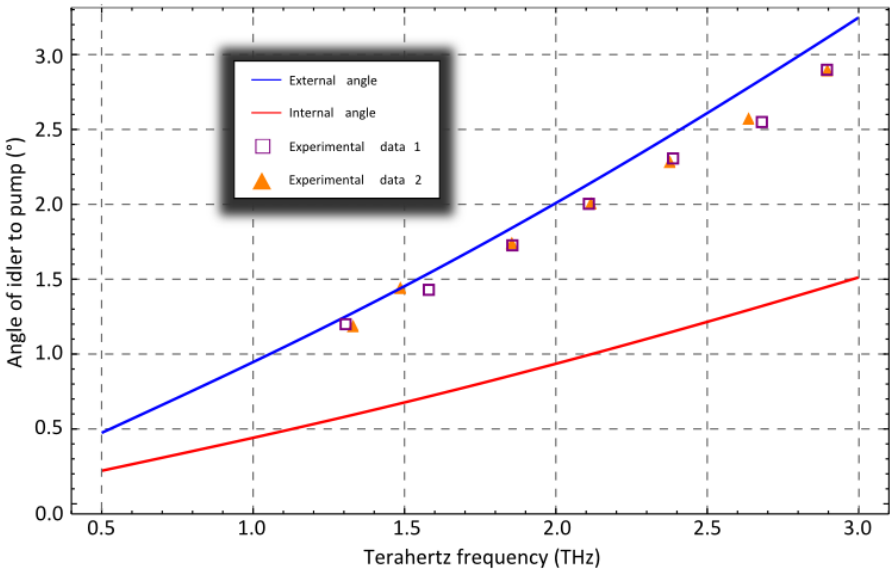

Figure 4.10: A graph showing the calculated values of the angular separation of the pump and idler, internal and external to the crystal, as a function of the terahertz frequency. Measured external angle data is also included.

4.5 Separated geometry method

4.5.1 Determination of initial solutions

The starting point for this method of modelling the performance of a particular grating vector in a hybrid phase-matching configuration is to assume that the presence of the grating vector produces a new effective pump wave vector, which is the resultant of the pump wave vector and the grating vector. Phase-matching can then be considered to take place between the effective pump, idler and terahertz wave vectors in a manner identical to that used for solving the non-collinear phase-matching conditions. Figure 4.11 illustrates this interpretation for both grating vector directions. For any given set of grating parameters the mathematical expressions linking the effective pump and original pump wave vectors are as follows:

$$k'_p \cos\gamma = k_p + G\cos\alpha \qquad \text{(horizontal)} \qquad (4.20)$$

$$k'_p \sin\gamma = G\sin\alpha \qquad \text{(vertical)} \qquad (4.21)$$

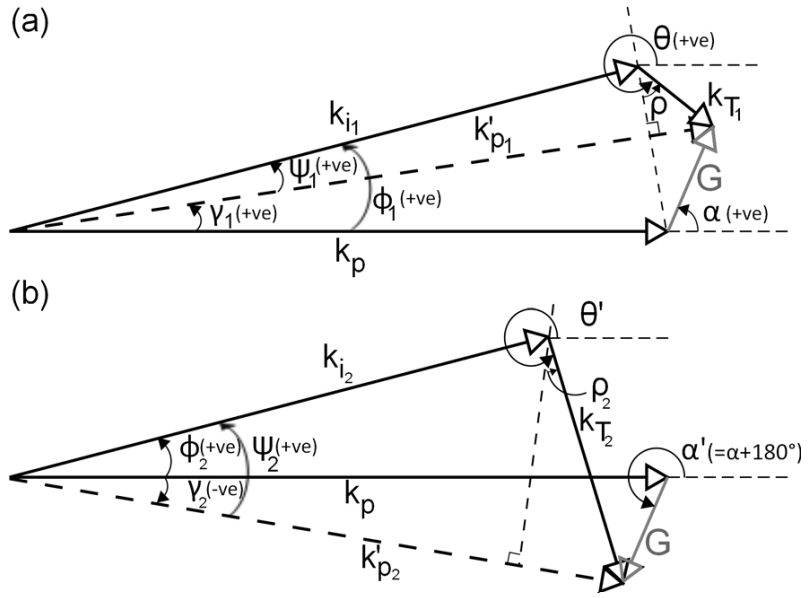

Figure 4.11: The "separated geometry" picture of the two phase-matching solutions for a given grating. Again, the vector lengths are not drawn to scale.

The above equations can be manipulated to produce the following relations:

$$\tan\gamma = \frac{G\sin\alpha}{k_p + G\cos\alpha} \tag{4.22}$$

$$k'_p = \frac{k_p + G\cos\alpha}{\cos\gamma} \tag{4.23}$$

Next, we turn to the triangle having sides k'_p, $k_{t_{1,2}}$ and $k_{i_{1,2}}$, the subscripts referring to situations (a) and (b) in figure 4.11. Two equations relating k_i, k_T and k'_p can be constructed:

$$k'_p = k_i\cos\psi + k_T\sin\rho \tag{4.24}$$

$$k_i\sin\psi = k_T\cos\rho \tag{4.25}$$

By re-writing the $\cos\psi$ term in equation 4.24 as $(1-\sin^2\psi)^{1/2}$ and re-arranging equation 4.25 for $\sin\psi$ we obtain:

$$k_i\left(1-\frac{k_T^2\cos^2\rho}{k_i^2}\right)^{1/2} + k_T\sin\rho = k'_p \tag{4.26}$$

Re-arranging in the following manner:

$$k_i^2\left(1-\frac{k_T^2\cos^2\rho}{k_i^2}\right) = \left(k'_p - k_T\sin\rho\right)^2$$

$$1-\left(\frac{k_T}{k_i}\right)^2\cos^2\rho = \left(\frac{k'_p}{k_i}\right)^2 + \left(\frac{k_T}{k_i}\right)^2\sin^2\rho - \frac{2k'_pk_T}{k_i^2}\sin\rho$$

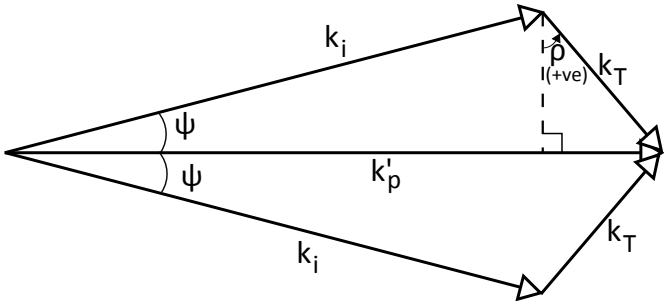

Figure 4.12: An angular separation between the pump and idler waves of either $(\gamma + \psi)$ or $(\gamma - \psi)$ satisfies the phase-matching conditions required to generate the selected terahertz frequency.

Substituting for $\cos^2\gamma$:

$$1 - \left(\frac{k_T}{k_i}\right)^2 (1 - \sin^2\rho) \quad = \quad \left(\frac{k'_p}{k_i}\right)^2 + \left(\frac{k_T}{k_i}\right)^2 \sin^2\rho - \frac{2k'_p k_T}{k_i^2}\sin\rho$$

Thus:

$$\begin{aligned} 1 - \left(\frac{k_T}{k_i}\right)^2 &= \left(\frac{k'_p}{k_i}\right)^2 - \frac{2k'_p k_T}{k_i^2}\sin\rho \\ 2k'_p k_T \sin\rho &= k'^2_p + k_T^2 - k_i^2 \\ \sin\rho &= \frac{\left(k'^2_p + k_T^2 - k_i^2\right)}{2k'_p k_T} \end{aligned} \tag{4.27}$$

Having determined the value of ρ equation 4.25 can be used to obtain $\sin\psi$. The corresponding values of θ can be obtained through consideration of the horizontal components of the wave vectors, which lead to the expression:

$$\cos\theta = \frac{k_p + G\cos\alpha - k_i\cos\phi}{k_T} \tag{4.28}$$

However α must be replaced by α' when ϕ takes a negative value.

Looking at figure 4.6 it is seen that there are two idler propagation angles that satisfy the phase-matching conditions for the chosen terahertz frequency. For this separated geometry method these solutions correspond the idler propagating at angles of $(\gamma + \psi)$ and $(\gamma - \psi)$ to the optic axis, as shown in figure 4.12.

4.5.2 Other phase-matching solutions for a particular idler angle

The next step is to extend this method to the analysis of competing solutions once an idler angle has been selected from the possible solutions calculated as

laid out above. Such a situation is analogous to that depicted in (b) of figure 4.11, where the idler propagation angle, ϕ, is fixed according to the earlier calculations.

Resolving the wave vectors corresponding to this situation into their horizontal and vertical components:

$$k'_i \cos\phi + k'_T \cos\theta' = k_p \cos 0 + G\cos\alpha' \qquad \text{(horizontal)}$$

$$k'_i \sin\phi + k'_T \sin\theta = k_p \sin 0 + G\sin\alpha' \qquad \text{(vertical)}$$

Using the substitutions:

$$A = G\sin\alpha'$$

$$B = G\cos\alpha'$$

$$k'_i = k_p - \eta k'_T$$

where

$$\eta = \frac{n_i}{n_T}$$

we can develop the following relationships:

$$k_p + B = k_p\cos\phi - \eta k'_T\cos\phi' + k'_T\cos\theta'$$

$$A = k'_p\sin\phi - \eta k'_T\sin\phi - k'_T\sin\theta'$$

Which leads to

$$k'_T\left(\sin\theta' - \eta\sin\phi\right) = \left(A - k'_p\sin\phi\right)$$

$$k'_T\left(\cos\theta' - \eta\cos\phi\right) = \left(k'_p - k_p\cos\phi + B\right)$$

$$\frac{\sin\theta' - \eta\sin\phi}{cos\theta' - \eta\cos\phi} = \frac{A - k_p\sin\phi}{k_p - k_p\cos\phi + B}$$

Let the right-hand side of the previous equation be called "χ" so that

$$\sin\theta' - \eta\sin\phi = \chi\cos\theta' - \chi\eta\cos\phi$$

Then letting $\eta\sin\phi = a$ and $\eta\cos\phi = b$,

$$\sin\theta - a' = \chi\cos\theta' - \chi\, b$$

$$\chi\cos\theta' = \sin\theta' + \chi\, b - a$$

Letting $c = (\chi\, b - a)$, squaring both sides and substituting for $\cos^2\theta'$

$$\chi^2\left(1 - \sin^2\theta'\right) = c^2 + 2c\sin\theta' + \sin^2\theta'$$

Thus:

$$\left(1 + \chi^2\right)\sin^2\theta' + 2c\sin\theta' + \left(c^2 - \chi^2\right) = 0 \tag{4.29}$$

The values of $\sin\theta'$ can then be found by solving equation 4.29 using the quadratic formula. The result is:

$$\sin\theta' = \frac{-c \pm \chi\sqrt{1 - c^2 + \chi^2}}{2\left(1 + \chi^2\right)} \tag{4.30}$$

The values of k_T (and subsequently ν_T) corresponding to the θ's obtained using equation 4.30 can then be calculated using the following relation:

$$k_T = \frac{A - k_p\sin\phi}{\sin\theta' - \eta\sin\phi} \tag{4.31}$$

However, since the calculation of θ' is based on an assumed value of n_T through the symbol η, several iterations must be carried out in order that the solutions converge. This is accomplished by first calculating ν_T on the basis of the assumed refractive index value, then calculating the actual value of n_T at that frequency using the function defined in section 4.2. Then θ', k_T and ν_T are re-calculated. Following this procedure, the solutions of ν_T and n_T will eventually converge to a consistent set of values.

It should be noted that the value of θ has the same sign in two quadrants, being positive in the first and fourth and negative in the second and third. Therefore for each value of $\sin\theta$ that is calculated there are two possible values of θ. It is necessary to be able to discriminate between these values to establish the direction of propagation of the terahertz in relation to the crystal surface. The method for doing so is to consider the value of $\cos\theta$ since its sign changes in different quadrants to the sine function. The expression used to calculate $\cos\theta$ is derived from the description of the horizontal components given at the beginning of this section:

$$\cos\theta = \frac{k_p + G\cos\alpha' - k'_i\cos\phi}{k'_T} \tag{4.32}$$

This method of analysing the effect of a grating vector in a non-collinear phase-matched situation is very elegant in that it can be completely solved without the use of technical computing software such as *Mathematica*. Some iteration is necessary due to its reliance on prior knowledge of the terahertz refractive index as described earlier in this section, however the values of n_T can be readily calculated using the function describing n_T as a function of the terahertz wavelength provided in section 4.2.

4.6 Composite geometry method

For this method the wave vectors are resolved into their horizontal and vertical components. Two phase-matching equations can then be constructed. For the vertical components:

$$k_i \sin\phi = G \sin\alpha + k_T \sin\theta \tag{4.33}$$

Resolving the horizontal components:

$$k_p + G\cos\alpha = k_i \cos\phi + k_T \cos\theta \tag{4.34}$$

If we let $x = \sin\phi$ and $y = \sin\theta$, then:

$$k_i x = A + k_T y \tag{4.35}$$

$$(k_p + B) = k_i \left(1 - x^2\right)^{1/2} + k_T \left(1 - y^2\right)^{1/2} \tag{4.36}$$

where $A = G\sin\alpha$ and $B = G\cos\alpha$. Rearranging equation 4.35 we obtain the expression:

$$y = \frac{(k_i x - A)}{k_T} \tag{4.37}$$

Hence expanding equation 4.36:

$$(k_p + B) = k_i \left(1 - x^2\right)^{1/2} + k_T \left(1 - \left(\frac{k_i x - A}{k_T}\right)^2\right)^{1/2} \tag{4.38}$$

Finally, equation 4.38 can be rearranged and set equal to zero as follows:

$$(k_p + B) - k_i \left(1 - x^2\right)^{1/2} - k_T \left(1 - \left(\frac{k_i x - A}{k_T}\right)^2\right)^{1/2} = 0 \tag{4.39}$$

Equation 4.39 can, with some effort, be expanded and rearranged to yield a quadratic equation, however the coefficients are no longer simple expressions so it is more effective to find solutions to equation 4.39 using *Mathematica* or similar software. Knowing the grating parameters and wave vector magnitudes of the pump, idler and terahertz corresponding to the desired phase-matching condition, equation 4.39 can be solved for x, where ϕ is the angle separating the pump and idler waves. As described in section 4.4 there are two solutions for each direction of G. The angle of the terahertz to the optic axis can then be calculated using equation 4.37.

Having established the values of ϕ that satisfy the phase-matching solutions for the selected terahertz frequency, the same method of assessing the competing solutions that was established for the separated geometry method can be used here.

4.7 Vector method

4.7.1 Introduction to the model

Figure 4.13 shows the vector representation of the situation in which the pump and idler are separated by an angle ϕ, which is the basis of the *Mathematica* program that was created to model the effect of a grating vector in a non-collinear phase-matching scheme. Unlike the composite geometry and separated geometry methods, the vector method does not require any iterations on the basis of a previously-assumed terahertz refractive index due to the way in which the terahertz wavelength is defined. However, the angle of the idler to the pump is changed iteratively in order to find the conditions that satisfy the phase-matching requirements so that the user-specified terahertz frequency is generated using a user-specified grating.

4.7.2 Relevant definitions

The magnitudes of the wave vectors are calculated using equation 4.2 and the grating vector magnitude is found using the expression $G = \frac{2\pi}{\Lambda}$, where Λ is the grating period. The refractive index data used for the infrared wavelengths (i.e. for

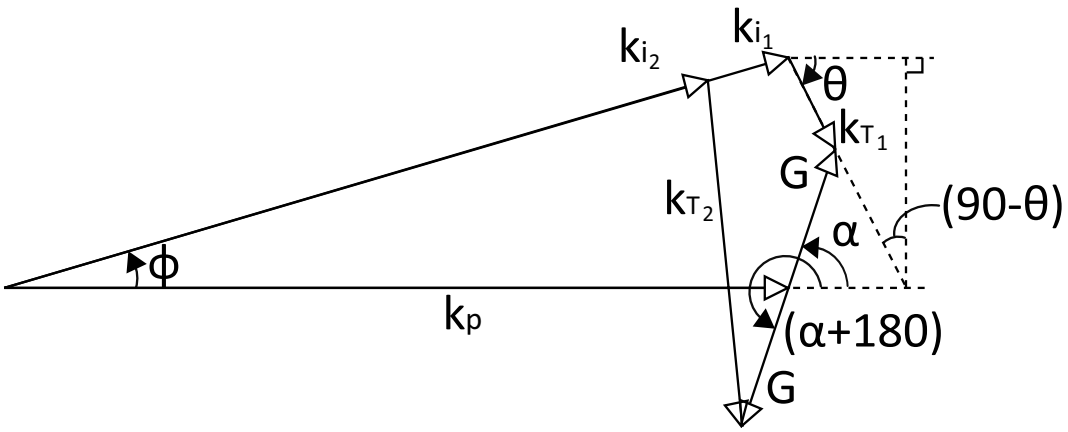

Figure 4.13: The vector representation of hybrid phase-matching when using a PPLN crystal. $k_{p,i,T}$ represent the wavevector magnitudes of the pump, idler and terahertz, respectively. The subscripts 1 and 2 represent the two solutions resulting from the grating being either at angle α or $(\alpha + 180)$ to the optic axis.

the pump and idler) is from [1] and the terahertz refractive index is based upon data provided in [3] as set out in section 4.2. The pump vector is denoted by $\underline{k}_p$ and points along the optic axis. The vectors describing the terahertz, idler and grating are resolved in terms of their components parallel and perpendicular to the optic axis as follows:

$$\text{terahertz vector} = \underline{k}_T = (k_T \cos\theta, k_T \sin\theta) \tag{4.40}$$

$$\text{idler vector} = \underline{k}_i = (k_i \cos\phi, k_i \sin\phi) \tag{4.41}$$

$$\text{grating vector}_1 = \underline{G}_1 = (G\cos\alpha, G\sin\alpha) \tag{4.42}$$

$$\text{grating vector}_2 = \underline{G}_2 = (G\cos(\alpha+180), G\sin(\alpha+180)) \tag{4.43}$$

where θ, ϕ and α specify angles to the optic axis.

The terahertz wavelength and hence the terahertz vector and refractive index are defined in terms of the pump and idler wavelengths (all wavelengths refer to free space):

$$\lambda_T = \frac{1}{\frac{1}{\lambda_p} - \frac{1}{\lambda_i}} \tag{4.44}$$

Defining the wavelength and refractive index in this way circumvents the need to iterate towards a convergent set of solutions since both the terahertz wavelength and refractive index are immediately known once an idler wavelength has been chosen.

4.7.3 The modelling procedure

The procedure, illustrated schematically in figure 4.14, is used to find the conditions under which a given PPLN crystal will generate a particular, user-defined, terahertz frequency. This is accomplished by finding the idler wave vector that satisfies the following condition:

$$\underline{k}_T - (\underline{k}_p - \underline{k}_i + \underline{G}_{1,2}) = 0 \tag{4.45}$$

Next, the angle of the idler to the pump is calculated. The terahertz vector is then fully defined since its angle to the pump can be calculated from $\tan^{-1}$(vertical component of k_T/vertical component of k_T). If that angle is less than zero then the angle of k_T to the PPLN:Si interface is 90° plus the angle; otherwise it is 90° minus the angle.

There are four possible ways of generating any terahertz frequency that is chosen, as has been explained previously. Figure 4.15 shows how this results from a graphical point of view. It is also apparent from the figure that each of the four solutions has a competing solution, arising from the idler angle being fixed by the cavity mirrors but the grating vector pointing in the opposite direction. It is necessary to investigate these other solutions to be able to identify which solution is most favourable in terms of overlap between the pump, idler and

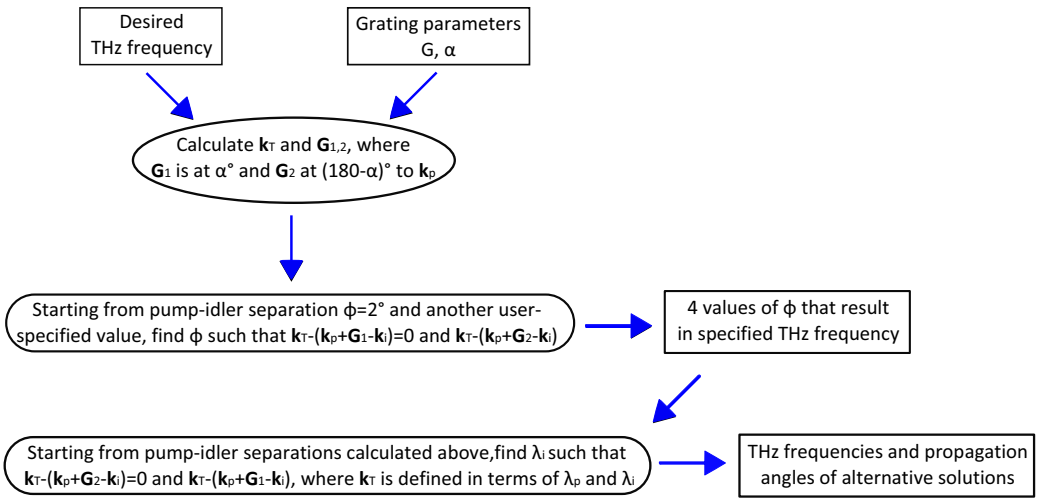

Figure 4.14: Data flow diagram showing the main steps in the *Mathematica* vector method program.

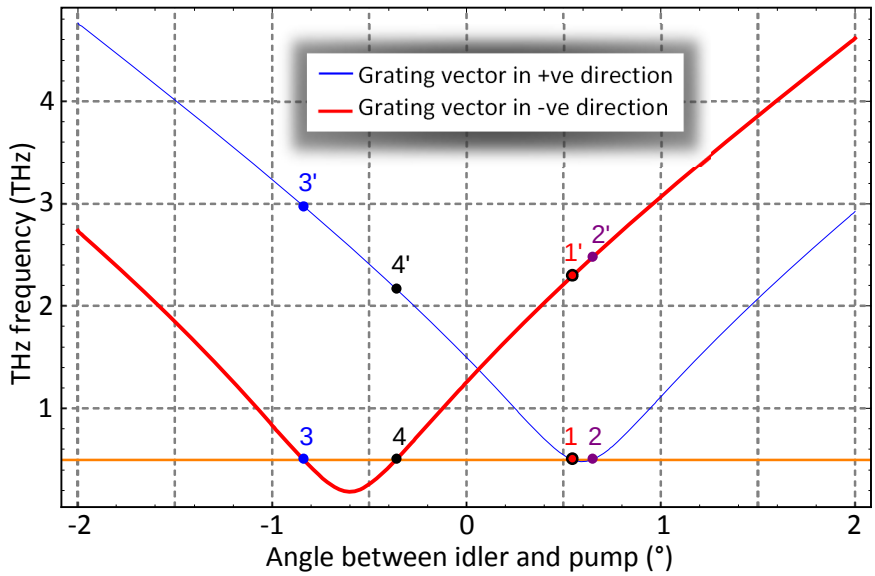

Figure 4.15: A plot showing angular separations of the pump and idler waves that satisfy the phase-matching conditions for the crystal specified in figure 4.9. The orange line is at a y-axis value marking the desired terahertz frequency and intersects each curve twice at the required pump-idler separations.

terahertz as per figures 4.9 and 4.13.

The four initial solutions are found as follows (the order of numbering here reflects the same order as in figure 4.15):

1. Calculated as outlined earlier in ths section and equation 4.45.
   $k_T = k_p - k_i + G_1$. The initial value of ϕ in this case is 2°.

2. Calculated as in **1** but with a different starting value for ϕ. In this case ϕ is a user-defined value as it must be altered slightly so that all four solutions are found - sometimes fewer than four solutions are found because the "FindRoot" routine in *Mathematica* does not always converge to the alternative solutions.

3. Calculated as in **1** but using the grating vector pointing in the opposite direction. $k_T = k_p - k_i + G_2$.

4. Calculated as per **3** but with the same user-defined starting value of ϕ as stated in **2**.

The angle of the terahertz wave vector is denoted by θ and is measured as

indicated in figure 4.13. In the data output from the program the value quoted is $(90\pm\theta)$ so that the angle is directly comparable with the critical angle.

Next, the competing solutions must be identified. The pump-idler separations are kept the same as for the solutions that were found initially. Then the idler wavelength and terahertz frequency that satisfy the phase-matching conditions on the basis of the grating vector pointing in the opposite direction to which it was originally oriented are calculated. Finally the eight total solutions are marked on graphs of terahertz frequency as a function of pump-idler angular separation and terahertz propagation angle as a function of pump-idler angular separation. The solutions are also tabulated so that the user can easily discern which solution will be the most favourable in terms of overlap, ability of the terahertz to exit the crystal, and so on. An example of the output is shown in figure 4.16. The complete program is provided, including annotations describing the various sections, in appendix D.

4.8 Predicted performance of the final PPLN crystal design

4.8.1 Collinear operation

Using the *Mathematica* program described in section 4.3 and shown in figure 4.9 a PPLN crystal was designed to produce radiation at a frequency of 0.92THz when used in the context where the pump and idler beams are collinear. The grating parameters required in order that this is the case are Λ=72.4μm and α=86.5°. The terahertz radiation impinges upon the interface between the PPLN and the silicon prisms at an angle of 28.4°. Since the grating vector is not orthogonal to the direction of propagation of the pump beam, there exists another solution to the phase-matching conditions, based on the grating vector pointing in the opposite direction. For this grating the second solution corresponds to a frequency of 0.87THz; the angle of this terahertz wave to the interface is 21.4°. Under these conditions the terahertz has a reduced overlap with the pump and idler in comparison to the solution at 0.92THz, so the

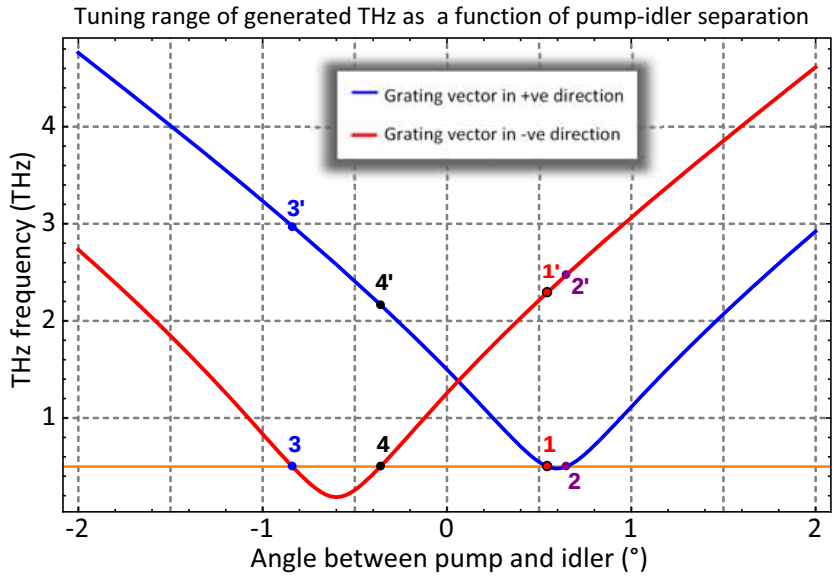

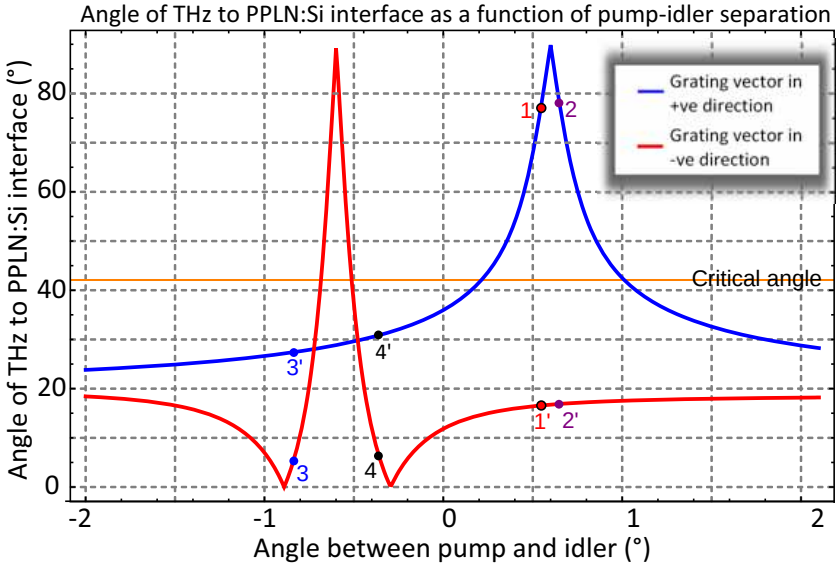

THz frequency: 0.5
Pump frequency: 1064.4
Pump angle: 0
Grating vector magnitude: 135475
Grating vector angle: 77.78
Starting point to look for root for sols 2,4: 1

Solution	P- I separation	THz frequency	Exit angle
1	0.545499	0.5	76.9855
1'	0.545499	2.29361	16.5749
2	0.648913	0.5	78.18
2'	0.648913	2.474311	16.888
3	-0.839137	0.5	5.22501
3'	-0.839137	2.97535	27.3977
4	-0.360692	0.5	6.42484
4'	-0.360692	2.16686	30.8471

Figure 4.16: Complete output of the *Mathematica* program described in the text. The orange line in the graph of terahertz exit angle as a function of pump-idler separation indicates the critical angle (the value for which is calculated on the basis of the specified terahertz frequency). Solutions lying above this line will not be extractable.

0.92THz solution will be generated preferentially.

4.8.2 Extent of tuning capable via temperature control

As mentioned previously, the only scope for tuning the output of the terahertz optical parametric oscillator based on PPLN where the pump and idler waves are collinear is to adjust the temperature of the PPLN crystal itself. This affects both the grating period and the refractive indices of the crystal.

In order to investigate the extent of tuning which would be possible using the crystal design currently under consideration it was necessary to source temperature-dependent refractive index data for both the terahertz and the infrared regions. For the terahertz region, the data used was obtained from [16] and the data of Schlarb et al. [2] was used for the pump and idler wavelengths. The terahertz refractive index is described by the following expression:

$$n[\lambda_p, \lambda_i, T] = A[T] + (B[T] \times (\nu_T[\lambda_p, \lambda_i/0.03)^2) + (C \times (\nu_T[\lambda_p, \lambda_i/0.03)^4) \quad (4.46)$$

where T is the temperature in °C and A, B, and C are coefficients of the refractive index polynomials of congruent lithium niobate. Values of A, B and C were provided for different doping levels of MgO and for temperatures of 10, 100, 200 and 300K (corresponding to -263.15, -173.15, -73.15 and 26.85°C, respectively). Fits were found to the data provided using *Mathematica* so that the entire temperature range could be explored.

The change in the grating period as a function of temperature then had to be accounted for. The approach adopted in [17] was used, however this data pertains to undoped congruent lithium niobate and is taken from [18] so it may not be appropriate for MgO:PPLN. The expansion of the crystal as a function of temperature is described by:

$$\Lambda[T] = \Lambda\left(1 + \alpha\,(T - 19) + \beta\,(T - 19)^2\right) \quad (4.47)$$

where T is the temperature in °C.

In order to establish the resulting terahertz frequencies at a given temperature, a similar approach to that used to find the solutions in the hybrid phase-matching

geometry was used, except that the idler was constrained to be collinear with the pump. Figure 4.17 shows the result of this modelling. The solid red and blue lines indicate the data based on fits to the values of A and B (C does not vary with temperature), whereas the dashed red and blue lines represent data based on an extrapolation of the fits to A and B to higher temperatures. The extent of tuning achieved by changing the crystal temperature by a fixed amount depends on what the starting temperature is. For example, by varying the temperature in the range -200 to -100°C, ≈20GHz of tuning is possible, whereas in changing the temperature across the range 0 to100°C results in ≈70GHz of tuning. However, from the model it is evident that the tuning range which is possible by varying the crystal temperature is much smaller than the tuning range that is achieved by changing the phase-matching angle in the non-collinear phase-matching geometry.

4.8.3 Non-collinear operation

All three methods of analysing the hybrid phase-matching geometry that were described earlier in this chapter have been used to characterise the terahertz

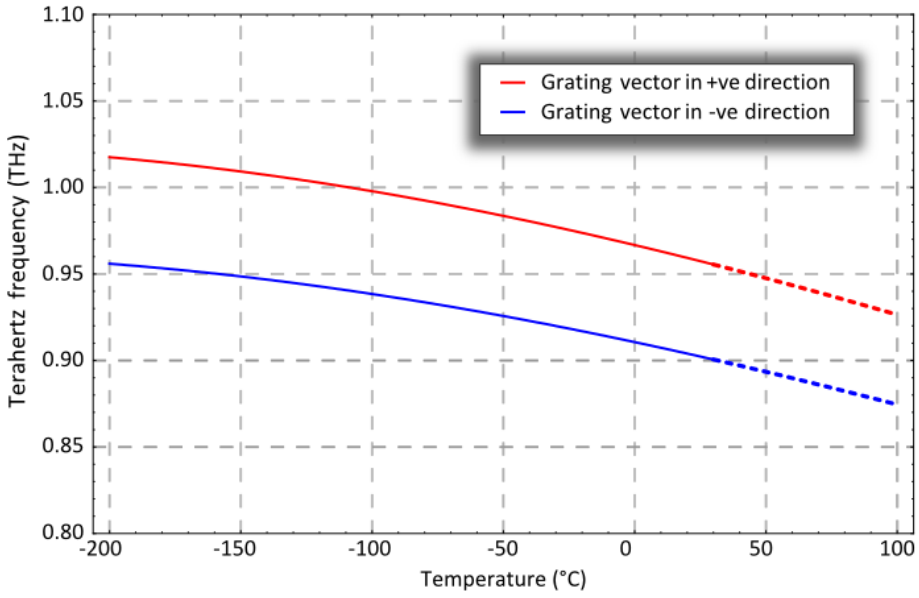

Figure 4.17: Results of modelling the effect of temperature on the terahertz frequency generated by the grating when the pump and idler waves are collinear. The terahertz frequency tunes across ≈30 GHz when the temperature is varied in the range 20 to 100°C.

Model	ϕ for (°) 0.5THz	θ for 0.5THz (°)	Alternative frequencies (THz)	Alternative angles (°)
Separated geometry	0.5953, 0.1875 -0.1649, -0.6187	-57.5826, 58.3655, -71.0559, 70.2723	2.0763, 1.2808, 1.2796, 2.1567	-67.7875, -67.7378, 62.9055, 65.1498
Composite geometry	0.5953, 0.1876 -0.1649, -0.6187	-57.5822,58.365, -71.0556, 70.2721	2.0763, 1.2809, 1.2796, 2.1567	-67.7875, -67.7377, 62.9055, 65.1498
Vector	0.5953, 0.1876 -0.1649, -0.6187	-57.5822, 58.365, -71.0556, 70.2721	2.0763, 1.2809, 1.2796, 2.1567	-67.7875, -67.7377, 62.9055, 65.1498

Table 4.1: Comparison of the values of ϕ and θ for 0.5THz generation and the alternative solutions for the new crystal design when each of the three modelling procedures is used.

output of the crystal design specified in the section above. The results of each modelling procedure will be presented in this section and then compared. For this purpose a frequency of 0.5THz was selected as the desired output of the intracavity terahertz optical parametric oscillator. Table 4.1 summarises the findings of the three methods and figure 4.18 shows the results obtained using the vector modelling method.

The models all indicate that it is possible to reach 0.5THz using this grating design. Of the four possible solutions only those for which the idler propagates at a positive angle will be considered owing to the location of the idler cavity mirrors in the laser system to be used (see figure 3.1 for example). Solution 2, having the idler at an angle of $\approx$0.6° to the pump (internal to the crystal) is the most logical of the two remaining solutions since the separation of the pump and idler is largest and it would therefore be easier to adjust the idler cavity mirrors to a suitable position without clipping the pump beam - any smaller angle would necessitate the lengthening of the idler cavity to the point that the pump and idler beams were separated enough and this in turn would lead to longer build-up times for the idler. Purely on the basis of the spatial overlap between the pump, idler and terahertz beams it is to be expected that the 0.5THz solution will be generated preferentially over the 2.07THz solution that it is in competition with. However other factors such as the terahertz gain as a function of frequency would have to be taken into consideration in order to anticipate the outcome of such a phase-matching scheme more fully.

4.8.4 Extent of tuning in the non-collinear setting

The possibility of tuning the terahertz output of the PPLN crystal was explored by using the vector modelling program to find the various solutions across the range (0.5-3)THz in steps of 0.1THz. By analysing the possible solutions on the basis of overlap alone, the tuning curve shown in figure 4.19 was produced. The angles plotted in the graph are all internal to the crystal. Data describing the pump-idler angular separation for phase-matching using a bulk lithium niobate crystal is also included. The data clearly shows that the effect of the grating vector is to increase the angular separation between the pump and idler waves required for phase-matching to take place, something which is particularly important in order to make the sub-1THz region accessible.

4.8.5 The effect of manufacturing accuracy

The manufacturing accuracy of the PPLN crystal was quoted as $\pm 0.02\mu$m in the grating period and $\pm 0.5°$ in the grating angle. The error in the period is derived from a variation in temperature of $\pm 10°$C, which presumably affects the crystal growth. The grating angle is influenced most by the polishing tolerances. Table 4.2 shows the effect of these manufacturing capabilities on the terahertz output for both collinear use and in the situation where a frequency of 0.5THz is desired.

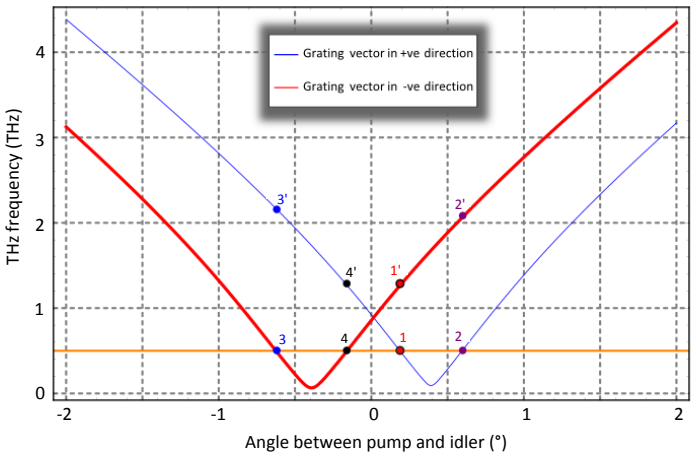

Solution	P-I separation	THz frequency	Exit angle
1	0.187566	0.5	31.635
1'	0.187566	1.28088	22.2623
2	0.595298	0.5	32.4178
2'	0.595298	2.07631	22.2125
3	0.618659	0.5	19.7279
3'	0.618659	2.15666	24.8502
4	0.164859	0.5	18.9444
4'	0.164859	1.27957	27.0945

Figure 4.18: The graph indicates the angular separations of the pump and idler beams required to produce radiation of 0.5THz on the basis of the grating parameters stated in the text. The table adjacent to the graph provides numerical values for the terahertz frequencies of all possible solutions as well as the angle of the terahertz to the material interface.

In the case of collinear operation the generated frequencies vary by only ±5GHz and the propagation angles by ±0.5° due to the manufacturing constraints. For the hybrid PPLN/non-collinear phase-matching system, the angular separation of pump and idler beams required for the generation of a frequency of 0.5THz is changed by only ±0.003°; the propagation angle of the terahertz is altered by a significantly larger value (±1°), however this is still a small enough change to be inconsequential in terms of extracting the terahertz through the side of the crystal.

4.8.6 The effect of pump wavelength variation

Recently, a tunable continuous-wave terahertz source based on intracavity difference frequency generation within a dual wavelength vertical external cavity surface emitting laser (VECSEL) has been demonstrated [13]. The nonlinear crystal employed in that system was a PPLN crystal with a slanted grating to enable the terahertz radiation to be extracted through the side of the crystal, very similar to the crystal design described and modelled in this chapter. Tuning of the terahertz frequency is achieved using an intracavity étalon. Given the reported output powers of several milliwatts of terahertz being generated via this

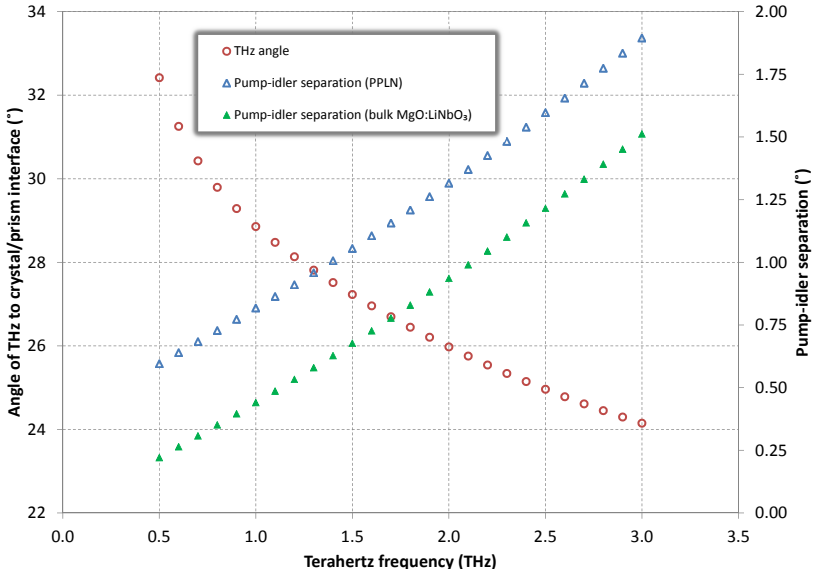

Figure 4.19: Graph showing the pump-idler separation and angle of the terahertz to the crystal/prism interface of the dominant solution as a function of chosen terahertz frequency. The angular separation of the pump and idler required for phase-matching with a bulk $LiNbO_3$ crystal (as per figure 4.10) is also included.

Grating	Collinear		0.5THz	Other solution
72.4μm, 86.5°	0.924THz, 29.1°	0.874THz, 22.0°	0.595°, 32.4°	2.076THz, 22.2°
72.4μm, 87°	0.920THz, 28.6°	0.877THz, 22.5°	0.598°, 31.5°	2.083THz, 22.4°
72.4μm, 86°	0.928THz, 29.6°	0.870THz, 21.5°	0.593°, 33.4°	2.069THz, 22.0°
72.3μm, 86.5°	0.925THz, 29.1°	0.875THz, 22.0°	0.596°, 32.4°	2.078THz, 22.2°
72.3μm, 87°	0.922THz, 28.6°	0.879THz, 22.5°	0.598°, 31.4°	2.085THz, 22.4°
72.3μm, 86°	0.929THz, 29.6°	0.872THz, 21.5°	0.593°, 33.4°	2.071THz, 22.0°
72.5μm, 86.5°	0.923THz, 29.1°	0.873THz, 22.0°	0.595°, 32.4°	2.074THz, 22.2°
72.5μm, 87°	0.919THz, 28.6°	0.876THz, 22.5°	0.597°, 31.4°	2.082THz, 22.4°
72.5μm, 86°	0.926THz, 29.6°	0.869THz, 21.5°	0.592°, 33.4°	2.067THz, 22.0°

Table 4.2: Details of how manufacturing capabilities affect the crystal performance when used both collinearly and non-collinearly for the generation of 0.5THz.

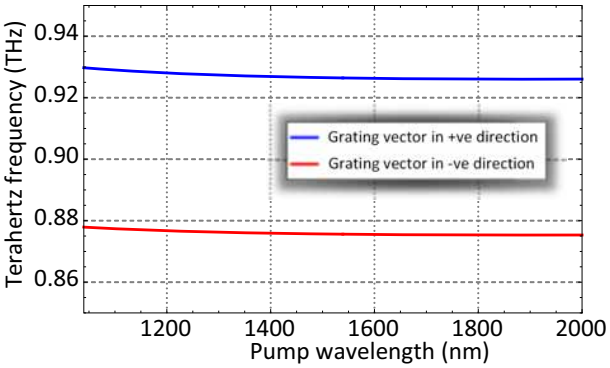

λ_p nm	ν_T 1 THz	λ_i 1 nm	ν_T 2 THz	λ_i 2 nm
1000	0.930337	1003.110771	0.878321	1002.936334
1100	0.929002	1103.759782	0.877393	1103.550239
1200	0.928055	1204.471262	0.876735	1204.223137
1300	0.927374	1305.245285	0.876262	1304.955091
1400	0.926884	1406.081946	0.875922	1405.746177
1500	0.926535	1506.981354	0.87568	1506.596481
1600	0.926295	1607.943628	0.875513	1607.506097
1700	0.926141	1708.968896	0.875407	1708.475126
1800	0.926057	1810.057296	0.875348	1809.503675
1900	0.926031	1911.208975	0.87533	1910.591855
2000	0.926054	2012.424086	0.875346	2011.739787

Figure 4.20: The output of the *Mathematica* program used to model the effect of changing the pump wavelength over the range (1–2)μm.

method we are keen to replicate the experiment at some point in the future using a selection of VECSELs operating at different wavelengths to which we have access.

The pump wavelength of the VECSELs potentially available to us lies in the region (1–2)μm. A *Mathematica* program was written to characterise the effect of changing the pump wavelength on the resulting terahertz frequencies that are generated. Basically, the model described in section 4.3 was modified to include a variation in the pump wavelength. Figure 4.20 shows how the terahertz frequency varies as the pump wavelength is changed. It shows that the choice of grating effectively fixes the terahertz frequencies that are produced, since the

frequencies change by only 3GHz across the tuning range of the pump. Therefore, the terahertz output frequency cannot be tuned by altering the pump wavelength, however it should be possible to replicate the experiment conducted by Scheller and colleagues [13] since the output frequency of the PPLN crystal is unaffected by the pump wavelength.

4.9 Conclusions

In this chapter, modelling procedures have been developed to predict the terahertz output of quasi-phase-matching schemes using any user-defined grating parameters. It should also be appreciated that, although the models devised have been utilised to design grating parameters for PPLN, they would be equally applicable to the analysis of other poled materials if appropriate Sellmeier equations were substituted into the models.

A grating has been designed that is capable of generating 0.5THz if used in the hybrid phase-matching geometry. This grating is also able to produce frequencies of 0.92THz or 0.87THz when used in a collinear phase-matching system. By controlling the temperature of the PPLN crystal these frequencies could be tuned by some 90GHz when the temperature is varied in the range (-200 to 100)°C. If a hybrid non-collinear phase-matching geometry were implemented, the tuning range could be extended to reach 0.5THz due to the grating effectively increasing the requisite pump-idler angular separation for the corresponding phase-matching condition, this being supported by the excellent agreement between the three modelling approaches. The grating has also been assessed in terms of its response to a change in the pump wavelength, from the point of view of its potential use in VECSEL systems. It was found that once a set of grating parameters has been chosen, the terahertz frequencies are effectively frozen, changing by approximately 3GHz when the pump wavelength is tuned across (1–2)μm.

In the next chapter, the grating design described here will be experimentally characterised.

References

[1] D. E. Zelmon, D. L. Small, and D. Jundt. Infrared corrected Sellmeier coefficients for congruently grown lithium niobate and 5 mol.% magnesium oxide –doped lithium niobate. *J. Opt. Soc. Am. B*, 14(12):3319–3322, Dec 1997.

[2] U. Schlarb and K. Betzler. Influence of the defect structure on the refractive indices of undoped and Mg-doped lithium niobate. *Phys. Rev. B*, 50:751–757, Jul 1994.

[3] E. D. Palik. *Handbook of Optical Constants of Solids*. Academic Press Inc. London, 1985.

[4] J. A. Armstrong, N. Bloembergen, J. Ducuing, and P. S. Pershan. Interactions between light waves in a nonlinear dielectric. *Phys. Rev.*, 127(6):1918–1939, Sep 1962.

[5] M. M. Fejer, G. A. Magel, D. H. Jundt, and R. L. Byer. Quasi-phase-matched second harmonic generation: tuning and tolerances. 28(11):2631–2654, 1992.

[6] G. K. Kitaeva. Terahertz generation by means of optical lasers. *Laser Physics Letters*, 5(8):559–576, 2008.

[7] L. E. Myers. Review of quasi-phasematching and periodically poled lithium niobate. In *Proc. IEEE 1996 National Aerospace and Electronics Conf. NAECON 1996*, volume 2, pages 733–739, 1996.

[8] P. A. Franken and J. F. Ward. Optical harmonics and nonlinear phenomena. *Rev. Mod. Phys.*, 35(1):23–39, Jan 1963.

[9] W. R. Bosenberg, A. Drobschoff, and D. C. Gerstenberger. Mid-infrared optical parametric oscillators based on quasi-phasematching. In *Proc. , Volume 1. IEEE Lasers and Electro-Optics Society Annual Meeting 8th Annual Meeting*, volume 1, pages 37–38, 1995.

[10] L. E. Myers and W. R. Bosenberg. Periodically poled lithium niobate and quasi-phase-matched optical parametric oscillators. 33(10):1663–1672, 1997.

[11] Y. J. Ding. Transforming conventional PPLN-based frequency converters to cover 13–30 microns: Bridging the gap between mid-infrared and terahertz regions. In *Proc. Conf. Lasers and Electro-Optics (CLEO)*, pages 1–2, 2011.

[12] Y. Sasaki, A. Yuri, K. Kawase, and H. Ito. Terahertz-wave surface-emitted difference frequency generation in slant-stripe-type periodically poled $LiNbO_3$ crystal. *Applied Physics Letters*, 81(18):3323–3325, 2002.

[13] M Scheller, J. M. Yarborough, J. V. Moloney, M. Fallahi, M. Koch, and S. W. Koch. Room temperature continuous wave milliwatt terahertz source. *Opt. Express*, 18(26):27112–27117, 2010.

[14] D. A. Walsh, P. G. Browne, M. H. Dunn, and C. F. Rae. Intracavity parametric generation of nanosecond terahertz radiation using quasi-phase-matching. *Optics Express*, 18(13):13951–13963, Jun 2010.

[15] D. Molter, M. Theuer, and R. Beigang. THz-OPO with a novel QPM-scheme. In *Proc. 34th Int. Conf. Infrared, Millimeter, and Terahertz Waves IRMMW-THz 2009*, pages 1–2, 2009.

[16] L. Pálfalvi, J. Hebling, J. Kuhl, A. Péter, and K. Polgár. Temperature dependence of the absorption and refraction of Mg-doped congruent and stoichiometric $LiNbO_3$ in the THz range. *J. Appl. Phys.*, 97:123505, 2005.

[17] O. Paul, A. Quosig, T. Bauer, M. Nittmann, J. Bartschke, G. Anstett, and J.A. L'huillier. Temperature-dependent sellmeier equation in the MIR for the extraordinary refractive index of 5% MgO doped congruent $LiNbO_3$. *Applied Physics B: Lasers and Optics*, 86:111–115, 2007. 10.1007/s00340-006-2414-8.

[18] Y. S. Kim and R. T. Smith. Thermal expansion of lithium tantalate and lithium niobate single crystals. *J. Appl. Phys.*, 40:4637, 1969.

5

Characterisation of PPLN-based OPOs

5.1 Introduction

This chapter presents the results of several experimental systems constructed using the PPLN crystals designed as described in chapter 4. As a first step, the validity of the modelling approach described in chapter 4 was tested by comparing the measured idler wavelengths to those expected from the model for all of the PPLN crystals available to us. This exercise necessitated the implementation of a more recent terahertz Sellmeier equation for MgO:$LiNbO_3$ to bring the predicted wavelengths into better agreement with those observed experimentally.

The characteristics of a collinear, PPLN-based terahertz OPO using the new PPLN crystal designed in chapter 4 has been quantified in relation to the performance of the non-collinear MgO:$LiNbO_3$ OPO that was extensively characterised in earlier chapters. The PPLN OPO was found to be inferior to the non-collinear OPO both in terms of the pump intensity needed to reach threshold and the amount of down-conversion that was measured. The performance of the OPO was also hampered by crystal damage, which occurred at lower pump intensities than for the bulk material. Reasons for the poorer operational characteristics of the PPLN terahertz OPO are presented along with possible future developments to improve the situation.

5.2 Initial measurements of PPLN crystals

Four PPLN crystals were characterised in relation to the observed idler wavelengths and OPO threshold, for comparison with an equivalent bulk $LiNbO_3$ intracavity terahertz OPO and in order to assess the accuracy of the modelling approach described in the previous chapter. Two of these crystals had been used successfully in terahertz OPOs previously [1] and a newly acquired crystal was of the design presented in chapter 4. In addition, a further crystal was available which incorporated a grating which was such that we had not previously been able to bring it above threshold. The experimental setup is shown in figure 5.1. The shared pump and idler cavity has an optical length of 24.6cm and the output coupler, M2, is 2% transmitting. In the case of the three pre-existing PPLN crystals, a 200mm focal length lens was inserted into the shared pump and idler to reduce the pump beam size sufficiently so as to pass through the PPLN crystal without clipping - a reduction from approximately 1mm diameter to approximately 0.6mm diameter; for the newly acquired PPLN crystal clipping of the pump beam by the crystal was not a problem since the crystal thickness was 3mm, however owing to the thermal lensing effects characterised in chapter 2, a lens of focal length 1m was incorporated into the cavity to stabilise the pump beam size. The 1m focal length lens was located a distance of approximately 14cm from the mirrored end of the Nd:YAG crystal and the 200mm focal length lens at a distance of 10cm measured from the same point (i.e. the mirrored end of the Nd:YAG crystal).

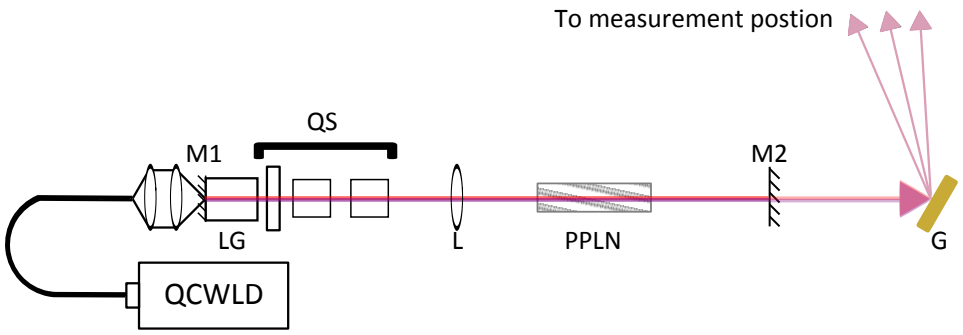

Figure 5.1: The layout of the collinear PPLN-based OPO. The lens, L, was used to control the pump beam size and to avoid the pump beam clipping the crystal. The gold grating, G, was used to separate the pump and idlers to obtain temporal measurements.

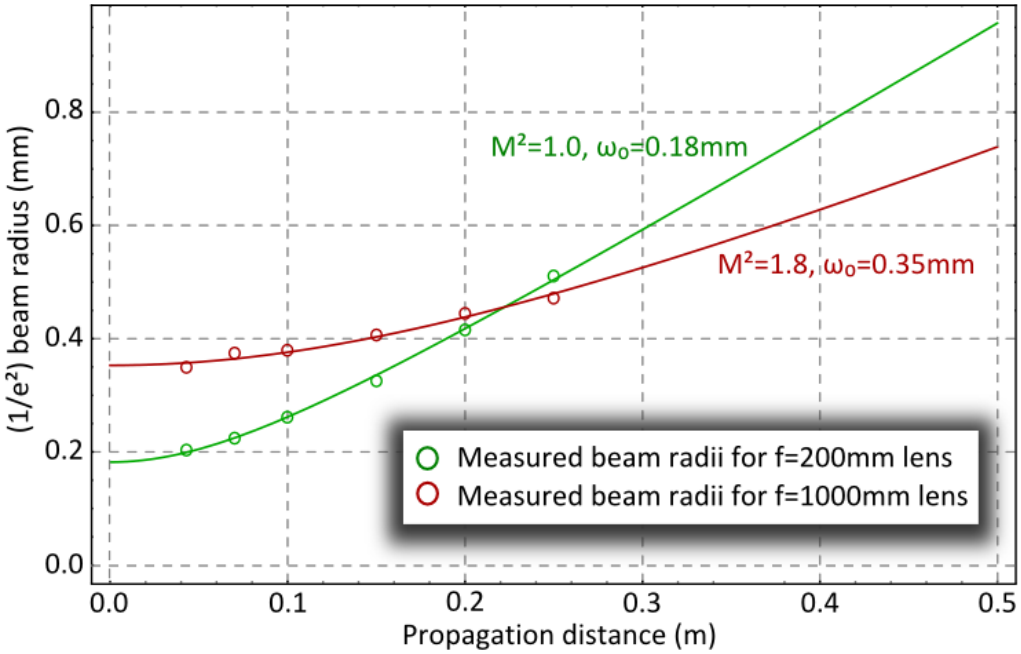

Figure 5.2: Graph showing the beam radii measured in the presence of 200mm and 1m focal length lenses in the shared pump and idler cavity. The circles represent the measured data and the solid lines indicate the calculated beam radii.

The effect of inserting the lens on the beam size is shown in figure 5.2. The beam diameters corresponding to an intracavity pump intensity of ≈75MWcm^{-2} were measured by translating a knife-edge across the 1064nm beam at a range of distances from the output coupler. The derivative of the power with position was then calculated and a Gaussian function was then fitted to the processed data in order to obtain the $(1/e^2)$ beam widths. *Mathematica* was used to fit a function of the form $w(z) = w_0 \times \sqrt{1 + M^2 \left(\frac{z\lambda}{\pi\, w_0^2}\right)^2}$ to the data and obtain values for the beam waist, w_0 and the beam quality parameter M^2 in each case. Since the beam waist is formed on the end mirror of the plane-plane cavity, the beam sizes indicated for the region (0 – 0.24)m reflect the beam sizes within the cavity itself.

The *Psst!* lasers and nonlinear optics modelling software package [2] was used to model the pump beam size inside the cavity to assess the beam size as it propagates through the PPLN crystal. Figure 5.3 shows the cavity models for the relevant cases. The $(1/e^2)$ beam diameters at approximately the mid-point of the PPLN crystal are 0.4086mm and 0.7104mm when using the 200mm and 1m focal length lenses, respectively.

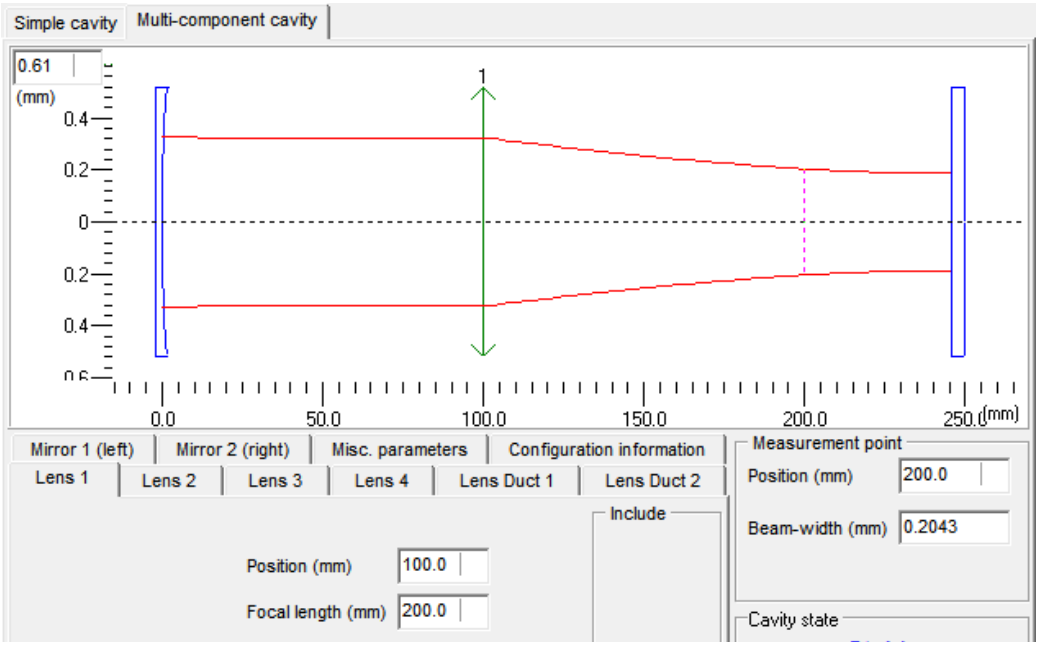

(a) The cavity with the 200mm focal length lens.

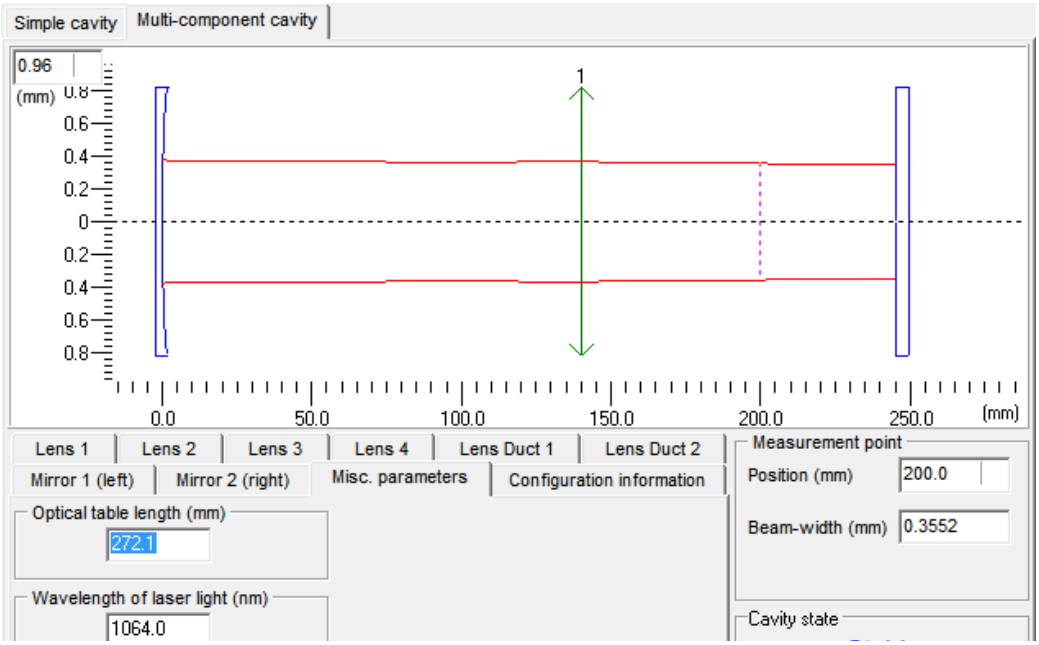

(b) The cavity with the 1m focal length lens.

Figure 5.3: Pump cavity models showing the effect of different lenses on the pump beam size. The beam widths shown in the figures are the $(1/e^2)$ half-widths and correspond to the approximate location of the centre of the PPLN crystal.

5.2.1 Agreement between PPLN model and measured emission wavelengths

An optical spectrum analyser (OSA) was used to measure the pump and idler wavelengths produced by each crystal. In this case the pump and idler can be observed on the same OSA trace because the beams share a cavity under the collinear phase-matching scheme. Table 5.1 summarises the idler wavelengths in terms of the values predicted using the modelling approach and those measured experimentally using the OSA. In most cases the agreement is good taking in to consideration the 0.2nm resolution bandwidth of the OSA. However for the Λ=35.74μm, α=23° grating there is a 1nm difference between the measured and predicted values. This discrepancy is consistent with the findings presented in a recent paper by Walsh [1] but it is nonetheless of concern so several potential explanations were explored in relation to reconciling the predicted and experimental data.

First of all we could surmise that the grating itself is not as specified. In order to account for a 1nm shift in the idler wavelength, the grating period would have to be reduced to 32.09μm. Although this change can account for the difference in wavelengths an error of this magnitude in the grating period is approaching 175 times the quoted manufacturing error, so it is unlikely to be the reason for the observed discrepancy.

Crystal parameters (grating period, angle)	Predicted idler wavelength (nm) I	II	Measured idler (nm)
72.4μm, 90°	1067.82		1067.9
42.4μm, 90°	1070.09		1070.23
35.74μm, 23°	1073.71	1068.89	1074.46
72.4μm, 86.5°	1067.92	1067.72	1067.82

Table 5.1: The predicted and measured idler wavelengths for the range of PPLN crystals that was characterised. The non-orthogonal gratings have two possible wavelengths due to the bi-directionality of the grating vector; for the orthogonal gratings there are still two solutions, however they are degenerate.

The second possibility is that the grating angle could be something other than 23°. No grating angle could be found that reproduced the measured idler wavelength - the closest value obtained was 1073.9nm, corresponding to the grating being collinear with the optic axis.

Finally, it is possible that the refractive index data used to model the PPLN might not be accurate. The original refractive index values were calculated from a fit of the form $n_T = Ae^{-\frac{\lambda_T-\lambda_0}{t_0}} + z$ to the data in Palik [3], since at that time no published Sellmeier equations were available. The choice of fit was arbitrary and the coefficients have no physical meaning. The values of the coefficients are:

$$\begin{aligned} \text{A} &= 3.8123 \\ \text{z} &= 5.07 \\ \lambda_0 &= \text{-}14.9\mu\text{m} \\ t_0 &= 65 \end{aligned}$$

and λ_T is the terahertz wavelength measured in μm.

As an initial step the value of z was varied to recover the measured idler wavelength. To achieve this, the value of z had to be changed from 5.07 to 4.60. The terahertz refractive index data corresponding to congruent lithium niobate with 6.1% MgO-doping at a temperature of 300K taken from Pálfalvi [4] was also compared with the original and shifted data, as shown in figure 5.4. The Pálfalvi data agrees most with the Palik data at low terahertz frequencies but with the shifted curve at high terahertz frequencies, an encouraging result given that the measured idler wavelengths corresponding to low terahertz frequencies were in much better agreement with the predicted wavelengths than those at the high frequency end.

Upon implementing the Pálfalvi refractive index data in the PPLN design and analysis procedure documented in chapter 4 the anticipated idler wavelength became 1074.42nm - only 0.04nm different from the measured value. Next, the effect of this new refractive index function on the other crystals' output wavelengths had to be established. Table 5.2 summarises the effects of using

Crystal parameters (grating period, angle)	Predicted idler wavelength (nm) z=5.07	z=4.60	Pálfalvi data	Measured idler (nm)
72.4μm, 90°	1067.82nm	1068.25	1067.91	1067.9nm
42.4μm, 90°	1070.09nm	1070.72	1070.32	1070.23nm
35.74μm, 23°	1073.71nm	1074.46	1074.54	1074.46nm
	1068.89	1068.98	1068.98	
72.4μm, 86.5°	1067.92	1068.38	1068.02	
	1067.72	1068.13	1067.80nm	1067.82nm

Table 5.2: A comparison of the predicted and measured idler wavelengths calculated on the basis of the three different formulae describing the terahertz refractive index of lithium niobate.

these alternative refractive index calculations on the expected idler and terahertz wavelengths and compares the calculated and measured data. When the Pálfalvi data is implemented in the PPLN modelling procedure described in chapter 4 the measured idler wavelengths for all of the available PPLN crystals are in excellent agreement with those anticipated by the model, a fact which is indicative of the accuracy and usefulness of the model.

5.3 Characterisation of the new PPLN crystal

The most recently acquired PPLN crystal has a grating design as described and modelled in chapter 4. The grating period is 72.4μm and the grating angle is 86.5° (measured with respect to the optic axis). Its dimensions are 40mm×5mm×3mm (length×width×thickness), meaning that intracavity focussing elements are not essential unlike the case for the 1mm-thick PPLN crystals. The benefits of not having to use strong focussing elements inside the cavity are two-fold - firstly the pump beam intensity will not be as high as when a 200mm focal length lens is used, which could lessen the likelihood of damage occurring and secondly the OPO can be compared more directly with the non-collinear terahertz OPO which has been extensively characterised previously (see chapters 2 and 3).

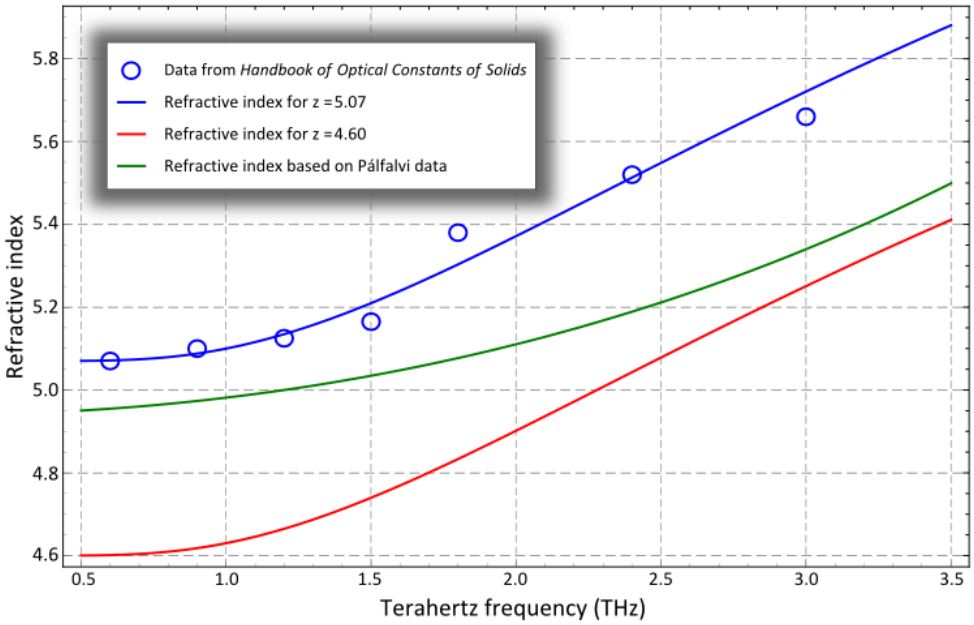

Figure 5.4: The terahertz refractive index based on two different data sets [3, 4].

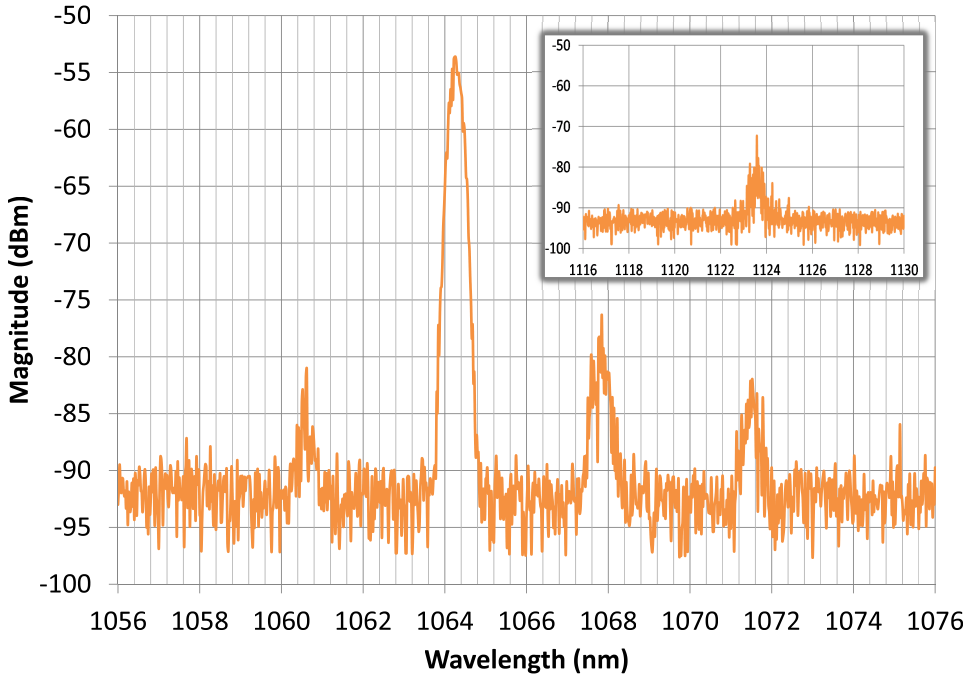

Figure 5.5: The power against wavelength trace recorded using the optical spectrum analyser for the 40mm-long PPLN crystal with grating parameters Λ=72.4μm and α=86.5°. (Inset: Another wavelength observed at ≈1124nm.)

5.3.1 Spectral data

Figure 5.5 shows the spectral content of the collinear OPO output generated using the PPLN crystal. Along with the pump at 1064.4nm and the idler at 1067.8nm, the trace shows two additional idlers at approximately 1071.5nm and 1075nm, which are produced as a result of cascaded difference frequency generation between the original idler and the terahertz; the presence of the shorter wavelength peak at approximately 1060.6nm is due to sum frequency generation between the pump and terahertz waves [1]. Shown in the inset is an additional wavelength at ≈1124nm that was initially observed when the collinear beam was separated into its constituent wavelength components using a diffraction grating.

5.3.2 OPO threshold and output power characteristic

Determining the operational point corresponding to OPO threshold is a significantly different process for collinear OPOs than it is for non-collinear ones. The technique used in earlier chapters has been to observe depletion of the pump pulse in both its temporal profile and its power; however since the idler beam now shares the same cavity as the pump beam it is impossible to block the idler cavity alone to cause cessation of the parametric process. Previous measurements [1, 5] also indicated that the amount of pump depletion would be too small to be observable using the pump beam temporal profile.

In order to establish the PPLN OPO threshold point, the spectral profile of the OPO output was viewed using the OSA whilst the pumping level was increased; the mean power (corresponding to the combined pump and idler powers) was also recorded as this was done. Observation of the idler wavelength on the OSA trace was indicative that the threshold point had been reached. Using this method the threshold of the OPO was found to be at 46.7A, equivalent to a diode peak power of ≈55W. Figure 5.6 shows the mean power measured as a function of the diode peak power. Damage to the crystal coatings was experienced at approximately the pumping level corresponding to the last data point in that graph (57.5W) - corresponding to around 40MWcm^{-2} intracavity pump intensity

- and is illustrated in figure 5.7.

Although an entire OSA trace is not acquired at one instant in time, the OSA's in-built "hold maximum" function was used to record the peak signal at each wavelength over a user-defined period of time (typically around 5 minutes) and the data is therefore taken to be representative of the relative powers contained within each wavelength. Figure 5.8 shows the OSA traces obtained for five points on the current-power graph at which the OPO is above threshold. The ratios of the peaks of each wavelength in the trace were used to scale the measured total

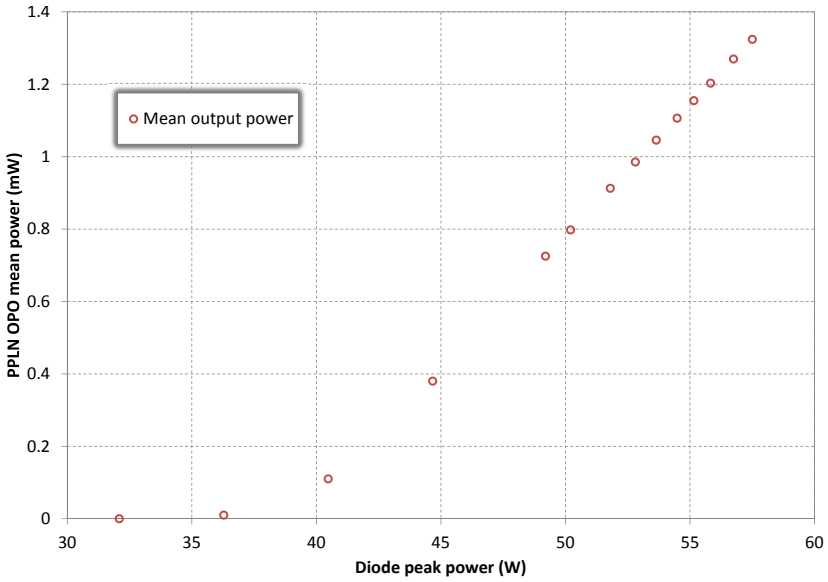

Figure 5.6: Mean power measurements of the combined output of the OPO.

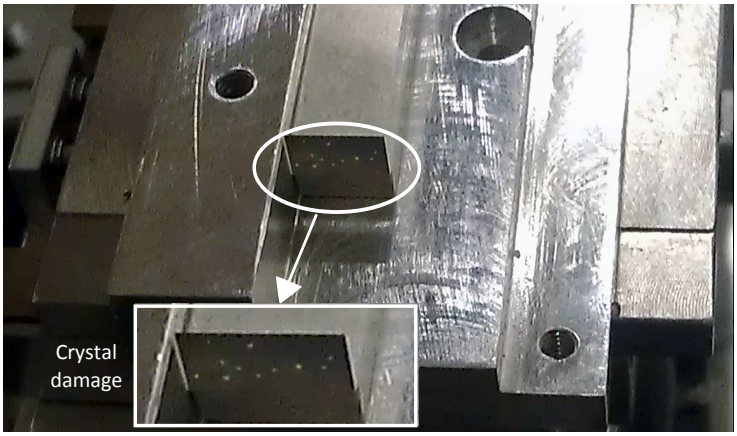

Figure 5.7: Image showing the damage to the optical coatings of the PPLN crystal.

power according to each wavelength so that the amount of pump depletion could be calculated. To do this, the peak amplitude at the pump wavelength (including its uncertainty) was measured, as were those of the idlers. The ratio of a given idler to the pump is then given by:

$$\text{Ratio of idler to pump } (\%) = 10^{\Delta pi/10} \times 100$$

where Δpi is the difference between the peak signals measured in dBm.

To make meaningful comparisons between the collinear and non-collinear systems, their operational characteristics had to be placed on a common scale, namely the intracavity pump intensity, since the pump cavity lengths were different for the two cases. The PPLN common pump and idler cavity had an optical length of 24.6cm whilst the pump cavity of the non-collinear system was 38.3cm long. Figure 5.9 shows the effect that changing the cavity length has on the pump beam size. The measurement points indicated in the diagrams are consistent with the midpoint of the nonlinear crystal. In the PPLN OPO cavity the pump beam has a $(1/e^2)$ radius of ≈0.33mm^2 through the crystal whilst the non-collinear OPO pump beam has a larger $(1/e^2)$ radius of ≈0.38mm^2.

In addition to the pump beam radius the duration of the undepleted pump pulse must be known so as to calculate the intracavity intensity. The expressions describing the calculation of the intracavity intensity is as follows:

$$\text{Intracavity intensity (Wcm}^{-2}) = \frac{\text{Intracavity peak power (W)}}{\pi\, r^2} \tag{5.1}$$

where

$$\text{Intracavity peak power (W)} = \frac{\frac{\text{mean power (W)}}{\text{repetition rate (Hz)}}}{\text{FWHM pulse duration (ns)}} \times \frac{1}{(1-R)} \tag{5.2}$$

r is the $(1/e^2)$ radius of the pump beam and R is the reflectivity of the pump cavity output coupler.

The intracavity intensities and FWHM undepleted pump pulse durations of both systems are shown as a function of the diode peak power in figure 5.10. For the PPLN the undepleted pump pulse duration was taken to be the same as the

measured temporal profile even above OPO threshold since an almost negligible amount of down-conversion had been observed (this will be elaborated upon in subsequent paragraphs). From the figure it is clear that the intensity of the pump increases more rapidly with diode power in the PPLN OPO than in the $MgO:LiNbO_3$ OPO. The pump pulse durations are also shorter at a given diode power for the PPLN OPO.

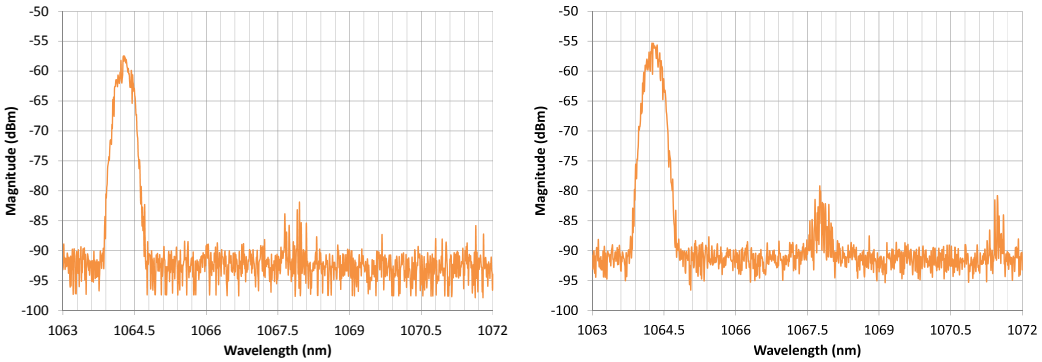

(a) 23.9W (b) 24.5W

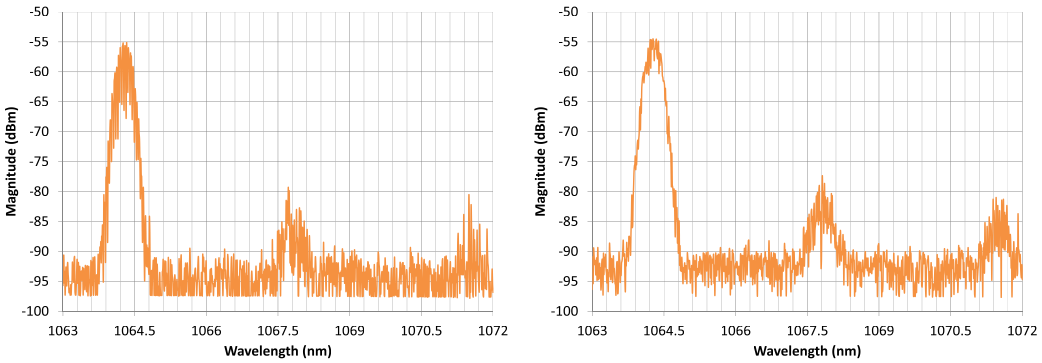

(c) 25.2W (d) 26.1W

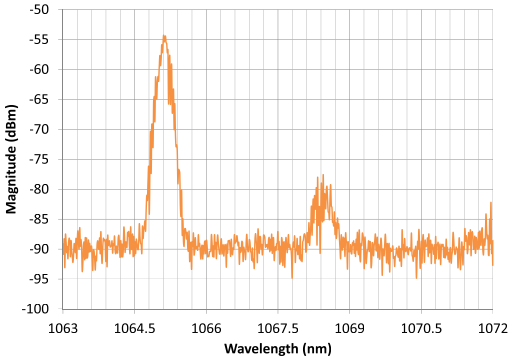

(e) 26.9W

Figure 5.8: OSA traces used to scale the output power in accordance with the ratio of the peak heights of each wavelength. The diode peak powers at which the traces were recorded are indicated.

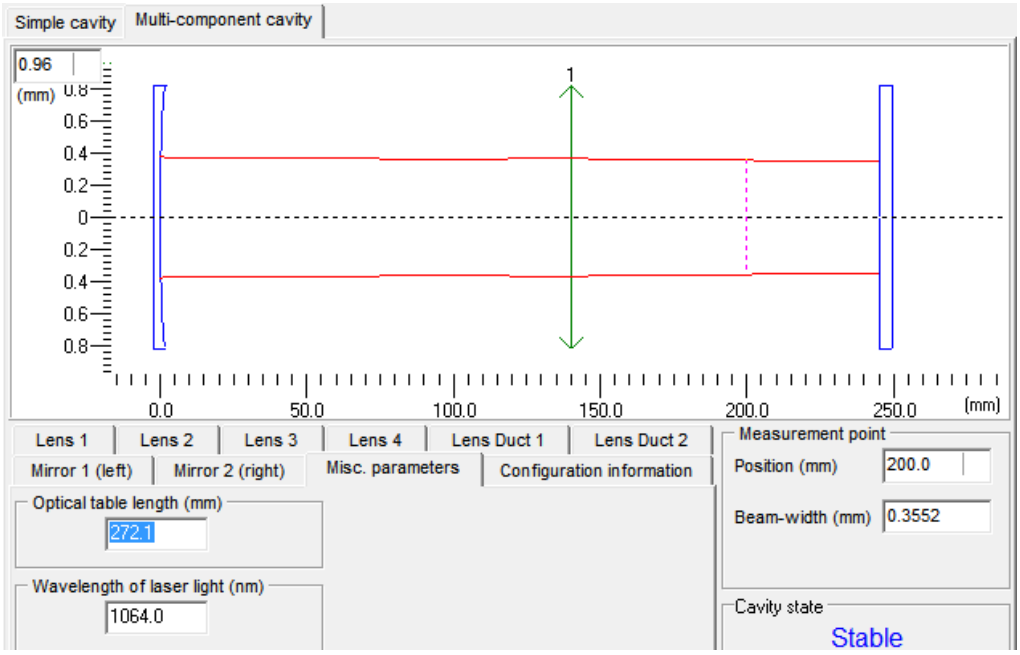

(a) 24.6cm PPLN shared pump and idler cavity

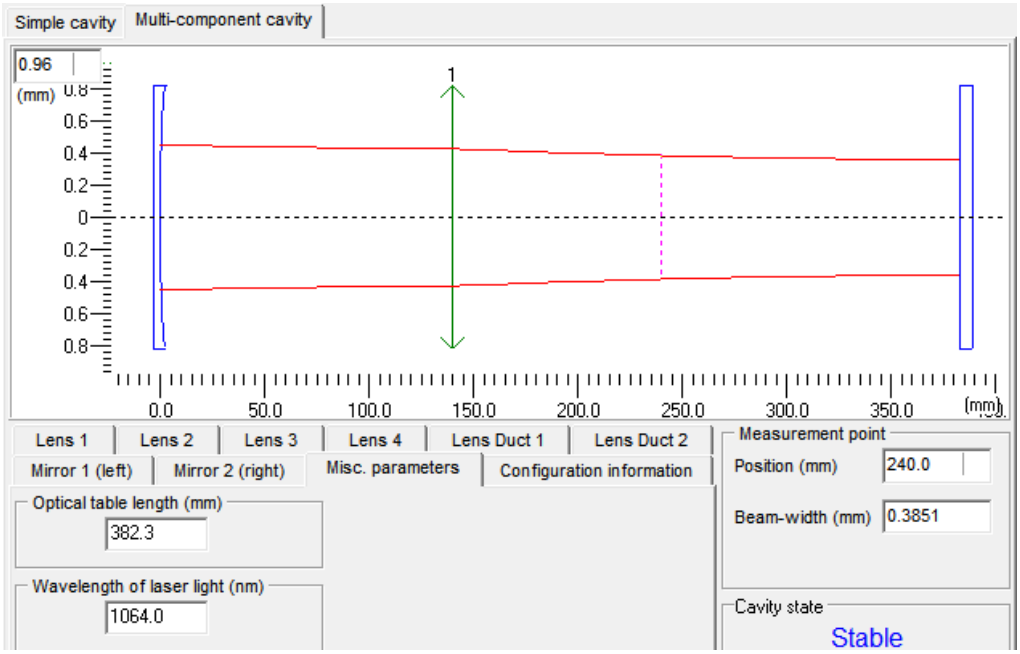

(b) 38.3cm MgO:$LiNbO_3$ pump cavity

Figure 5.9: The effect that changing the pump cavity length has on the size of the pump beam size through the nonlinear crystal.

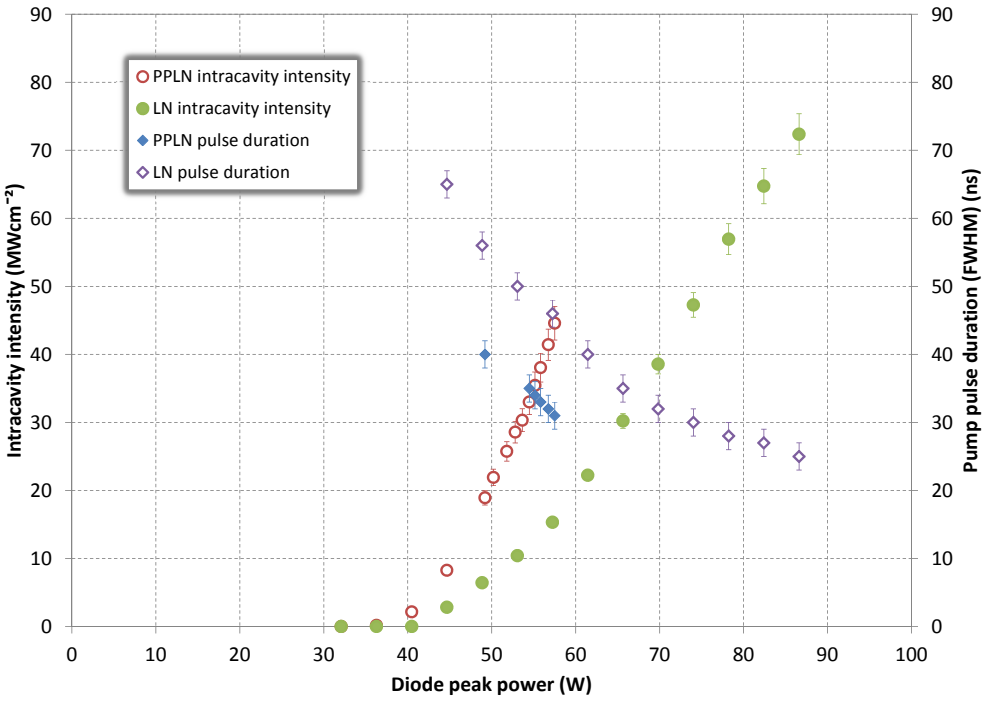

Figure 5.10: Measured undepleted pump pulse intensities and FWHM durations for the PPLN and $MgO:LiNbO_3$ OPOs.

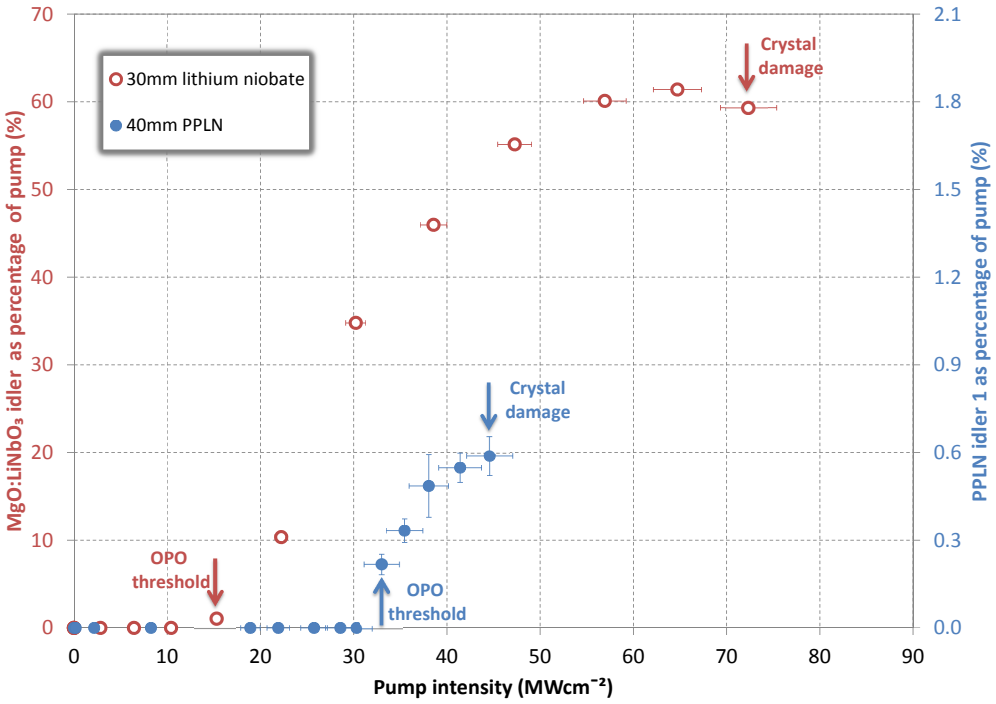

Figure 5.11: A direct comparison of the amount of first idler produced by the collinear and non-collinear OPOs. The vertical scale for the PPLN data is on the right side of the graph.

A direct comparison between the PPLN and the non-collinear MgO:$LiNbO_3$ terahertz OPOs is made in terms of the amount of down-conversion in figure 5.11. The error bars are representative of the uncertainties arising from the accuracy of temporal measurements and the changing pump radius as it propagates through the nonlinear crystal under analysis. The down-conversion values for the PPLN OPO are also subject to the accuracy with which the wavelength peaks in the OSA traces could be measured. The non-collinear OPO reaches threshold at 15MWcm^{-2} and the crystal coatings do not experience damage until an intracavity pump intensity of 72MWcm^{-2} is reached, which means that the device can be operated at up to 4.7 times OPO threshold where pump depletion levels of greater than 50% are readily obtainable. The PPLN-based collinear OPO does not have such desirable operational characteristics - a higher pump intensity of 32MWcm^{-2} is required to reach OPO threshold, the crystal coatings experience damage at only 44MWcm^{-2}, which means the device can only be operated at a maximum of 1.4 times threshold, with pump depletions of only around 0.6% being attained before the onset of coating damage. The slope efficiency is also much poorer than in the case of the non-collinear OPO - comparing the 1.4 times threshold condition in each system, the PPLN OPO only reaches 0.6% depletion whereas the non-collinear OPO has already achieved 10% (this measured at a pump intensity of $\approx$22MWcm^{-2}). Even if the PPLN could be used at pump intensities of 72MWcm^{-2} the slope of the existing plotted data implies that only $\approx$2% depletion would be reached as opposed to the 60% observed in the MgO:$LiNbO_3$ system.

5.4 Factors affecting the performance of PPLN-based systems

Despite the increased overlap between the pump and idler waves in the collinear OPO system, its threshold is higher than the non-collinear OPO and its conversion efficiency is also much poorer. Here we examine other properties of the system affecting these aspects of the OPO's operation.

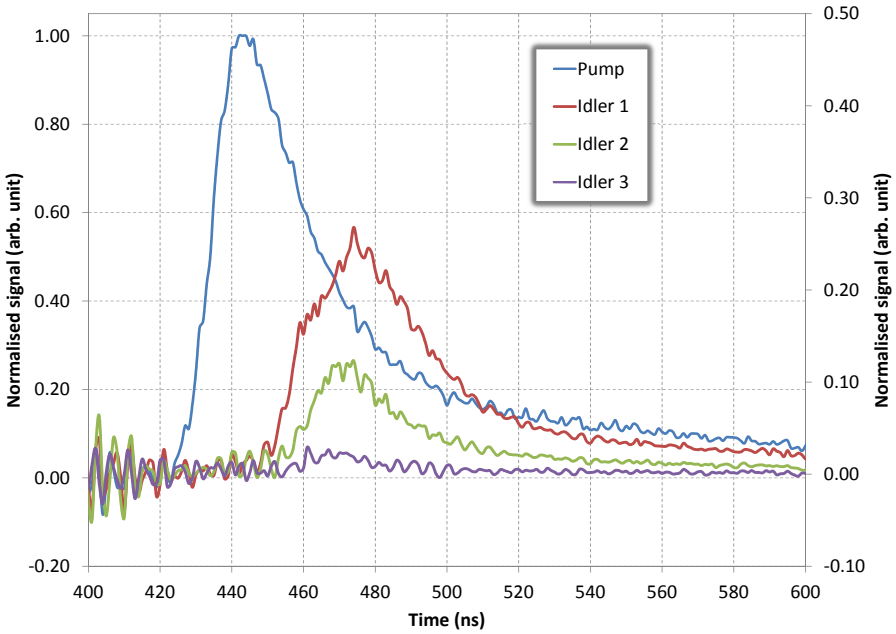

(a) Temporal profiles of the pump and idlers in the PPLN OPO.

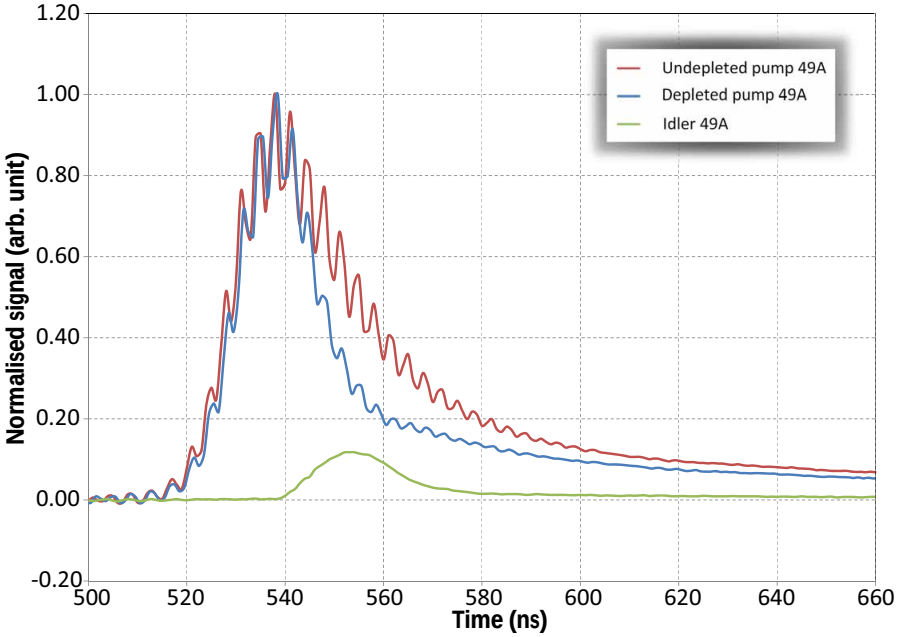

(b) Temporal profiles of the pump and idler in the non-collinear OPO.

Figure 5.12: The temporal profiles of the pump and idlers observed from the collinear PPLN OPO and the non-collinear MgO:$LiNbO_3$ OPO. The temporal profiles were averaged over multiple acquisition steps to minimise the influence of pulse-to-pulse jitter (64 averages for the PPLN system and 8 averages for the MgO:$LiNbO_3$ system). To improve the clarity of the graphs the idler amplitudes are referenced to a pump amplitude that has been normalised.

5.4.1 Temporal measurements

To be able to measure the temporal profiles of the pump and idlers, the beams had to be separated using a diffraction grating, as shown in the schematic figure 5.1. Using the same detectors as described in chapter 3, simultaneous measurements of the pump and idlers could be made, the results of which are shown in figure 5.12. The PPLN measurements were made at an intracavity pump intensity of $\approx$0.43MWmm^{-2} (close to the damage point) and the measurements of the non-collinear system were made just above OPO threshold, at $\approx$0.18MWmm^{-2}. In the collinear PPLN system the build-up time of the idler pulses is such that they are delayed from the peak of the pump pulse by almost 10ns, this resulting in a reduction in the energy available for the downconversion process; in the non-collinear system the idler pulse builds up very much nearer to the pulse even when the device is only just above threshold. Although the output at 1124nm has a steeper rising edge the idler waves build up simultaneously, indicating that those other than the first idler at 1067.8nm are generated through difference frequency mixing since there is no additional build-up time, as would be characteristic of another parametric generation process.

The reason behind the delayed build-up of the idlers with respect to the pump in the collinear OPO is that the idler cavity has a length of 24.6cm, almost twice the length of the idler cavity in the non-collinear system, which is only 13cm long. The exponential gain is given by the expression

$$G = \cosh^{2\times M\times N}(\Gamma l) \tag{5.3}$$

where

$$\Gamma^2 L^2 = \frac{8\pi^2 d_{eff}^2}{c\epsilon_0 n_p n_i n_T \lambda_i \lambda_T} I_p l^2 \tag{5.4}$$

and M and N are the number of round-trips of the idler cavity during the pump pulse and the number of interaction segments along the length of the crystal (due to the walk-off of the terahertz beam), respectively and l is the walk-off or absorption limited interaction length. As a result of the increased idler cavity

length it takes longer for the gain to reach the approximate 140dB needed for the device to reach threshold.

5.4.2 The magnitude of d_{eff} in PPLN

Another major factor affecting the amount of gain experienced by the parametric interactions is the reduction in the effective nonlinear coefficient (d_{eff}) as a result of the periodic poling. As shown in equations 4.4-4.6 of chapter 4 the effective nonlinear coefficient is reduced by at least a factor of $\frac{2}{\pi}$, for first order quasi-phase-matching (QPM). In the case where QPM is being used as an alternative to birefringent phase-matching (BPM), the reduction in d_{eff} is acceptable only when the reduced value is still larger than the nonlinear tensor component that was accessible through BPM. However due to the polarisation states of the fields in the terahertz OPO the highest d_{eff} was already being exploited with the bulk material; hence in switching to PPLN we actually experience a reduction in the value of d_{eff} by a factor of $\frac{2}{\pi}$, from 125pmV^{-1} to 80pmV^{-1}. Even if damage were not a problem for the PPLN crystal and it could be subjected to the same intracavity intensities as the bulk MgO:LiNbO$_3$ the value of Γ would be reduced by the same factor of $\frac{2}{\pi}$ due to its linear dependence on d_{eff} (equation 5.4); consequently this would also reduce the exponential gain, G (equation 5.3).

5.4.3 Collinear idler cavity losses

One of the factors contributing to the poor performance of the PPLN crystals in relation to the bulk LiNbO$_3$ crystals is the increased idler cavity length, which results in the idler making fewer round-trips during the pump pulse and hence reduces the gain. As well as the impact of the increased idler cavity length, the magnitude of the losses of the collinear cavity must also be considered. Whereas for the non-collinear terahertz OPO the idler cavity contained only the nonlinear crystal, under collinear conditions the same cavity serves as both the pump cavity and the idler cavity and hence the idler cavity now also includes the electro-optic Q-switch, which comprises a quarter-wave plate, Pockels cell and polarising air-spaced beam cube as well as any lenses that may be required in order to ensure the beam dimensions are such that they can pass through the

PPLN crystal unhindered. As characterised in chapter 2, the pump cavity parasitic loss was determined to be ≈23%, significantly higher than the parasitic loss of the off-axis idler cavity which was found to have a parasitic loss in the region of (13-19)%.

Although the pump and idler wavelengths are very close in value the optical components in the pump laser cavity such as the Q-switching elements were all specified for operation at 1064nm and not the region (1068–1080)nm (the approximate wavelength region of the idler). In order to assess the additional losses that would be experienced by a collinearly propagating idler, an external cavity diode laser (ECDL) centred at 1072nm was purchased from Toptica Photonics. This laser is capable of producing up to 70mW of single-frequency optical output, which by careful selection of operating temperature, drive current and piezo motor grating scan range, is smoothly tunable across the idler wavelength range. By making simple transmission measurements the additional losses experienced at the idler wavelengths could be accurately quantified.

For the polarising beam-cube and Pockels cell, there was found to be negligible difference in their transmission at the pump and idler wavelengths. There were two quarter-wave plates available for use in the system - one described as zero order and the other described as high order; these were found to have a greater impact on the losses experienced by the idler wavelengths. Measurements of the loss due to these wave plates was made as a function of wavelength, following the procedure described below.

The transmission of an ideal wave plate located between a pair of parallel linear polarisers is described by:

$$I = I_0 \left(cos^4\theta + \sin^4\theta + 2\cos\delta\cos^2\theta\sin^2\theta \right)$$

where θ is the angle of the fast axis of the wave plate relative to the polarisers and δ is the retardation of the wave plate. For the special case of the wave plate's fast axis being at angle of $\theta = \frac{\pi}{4}$ radians, the expression describing the transmission becomes simplified:

$$I = I_0 \left(\frac{1}{2} + \frac{1}{2} \cos \delta \right) \tag{5.5}$$

Hence a perfect quarter-wave plate, for which $\delta = \frac{\pi}{2}$, exhibits a minimum in its transmission when its fast axis is at an angle of $\frac{\pi}{4}$ radians. A non-perfect quarter-wave plate will differ from 50% transmission as illustrated by figure 5.13, allowing the value of δ to be determined for a particular wavelength according to equation 5.5 by measuring the ratio $\frac{I}{I_0}$.

The experimental setup used to characterise the wave plates is shown in figure 5.14. The polarised light emergent from the ECDL was passed through an optical isolator. The wave plate to be measured was placed in the path of the laser beam before the second polariser and the intensity of light transmitted through the system was detected by a detector connected to a phase sensitive detector (PSD) (Stanford Research Systems). A second PSD was used to create a balanced detection system by monitoring the radiation prior to it encountering the wave plate (see figure 5.14), removing any effects on the transmitted intensity due to fluctuations in the laser output. The output of the reference PSD was connected to an auxiliary input of the second PSD and the ratio function was used to obtain

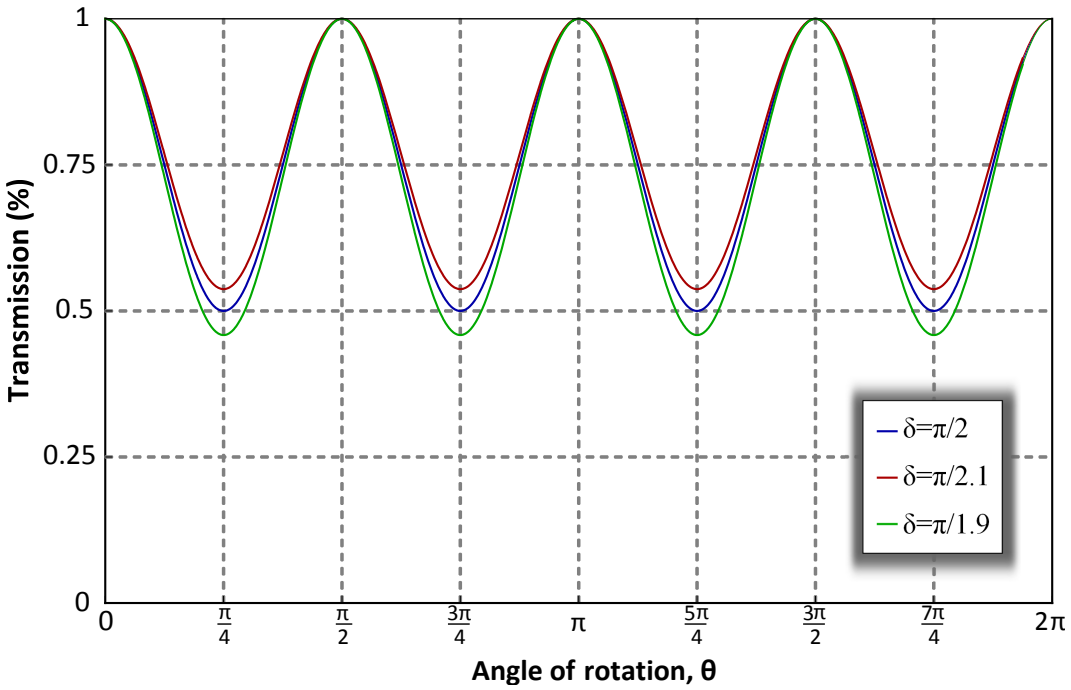

Figure 5.13: The effect of the value of δ differing from $\frac{\pi}{2}$.

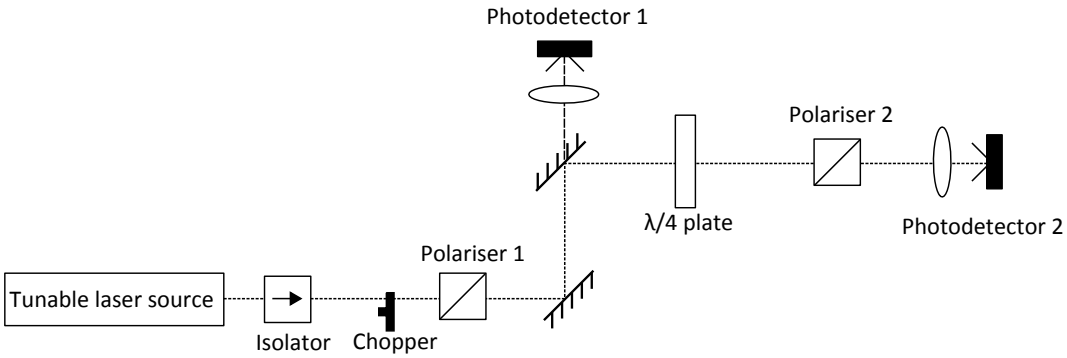

Figure 5.14: The experimental setup used to characterise the quarter-wave plates.

a value corresponding to the intensity of the measured light. The ratios were normalised to the maximum ratio to obtain meaningful transmission values (that is, $\frac{I}{I_0}$ was quantified).

Figure 5.15 provides the results of the measurements of δ as a function of wavelength in the region 1064-1071nm for both wave plates. The two sets of data in each graph represent the δ values measured when travelling in either direction through the wave plates. This is an important finding since the pump and idler waves pass both ways through the wave plate in a round-trip of the cavity.

In order to assess the round-trip loss as a result of a particular quarter-wave plate it is necessary to construct an *ABCD* ray transfer matrix describing the laser cavity [6], which is shown schematically in figure 5.16. When the Pockels cell is inactive light passes through it unchanged (in the diagram this is indicated by the absence of the Pockels cell). After passing through the quarter-wave plate the light becomes circularly polarised and upon reflection it then takes on a polarisation state orthogonal to its original polarisation, and is hence rejected by the polariser. The cavity is switched to the high-Q state by the application of a potential (typically a few kV) across the Pockels cell, which then itself behaves as a quarter-wave plate and allows the laser pulse to build up by either cancellation of or addition to the effect of the first quarter-wave plate. A single round-trip of the high-Q laser cavity can be described by multiplying together the following sequence of matrices, which describe the optical components individually [7]:

$$[\mathrm{POL}][\mathrm{PC}][\lambda/4][\lambda/4][\mathrm{PC}][\mathrm{POL}]$$

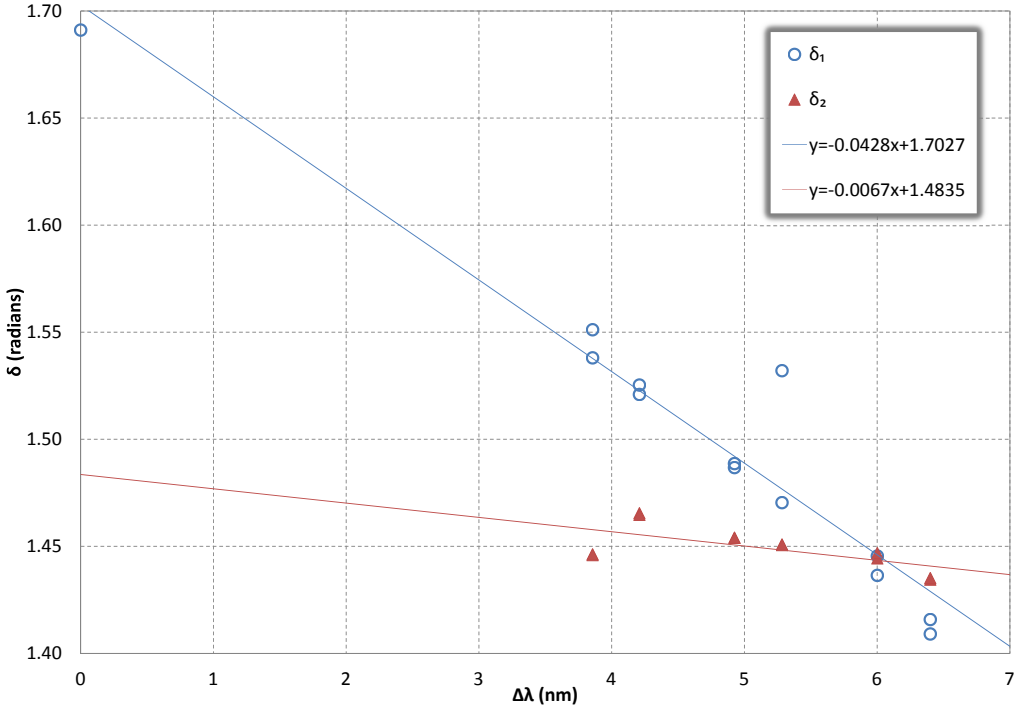

(a) High order quarter-wave plate

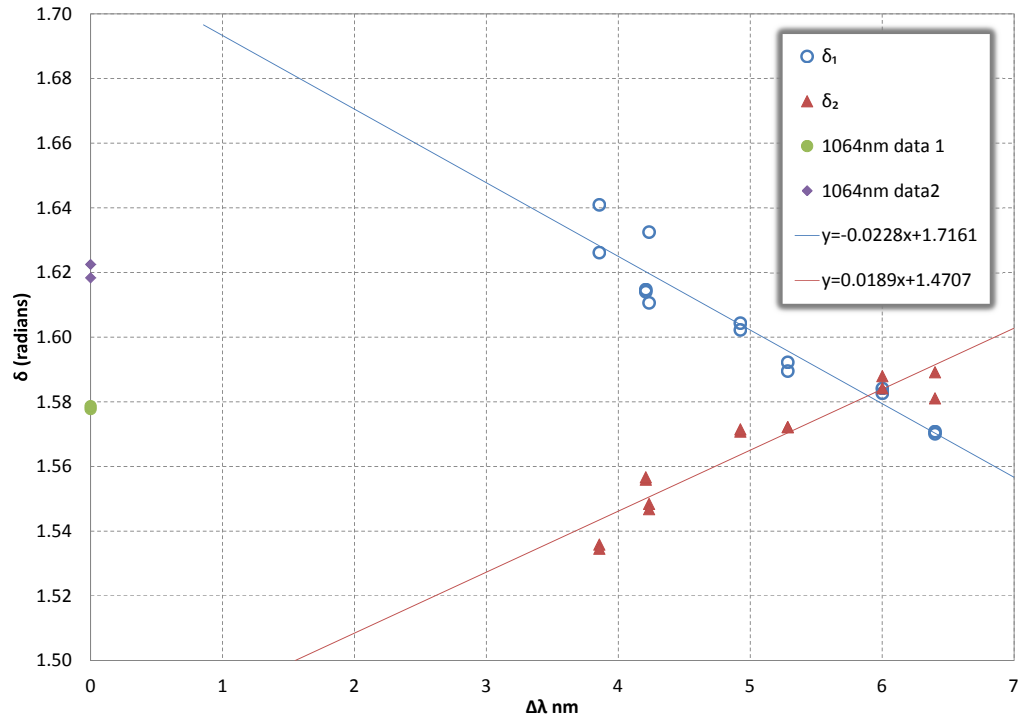

(b) Low order quarter-wave plate

Figure 5.15: The measured δ values for the high and low order quarter-wave plates.

In the low-Q situation:

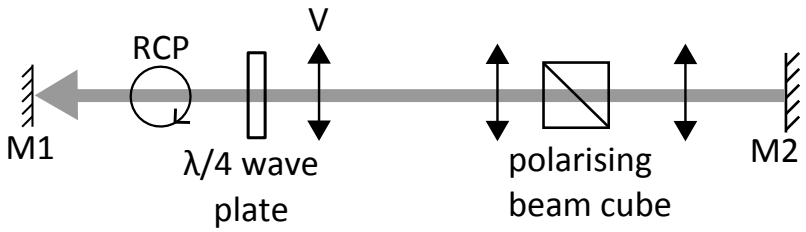

Then upon reflection:

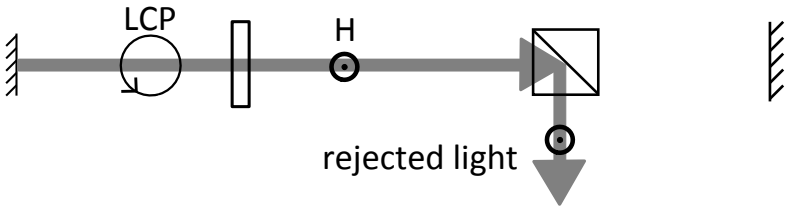

In the high-Q situation:

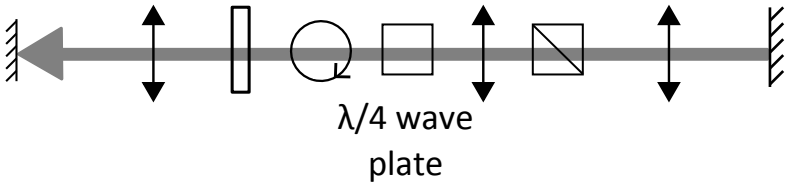

Then upon reflection:

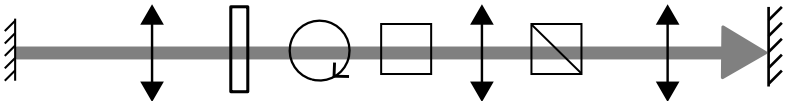

Figure 5.16: Diagrams illustrating the consequence of the quarter-wave Q-switch layout on polarisation when the Q-switch is closed (the "low-Q" case) or with the Q-switch open (the "high-Q" case). The arrows and circles represent the polarisation state of the laser light at various points in the cavity, with "V" being vertical and "H" being horizontal polarisation. "RCP" and "LCP" indicate right- and left-hand circular polarisation, respectively.

which is equivalent to:

$$[\text{POL}][\text{PC}][\lambda/2][\text{PC}][\text{POL}]$$

where the matrices for each of the elements are given below.

The Jones matrix for a linear retarder with retardance δ and at an angle θ is:

$$\begin{bmatrix} \cos^2\theta + \sin^2\theta\, e^{-i\delta} & \cos\theta\sin\theta(1-e^{-i\delta}) \\ \cos\theta\sin\theta(1-e^{-i\delta}) & \cos^2\theta\, e^{-i\delta} + \sin^2\theta \end{bmatrix}$$

which can be simplified for the case where the fast axis of the retarder is at 45°:

$$\frac{1}{2}\begin{bmatrix} (1+e^{-i\delta}) & (1-e^{-i\delta}) \\ (1-e^{-i\delta}) & (1+e^{-i\delta}) \end{bmatrix}$$

Treating the Pockels cell as an ideal quarter-wave plate and the quarter-wave plate as a half-wave plate having retardance $(\delta_1+\delta_2)$ we can derive their matrices as:

$$\text{Pockels cell} = [PC] = \frac{1}{2}\begin{bmatrix} 1-i & 1+i \\ 1+i & 1-i \end{bmatrix}$$

$$\text{Half-wave plate} = [\lambda/2] = \frac{1}{2}\begin{bmatrix} (1+e^{-i\delta}) & (1-e^{-i\delta}) \\ (1-e^{-i\delta}) & (1+e^{-i\delta}) \end{bmatrix}$$

where δ=δ_1+δ_2 is the retardance of the wave plate measured experimentally as described previously. Figure 5.17 provides the values of $\delta_1+\delta_2$ obtained experimentally from the results shown in figure 5.15. The polarising beam cube is described by the matrix:

$$\text{Polariser} = [POL] = \begin{bmatrix} 0 & 0 \\ 0 & 1 \end{bmatrix}$$

Hence the matrix derived for a round-trip of the high-Q laser cavity is:

$$\begin{bmatrix} 0 & 0 \\ 0 & \begin{array}{l}(\frac{1}{2}-\frac{i}{2})((\frac{1}{4}+\frac{i}{4})(1-e^{-i\delta})+(\frac{1}{4}-\frac{i}{4})(1+e^{-i\delta})) \\ +(\frac{1}{2}+\frac{i}{2})((\frac{1}{4}-\frac{i}{4})(1-e^{-i\delta})+(\frac{1}{4}+\frac{i}{4})(1+e^{-i\delta})\end{array} \end{bmatrix} \tag{5.6}$$

Now in order to determine the intensity after one round-trip through this system the matrix in equation 5.6 must be multiplied by its complex transpose, the row matrix. For an ideal half-wave plate this yields the following:

$$\begin{bmatrix} 0 & 0 \\ 0 & 1 \end{bmatrix}$$

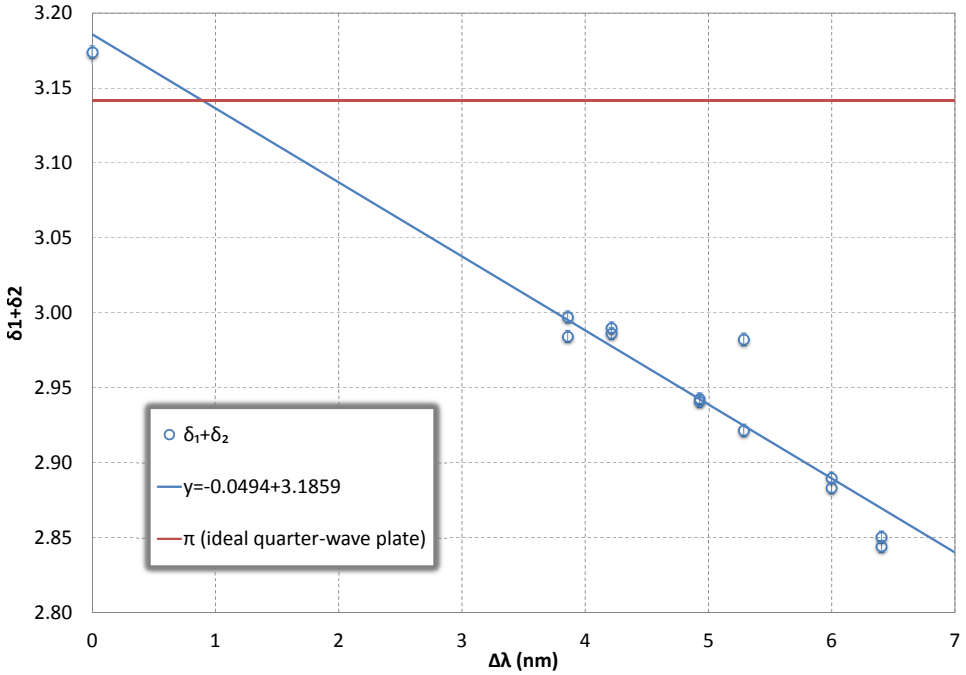

(a) High order quarter-wave plate

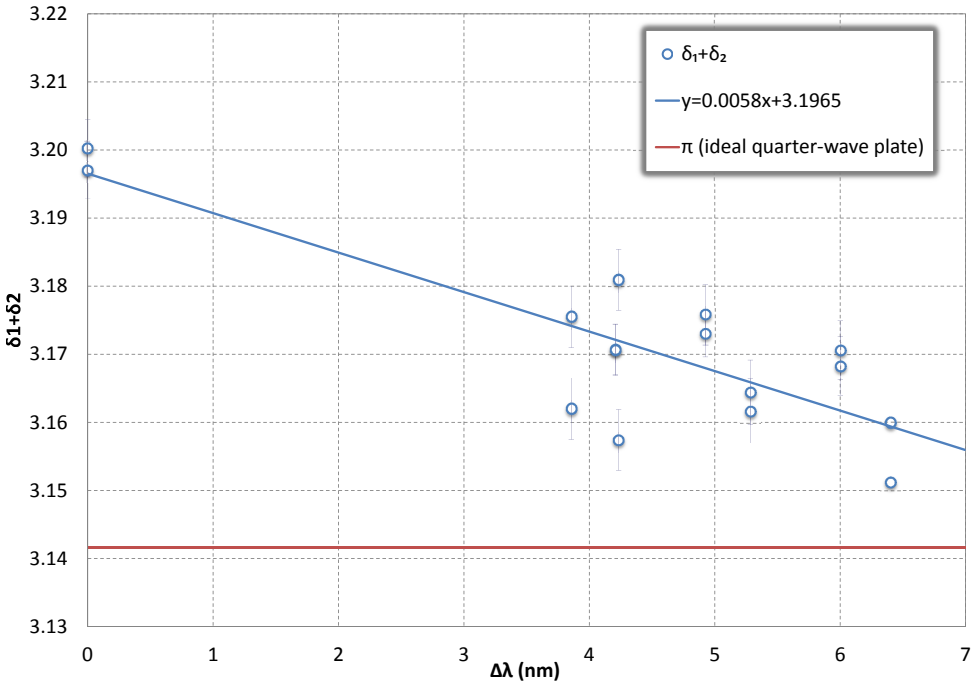

(b) Low order quarter-wave plate

Figure 5.17: The combined δ values for the high and low order quarter-wave plates. A reference line is drawn at a value π, which is the value corresponding to a double-pass through an ideal quarter-wave plate showing no wavelength dependence.

where the intensity is normalised. So for an ideal system the intensity is at a maximum after a round-trip. Having established the output intensity, the loss can be calculated simply using the relationship loss = (1-output intensity). Based on the measurements of δ_1 and δ_2 *Mathematica* was used to compute the resulting intensity.

The loss of each wave plate is shown as a function of the wavelength in figure 5.18. The difference in the loss due to each wave plate becomes more apparent as the idler wavelength is increased. For the case of the new 40mm-long PPLN crystal, the additional loss experienced by the collinear idler is only around 0.5% per round-trip of the cavity but for the other PPLN crystals being studied this figure will rise to the region of (1-3)% per round-trip, taking the total loss of the collinear idler cavity to a level of between ≈25.5% and ≈29% depending on the idler wavelength.

Figure 5.18: The calculated loss due to each of the wave plates, based on experimental results. The zero-order wave plate exhibits the lower loss over the range of idler wavelengths and so is more desirable for use in systems where the idler propagates collinearly with the pump.

5.5 PPLN in a hybrid phase-matching system

5.5.1 Introduction and motivation

Based on the outcomes of the experiments involving the use of PPLN in a collinear phase-matching geometry it was decided to implement a hybrid non-collinear phase-matching system. The benefits of such a scheme would be two-fold:

Firstly, the high loss of the common pump and idler cavity as well as the additional length of the idler cavity would be obviated. The intersecting idler cavity parasitic loss has been measured as ≈18% - almost 10% less than the parasitic loss of the idler cavity in the collinear setup - and the effect of cavity length on the OPO threshold has also been demonstrated previously (see chapter 2). Secondly, the successful implementation of a hybrid non-collinear phase-matching scheme would allow the output of the PPLN to be tuned, something which is not possible in the collinear phase-matching system other than by controlling the temperature of the PPLN crystal, which in itself would only provide a tuning range of ≈30GHz when the temperature is changed by ≈100°C. This section describes the experimental steps taken towards the realisation of a hybrid non-collinear phase-matching scheme using the same 40mm PPLN crystal that has been characterised in the earlier parts of this chapter.

5.5.2 Experimental setup

The experimental configuration adopted for the hybrid phase-matching scheme is shown in figure 5.19 and is essentially the same as was used for the basic non-collinear phase-matching system. The pump cavity is ≈38cm in length and is formed by mirrors M1 and M2, which are >98% reflecting and 98% reflecting at 1064nm, respectively. The lens, L, has a focal length of 1m and serves to prevent changes in the beam size occurring due to the influence of thermal lensing (see chapter 2). A quarter-wave plate, Pockels cell and air-spaced polarising beam cube make up the electro-optic Q-switch. The idler cavity is

formed by the three mirrors M3-M5, which are 90% reflecting, highly reflecting at 45° and highly reflecting respectively; the idler cavity length is ≈13cm - almost half the length of the collinear idler cavity utilised in the collinear phase-matching system. The nonlinear material used was either the 40mm piece of PPLN characterised previously, or a 30mm or 70mm piece of MgO:$LiNbO_3$ used for purposes of comparison.

5.5.3 Choice of terahertz frequency

In order to maximise the likelihood of realising the hybrid configuration with the PPLN crystal, a 70mm-long bulk MgO:$LiNbO_3$ crystal was first placed inside the intersecting pump and idler cavities. The OPO threshold was then characterised as a function of idler wavelength to identify the most suitable operating point for the PPLN in terms of finding the point of minimum threshold, hence minimising the likelihood of damage occurring when operating above threshold. The idler wavelength found to exhibit the lowest threshold was measured through the output of mirror M3 using an optical spectrum analyser to be 1073.16nm, corresponding to a terahertz frequency of 2.3THz. Incorporating a mirror with a large radius of curvature (6m) was found to further reduce the threshold of the OPO by ≈1MWmm^{-2} pump intensity over an idler cavity constructed solely of plane mirrors, as shown in figure 5.20. The energy characteristic and temporal profiles of the pump and idler were then re-measured, this time utilising a 30mm MgO:$LiNbO_3$ crystal so that the gain-length product was more analogous to that for the PPLN crystal, allowing a more direct comparison to be made between the two materials. Figure 5.21 shows this energy and temporal data. The idler pulse is seen to build up at the peak of the pump pulse where the energy available for

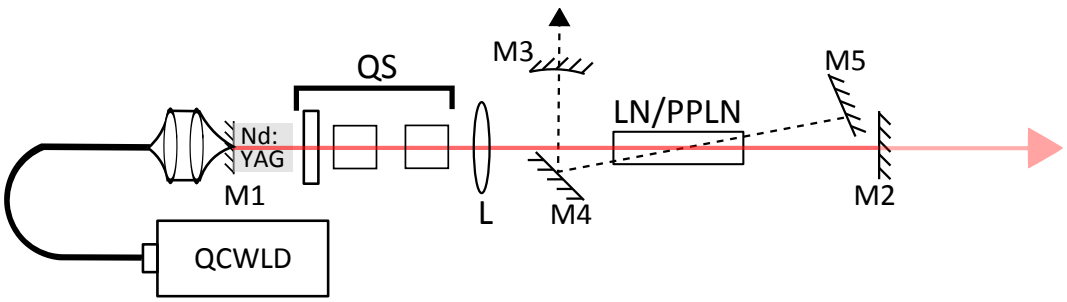

Figure 5.19: Experimental setup of the PPLN hybrid phase-matching OPO.

down-conversion is maximised.

5.5.4 Determination of phase-matching angles

Having decided on the optimal idler wavelength for the hybrid phase-matching experiment it was then necessary to establish what angular separation of the pump and idler would be required to produce that idler wavelength using the PPLN crystal, since the grating vector changes the angular separation with respect to that for the bulk material. One of the *Mathematica* programs described in chapter 4 was used to do this, with the results summarised below.

Figure 5.22 identifies the angular separations of the pump and idler that satisfy the phase-matching equations for the generation of 2.3THz due to both grating directions. For each solution at 2.3THz there is a competing frequency that could be generated due to the grating vector pointing in the opposite direction. The solution that will dominate will be that which has the greater overlap between all three interacting fields, so each case must be examined to determine where the

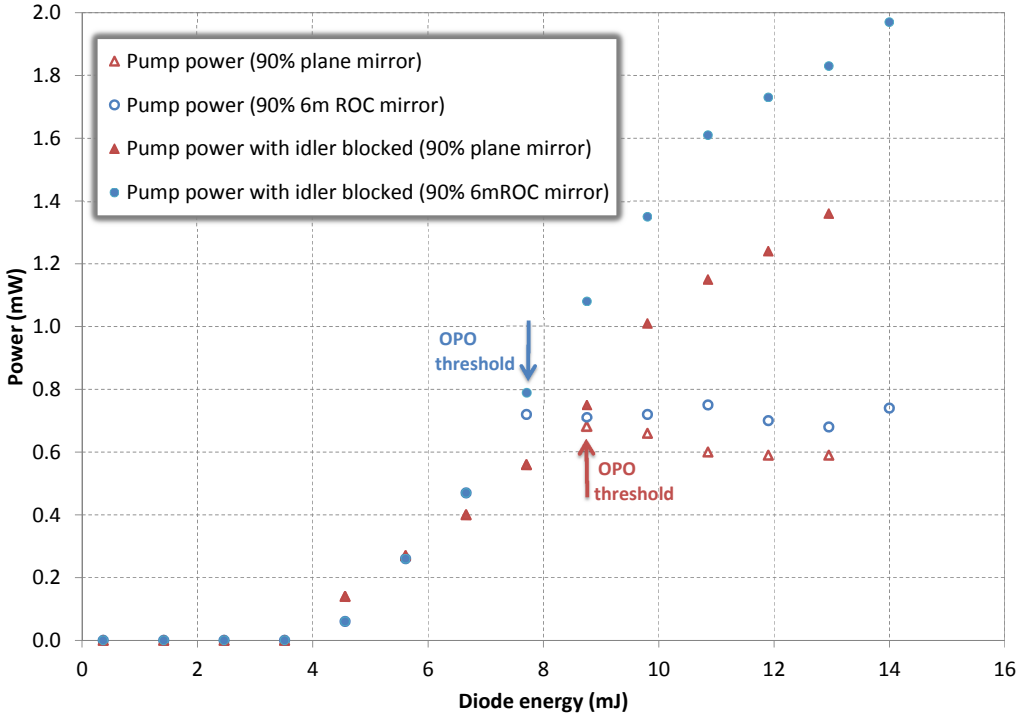

Figure 5.20: The threshold of the OPO is reduced by introducing a small amount of curvature to the output coupler of the idler cavity.

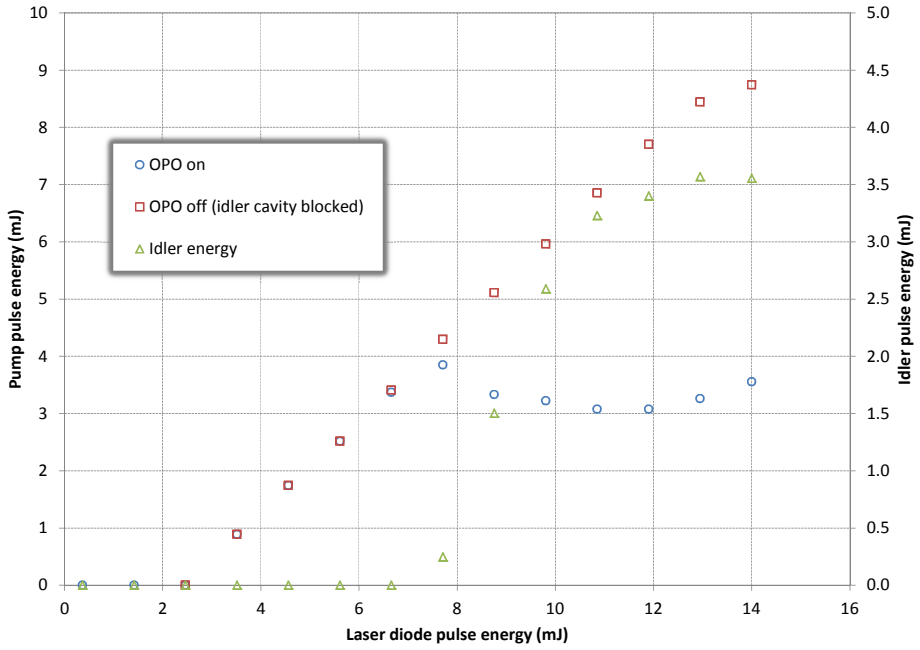

(a) The energy characteristic of the OPO. The OPO threshold corresponds to ≈6.6mJ of laser diode pulse energy and reaches depletion levels of 56%.

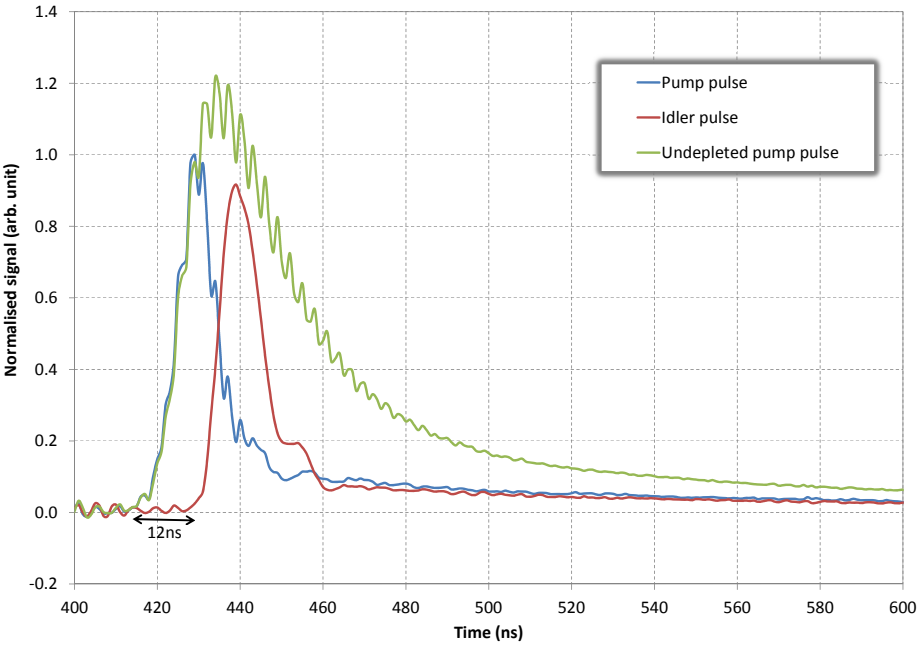

(b) The temporal profiles of the pump and idler pulses corresponding to a diode pulse energy of ≈12mJ. The time delay between the build up of the pump and idler pulses is around 12ns under these operating conditions.

Figure 5.21: The energy characteristic of the OPO and temporal profiles of the pump and idler pulses corresponding to a diode pulse energy of ≈12mJ.

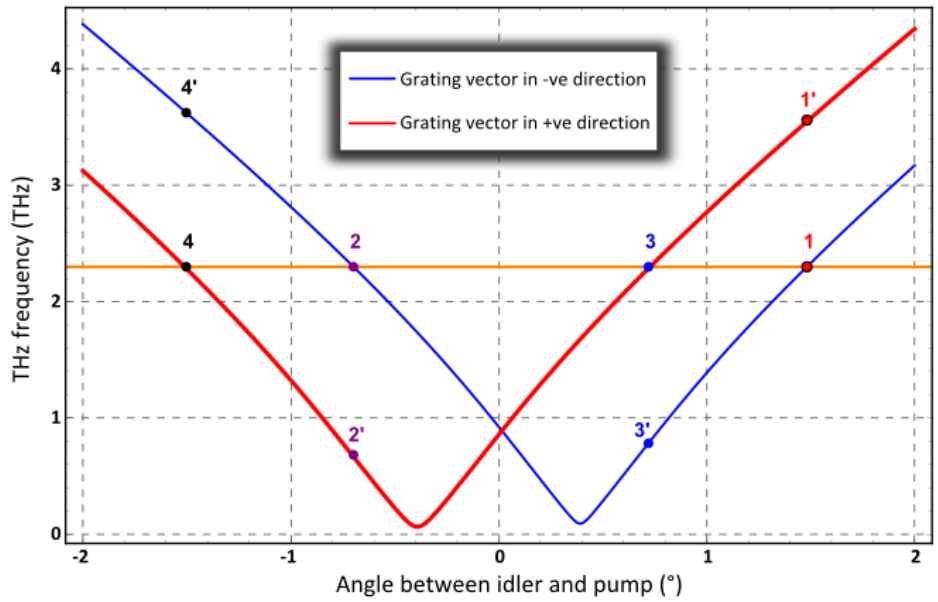

Figure 5.22: The angles satisfying the phase-matching solutions for the generation of 2.3THz for a PPLN crystal with a grating angle of 86.5°.

2.3THz solution is most likely to be observed. It should be noted that although four independent solutions are identified using the program, in fact only two of these must be considered due to the positioning of the idler cavity mirrors, which precludes those solutions for which the angle is defined as being negative.

Examining the competing solutions identified in table 5.3 it can be seen that the dominant solutions are 1 and 3′, due to these exhibiting the greater degree of overlap (the terahertz angle is specified relative to the pump beam, which also

Solution number	THz frequency (THz)	Idler wavelength (nm)	External angular separation (°)	THz angle (°)
1	2.30	1072.75	1.48	-64.66
1’	3.56	1077.61	1.48	-68.81
3	2.30	1072.75	0.72	-67.94
3’	0.78	1066.96	0.72	-60.11

Table 5.3: The angular separations and idler wavelengths satisfying the phase-matching conditions required for the generation of 2.3THz radiation, along with the alternative frequencies arising from the opposite grating direction.

defines the optic axis). Of these, only solution 1 produces a frequency of 2.3THz. The next step was to translate the angular separation of the pump and idler for the PPLN into a corresponding terahertz frequency and idler wavelength for the bulk material. This would allow the alignment of the idler cavity to be completed with a MgO:$LiNbO_3$ crystal present in the cavity before replacing it with the PPLN crystal. The phase-matching angle ϕ can be calculated using the cosine rule as follows:

$$k_T^2 = k_i^2 + k_{i2}^2 - 2k_i k_{i2}\cos\phi$$

where k_i is given by

$$k_{i2} = k_p - \frac{n_0}{n_T}k_T$$

Hence substituting for k_i we have

$$k_T^2 = 2k_p^2 + \frac{2n_0}{n_T}k_T^2 - 2\frac{n_0}{n_T} - 2k_p^2\cos\delta + 2k_p\frac{n_0}{n_T}k_T\cos\phi$$

and by rearranging for $\cos\phi$

$$\cos\phi = \frac{k_p^2 - 2\frac{n_0}{n_T}k_T k_p + \frac{n_0^2}{n_T^2}k_T^2 + k_p^2 - k_T^2}{2(k_p - \frac{n_0}{n_T}k_T)k_p}$$

which can simplified to yield the final expression

$$\cos\phi = \frac{k_p - \frac{n_0}{n_T}k_T}{2k_p} + \frac{k_p^2 - k_T^2}{2(k_p - \frac{n_0}{n_T}k_T)k_p} \tag{5.7}$$

Figure 5.23 shows the above relationship graphically for the frequency range (0.5-3)THz.

5.5.5 Operational characteristics of non-collinear system using bulk material

Having identified the most suitable value of ϕ for the hybrid phase-matching experiment (an internal phase-matching angle of 0.7°, or 1.48° externally), the relationship between the angle and the resulting terahertz and idler wavelength combination was used to establish that the terahertz OPO based on bulk

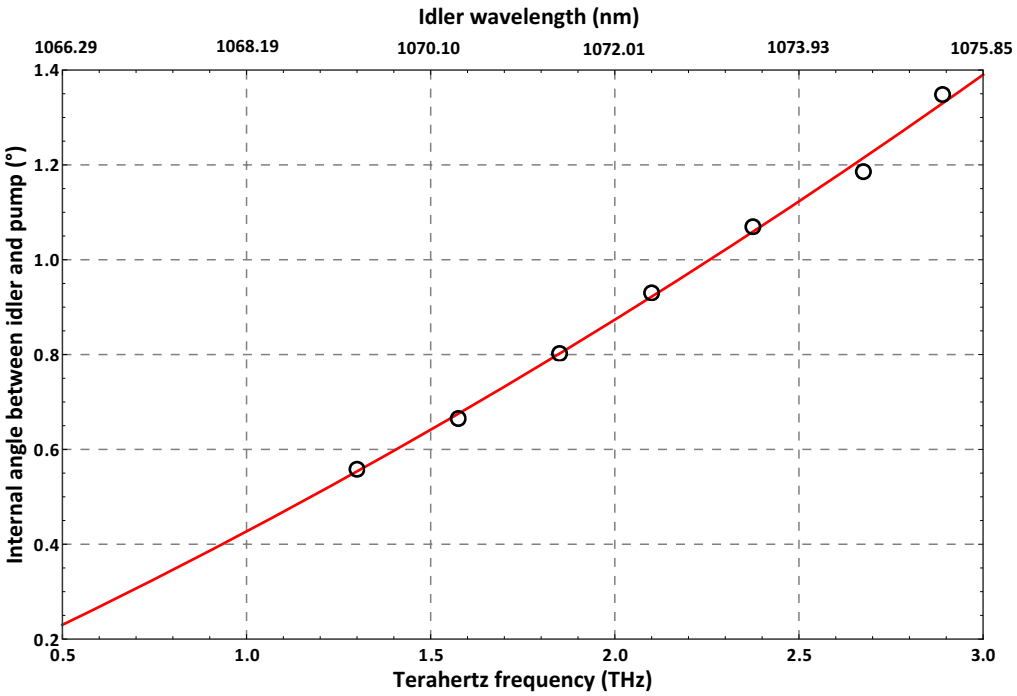

Figure 5.23: Tuning of the intracavity THz OPO with idler cavity angle (specified inside the crystal) when using a bulk $LiNbO_3$ crystal in a non-collinear phase-matching arrangement.

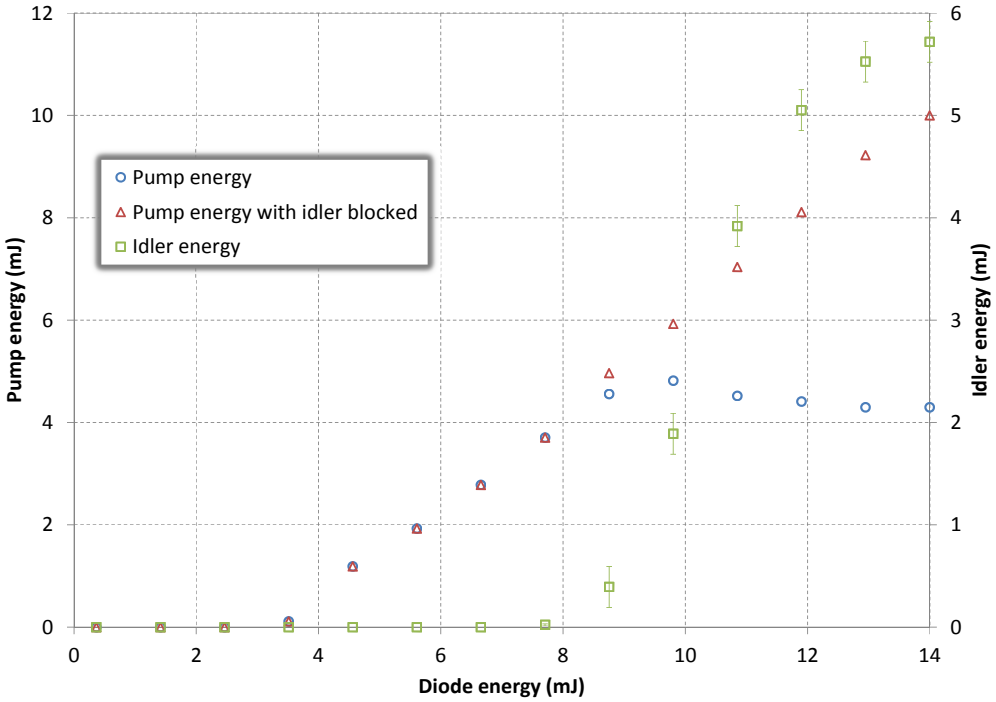

Figure 5.24: The measured energies at the pump and idler wavelengths as a function of the diode pump energy for the 30mm-long bulk material.

MgO:$LiNbO_3$ should be tuned to a wavelength of approximately 1070.47nm to ensure the idler cavity was at the correct angle to produce 2.3THz with the PPLN crystal in the same idler cavity. Figure 5.24 provides details of the energy characteristic for the bulk material in a 13cm-long idler cavity for which the output coupler is a 90% reflecting mirror having a radius of curvature of 6m. The amount of down-conversion of the pump is not as great as for the 2.3THz operating point (figure 5.20), due primarily to the change in idler wavelength. The pump power was recorded for comparison with the output power from the PPLN crystal, so that the gain in each case could be assessed.

5.5.6 Outcome of PPLN experiments

With the PPLN crystal in place the same output power was measured as corresponded to the MgO:$LiNbO_3$ threshold point for the same cavity setup (1.03mW in the pump at 60A drive current), however no flashes of downconversion - usually observed intermittently when the OPO is just below threshold - were visible. Examining the exponential gain present in each of the systems makes clear the reason why this was case:

For the 30mm MgO:$LiNbO_3$ crystal, the pump power at OPO threshold was measured to be 1.03mW and the pulse duration (FWHM) at that point was 30ns. Taking the pump beam radius to be ≈0.57mm the intracavity intensity is $1.2458\times10^{11}\mathrm{Wm}^{-2}$. From the Kawase terahertz absorption data [8], the absorption coefficient at 1.6THz in the range (27.6-32.6)cm^{-1}. Using the absorption length gain analysis (see chapter 2) yields a total gain of between 131dB and 154dB, clearly satisfying the accepted 140dB requirement to reach threshold [9]. Examining the case for the PPLN crystal, which is 10mm longer than the MgO:$LiNbO_3$ crystal, and accepting that the intracavity intensity is unchanged it is found that the exponential gain at 2.3THz is now reduced to between 30dB and 40dB, a consequence of the reduced effective nonlinear coefficient and the increased terahertz absorption coefficient, which now takes a value of (60-80)cm^{-1}. For the gain to equal that for the bulk material the intracavity intensity would have to be more than four times that which was measured!

Although no evidence of non-collinear idler generation was seen, the device maintained its collinear operation throughout the course of the experiments. This is most likely due to the fact that despite the collinear idler cavity being almost three times the length of the off-axis cavity, the terahertz absorption coefficient at 0.9THz is only (8.3-17.1)cm^{-1}. This means that the calculated exponential gain in this case is between 46dB and 91dB, significantly higher than for the non-collinear configuration.

5.6 Conclusions

The collinear PPLN-based terahertz OPO has been implemented and extensively characterised in this chapter. The generated idler and terahertz frequencies are in excellent agreement with those predicted using the *Mathematica* modelling code developed for the purpose of crystal design. However, despite the increased interaction between the pump, idler and terahertz fields as a result of the collinearisation of the pump and idler the OPO was not able to be brought very far above threshold and the downconversion efficiency was poor in comparison to the non-collinear OPOs.

A significant set-back in the use of the newly-designed PPLN crystal was the early onset of damage. The coatings were applied by the crystal manufacturer rather than by a specialist coating company. It may be that higher pump intensities could be reached if the PPLN were to be re-coated with more robust coatings; this option is being actively investigated at the time of writing.

The increased idler cavity length and losses have also hampered the performance of the PPLN OPO. If the cavity could be made shorter then the OPO threshold would be reduced. Shortening of the cavity could be achieved by using mirrors that are transmitting at the pump wavelength and reflecting at the idler wavelength to form an idler cavity within the existing pump cavity but still maintaining the condition of collinearity between the pump and idler waves; Minamide et al. have demonstrated an extracavity terahertz OPO using this approach [10]. A pair of filters (Semrock, “MaxLine LL01-1064-12.5”) having a

suitably rapid transition between ≈95% transmission at 1064nm and ≈0.5% transmission at 1068nm were purchased to attempt to replicate such a system in the context of our intracavity OPO, however the damage threshold of the filters was too low so that damage was encountered before the onset of idler generation. The production of filters having a high enough damage threshold for intracavity use was too prohibitively expensive to be pursued further.

Attempts were made to realise the novel, hybrid non-collinear scheme that was identified in chapter 4. As a result of the collinearisation of the pump and idler waves, the collinear idler cavity is ≈10% lossier than the idler cavity in the non-collinear phase-matching system. The higher loss and increased round-trip time create a reduction in the parametric gain, so the possibility of being able to overcome the collinear phase-matching process using a non-collinear idler cavity seemed plausible. To date, no evidence of a non-collinear process has been observed, but the configuration could be further optimised in terms of the phase-matching angle idler cavity length to maximise the likelihood of a non-collinear process being brought above threshold.

References

[1] D. A. Walsh, P. G. Browne, M. H. Dunn, and C. F. Rae. Intracavity parametric generation of nanosecond terahertz radiation using quasi-phase-matching. *Optics Express*, 18(13):13951–13963, Jun 2010.

[2] M. Dunn, B. Sinclair, P. Lindsay, and A. Gillies. Photonics simulation software for teaching (psst!). http://www.st-andrews.ac.uk/~psst/ (accessed 17/02/2012).

[3] E. D. Palik. *Handbook of Optical Constants of Solids*. Academic Press Inc. London, 1985.

[4] L. Pálfalvi, J. Hebling, J. Kuhl, A. Péter, and K. Polgár. Temperature dependence of the absorption and refraction of Mg-doped congruent and stoichiometric $LiNbO_3$ in the THz range. *J. Appl. Phys.*, 97:123505, 2005.

[5] D. A. Walsh. *Intracavity Terahertz Optical Parametric Oscillators*. PhD thesis, University of St Andrews, 2010.

[6] H. Kogelnik and T. Li. Laser beams and resonators. *Applied Optics*, 5:1550–1567, 1966.

[7] A. Gerrard and J. M. Burch. *Introduction to matrix methods in optics*. Wiley-Interscience, 1975.

[8] I. Shoji, T. Kondo, A. Kitamoto, M. Shirane, and R. Ito. Absolute scale of second-order nonlinear-optical coefficients. *J. Opt. Soc. Am. B*, 14(9):2268–2294, Sep 1997.

[9] S. Brosnan and R. Byer. Optical parametric oscillator threshold and linewidth studies. 15(6):415–431, 1979.

[10] H. Minamide, T. Ikari, and H. Ito. Tunable quasi-monolithic THz-wave parametric oscillator in a ring-cavity configuration. In *Proc. Joint 31st Int. Conf. Infrared Millimeter Waves and 14th Int. Conf. Teraherz Electronics IRMMW-THz 2006*, 2006.

6

Injection seeding in bulk $LiNbO_3$ and PPLN systems

6.1 Introduction

This chapter presents the results of a series of experiments which sought to investigate the potential of injection seeding to bring the PPLN devices discussed in earlier chapters above threshold more readily and hence to improve down-conversion efficiency. Particular successes were realised through the use of injection seeding in the non-collinear phase-matching scheme making use of the bulk material and in a collinear phase-matching scheme utilising a pre-existing PPLN crystal with an orthogonal grating; the performance of the collinear phase-matched PPLN OPO was improved to the extent that depletion was observed on the temporal profile of the pump pulse - previously the parametric process had been too weak for this to be evident. Attempts were also made to use the seed laser to switch the idler and terahertz wavelengths generated using a non-orthogonal grating crystal by using the seed laser to bring the alternative collinear idler wavelength above threshold more quickly than that usually observed. Due to unforeseen complications arising from uncertainties in the expected terahertz wavelengths as well as a relatively complicated detection system this was unfortunately unable to be realised at this time.

The experimental strategy behind the results presented in this chapter is as

follows:

Firstly the benefit of injection seeding was assessed in terms of its effect in the bulk, non-collinear phase-matching system. This system was deemed to be an ideal test-bed for injection seeding due to it having been extensively characterised and owing to its robust and reproducible nature (see chapter 2).

Secondly, the potential of a hybrid non-collinear phase-matching scheme was explored. The possibility of this novel phase-matching geometry and its benefits (in terms of adding tunability to the PPLN system and increasing the overall tuning range of the non-collinear system) have been described in previous chapters (4 and 5). The motivation was to use injection seeding to overcome the collinear phase-matching process, which had persisted in the previous attempts to realise the hybrid non-collinear phase-matching geometry (see chapter 5).

Finally, given that collinear phase-matching schemes had proved successful with regard to the excellent agreement between the modelling procedure (chapter 4) and the measured spectral output of the devices (see chapter 5) it was highly desirable to attempt to improve the down-conversion efficiency of these devices in order to make them more practicable by employing the technique of injection seeding.

A discussion of the effect of the seed laser on the gain, both at and above threshold, will be made in relation to the experimental observations. In that vein the use of injection seeding has provided great insight into the capabilities and limitations of PPLN-based terahertz OPOs and points the way to where improvements might be made to increase the viability of these systems. At the time of writing this thesis these results are also being prepared for publication.

Injection seeding is a technique that has been widely used to achieve high spectral purity in a range of OPOs [1–3]. The use of injection seeding to produce a nearly transform-limited linewidth terahertz OPO was investigated by a colleague, Dr David Walsh [4]; a similar study was carried out by Imai and colleagues at RIKEN

for an extra-cavity terahertz OPO [5]. Despite the well-known benefits of injection seeding on the spectral quality of the OPO output, it seems that the impact of injection seeding upon the OPO threshold has gone uncharacterised prior to the work presented here.

6.1.1 The seed laser

The laser used for the purpose of injection seeding was a Toptica Photonics DL100 external cavity diode laser (ECDL) in Littrow configuration. The diode was centred at 1072nm and rated to provide up to 180mW of single mode output, of which ≈70mW could be coupled out of the ECDL. The linewidth of the output was <1MHz and the wavelength could be tuned over the range (1066-1081)nm.

The interplay between several factors determines the single mode frequency that is emitted by the ECDL:

1. The broad (≈5000GHz wide) gain bandwidth of the semiconductor gain medium.
2. The internal resonator mode structure (≈64GHz spacing), which is defined by the optical length of the laser diode cavity.
3. The external resonator mode structure (≈9GHz spacing), defined by the distance from the diode rear mirror to the grating.
4. The grating profile (≈50GHz wide), which is shifted by altering the grating angle.

Coarse tuning of the output frequency was effected by changing the angle of the Littrow grating to select a range within the range defined by both the broad gain bandwidth of the semiconductor gain medium and by the modes supported by the cavity formed between the diode's back facet and the feedback elements. In practice this is achieved via a screw, as shown in figure 6.1. Fine tuning of the single mode frequency was achieved using a piezo actuator to control the grating angle. Since a change of the grating angle is accompanied by a change in the length of the external resonator, a ramp must be applied to the laser diode current to suppress mode-hops by changing the length of the internal resonator.

Through careful initial setup of the operating temperature, drive current and piezo actuator scan range, mode-hop-free tuning ranges of >3GHz were obtained.

6.2 Investigations into seeding in the non-collinear phase-matching system with the bulk material

6.2.1 The system under consideration

The non-collinear phase-matched intracavity terahertz OPO based on bulk MgO:$LiNbO_3$ is robust and well-characterised (see chapters 2 and 5) so it was an ideal test system in which to trial injection seeding in terms of its ability to reduce OPO threshold and improve the down-conversion efficiency. A similar intracavity terahertz OPO had already been used to demonstrate the benefits of injection seeding in terms of narrowing the linewidth of the source [4].

For injection seeding to be successful it is necessary that the seed laser path is exactly collinear with the existing idler path. The system of optics used to couple the seed laser into the off-axis idler cavity is shown schematically in figure 6.2. As described previously the pump laser comprised a Nd:YAG crystal, one end of

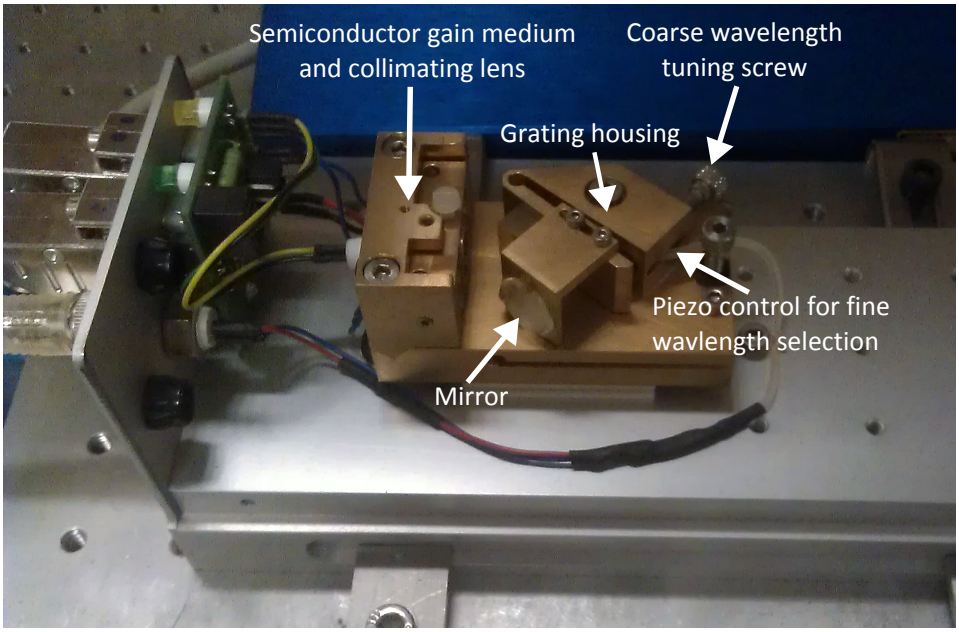

Figure 6.1: Annotated photograph of the ECDL100, indicating its salient features.

which was coated to be a high reflector (HR) so as to act as a mirror, M1, for the pump laser cavity; M2, a mirror of 98% reflectivity to allow monitoring of the pump wave; and the Q-switching components - a zero-order quarter-wave plate, Pockels cell and beam cube polariser. The nonlinear medium (LN) was a 30mm MgO:$LiNbO_3$ crystal. The intersecting idler cavity was formed by mirrors M3, a 98% reflector with radius of curvature of 5m; M4, a high reflector at 45°; and M5, a 70%-reflecting plane mirror, chosen to allow radiation from the seed laser to be coupled into the idler cavity. M3 was chosen to be partially transmitting to allow the observation of the power transmitted through the idler cavity as the seed laser wavelength was tuned over a frequency range of approximately 2GHz. A Fabry-Pérot interferometer (FP) was used to monitor the mode-hop-free tuning range of the seed laser. M6-M9 were all high reflectors at 45° and were used to steer the seed laser beam into the idler cavity.

The OPO having been tuned to produce an idler wavelength of 1070.5nm (previously identified as the wavelength of lowest threshold), its path was defined by a series of apertures to allow the seed laser to be directed back along the same path. The seed laser light was first passed through a 60dB optical isolator (ISO) and an anamorphic prism pair (APP) for ellipticity correction before being sent along the path of the idler beam by a series of HR at 45° mirrors (M6-M9).

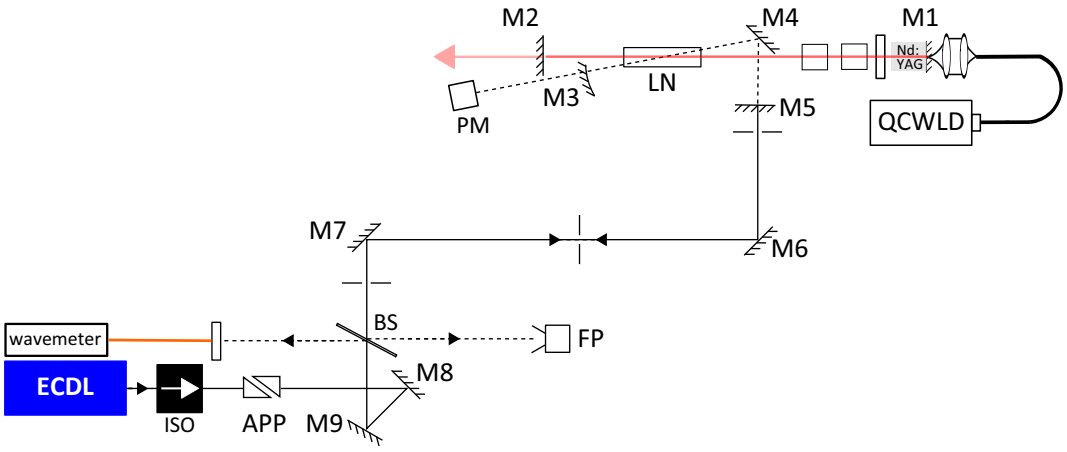

Figure 6.2: Seed laser coupling optics.

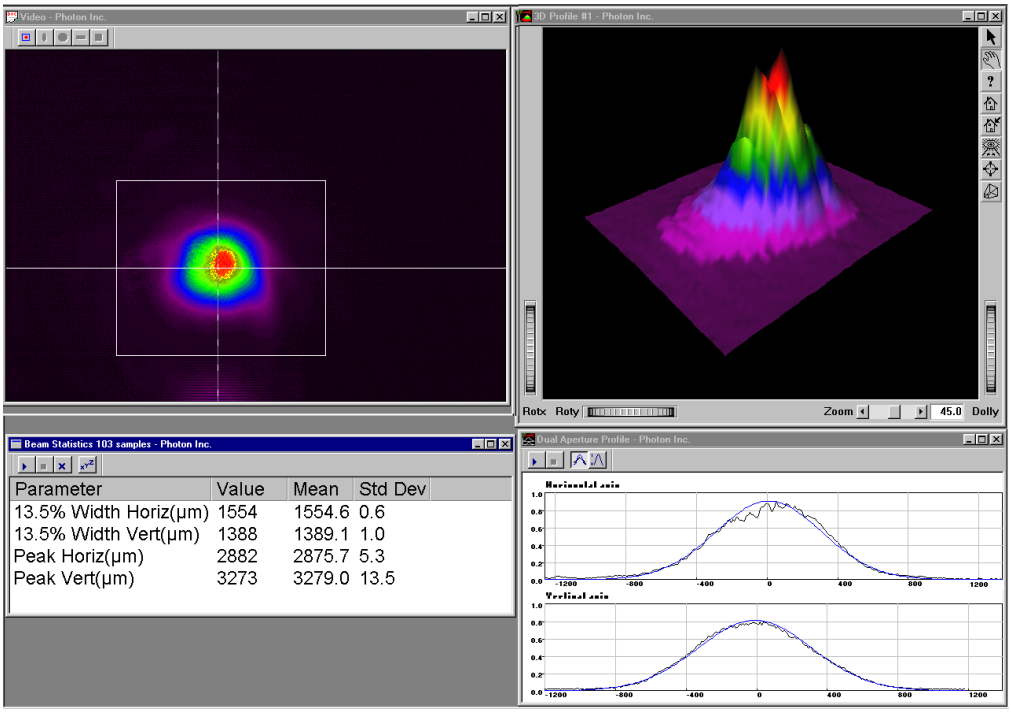

Parameter	Value	Mean	Std Dev
13.5% Width Horiz(µm)	1554	1554.6	0.6
13.5% Width Vert(µm)	1388	1389.1	1.0
Peak Horiz(µm)	2882	2875.7	5.3
Peak Vert(µm)	3273	3279.0	13.5

(a) The seed laser beam profile measured ≈18cm from the entrance to the idler cavity.

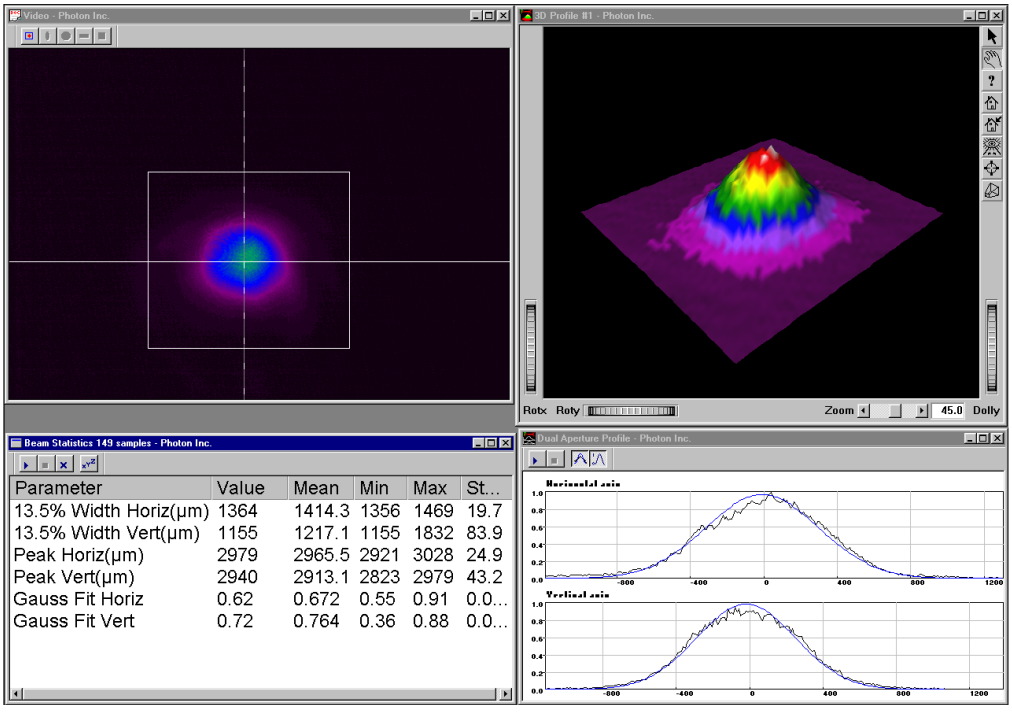

Parameter	Value	Mean	Min	Max	St...
13.5% Width Horiz(µm)	1364	1414.3	1356	1469	19.7
13.5% Width Vert(µm)	1155	1217.1	1155	1832	83.9
Peak Horiz(µm)	2979	2965.5	2921	3028	24.9
Peak Vert(µm)	2940	2913.1	2823	2979	43.2
Gauss Fit Horiz	0.62	0.672	0.55	0.91	0.0...
Gauss Fit Vert	0.72	0.764	0.36	0.88	0.0...

(b) The idler beam profile measured ≈18cm from the entrance to the idler cavity.

Figure 6.3: Comparison of the seed and idler beam widths at a fixed point outside the idler cavity.

It is important to ensure that the cavity mode being seeded is at the peak of the phase-matched gain curve since once the pulse enters the pump-depleted regime the modes that experience higher gain can overtake the seeded mode [1, 3]. An Angstron WL7 wavemeter [6] was used to measure the idler wavelength generated by the unseeded OPO. The seed laser was then tuned to match the generated wavelength and then fine-tuned to bring it on resonance with the cavity. Although for long-term use it would be necessary to employ a cavity locking technique such as the Pound-Drever-Hall method to maintain the resonance of the seed laser with an axial mode of the idler cavity, in this case such a scheme was omitted because the long-term operation of the OPO was not under consideration and the seed laser could be brought back on resonance easily by adjusting the piezo actuator.

The spatial characteristics of the seed laser and idler beams were measured using the BeamPRO CCD system and are shown in figure 6.3. The seed laser beam is very close to being circular and has a Gaussian intensity distribution. Measurements taken at several distances from the entry point to the off-axis idler cavity indicated that the beam was collimated and since the seed laser beam dimensions were very close to those of the idler beam a mode-matching lens was deemed superfluous.

6.2.2 Cavity enhancement factor

For the purpose of subsequent gain calculations it was necessary to know the magnitude of the circulating intensity due to the seed laser. On resonance, the power inside a Fabry-Perot cavity is related to the power incident on it by the following equation [7]:

$$\frac{P_{\text{internal}}}{P_{\text{incident}}} = \frac{T_1}{\left(1-(R_1R_2)^{\frac{1}{2}}\right)^2} = \frac{T_1}{\left(1-\sqrt{(1-A_1-T_1)(1-A_2)}\right)^2} \tag{6.1}$$

where T_i,R_i and A_i are the power transmission, reflection and loss coefficients of the input mirror (i=1) or the rear mirror (i=2). The transmission of the rear mirror (M3, equal to 2%) is included in the loss, A_2 and in the present case the parasitic loss of the idler cavity is also assigned to A_2 so that A_1=0. Figure 6.4 shows the power ratio calculated on the basis of a parasitic loss suitable to the idler cavity

currently under discussion, ≈23% so that including the transmission loss of the rear mirror, M3, A_2=25%. It can be seen that as expected the power ratio reaches a maximum when the transmission of the input mirror (T_1) equals the parasitic and output coupling losses of the rear mirror (A_2); this condition corresponds to impedance-matching, being such that when the cavity is on resonance there is zero net reflection of the seed radiation from the input mirror M5. The choice of 30% transmission for M5 is close to fulfilling the impedance-matching criterion.

The internal power in the idler cavity was quantified by measuring the power transmitted by the 98%-reflecting rear mirror (M3) of the idler cavity as a function of the seed laser wavelength. This was achieved by using LabVIEW to simultaneously capture data from a thermal power meter positioned so as to measure the idler output by the 98% reflector and data from the Angstrom wavemeter. The variation of the idler cavity transmission with seed laser wavelength is shown in figure 6.5. The power transmitted on resonance is ≈1.03mW, implying an intracavity power of ≈51.5mW. The power incident on the idler cavity was measured as ≈14mW, suggesting a power enhancement factor of 3.68, which is in reasonable agreement with the ratio expected from figure 6.4.

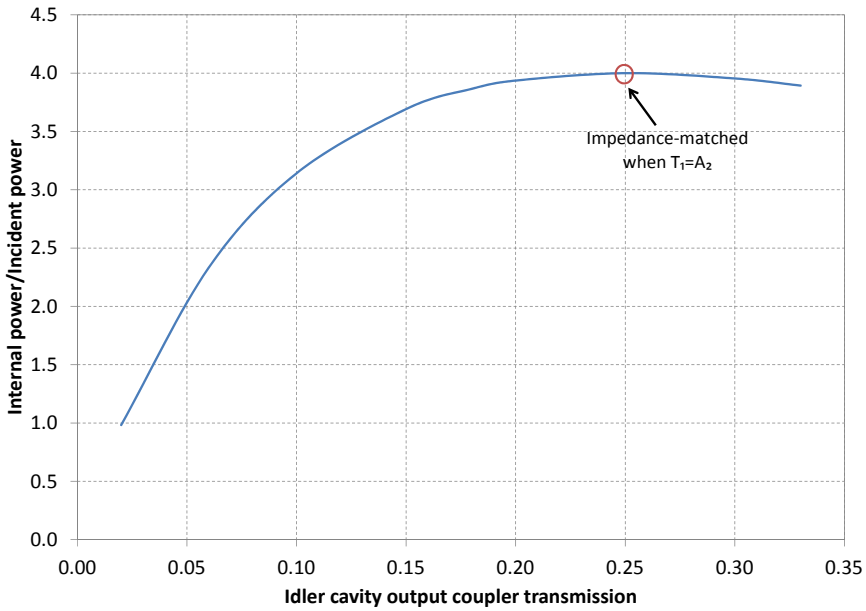

Figure 6.4: The variation of the power enhancement factor with the transmission of the input mirror of the intersecting idler cavity.

6.2.3 The change in threshold as a result of injection seeding

To quantify the effect that injection seeding had on the threshold of the OPO the pump intensity to reach threshold in both cases was measured. When the idler cavity was seeded with ≈68mW (18.6mW measured outside the idler cavity) the intracavity pump intensity required for the OPO to reach threshold was reduced from 20.6MWcm^{-2} to 16.2 MWcm^{-2}, as may be deduced from figure 6.6.

The pump and idler temporal profiles (which were acquired simultaneously) for the seeded and unseeded configurations, but with all other conditions held constant, are shown in figure 6.7. The intensities are ratioed to the pump in the unseeded configuration and for clarity the idler intensities are plotted on the secondary vertical axis. The Q-switch noise appears much larger in the idler traces because the OPO has only just exceeded threshold, so the intensity of the idler is very low. Figure 6.7b shows the effect of the seed laser when it is introduced at the original threshold point. In the case where the seed field is

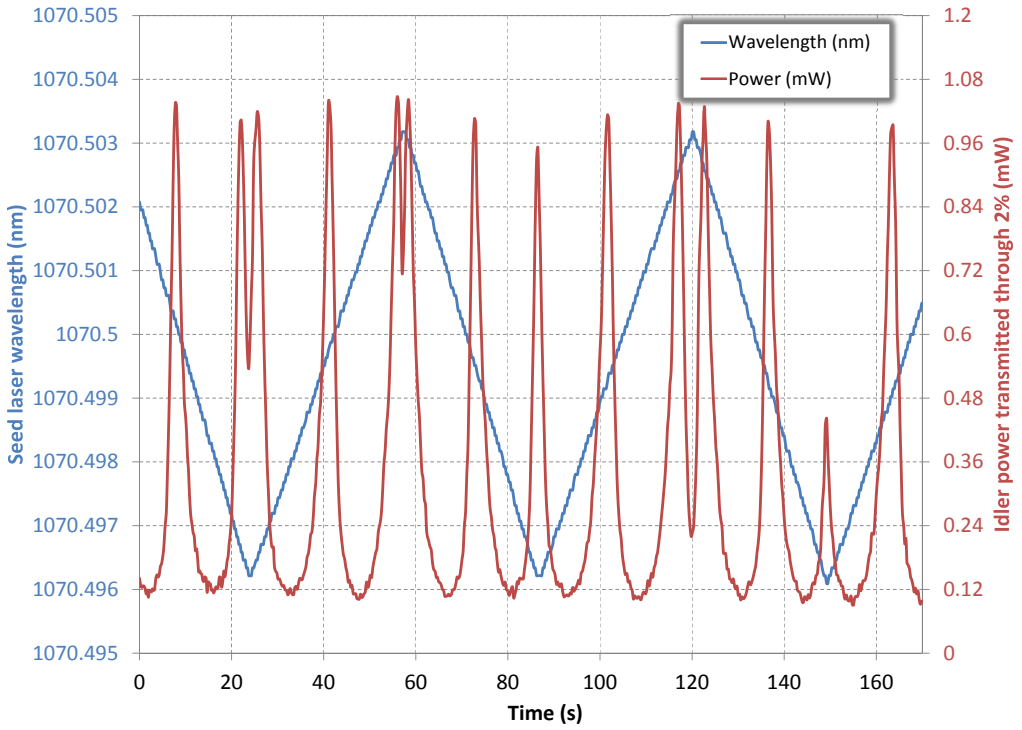

Figure 6.5: The measured variation in the transmission of the idler cavity as the seed laser was tuned on and off resonance.

present the amount of pump depletion is increased from a few percent (as seen in figure 6.7a) to ≈21%. With seeding the magnitude of the idler is ≈10 times what it is in the unseeded case; the seeded idler pulse also builds up ≈10ns earlier than does the unseeded idler.

6.2.4 Effect of seed when operating above threshold

At an intracavity pump intensity of 32.2MWcm^{-2} (a drive current of 70A), which corresponded to ≈1.56 times above threshold, the temporal profile of the pump and idler pulses were measured when the idler cavity was again seeded with ≈68mW of ≈1070.5nm radiation. The blue solid and dashed lines in figure 6.8 indicate the relevant temporal profiles. The seeding was then removed and the pump intensity was increased to the point that the idler achieved the same temporal profile as in the seeded case, indicated by the red solid and dotted lines in figure 6.8. The intracavity pump intensity had to be increased to 34.8MWcm^{-2} (a drive current of 71.5A) for the same idler amplitude to be produced, which corresponded to ≈1.69 times above threshold. This result is indicative that the seed laser provided a field equivalent to the difference in pump intensities, 2.6MWcm^{-2} in the range ≈1.6-1.7 times above threshold.

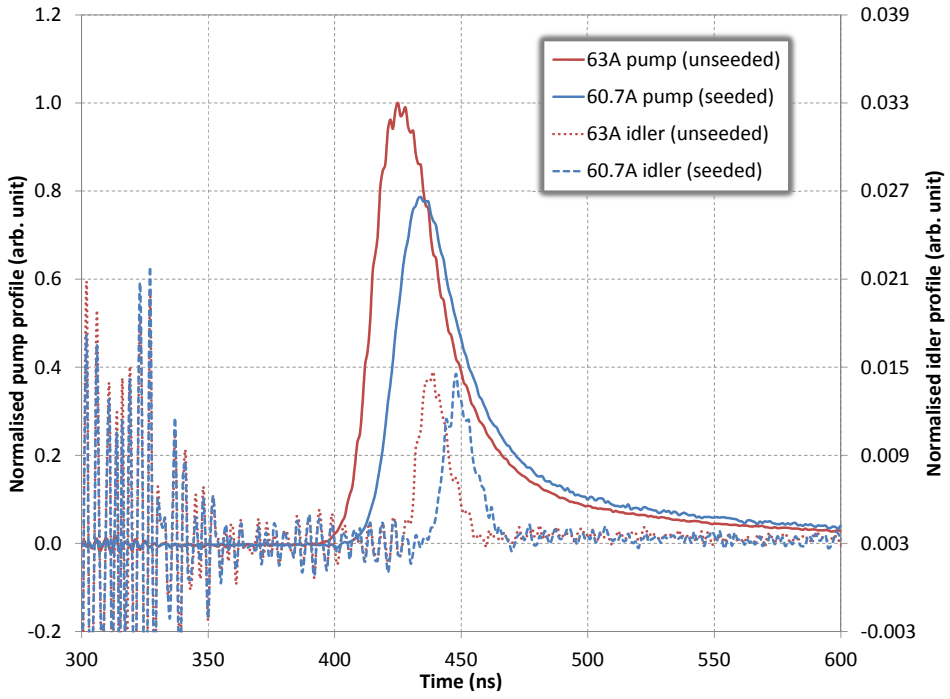

Figure 6.6: Pump and idler temporal profiles at OPO threshold with and without injection seeding.

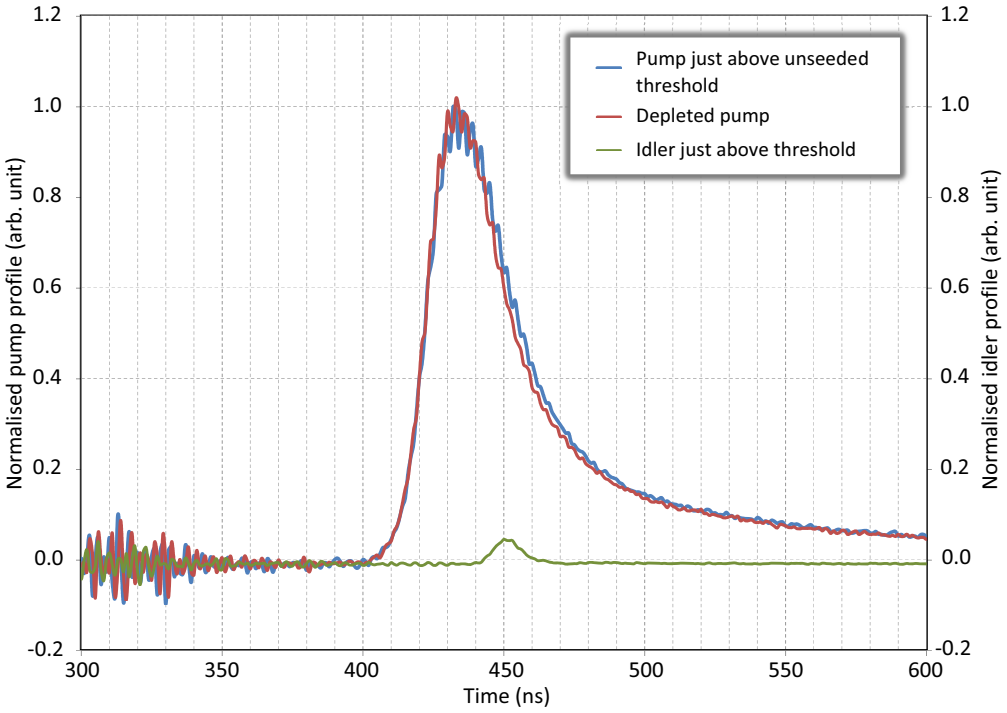

(a) Pump and idler temporal profiles just above OPO threshold without injection seeding.

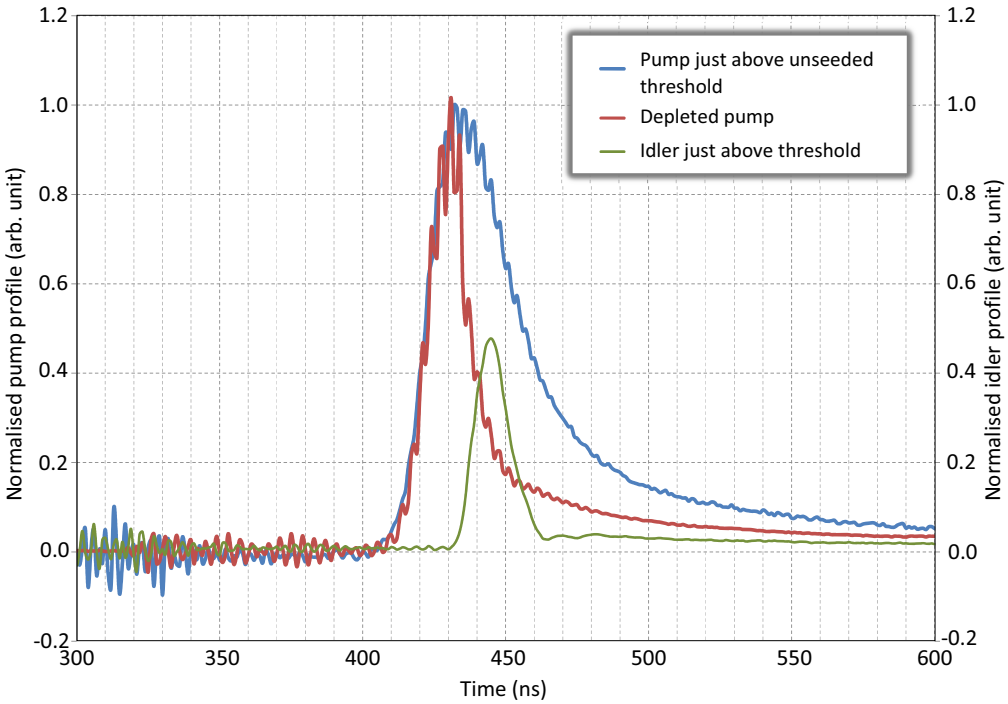

(b) Effect of injection seeding when operating at the same point as in figure 6.7a just above threshold.

Figure 6.7: Graphs showing the increased pump depletion due to the presence of the seed field.

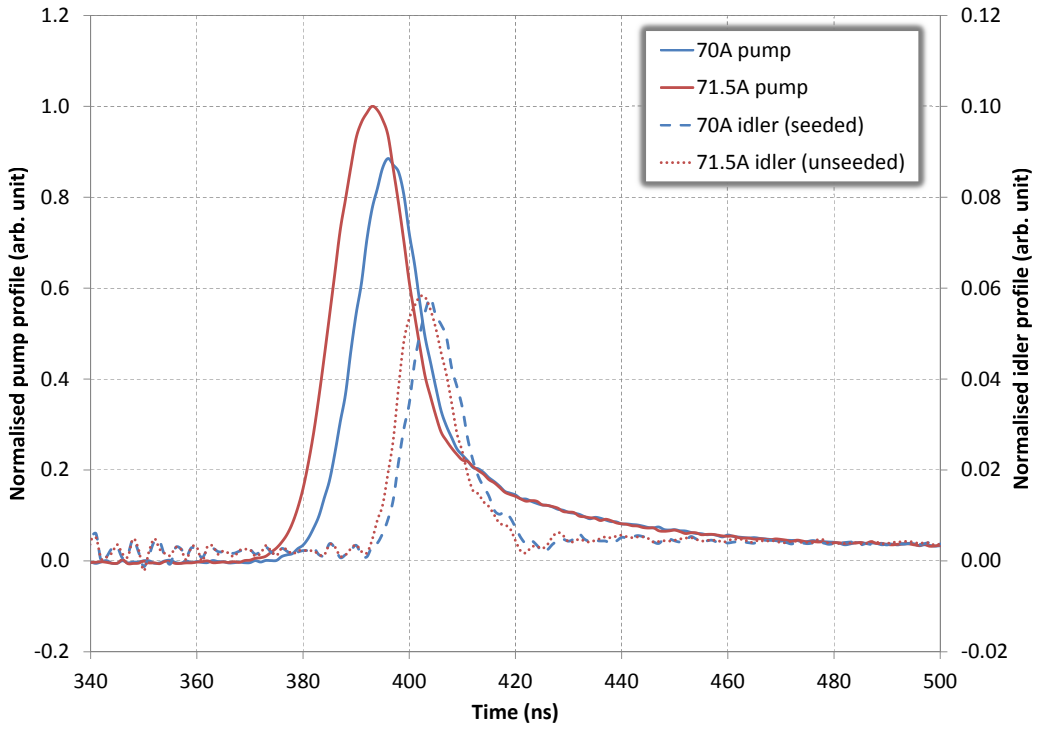

Figure 6.8: Pump and idler temporal profiles showing the difference between the pump profiles corresponding to the production of the same idler amplitude with and without seeding.

6.3 Injection seeding in a system utilising a PPLN crystal with orthogonal grating

6.3.1 System configuration

Having successfully generated terahertz radiation using several different PPLN grating designs it was highly desirable to attempt to improve the down-conversion efficiency of the collinear phase-matching systems by the introduction of injection seeding. The experimental setup used to achieve this is shown in figure 6.9.

The nonlinear medium in this case was a 30mm-long PPLN crystal with a grating period of 42.4μm at an angle of 90° to the optic axis. A 200mm focal length lens (L) was used to reduce the pump beam size to avoid clipping of the PPLN crystal (as described in chapter 5). M1 and M2 form the shared pump and idler cavity, with M1 being a high reflector and M2 having a reflectivity of 80% - this

reflectivity resulting in the cavity being closest to impedance-matched for the seed laser input. The cavity length was ≈24.5cm. M3-M5 are the 45° high reflectivity mirrors used for coupling the seed laser into the OPO cavity and M6 is a flip-mirror used for guiding the output of the collinear OPO to either an optical spectrum analyser (OSA) or a blazed diffraction grating (G), after which the pump and idler beams could be observed using a photodiode (PD) mounted on a translation stage to access the spatially separated beams.

The PPLN crystal produced an idler wavelength of ≈1070.3nm, with another idler (produced as a result of difference frequency generation between the first idler and the terahertz) at ≈1076.5nm, as shown in figure 6.10. Due to the fact that an 80% reflecting mirror was being used as the output coupler for the pump and idler a variable beam splitter (BS) had to be used to direct sufficient power towards the OSA/diffraction grating, meaning that the amount of seed laser power incident on the OPO was reduced to a maximum of ≈22mW even though the seed laser was capable of producing ≈75mW.

6.3.2 Reduction of OPO threshold due to injection seeding

Following an approach similar to that described in section 6.2.3, the effect of injection seeding on the PPLN OPO threshold point was characterised. A variable filter was used to attenuate the amount of seed power incident on the OPO cavity and the power was varied in the range (0-7)mW.

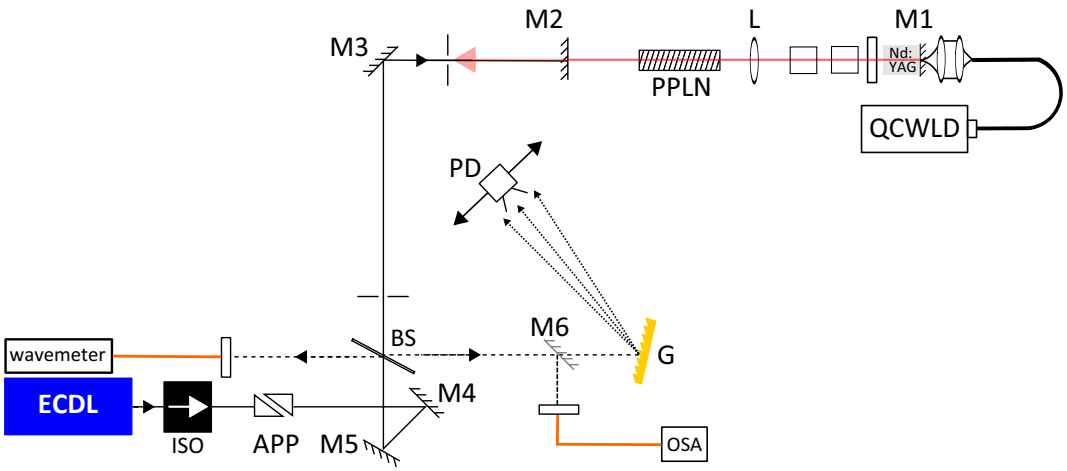

Figure 6.9: Schematic of the experimental layout for the collinear seeding experiments.

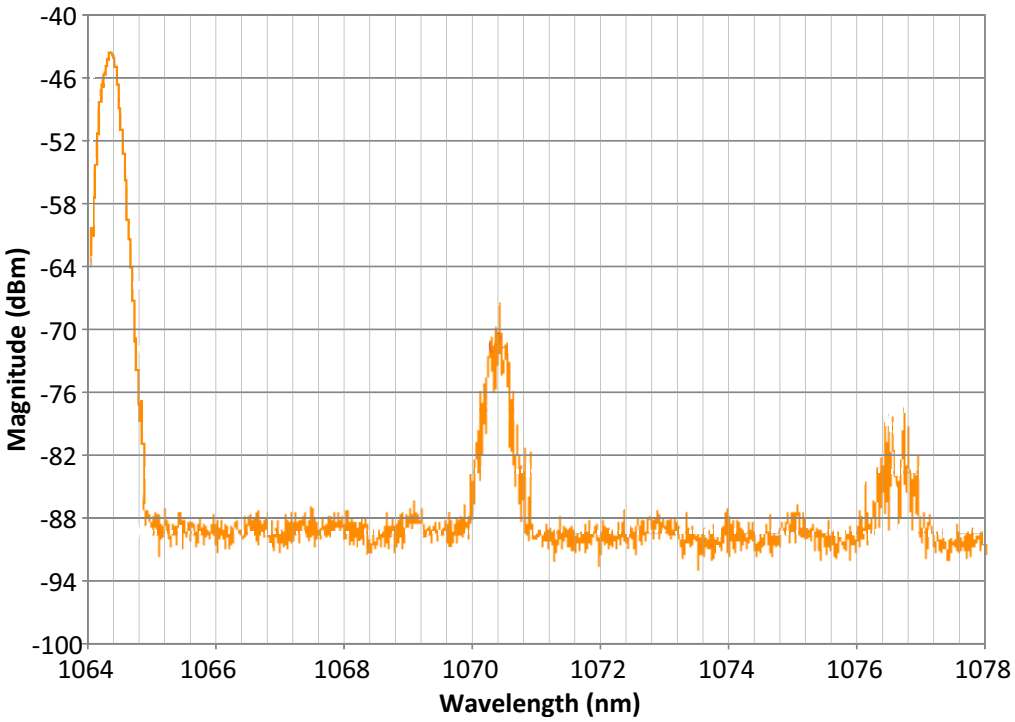

Figure 6.10: The measured spectral output of the PPLN crystal used in the collinear seeding experiments.

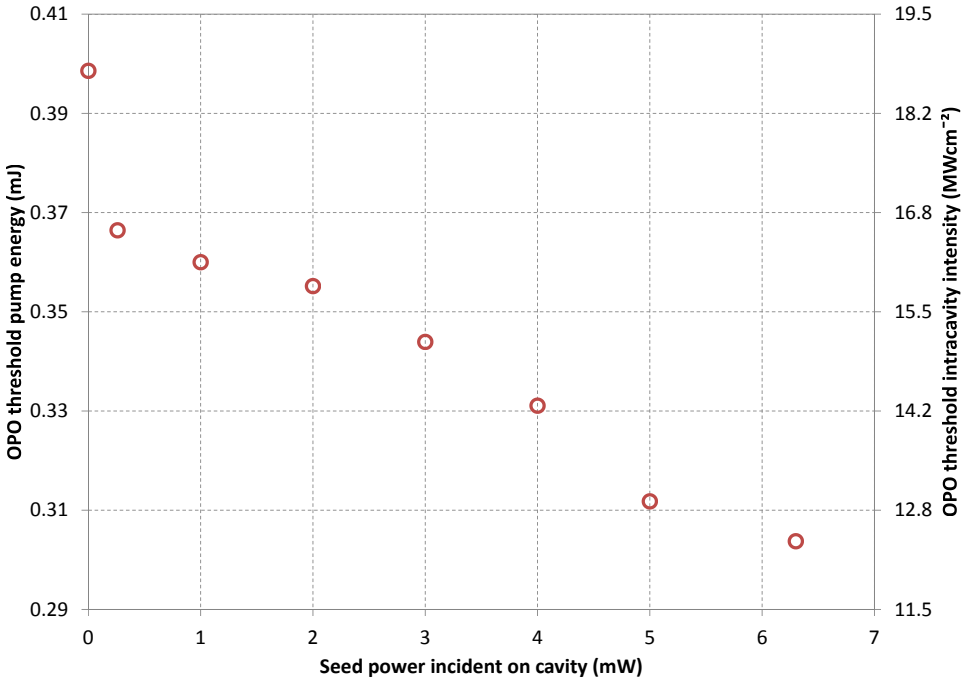

Figure 6.11: The measured OPO threshold (in terms of pulse energy and intracavity intensity) as a function of the input seed laser power. The cavity enhancement factor is 4.32.

Figure 6.11 shows that the seed laser is effective in reducing the OPO threshold pump intensity by ≈6MWcm^{-2}, equivalent to a reduction in the pump pulse energy of 0.04mJ, when seeding with 6.3mW incident on the cavity. Here, the cavity enhancement factor is 4.32 on the basis of a parasitic loss (A_2 in equation 6.1) of 23% and a 20% transmitting output coupler (T_1 in equation 6.1). It should be noted that the intracavity intensities corresponding to OPO threshold are lower than those measured for the 40mm-long PPLN (see chapter 5) by a factor of ≈1.75, indicating that a material problem specific to the 40mm-long PPLN crystal may be the cause of its low damage threshold.

6.3.3 Improvement in down-conversion efficiency with injection seeding

As described in chapter 5, the usual methods for measuring the amount of pump depletion, which involve preventing the idler from being resonated, are impossible to use in the present case of collinear pump and idler beams since blocking the idler beam also blocks the pump beam. Therefore, the total output power of the OPO must be ratioed according to the ratios of the peaks at each wavelength on a corresponding OSA trace (see chapter 5) as determined from figure 6.12. In this manner it was established that the amount of pump depletion observed at a pump intensity of 62MWcm^{-2} was ≈1%. The magnitude of the second idler relative to the pump was ≈0.2%.

The seed laser field was then introduced and its effect on the amount of pump depletion was quantified by observation of the temporal profile of the pump and the first idler. The procedure for doing so was as follows:

1. The ratio of the peak power of the first idler to the pump at a fixed pumping level and without injection seeding was known from the power calibration using the OSA trace. The temporal profile of the idler and the pump had also been acquired.

2. The ratio of the peak idler amplitude in the temporal profile and in the presence of seeding relative to that without seeding was taken to be representative of the ratio of the idler peak powers (see figure 6.13a).

3. The amount of idler produced could then be expressed as a percentage of the peak pump power. The result of these calculations is displayed in figure 6.13b. The yellow pentagons and orange triangles mark the extremes of the idler values (due to uncertainties in the ratios from the OSA trace) and the red circles mark the mid-values.

As can be seen from figure 6.13, injection seeding resulted in almost a five-fold increase in the idler power, leading to the idler reaching as much as 7% of the pump peak power. This result represented such an improvement in the unseeded performance of the PPLN OPO that it was decided to increase both the level of pumping and the seed power. The pump intensity was increased to $\approx$90MWcm^{-2}, corresponding to $\approx$4.8 times above threshold, and the incident seed power was increased to include the range (11-20)mW.

The reference point central to deducing the ratio of the idler power to the pump power was again the OSA trace corresponding to an intracavity pump intensity of 62MWcm^{-2} (3.3 times above threshold) (figure 6.12). This single point can be

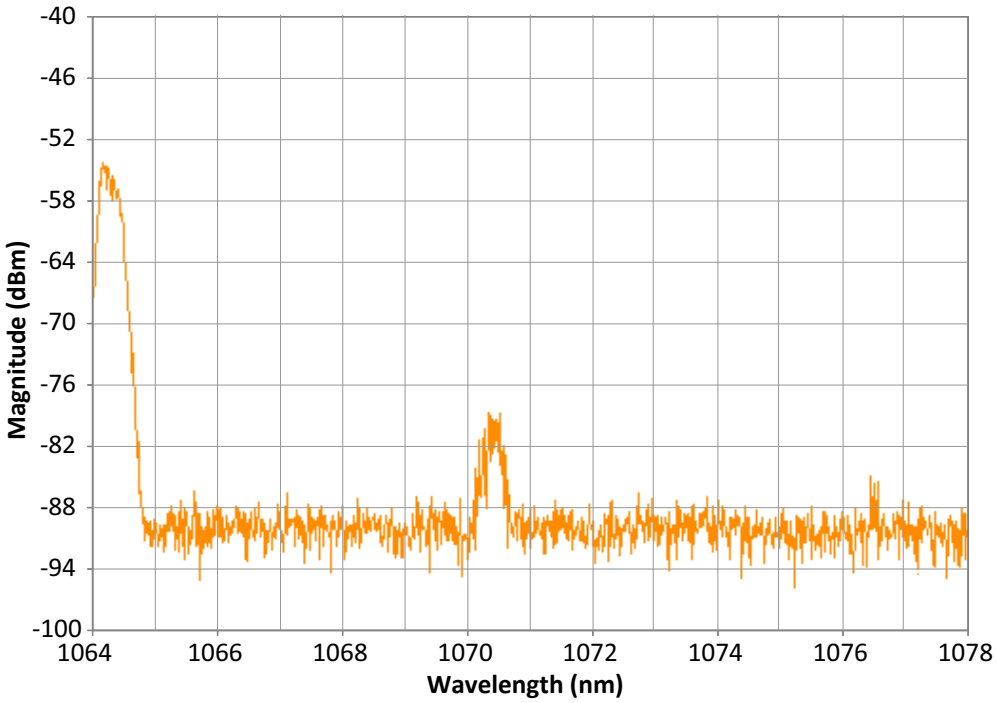

Figure 6.12: The relative strengths of the pump and idlers produced by the PPLN crystal at an intracavity pump intensity of 62MWcm^{-2}.

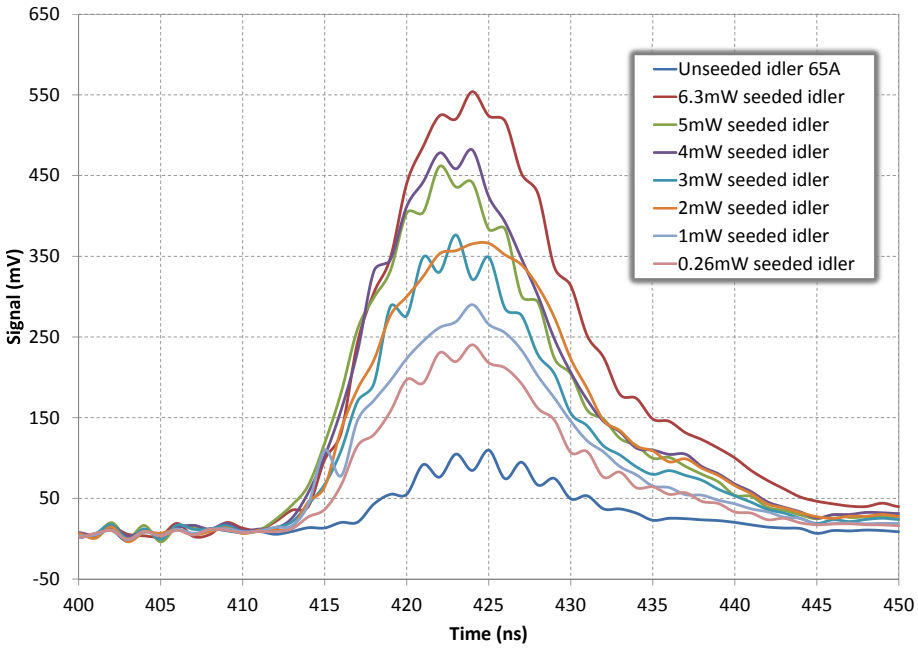

(a) The effect of the seeding level on the produced idler amplitude. The seed power levels refer to the measured power incident on the shared pump and idler cavity, which has an enhancement factor of 4.32.

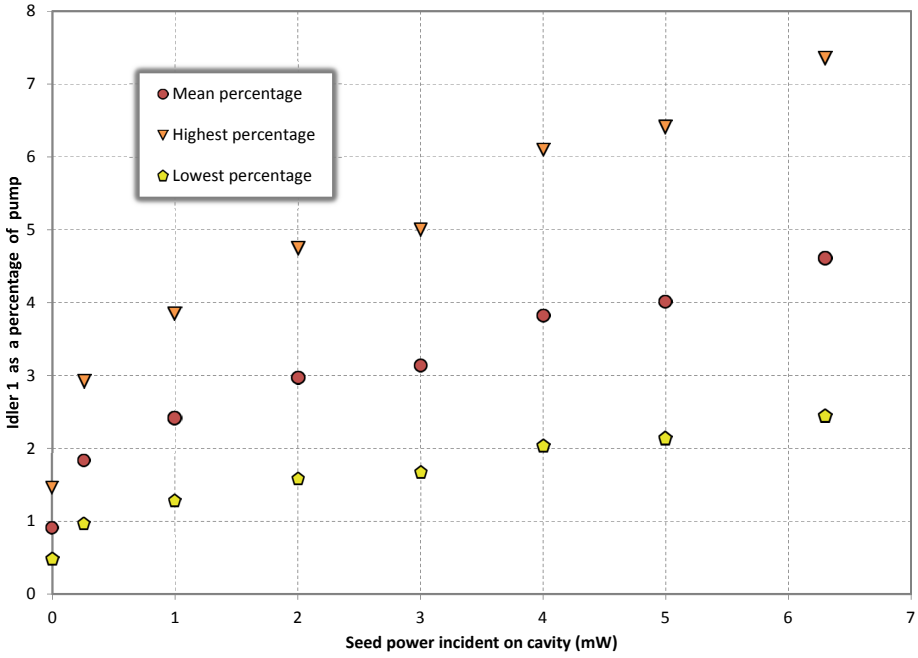

(b) The amount of idler produced by the parametric process as a function of the input seed power, which is enhanced by a factor of 4.32 by the cavity.

Figure 6.13: Graphs showing the effect of the seed laser on the temporal profile of the idler pulse and on the peak idler power.

used to calculate the idler power at higher pump intensities using the ratio of the peak of the idler temporal profiles as a scaling factor, i.e. as shown in figure 6.13a. For the seeded case the idler powers are calculated in the same manner. The outcome of this approach is shown in figure 6.14.

By calculating the idler as a percentage of the pump power the effect of changing the pumping condition is normalised out and the direct effect of the seed power on the idler can be seen. The graph shown in figure 6.13b can be extended to show the influence of higher seed powers on the generated idler. Figure 6.15 illustrates the effect of the seed on the generated idler. The uncertainty in the initial ratio of idler to pump derived from figure 6.12 is reflected in the fact that there are three trends displayed in the graph indicating the possible extent of the calculated values. It is seen from the data that by increasing the incident seed power to 20mW, the generated idler is over eight times greater than it is when seeding is not present. As mentioned previously, the incident seed power was limited to 20mW by the system diagnostics required for the experiment.

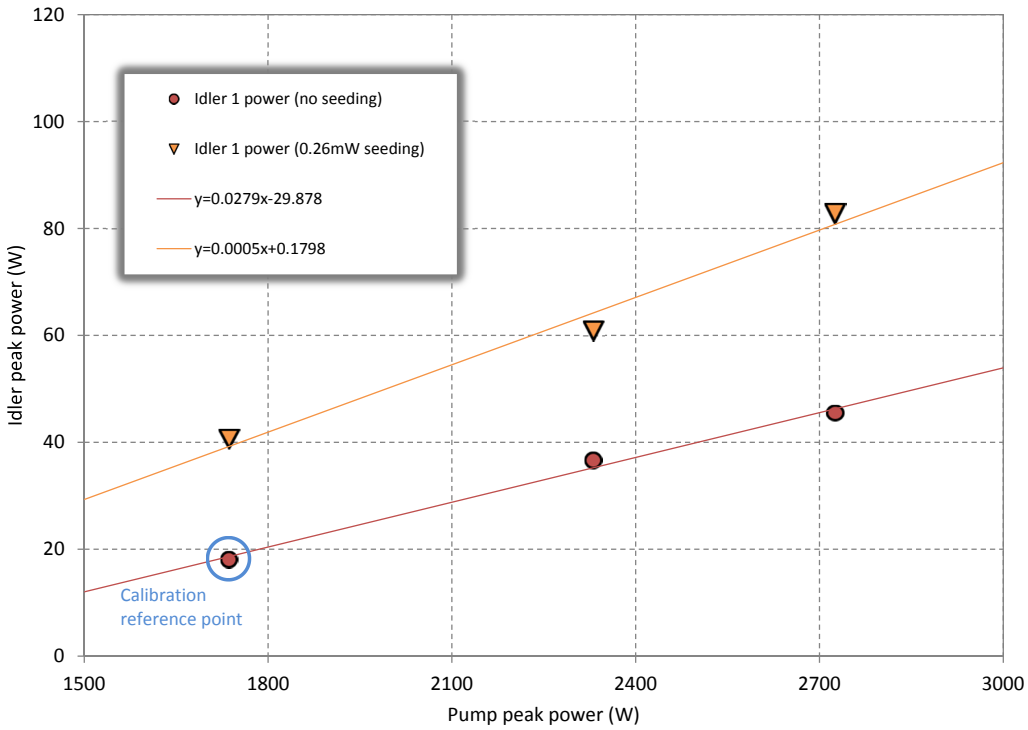

Figure 6.14: Example showing how the idler power scales with both pump power and seeding.

The data in figure 6.15 shows a marked improvement in the production of the idler (and consequently the terahertz) due to the use of injection seeding. However, for the collinear phase-matching geometries to rival the intracavity OPOs based on bulk MgO:$LiNbO_3$, which reach levels of greater than 50% pump depletion, much more seed power would be required. In future work, a better balance would have to be found to enable simultaneous seeding and monitoring of the system to take place more effectively.

6.3.4 Effect of seeding off-resonance

The wavelength of the seed laser was manually scanned through several resonances using the piezo actuator. Resonances were found to be spaced by ≈170MHz. Figure 6.16 shows the effect of seeding on and off resonance with a pump intensity of 90MWcm^{-2} (4.8 times threshold) and with an incident seed power of ≈2mW. It is apparent that seeding off-resonance is equivalent to the condition of no seeding.

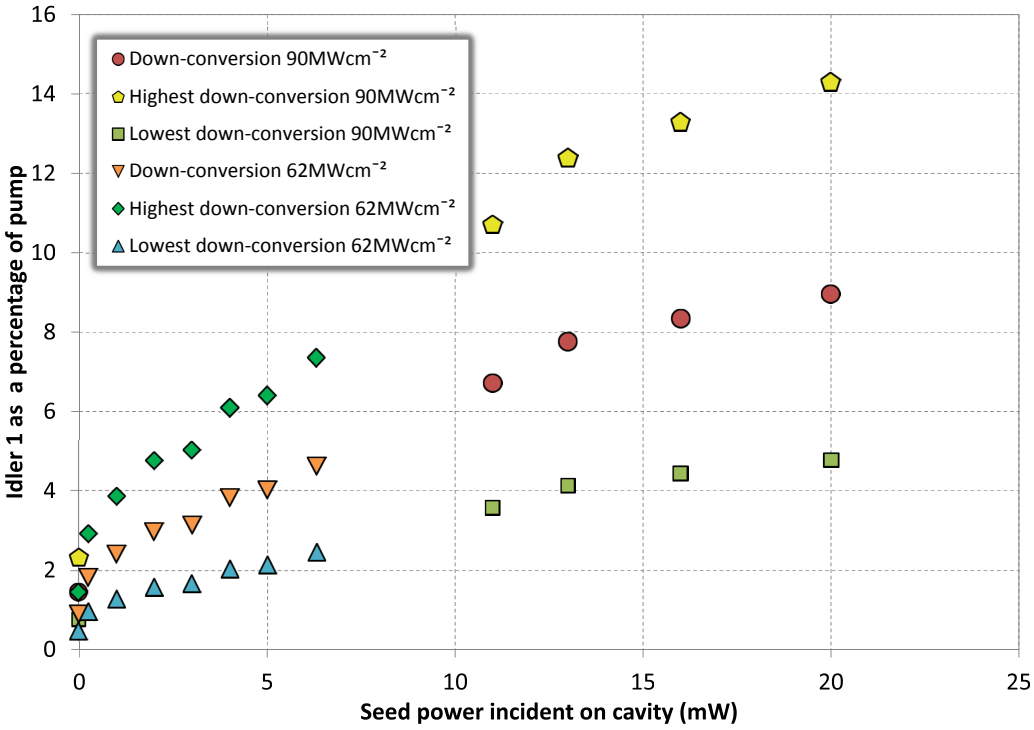

Figure 6.15: The generated idler as a function of the incident seed power. The data represents two pump intensities (62MWcm^{-2} and 90MWcm^{-2}) but the idler has been normalised to the pump so that the data can be shown in the same plot. The cavity enhancement factor is 4.32.

6.3.5 Effect of seeding the second idler

When the seed wavelength was centred on the idler wavelength of ≈1070.5nm, the second idler generation efficiency also increased incrementally with the amount of seed power incident on the pump and idler cavity as shown in figure 6.17.

To investigate the effect of seeding at the wavelength of the second idler at ≈1076.5nm, the wavelength of the seed laser was again manually tuned to the appropriate wavelength, initially using the grub screw shown in figure 6.1 and then using the piezo actuator to fine-tune the wavelength. No variation in the magnitude of the second or first idler was observed as the seed laser power at the second idler wavelength was increased, indicating that the seeding the second idler does not enhance the production of the first idler (and consequently the terahertz) generated through the initial parametric process.

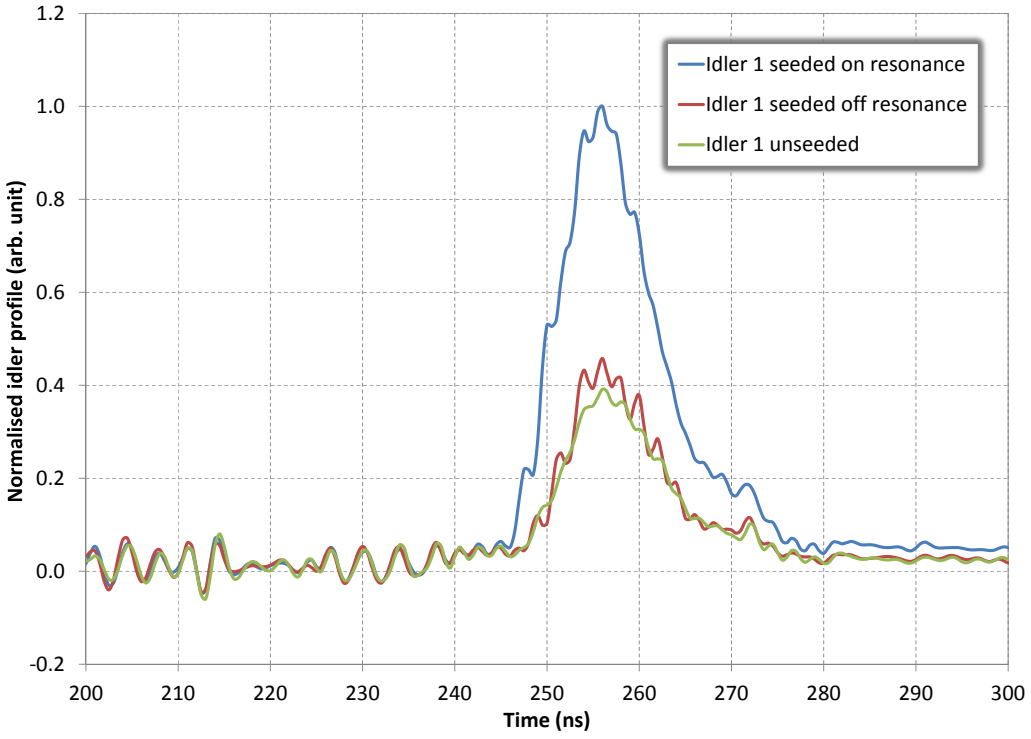

Figure 6.16: The effect of seeding the first idler on and off resonance.

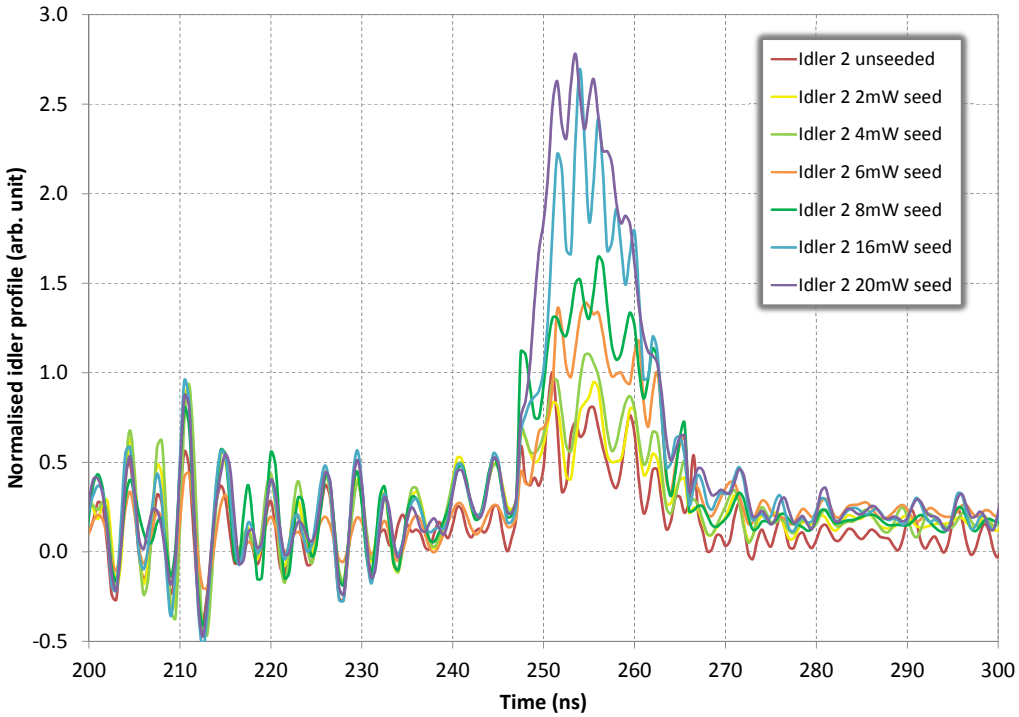

Figure 6.17: The increase in the second idler as a function of the seed power, corresponding to an intracavity pump intensity of 90MWcm^{-2} (4.8 times above threshold).

6.3.6 Measurable pump depletion using injection seeding

While observing the temporal profile of the pump pulse corresponding to 4.8 times above threshold it was recognised that depletion of the pump pulse was occurring, this being verified either by blocking the path of the seed laser or by tuning its wavelength to an off-resonance value. This effect was only seen for incident seed powers greater than or equal to 13mW (56.2mW inside the cavity). Temporal profiles of the depleted and undepleted pump and the idler corresponding to a seed powers of 16mW are shown in figure 6.18. Although the amount of depletion is very small it is, however, quantifiable. The areas under the depleted and undepleted pump temporal profiles were compared using $Origin$ and in the present case $\approx$3.35% depletion was measured. In relation to figure 6.15 this measured pump depletion is roughly consistent with the data on the lowest curve.

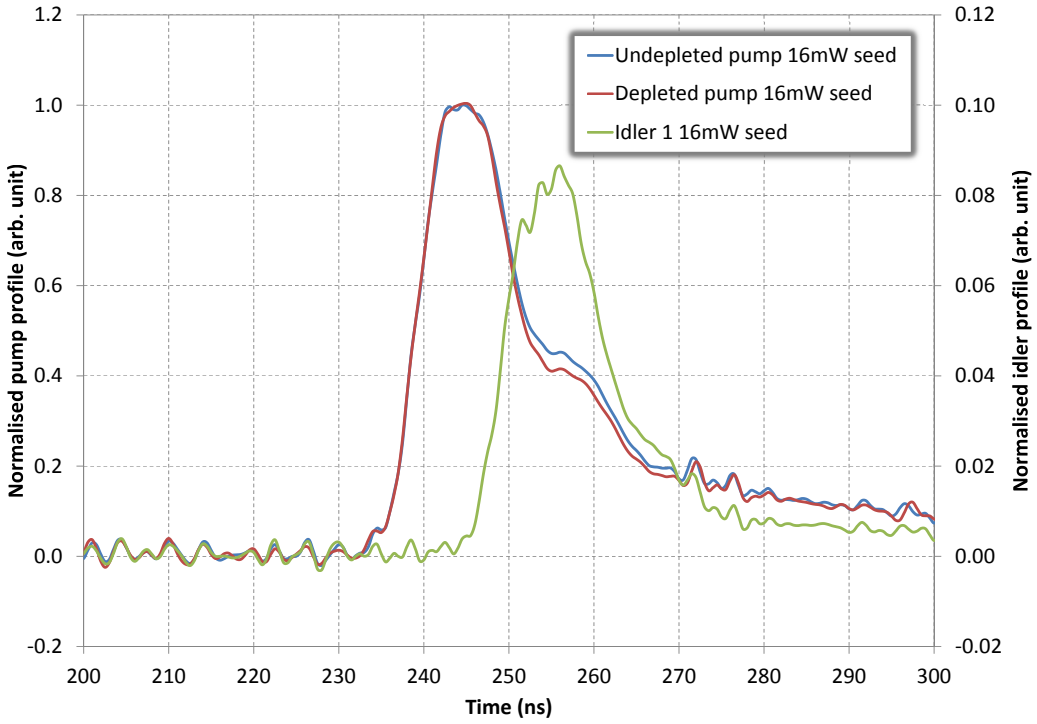

Figure 6.18: Measured pump and idler temporal profiles corresponding to a fixed pump intensity of 90MWcm^{-2} and for a seed power of 16mW (69.1mW inside the cavity). A pump depletion of 3.35% was measured.

6.4 Injection seeding in a system utilising a PPLN crystal with non-orthogonal grating

Further to the improvement of the performance of PPLN OPOs based on collinear phase-matching geometries, an attempt was made to switch the output terahertz frequency of a PPLN crystal with a non-orthogonal grating by injection seeding at the idler wavelength corresponding to the other phase-matching solution.

The experimental setup remained the same as that shown in figure 6.9 except that the PPLN crystal parameters in this case were a grating period of 35.75μm and a grating angle of 67°. Modelling of these grating parameters indicated that the possible idler wavelengths were 1074.54nm and 1068.98nm, corresponding to ≈2.6THz and ≈1.2THz, respectively. The idler wavelength which was measured was 1074.46nm, very close to that expected.

The seed laser was tuned so that its output wavelength was ≈1069nm and the wavelength was then scanned in steps of ≈0.0005nm across the range (1068.9-1069.1)nm to look for a change in the OSA trace. The fast photodiode could not be used to look for the new idler pulse since its position following the diffraction was unknown. The ≈1068.98nm idler could not be observed directly on the OSA either, since the back-reflection of the seed laser from the non-impedance-matched pump and idler cavity was enough to swamp the parametrically-generated idler wavelength. Instead, a reduction in the original idler wavelength at 1074.46nm was sought, this being an indicator of the other wavelength being produced.

No evidence of the 1068.98nm idler wavelength was ever observed. A number of factors may be behind the inability to generate the alternative phase-matching solution:

Firstly, the seed laser power may have been too low to provide sufficient gain for the alternative solution. This could be improved by altering the coupling optics at the expense of the power directed from the output of the OPO directed towards the OSA or grating.

Secondly, the seed laser wavelength may have to be tuned over a greater range. The wavelength of the alternative solution was still somewhat uncertain due to discrepancies in the refractive index data used (see chapter 5).

Further attempts to realise the switching of the idler wavelength will be made in the future with improvements having been made with regard to the limitations of the present experimental setup.

6.5 Injection seeding of a hybrid non-collinear phase-matching system

Following the successful implementation of injection seeding in intracavity terahertz OPOs based on both bulk MgO:$LiNbO_3$ and PPLN, the same approach

was applied to the hybrid non-collinear phase-matching configuration (described in chapters 4 and 5).

The experimental setup was the same as that shown in figure 6.2 with the bulk MgO:$LiNbO_3$ crystal being replaced by the 40mm-long PPLN crystal (72.4μm grating period, 86.5° grating angle). Before replacing the nonlinear crystal, the idler wavelength produced by the bulk crystal was tuned to 1070.5nm, which corresponded to a phase-matching angle consistent with the production of terahertz radiation at a frequency of 2.3THz when using the PPLN crystal. As described in chapter 5, this frequency was chosen because it was found to have the lowest threshold when using the bulk material. Having set the idler cavity up in that configuration and brought the seed laser on resonance with the cavity, the seed wavelength should only have to be tuned to 1072.75nm to seed the generation of 2.3THz.

No evidence of off-axis idler production was seen however. As before, the collinear process was maintained although the output power of the PPLN crystal had degraded with respect to the original measurements shown in figure 5.6. The power could be increased momentarily by translating the crystal through the pump beam but then rapidly decreased again despite many attempts to improve its performance on a longer timescale. It is uncertain whether this effect is a direct consequence of the crystal damage incurred during previous experiments or whether it is a material effect particular to this crystal, however it rendered the crystal unusable.

6.6 The influence of injection seeding in terms of parametric gain

The data corresponding to the measured reduction in OPO threshold as a function of the seed power can be used to calculate the approximate gain equivalence of seeding. This can be done by evaluating the total gain (in dB) as described in chapter 2 for the pump intensities corresponding to OPO threshold

in the seeded and unseeded configurations. Figure 6.19 shows the outcome of this evaluation for the two methods of calculating gain that include the effect of terahertz absorption (which yielded the most consistent results in chapter 2). A seed power of 6.3mW (27.2mW inside the cavity) results in a reduction in the threshold gain of ≈(9.7-12.5)dB.

By fitting trendlines of the form $y = Ax^B$ to the two data sets, the potential effect of higher seeding powers on the threshold gain could be investigated (although this data was not verified experimentally). Extrapolating the gain reduction fits it is seen that for 13mW of seed power, the equivalent reduction in the gain required to reach OPO threshold is in the range (14.9-19.2)dB, when operating at a pump intensity of 62MWcm^{-2}. If we then assume that this is also the equivalent gain contributed by seeding above threshold then the pump intensity needed to reach the point of achieving measurable pump depletion without seeding can be estimated.

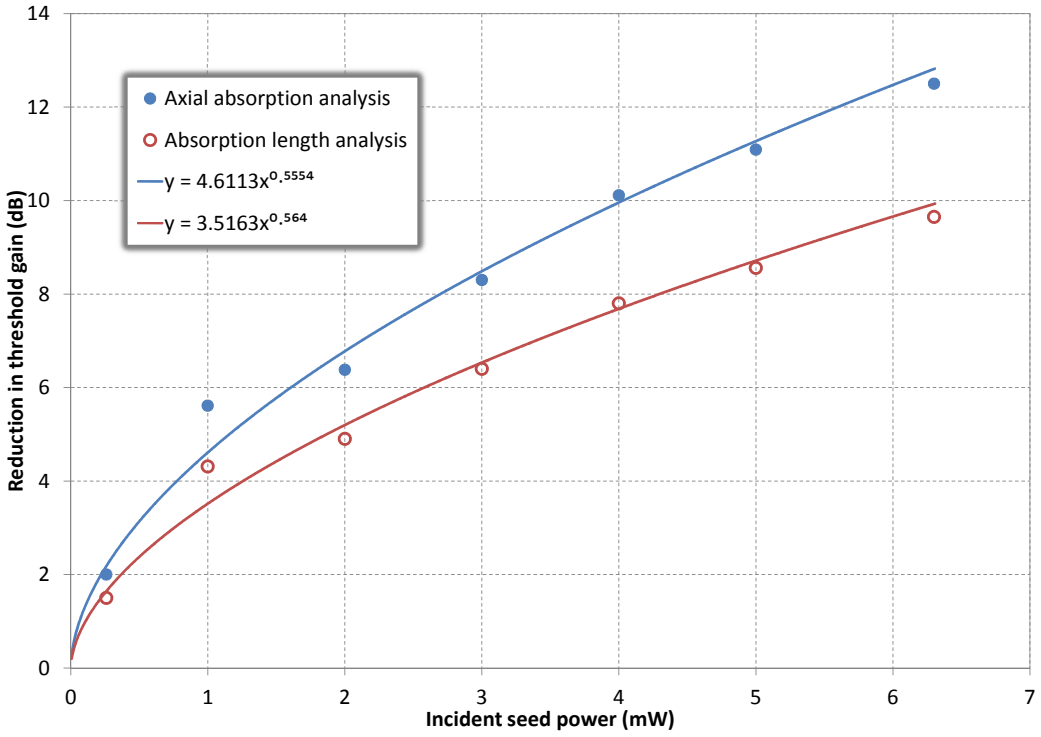

Figure 6.19: The calculated reduction in gain at threshold in the presence of injection seeding calculated using two different methods, which are described in chapter 2. The cavity enhancement factor is 4.32.

The pump intensity corresponding to the observation of pump depletion was 90MWcm^{-2}. On its own, this is equivalent to ≈100dB of gain according to the calculations described in chapter 2 and using the measured pump pulse duration of 15ns. Disregarding the fact that this value is lower than the prescribed 140dB to reach oscillation threshold, the seed laser brings the total gain to (114.9-119.2)dB. To achieve the same amount of gain without seeding the pump intensity would need to be increased to (104-108)MWcm^{-2}, which based on experience with the same PPLN crystal implies operating at a level bordering on the point of damage. The benefit of using seeding in this context is clear.

6.7 Conclusions

This chapter has explored the use of injection seeding in several cavity configurations using both bulk and periodically-poled MgO:$LiNbO_3$ crystals.

In the case of the non-collinear phase-matching system using the bulk material, injection seeding is seen to improve what is already a robust and efficient device. The OPO threshold has been reduced by 4MWcm^{-2} and the down-conversion efficiency increased by ≈20% using injection seeding. Although the seeding configuration may be viewed as being quite complex to implement, it can provide the dual benefit of narrower linewidths [4] and the improved operation demonstrated here. It therefore provides a useful improvement to this well-characterised system.

Improvements in device performance have also been observed as a result of injection seeding in the PPLN-based devices using collinear phase-matching. Modest seed powers (≈6.3mW enhanced to 27.2mW) result in a threshold intensity reduction of 6MWcm^{-2} and can produce an almost 5-fold improvement in the idler field generated. Going to higher seed powers (at least 13mW, enhanced to 56.2mW) results in measurable pump depletions at the level of several percent, with a maximum of ≈3.35% attained for a 16mW seed (enhanced to 69.1mW). Although it would be necessary to go to much higher seed powers to reach the several tens of percent depletion seen in the devices

based on the bulk material, the results presented here represent a significant improvement on previously characterised PPLN-based devices and this approach will aid their progression.

A novel, hybrid non-collinear phase-matching scheme using the PPLN crystals has been identified and attempts were made to realise the concept. Although they have not been successful at this stage, further work will be undertaken in this direction as it is a promising means of both implementing tuning in the PPLN device and extending the tuning range achievable using the conventional non-collinear phase-matched system based on the bulk material. To improve the likelihood of the hybrid system being brought above threshold a more comprehensive study of the optimal phase-matching angle will have to be undertaken, in order to assess the where the largest gain will be available.

References

[1] J. E. Bjorkholm and H. G. Danielmeyer. Frequency control of a pulsed optical parametric oscillator by radiation injection. *Applied Physics Letters*, 15:171–173, 1969.

[2] Y. K. Park, G. Giuliani, and R. L. Byer. Single axial mode operation of a q-switched Nd:YAG oscillator by injection seeding. *IEEE Journal of Quantum Electronics*, 20:117–125, 1984.

[3] D. C. Hovde, J. H. Timmermans, G. Scoles, and K. K. Lehmann. High power injection seeded optical parametric oscillator. *Optics Communications*, 83:294–300, 1991.

[4] D. Walsh, D. J. M. Stothard, T. J. Edwards, P. G. Browne, C. F. Rae, and M. H. Dunn. Injection-seeded intracavity terahertz optical parametric oscillator. *J. Opt. Soc. Am. B*, 26:1196–1202, 2009.

[5] K. Imai, S. Sugawara, J. Shikata, K. Kawase, H. Minamide, and H. Ito. The effect of injection seeding on terahertz parametric oscillation. *Electronics and Communications in Japan*, 86:26–32, 2003.

[6] Angstrom WS7-L MC Wavelength Meter, HighFinesse GmbH, Tübingen, Germany.

[7] P. Fritschel, D. Shoemaker, and R. Weiss. Demonstration of light recycling in a Michelson interferometer with Fabry-Pérot cavities. *Applied Optics*, 31:1412–1418, 1992.

7

Conclusions and future prospects

This thesis has described the comprehensive characterisation of intracavity terahertz optical parametric oscillators based on MgO-doped lithium niobate in its bulk and periodically-poled forms. The experimental research presented here has led to a more fundamental understanding of the intracavity terahertz OPO as a system and the work on PPLN may be viewed as a step towards the final embodiment of a practical source of terahertz radiation based on this material. Here, in addition to reviewing in more detail the research outcomes from the present work, some of the additional research that would be required to further advance the contributions to the field represented by this thesis will be identified in relation to the findings of the preceding chapters.

Chapter 2 characterised the terahertz OPO based on non-collinear phase-matching and MgO:$LiNbO_3$ as the nonlinear medium. The problems relating to the use of a plane output coupler in the pump cavity were highlighted by measurements of the beam profile at varying pump intensities; however the subsequent use of an intracavity lens stablised the mode size very successfully (important in allowing meaningful calculations of parametric gain, etc. to be carried out). The parasitic losses of the pump and idler cavities were determined experimentally and, in the case of the idler cavity, were found to agree well with the predicted Fresnel loss of the cavity. Despite the pump cavity parasitic loss being higher than was originally anticipated, the consequence of that finding is minimal in terms of the generated idler and terahertz fields, since the

down-conversion process takes place at the peak of the pump pulse; because of this, all of the pump energy initially available is down-converted before the parasitic loss can take effect. A deeper understanding of the factors affecting the performance of the terahertz OPO in terms of its threshold and down-conversion efficiency have allowed meaningful gain calculations to be carried out on the basis of experimentally-characterised, optimised devices. Finally, the device described in this chapter has been incorporated into an easy-to-use terahertz spectrometer. Thanks to advances made in relation to terahertz detectors, the terahertz spectrometer is now a fully room-temperature device. The addition of computer-controlled tuning of the terahertz frequency renders the spectrometer more applicable to a range of users because spectra can be quickly and reliably obtained. Further improvements that could be implemented in the spectrometer system include the computer control of the intracavity étalons to enable higher-resolution spectroscopy to be carried out, and the development of a balanced detection system would remove the need for reference scans to be obtained to account for water vapour absorption.

In chapter 3, the phenomenon of difference frequency generation between the idler and terahertz waves was described in detail. To our knowledge, the work presented in that chapter represents the first observation of this effect in bulk lithium niobate. In order to categorise the effect, a series of rigorous measurements were made of the spectral, temporal, spatial and energy characteristics of the second idler that was generated. A model was developed to assess the anticipated enhancement of the original terahertz field due to its amplification through the difference frequency generation process. It was found that the experimental data was consistent with a terahertz enhancement of 50%. However, significantly greater enhancements are to be expected by resonating the second idler, or operating the device at higher pump powers than those presently available.

Chapters 4 and 5 present the strategy for the design and characterisation of terahertz OPOs based on PPLN. Three different models were developed for the design process, all of which exhibit excellent agreement both between

themselves and with the experimental data corresponding to the manufactured crystals. These models are equally applicable to other periodically-poled materials, which may prove to be useful should these materials emerge as alternative nonlinear media for terahertz generation. It was recognised that the grating vector is bipolar, which introduces additional solutions to the phase-matching conditions. These must be identified and assessed in order to ensure that the correct grating design parameters are calculated to yield the output terahertz frequency desired.

A number of devices were constructed and then an experimental comparison between the performance of the PPLN and the MgO:$LiNbO_3$ OPOs revealed that, despite the initial benefits of using poled materials, there are significant drawbacks related to this configuration. Devices based on PPLN crystals were found to have higher thresholds, lower slope efficiencies and lower damage thresholds than those based on bulk crystals, problems which were compounded by the increased length and loss of the collinear idler cavity with respect to the non-collinear idler cavity. A number of potential routes to improving the collinear cavity were identified, including the shortening of the idler cavity by using so-called "super mirrors" that are transmitting at the pump wavelength and highly reflecting at the idler wavelength.

A novel, hybrid phase-matching scheme involving the use of PPLN in a non-collinear idler cavity was identified and its expected tuning range modelled. Although this phase-matching condition has yet to be realised experimentally, we are confident that it will be once a deeper consideration of the phase-matching and corresponding gain criteria has been undertaken.

Finally, chapter 6 discussed the use of injection seeding to lower the threshold of the terahertz OPOs and improve their down-conversion efficiency. This proved to be a very successful technique in both the bulk MgO:$LiNbO_3$ and PPLN systems. In the original non-collinear terahertz OPO, threshold was reduced by a fifth when seeding with only modest seed powers ($\approx$68mW) and when the seeding was introduced at OPO threshold, the pump depletion was increased

from ≈2% to ≈20%. In the PPLN terahertz OPO, seeding reduced OPO threshold to the extent that depletion could be observed in the temporal profile of the pump - something which had not been observed previously. If the coupling optics and diagnostics for the seed laser can be reconfigured so that more seed power can be input to the shared pump and idler cavity, greater amounts of pump depletion may be achieved, however it is unlikely that seeding alone will produce PPLN-based terahertz OPOs that rival the non-collinear terahertz OPO in terms of the amount of terahertz generated. Injection seeding may also play a significant role in the development of the hybrid phase-matching system if it can be used to overcome the collinear phase-matching solution which currently dominates the parametric process.

The terahertz spectral region is of great interest to the scientific community, in particular to the future beneficiaries of the potential applications it offers. The work presented in this thesis describes significant and timely enhancements of the current state-of-the-art for parametric sources of terahertz radiation. Technical advances with regard to device development have been complemented by the attainment of a deeper conceptual understanding of the science involved, promising further developments in the field and ultimately making the terahertz region more widely accessible.

A

Inclusion of absorption loss in the coupled wave equations

The frequencies involved in the parametric process are defined as:

$\omega_3 \rightarrow$ pump

$\omega_2 \rightarrow$ terahertz

$\omega_1 \rightarrow$ idler

The waves are treated as plane waves and the process is assumed to be phase-matched (Δk=0). The pump is considered to be strong and undepleted.

The coupled wave equations in the presence of terahertz absorption are:

$$\frac{dE_{20}}{dz} = i\kappa_2 E_{30} E_{10}^* - \gamma_2 E_{20} \tag{A.1}$$

$$\frac{dE_{10}}{dz} = i\kappa_1 E_{30} E_{20}^* \tag{A.2}$$

$$\frac{dE_{30}}{dz} = 0 \tag{A.3}$$

and κ_i is given by

$$\kappa_i = \frac{\omega_i \chi^{(2)}}{2 n_i c \epsilon_0} \tag{A.4}$$

where $\chi^{(2)}$ is the nonlinear susceptibility of the material, ω_i is the frequency of the wave under consideration, n_i is the appropriate refractive index and γ_2 is the

field amplitude absorption coefficient (equal to half the value of the intensity absorption coefficient, α).

Solving for E_{10}:

$$\begin{aligned}\frac{d^2E_{10}}{dz^2} &= i\kappa_1 E_{30}\frac{dE_{20}}{dz} \\ &= i\kappa_1 E_{30}\left(-i\kappa_2 E_{30}E_{30}^* - \gamma_2 E_{20}^*\right) \\ &= \kappa_1\kappa_2 E_{30}E_{30}^* E_{10} - i\kappa_1 E_{30}\gamma_2 E_{20}^*\end{aligned} \tag{A.5}$$

Substituting for E_{20}^* from equation A.2

$$\frac{d^2E_{10}}{dz^2} = \kappa_1\kappa_2\left(E_{30}E_{30}^*\right)E_{10} - \cancel{i\kappa_1 E_{30}}\gamma_2\frac{dE_{10}}{dz}\frac{1}{\cancel{i\kappa_1 E_{30}}}$$

Rearranging gives

$$\frac{d^2E_{10}}{dz^2} + \frac{dE_{10}}{dz} - \kappa_1\kappa_2\left(E_{30}E_{30}^*\right)E_{10} = 0$$

where the substitution $\kappa^2 = \kappa_1\kappa_2\left(E_{30}E_{30}^*\right)$ is used to reduce the above expression to

$$\frac{d^2E_{10}}{dz^2} + \frac{dE_{10}}{dz} - \kappa^2 E_{10} = 0 \tag{A.6}$$

Next the solution $E_{10} = e^{(\alpha+i\beta)z}$ is tried:

$$-e^{(\alpha+i\beta)z}\kappa^2 + e^{(\alpha+i\beta)z}\gamma_2\left(\alpha+i\beta\right) + e^{(\alpha+i\beta)z}\left(\alpha+i\beta\right)^2 = 0$$

which reduces to

$$\alpha^2 + \alpha\gamma_2 - \kappa^2 + 2\alpha i\beta + \gamma i\beta + i\beta^2 = 0 \tag{A.7}$$

Equation A.7 can be separated into its constituent real and imaginary parts:

$$\alpha^2 - \beta^2 + \gamma_2\alpha - \kappa^2 = 0 \qquad \text{(Real)} \tag{A.8}$$

$$i\left(2\alpha\beta + \gamma_2\beta\right) = 0 \qquad \text{(Imaginary)} \tag{A.9}$$

From equation A.9 it can be deduced that

$$\alpha = \frac{-\gamma_2}{2} \tag{A.10}$$

so that substituting for α in the real part

$$\begin{aligned} \frac{\gamma_2^2}{4} - \beta^2 + \frac{\gamma_2}{2} - \kappa^2 &= 0 \\ \Rightarrow \beta^2 &= \left(\frac{\gamma_2^2}{4} - \kappa^2\right) \\ \Rightarrow \beta &= \mp\left(\frac{\gamma_2^2}{4} + \kappa^2\right)^{\frac{1}{2}} \end{aligned} \tag{A.11}$$

So

$$(\alpha + i\beta) = \frac{-\gamma_2}{2} \mp \left(\frac{\gamma_2^2}{4} + \kappa^2\right)^{\frac{1}{2}} \tag{A.12}$$

therefore

$$E_{10} = ae^{\frac{-\gamma_2}{2} - \left(\frac{\gamma_2^2}{4} + \kappa^2\right)^{\frac{1}{2}} z} + be^{\frac{-\gamma_2}{2} + \left(\frac{\gamma_2^2}{4} + \kappa^2\right)^{\frac{1}{2}} z} \tag{A.13}$$

If $\gamma_2 = 0$,

$$E_{10} = ae^{-\kappa z} + be^{\kappa z} \tag{A.14}$$

and when $z = L$

$$E_{10} = ae^{-\kappa L} + be^{\kappa L} \tag{A.15}$$

so from comparison with equation 2.18

$$\kappa = \Gamma \tag{A.16}$$

since $ae^{-\kappa L} + be^{\kappa L} = \cosh(\kappa L)$. Therefore,

$$E_{10} = ae^{\frac{-\gamma_2}{2} - \left(\frac{\gamma_2^2}{4} + \Gamma^2\right)^{\frac{1}{2}} z} + be^{\frac{-\gamma_2}{2} + \left(\frac{\gamma_2^2}{4} + \Gamma^2\right)^{\frac{1}{2}} z} \tag{A.17}$$

Expressions for a and b can now be deduced from the boundary conditions.

At $z = 0$,

$$E_{10}(0) = a + b \tag{A.18}$$

and

$$\frac{dE_{10}}{dz} = a\left(\frac{-\gamma_2}{2} - \left(\frac{\gamma_2^2}{4} + \Gamma^2\right)^{\frac{1}{2}}\right) + b\left(\frac{-\gamma_2}{2} + \left(\frac{\gamma_2^2}{4} + \Gamma^2\right)^{\frac{1}{2}}\right) = 0 \quad \text{(A.19)}$$

which, by making the appropriate substitutions, can be written as

$$\frac{dE_{10}}{dz} = aA + bB = 0 \quad \text{(A.20)}$$

Thus

$$\begin{aligned} &Aa + B\left(E_{10}\left(z=0\right) - a\right) = 0 \\ &\Rightarrow b = \left(E_{10}\left(0\right) - a\right) \\ &\Rightarrow aA + B\left(E_{10}\left(0\right) - a\right) = 0 \\ &\Rightarrow a\left(A - B\right) = -BE_{10}\left(0\right) \\ &\Rightarrow a = \frac{B}{B-A}E_{10}\left(0\right) \qquad \text{and} \qquad b = \frac{-A}{B-A}E_{10}\left(0\right) \end{aligned} \quad \text{(A.21)}$$

Now the expressions for a and b can be substituted back into the boundary conditions:

$$\begin{aligned} &\left(B - A\right) = 2\left(\frac{{\gamma_2}^2}{2} + \Gamma^2\right)^{\frac{1}{2}} = \tilde{\Gamma} \\ &E_{10}\left(L\right) = \frac{B}{B-A}E_{10}\left(0\right)e^{\frac{-\gamma_2 L}{2} - \left(\frac{\gamma_2^2}{4} + \Gamma^2\right)^{\frac{1}{2}}L} - \frac{A}{B-A}E_{10}\left(0\right)e^{\frac{-\gamma_2 L}{2} + \left(\frac{\gamma_2^2}{4} + \Gamma^2\right)^{\frac{1}{2}}L} \\ &\Rightarrow \left(\frac{E_{10}\left(0\right)}{B-A}e^{-\frac{\gamma_2 L}{2}}\right) \times \left(Be^{-\left(\frac{\gamma_2^2}{4} + \Gamma^2\right)} - Ae^{\left(\frac{\gamma_2^2}{4} + \Gamma^2\right)}\right) \end{aligned}$$

where

$$\frac{B}{B-A} = \frac{\left(\frac{-\gamma_2^2}{2} + \frac{\tilde{\Gamma}}{2}\right)}{\tilde{\Gamma}} = \frac{1}{2}\left(1 - \frac{\gamma_2}{\tilde{\Gamma}}\right) \quad \text{(A.22)}$$

and

$$\frac{A}{B-A} = \frac{\left(\frac{-\gamma_2^2}{2} - \frac{\tilde{\Gamma}}{2}\right)}{\tilde{\Gamma}} = \frac{1}{2}\left(1 + \frac{\gamma_2}{\tilde{\Gamma}}\right) \quad \text{(A.23)}$$

Thus

$$E_{10}\left(L\right) = \left(E_{10}\left(0\right)e^{-\frac{\gamma_2 L}{2}}\right) \times \frac{1}{2}\left(\left(\left(1 - \frac{\gamma_2}{\tilde{\Gamma}}\right)e^{-\frac{\tilde{\Gamma}L}{2}}\right) + \left(\left(1 + \frac{\gamma_2}{\tilde{\Gamma}}\right)e^{\frac{\tilde{\Gamma}L}{2}}\right)\right) \quad \text{(A.24)}$$

Gain is defined as $\frac{E_{10}(L)}{E_{10}(0)}$, so:

$$\frac{E_{10}(L)}{E_{10}(0)} = e^{-\frac{\gamma_2 L}{2}} \times \frac{1}{2}\left(\left(\left(1-\frac{\gamma_2}{\tilde{\Gamma}}\right)e^{-\frac{\tilde{\Gamma}L}{2}}\right)+\left(\left(1+\frac{\gamma_2}{\tilde{\Gamma}}\right)e^{\frac{\tilde{\Gamma}L}{2}}\right)\right) \tag{A.25}$$

which can also be expressed as

$$\frac{E_{10}(L)}{E_{10}(0)} = e^{-\frac{\gamma_2 L}{2}} \times \left(\cosh\left(\frac{\tilde{\gamma}L}{2}\right)+\frac{\gamma_2}{\tilde{\gamma}}\sinh\left(\frac{\tilde{\gamma}L}{2}\right)\right) \tag{A.26}$$

B

Inclusion of phase mismatch in the coupled wave equations

The frequencies involved in the difference frequency generation process are defined as:

$\omega_3 \rightarrow$ pump (first idler from parametric process)

$\omega_2 \rightarrow$ second idler

$\omega_1 \rightarrow$ terahertz

The waves are treated as plane waves and the pump is considered to be strong and undepleted.

The coupled wave equations in the presence of a phase mismatch, δk are:

$$\frac{dE_{10}}{dz} = i\kappa_1 E_{30} E_{20}^* e^{i\Delta kz} \tag{B.1}$$

$$\frac{dE_{20}}{dz} = i\kappa_2 E_{30} E_{10}^* e^{i\Delta kz} \tag{B.2}$$

$$\frac{dE_{30}}{dz} = 0 \tag{B.3}$$

and κ_i is given by

$$\kappa_i = \frac{\omega_i \chi^{(2)}}{2 n_i c \epsilon_0} \tag{B.4}$$

where $\chi^{(2)}$ is the nonlinear susceptibility of the material, ω_i is the frequency of the wave under consideration, n_i is the appropriate refractive index and Δk is the phase-mismatch.

Decoupling the equations:

$$\frac{d^2E_{10}}{dz^2} = \left(i\kappa_1 E_{30}\frac{dE_{20}^*}{dz} - \kappa_1\Delta k E_{30}E_{20}^*\right)e^{i\Delta kz}$$

Substituting for E_{20}^*

$$\frac{d^2E_{10}}{dz^2} = \left(\kappa_1\kappa_2|E_{30}|^2E_{10} + i\Delta k\frac{dE_{10}}{dz}\right) \tag{B.5}$$

and by analogy

$$\frac{d^2E_{20}}{dz^2} = \left(\kappa_1\kappa_2|E_{30}|^2E_{20} + i\Delta k\frac{dE_{20}}{dz}\right) \tag{B.6}$$

Next, the solution $E_{10} \approx e^{i\gamma z}$ is tried (γ can be complex):

$$\begin{aligned} -\gamma^2 &= \kappa_1\kappa_2|E_{30}|^2 + i\Delta k\,(i\gamma) \\ \Rightarrow\gamma^2 &- \Delta k + \kappa_1\kappa_2|E_{30}|^2 = 0 \end{aligned}$$

Solving for γ using the quadratic formula yields

$$\gamma = \Delta k \pm \sqrt{\Delta k^2 - 4\kappa_1\kappa_2|E_{30}|^2} \tag{B.7}$$

In the case where $\Delta k^2 > 4\kappa_1\kappa_2|E_{30}|^2$, the term under the $\sqrt{}$ in equation B.7 is always positive.

However, when $\Delta k = 0$,

$$\gamma = \pm i\sqrt{\kappa_1\kappa_2|E_{30}|^2} \tag{B.8}$$

and the solution is

$$E_{10} \approx e^{\pm\sqrt{\kappa_1\kappa_2|E_{30}|^2}z} \tag{B.9}$$

which describes the exponential gain/loss

$$E_{10} = Ae^{\Gamma z} + Be^{-\Gamma z} \tag{B.10}$$

where

$$\Gamma = \sqrt{\kappa_1 \kappa_2 |E_{30}|^2} \tag{B.11}$$

and Γ describes the exponential gain/loss in the absence of a phase mismatch.

(B.12)

So when $\Delta k \neq 0$ and $\left(\frac{\Delta k}{2}\right)^2 > \Gamma^2$:

$$i\gamma z = i\left(\frac{\Delta k}{2} \pm \sqrt{\left(\frac{\Delta k}{2}\right)^2 - \Gamma^2}\right) z$$

and the general solution is of the form

$$E_{10} = \left(Ae^{i\surd} + Be^{-i\surd}\right) e^{\frac{i\Delta k z}{2}} \tag{B.13}$$

where

$$\surd = \sqrt{\left(\frac{\Delta k}{2}\right)^2 - \Gamma^2}$$

and by analogy

$$E_{20} = \left(Ce^{i\surd} + De^{-i\surd}\right) e^{\frac{i\Delta k z}{2}} \tag{B.14}$$

A, B, C and D can be evaluated by considering the boundary conditions.

At $z = 0$,

$$\frac{dE_{10}}{dz} = i\kappa_1 E_{30} E_{20}^* (0) \tag{B.15}$$

$$\frac{dE_{20}}{dz} = i\kappa_2 E_{30} E_{10}^* (0) \tag{B.16}$$

so that

$$\frac{dE_{10}}{dz}(0) = \left(i\surd A - i\surd B\right) + (A+B)\left(-i\frac{\Delta k}{2}\right) \tag{B.17}$$

$$= i\kappa_1 E_{30} E_{20}^* (0) \tag{B.18}$$

and

$$E_{10}(0) = A + B \tag{B.19}$$

Hence

$$i\kappa_1 E_{30} E_{20}^{*}(0) = i\sqrt{}A - i\sqrt{}\left(E_{10}(0) - A\right) - \left(-\frac{i\Delta k}{2}\right) E_{10}(0) \tag{B.20}$$

Solving for A:

$$\begin{aligned} 2i\sqrt{}A &= \left(i\sqrt{} - i\frac{\Delta k}{2}\right) E_{10} + i\kappa_1 E_{30} E_{20}^{*}(0) \\ \Rightarrow A &= \left(\frac{1}{2} - \frac{\Delta k}{4\sqrt{}}\right) E_{10}(0) + \frac{\kappa_1 E_{30}}{2\sqrt{}} E_{20}^{*}(0) \end{aligned} \tag{B.21}$$

Solving for B:

$$\begin{aligned} B &= E_{10}(0) - \frac{1}{2} E_{10}(0) + \frac{\Delta k}{4\sqrt{}} E_{10}(0) - \frac{\kappa_1 E_{30}}{2\sqrt{}} E_{20}^{*}(0) \\ \Rightarrow B &= \left(\frac{1}{2} + \frac{\Delta k}{4\sqrt{}}\right) E_{10}(0) - \frac{\kappa_1 E_{30}}{2\sqrt{}} E_{20}^{*} \end{aligned} \tag{B.22}$$

Substituting equations B.21 and B.22 into the previous solutions:

$$\begin{aligned} E_{10}(z) &= \left(\frac{1}{2}\left(e^{i\sqrt{}z} + e^{-i\sqrt{}z}\right) - \frac{\Delta k}{4\sqrt{}}\left(e^{i\sqrt{}z} + e^{-i\sqrt{}z}\right)\right) e^{\frac{i\Delta kz}{2}} E_{10}(0) \\ &\quad + \left(\frac{\kappa_1 E_{30}}{2\sqrt{}}\left(e^{i\sqrt{}z} - e^{-i\sqrt{}z}\right)\right) e^{\frac{i\Delta kz}{2}} E_{20}^{*}(0) \\ &= \left(\cos\left(\sqrt{}z\right) - \frac{\Delta k}{2\sqrt{}} i\sin\left(\sqrt{}z\right) E_{10}(0) + \frac{\kappa_1 E_{30}}{\sqrt{}} i\sin\left(\sqrt{}z\right) E_{20}^{*}(0)\right) e^{\frac{i\Delta kz}{2}} \\ E_{10}(z) &= \left(\left(\cos\left(\sqrt{}z\right) - \frac{i\Delta k}{2\sqrt{}}\sin\left(\sqrt{}z\right)\right) E_{10}(0) + \left(\frac{i\kappa_1 E_{30}}{\sqrt{}}\sin\left(\sqrt{}z\right)\right) E_{20}^{*}(0)\right) e^{\frac{\Delta kz}{2}} \end{aligned} \tag{B.23}$$

By analogy:

$$E_{20}(z) = \left(\left(\cos\left(\sqrt{}z\right) - \frac{i\Delta k}{2\sqrt{}}\sin\left(\sqrt{}z\right)\right) E_{20}(0) + \left(\frac{i\kappa_2 E_{30}}{\sqrt{}}\sin\left(\sqrt{}z\right)\right) E_{10}^{*}(0)\right) e^{\frac{\Delta kz}{2}} \tag{B.24}$$

So for a nonlinear crystal having N total segments across the crystal length, l, the field in any particular segment, n, is described by:

$$E_T(n) = \eta_{TT} A_T(0) + \eta_{T2} A_2^{*}(n-1) \qquad \text{for the terahertz field} \tag{B.25}$$

$$E_{20}(n) = \eta_{2T} A_T^{*}(0) + \eta_{22} A_2(n-1) \qquad \text{for the second idler} \tag{B.26}$$

where

$$\eta_{TT} = \eta_{22} = \left(\cos\left(\sqrt{}z\right) - \frac{i\Delta k}{2\sqrt{}} \sin\left(\sqrt{}l\right) \right) e^{\frac{i\Delta kl}{2}} \tag{B.27}$$

$$\eta_{T2} = \frac{\kappa_T}{\sqrt{}} \sin\left(\sqrt{}l\right) e^{\frac{i\Delta kl}{2}} \tag{B.28}$$

$$\eta_{2T} = \frac{\kappa_2}{\sqrt{}} \sin\left(\sqrt{}l\right) e^{\frac{i\Delta kl}{2}} \tag{B.29}$$

where the subscripts T and 2 denote the terahertz and second idler fields, respectively.

(B.30)

When carrying out calculations on the basis of these relations, it is necessary to relate $\kappa_2|E_{30}|$ and $\kappa_T|E_{30}|$ to Γ, which is an experimentally-determined quantity. From equation B.11, it can be seen that:

$$\Gamma^2 = \kappa_1\kappa_2 E_{30}E_{30}^*$$

The following relationship also applies to κ_1 and κ_2

$$\frac{\kappa_T}{\kappa_2} = \frac{\nu_2 n_{10}}{\nu_{10} n_2} = \mathfrak{R} \tag{B.31}$$

so

$$\kappa_2 = \mathfrak{R}\kappa_T \tag{B.32}$$

and

$$\kappa_T = \frac{\kappa_2}{\mathfrak{R}} \tag{B.33}$$

Then

$$\kappa_2|E_{30}| = \sqrt{\mathfrak{R}}\Gamma \tag{B.34}$$

and

$$\kappa_T|E_{30}| = \frac{\Gamma}{\sqrt{\mathfrak{R}}} \tag{B.35}$$

which is expressed as

$$\kappa_2|E_{30}| = \sqrt{\Re}\Gamma e^{i\phi} \tag{B.36}$$

and

$$\kappa_T|E_{30}| = \frac{\Gamma}{\sqrt{\Re}} e^{i\phi} \tag{B.37}$$

when evaluated numerically.

C

Mathematica collinear phase-matching model

The variables **A** to **z** in the code below are the terms in the Sellmeier equation decribing the terahertz regfractive index, **ne[f]**, which is derived from the *"Handbook of Optical Constants of Solids"*, 1985 edition. **f** is the terahertz frequency, expressed in THz. **n2** and **n0** are the refractive indices of lithium niobate at the pump and idler wavelengths, here defined as constant values since the refractive index varies by around 0.001 across the tuning range of the idler wavelength.

The critical angle for the prism-crystal interface, $\theta\mathbf{crit}[\mathbf{n2}\_, \mathbf{f}\_]$, is calculated to allow the specification of the terahertz propagation angle relative to the critical angle. The user of the program enters the amount, **l**, below the critical angle at which the generated terahertz should propagate.

The grating properties, $\alpha\mathbf{G}(\mathbf{1})$ and **G**, required to generate the user-specified terahertz frequency propagating at the desired angle to the crystal-prism interface, are calculated. The terms **a, b** and **c** are the coefficients in the quadratic formula, which are necessary to the identification of the alternative phase-matching solution. They allow $\alpha\mathbf{G}(\mathbf{2})$, the propagation angle of the second solution, to be calculated. From $\alpha\mathbf{G}(\mathbf{2})$, the second terahertz frequency, $\nu\mathbf{T2}$, can be found.

```
A=3.8123;
I0=-14.90;
t0=65;
n2=3.418;
n0=2.15;
ne[f_]:=A*Exp[-((((3*10^8)(10^6)/(f*10^12))-I0))/t0]+z
θcrit[f_]:=ArcSin[n2/ne[f]]/Degree
ϕ[f_,I_]:=90-(θcrit[f]-I)
αG(1)[f_,I_]:=ArcTan[Sin[ϕ[f,I] Degree]/(Cos[ϕ[f,I] Degree]-(n0/ne[f]))]/Degree
αG(2)[f_,I_]:=180-αG(1)[f,I]
G[f_,I_]:=2*Pi*ne[f]*(f*10^12)*Sin[ϕ[n2,f,I] Degree])/((3*10^8)*Sin[αG[f,I] Degree])
GP[f_,I_]:=(2*Pi*(1*10^6))/G[n2,f,I,n0]
a[f_,I_]:=(Tan[αG(2)[f,I] Degree])^2+1
b[f_,I_]:=2*(n0/ne[f])*(Tan[αG(2)[f,I] Degree])^2
c[f_,I_] := ((n0/ne[f])^2*(Tan[αG(2)[f, I] Degree])^2)-1
b2[f_, I_,n_]:=-2*(n0/n)*(Tan[αG(2)[f, I] Degree])^2
c2[f_,I_,n_]:=((n0/n)^2*(Tan[αG(2)[f,I] Degree])^2) - 1
rootplus[f_,I_] := (-b[f,I]+√[(b[f, I])^2 − 4 ∗ a[f, I] ∗ c[f, I])/(2*a[f,I])
rootminus[f_,I_] := (-b[f,I]-√[(b[f, I])^2 − 4 ∗ a[f, I] ∗ c[f, I])/(2*a[f,I])
rootminus2[f_,I_] := (-b2[f,I]-√[(b2[f, I])^2 − 4 ∗ a[f, I] ∗ c2[f, I])/(2*a[f,I])
νT[f_,I_]:=(G[f,I]*(3*10^8)*Sin[αG(2)[f,I]
Degree])/(2*Pi*ne[f]*Sin[ArcCos[rootminus[f,I]]]) /(1*10^12)
f1[f_,I_]:=νT[f,I];
con[f_,I_]:=Module[,
Label[begin];
    If[Abs[freq - f1[f,I]]<10^−8, Goto[end]];
    freq=f1[f,I];
    n=ne[freq];
    f1[f,I]=(G[f,I]*(3*10^8)*Sin[αG(2)[f,I] Degree])/(2*Pi*n*Sin[ArcCos[rootminus2[f,I]
      ]])/(1*10^12);
    Goto[begin];
    Label[end]; freq, n, ArcCos[rootminus[f,I]] / Degree]
```

The **DynamicModule** environment allows calculations to be carried out as the variables are changed dynamically. Execution of the code creates a grid containing the outcome of the numerical calculations of grating parameters which will result in the production of the specified terahertz frequency and propagation angle; the second solution to the phase-matching conditions, which arises from the bi-directionailty of the grating vector, **G**, is identified. There are input fields for user-specified values of **f** (the terahertz frequency) and since the other terahertz frequency is not initially known, iterative steps must be taken to reach the final value, where the refractive index and frequency values are consistent with each other. This is achieved through the **con[f,l]** function, which checks whether the agreement between the frequency calculated for the most recent iteration is $<10^{-8}$ different from the previous iteration. If that is the case, then the solution is deemed to have converged to a fixed value.

```
DynamicModule[f=1,l=1,
 Deploy[
  Style[
   Panel[
    Grid[
     Transpose[{{Style["Desired THz frequency", Red], Style["Amount below critical
      angle(°)", Red],
     "Refractive index at this THz frequency", Critical angle (°)",
     "θ, angular separation of terahertz and pump/idler (°)", "α(°)", "α2(°)", "G
      (m−1)", "Grating Period (μm)",
     "Angle from first solution of quadratic formula (°)",
     "Angle from second solution of quadratic formula(°)",
     "Second THz frequency (THz) (initial calculation)",
     "Convergent solution (νT2, nT at νT2, angle of νT2 to pump/idler)"},
     {InputField[Dynamic[f], Number],
     InputField[Dynamic[l], Number],
     InputField[Dynamic[ne[f]], Enabled→False],
     InputField[Dynamic[θcrit[f]], Enabled→False],
     InputField[Dynamic[ϕ[f,l]], Enabled→False],
```

```
    InputField[Dynamic[αG(1)][f,l]], Enabled→False],
    InputField[Dynamic[αG(2)][f,l]]], Enabled→False],
    InputField[Dynamic[G[f,l]], Enabled→False],
    InputField[Dynamic[GP[f,l]], Enabled→False],
    InputField[Dynamic[ArcCos[rootplus[f,l]]/Degree], Enabled→False],
    InputField[Dynamic[ArcCos[rootminus[f,l]]/Degree], Enabled→False],
    InputField[Dynamic[νT[f,l]], Enabled→False],
    InputField[Dynamic[con[f,l]], Enabled→ False]}}], Alignment→Right],
     ImageMargins→10],
DefaultOptions→{InputField→{ContinuousAction→True,FieldSize→{{1,30},{1,30}}}}]]]
```

D

Mathematica hybrid system model

This first section of code defines the pump and idler refractive indices (**np** and **ni**) as well as the magnitudes of the wave vectors associated with these wavelengths. The quantities **A** to **z** are required to calculate the terahertz refractive index, **nt**[λ**p,**λ**i**], which is defined in terms of the pump and idler wavelengths so that no iterative steps are needed. The Sellmeier in use is that derived from the *"Handbook of Optical Constants of Solids"*, 1985 edition.

The critical angle for the prism-crystal interface is calculated to allow the phase-matching solutions to be scrutinised in terms of the terahertz wave's ability to be extracted from the crystal. The wave vectors themselves are then calculated; the program user can specify propagation angles for the pump and idler waves relative to the optic axis. The grating vector is calculated on the basis of user-specified grating period and angle values. The bi-directional nature of the grating vector is accounted for by the presence of a second grating vector defined at an angle of 180° to the original vector. The angles are all specified internal to the crystal.

Differ1 and **Differ2** represent the magnitudes of the gap in the phase-matching diagram formed by the pump, idler and grating vectors and **VectorDiffer1** and **VectorDiffer2** represent the corresponding vectors. These are used to determine the terahertz wavelength and propagation direction that satisfy a particular set of phase-matching conditions.

```
Off[FindRoot::"precw"]
Off[FindRoot::"lstol"]
Off[FindRoot::"nlnum"]
Off[ReplaceAll::"reps"]
Needs["PlotLegends`"
np=2.147;
ni=2.147;
kp[λp_]:=2π*np/(λp*10^-9)
ki[λi_]:=2π*ni/(λi*10^-9)
A=3.8123;
λ0=-14.90;
t0=65;
z=5.07;
λt[λp_,λi_]:=N[1/((1/(λp*10^-9)) - (1/(λi*10^-9)))]
nt[λp_,λi_]:=A*Exp[-(((λt[λp,λi]*10^6) - λ0))/t0]+z
ne[n_]:=A*Exp[-((((3*10^8) (10^6)/(n*10^12)) - λ0))/t0]+z
θcrit[n_]:=ArcSin[3.418/ne[n]]/Degree
kt[λp_,λi_]:=(2π*nt[λp,λi])/λt[λp,λi]
vectorp[Λp_,θ_]:={kp[λp]*Cos[θ Degree], kp[λp]*Sin[θ Degree]}
vectori[Λi_,ϕ_]:={ki[λi]*Cos[ϕ Degree], ki[λi]*Sin[ϕ Degree]}
vectorG[G_,α_] := {G*Cos[(α) Degree],G*Sin[(α) Degree]}
vectorG2[G_,α_] := {G*Cos[(α-180) Degree],G*Sin[(α-180) Degree]}
Differ1[λp_,θ_,λi_,ϕ_,G_,α_]:= Norm[vectorp[λp,θ]-vectori[λi,ϕ]+vectorG[G,α]]
Differ2[λp_,θ_,λi_,ϕ_,G_,α_]:= Norm[vectorp[λp,θ]-vectori[λi,ϕ]+vectorG2[G,α]]
VectorDiffer1[λp_,θ_,λi_,ϕ_,G_,α_]:=vectorp[λp,θ]-vectori[λi,ϕ]+vectorG[G,α]
VectorDiffer2[λp_,θ_,λi_,ϕ_,G_,α_]:=vectorp[λp,θ]-vectori[λi,ϕ]+vectorG2[G,α]
```

The **Manipulate** environment allows the expression contained within the environment to be evaluated with controls added to enable interactive manipulation of the specified variables. The terms **freq1** to **freq4** are returned in the form {idler angle, terahertz frequency} and are calculated on the basis of a terahertz frequency specified by the user. The angle ϕ is the idler angle and it is

found by establishing the angle for which the terahertz vector is equal to the gap between the other vectors. **n** is the user-specified terahertz frequency. There are four solutions because the idler wave is allowed to propagate at angle to the pump and there are two solutions on each side of the pump due to the nature of the grating vector.

The terahertz propagation angle for each of the identified solutions (**angle1** to **angle4**) is found by taking the inverse tangent of the ratio of the terahertz vector's vertical and horizontal components.

The **If** term ensures that the angle is referenced to the normal, for comparison with the critical angle.

```
Manipulate[
freq1=
  {ϕ/.FindRoot[3*10^-4/λt[λp,λi/.Flatten[FindRoot[kt[λp,λi]-Differ1[λp, 0,λi,ϕ,G,α]
  ==0,λi,1064.1,AccuracyGoal→7, WorkingPrecision→60]]] == n, ϕ,2],n};
freq2=
  {ϕ/.FindRoot[3*10^-4/λt[λp,λi/.Flatten[FindRoot[kt[λp,λi]-Differ1[λp, 0,λi,ϕ,G,α]
  ==0,λi,1064.1,AccuracyGoal→7, WorkingPrecision→60]]] == n, ϕ,s],n};
freq3=
  {ϕ/.FindRoot[3*10^-4/λt[λp,λi/.Flatten[FindRoot[kt[λp,λi]-Differ2[λp, 0,λi,ϕ,G,α]
  ==0,λi,1064.1,AccuracyGoal→7, WorkingPrecision→60]]] == n, ϕ,2],n};
freq4=
  {ϕ/.FindRoot[3*10^-4/λt[λp,λi/.Flatten[FindRoot[kt[λp,λi]-Differ2[λp, 0,λi,ϕ,G,α]
  ==0,λi,1064.1,AccuracyGoal→7, WorkingPrecision→60]]] == n, ϕ,p],n};
angle1 =
  If[
   ArcTan[VectorDiffer1[λp, 0,λi/.FindRoot[kt[λp,λi]-Differ1[λp,0,λi,freq1[[1]],G,α]
   ==0,{λi, 1064.1},AccuracyGoal→4,WorkingPrecision→60],freq1[[1]],G,α][[2]]/
    VectorDiffer1[Λp,0,λi/.FindRoot[kt[λp,λi]-Differ1[λp,0,λi,freq1[[1]],G,α]==0,
    {λi, 1064.1},AccuracyGoal→4,WorkingPrecision→60],freq1[[1]],G,α][[1]]]
    /Degree<0,
```

```
    90 +
     ArcTan[VectorDiffer1[λp,0,λi/.FindRoot[kt[λp,λi]-Differ1[λp,0,λi,freq1[[1]],G,α]
     ==0,{λi,1064.1},AccuracyGoal→4,WorkingPrecision→60],freq1[[1]],G,α][[2]]/
      VectorDiffer1[λp,0,λi/.FindRoot[kt[λp,λi]-Differ1[λp,0,λi,freq1[[1]],G,α]==0,
     {λi,1064.1},AccuracyGoal→4,WorkingPrecision→60],freq1[[1]],G,α][[1]]]/Degree,
    90 -
     ArcTan[VectorDiffer1[λp,0,λi/.FindRoot[kt[λp,λi]-Differ1[λp,0,λi,freq1[[1]],G,α]
     ==0,{λi,1064.1},AccuracyGoal→4,WorkingPrecision→60],freq1[[1]],G,α][[2]]/
      VectorDiffer1[λp,0,λi/.FindRoot[kt[λp,λi]-Differ1[λp,0,λi,freq1[[1]],G,α]==0,
     {λi,1064.1},AccuracyGoal→4,WorkingPrecision→60],freq1[[1]],G,α][[1]]]/Degree;
angle2 =
    If[
     ArcTan[VectorDiffer1[λp, 0,λi/.FindRoot[kt[λp,λi]-Differ1[λp,0,λi,freq2[[1]],G,α]
     ==0,{λi, 1064.1},AccuracyGoal→4,WorkingPrecision→60],freq2[[1]],G,α][[2]]/
      VectorDiffer1[Λp,0,λi/.FindRoot[kt[λp,λi]-Differ1[λp,0,λi,freq2[[1]],G,α]==0,
      {λi, 1064.1},AccuracyGoal→4,WorkingPrecision→60],freq2[[1]],G,α][[1]]]
      /Degree<0,
    90 +
     ArcTan[VectorDiffer1[λp,0,λi/.FindRoot[kt[λp,λi]-Differ1[λp,0,λi,freq2[[1]],G,α]
     ==0,{λi,1064.1},AccuracyGoal→4,WorkingPrecision→60],freq2[[1]],G,α][[2]]/
      VectorDiffer1[λp,0,λi/.FindRoot[kt[λp,λi]-Differ1[λp,0,λi,freq2[[1]],G,α]==0,
     {λi,1064.1},AccuracyGoal→4,WorkingPrecision→60],freq2[[1]],G,α][[1]]]/Degree,
    90 -
     ArcTan[VectorDiffer1[λp,0,λi/.FindRoot[kt[λp,λi]-Differ1[λp,0,λi,freq2[[1]],G,α]
     ==0,{λi,1064.1},AccuracyGoal→4,WorkingPrecision→60],freq2[[1]],G,α][[2]]/
      VectorDiffer1[λp,0,λi/.FindRoot[kt[λp,λi]-Differ1[λp,0,λi,freq2[[1]],G,α]==0,
     {λi,1064.1},AccuracyGoal→4,WorkingPrecision→60],freq2[[1]],G,α][[1]]]/Degree;
angle3 =
    If[
     ArcTan[VectorDiffer2[λp, 0,λi/.FindRoot[kt[λp,λi]-Differ2[λp,0,λi,freq3[[1]],G,α]
     ==0,{λi, 1064.1},AccuracyGoal→4,WorkingPrecision→60],freq3[[1]],G,α][[2]]/
      VectorDiffer2[Λp,0,λi/.FindRoot[kt[λp,λi]-Differ2[λp,0,λi,freq3[[1]],G,α]==0,
      {λi, 1064.1},AccuracyGoal→4,WorkingPrecision→60],freq3[[1]],G,α][[1]]]
```

```
    /Degree<0,
   90 +
    ArcTan[VectorDiffer2[λp,0,λi/.FindRoot[kt[λp,λi]-Differ2[λp,0,λi,freq3[[1]],G,α]
    ==0,{λi,1064.1},AccuracyGoal→4,WorkingPrecision→60],freq3[[1]],G,α][[2]]/
     VectorDiffer2[λp,0,λi/.FindRoot[kt[λp,λi]-Differ2[λp,0,λi,freq3[[1]],G,α]==0,
    {λi,1064.1},AccuracyGoal→4,WorkingPrecision→60],freq3[[1]],G,α][[1]]]/Degree,
   90 -
    ArcTan[VectorDiffer2[λp,0,λi/.FindRoot[kt[λp,λi]-Differ2[λp,0,λi,freq3[[1]],G,α]
    ==0,{λi,1064.1},AccuracyGoal→4,WorkingPrecision→60],freq3[[1]],G,α][[2]]/
     VectorDiffer2[λp,0,λi/.FindRoot[kt[λp,λi]-Differ2[λp,0,λi,freq3[[1]],G,α]==0,
    {λi,1064.1},AccuracyGoal→4,WorkingPrecision→60],freq3[[1]],G,α][[1]]]/Degree;
angle4 =
   If[
    ArcTan[VectorDiffer2[λp, 0,λi/.FindRoot[kt[λp,λi]-Differ2[λp,0,λi,freq4[[1]],G,α]
    ==0,{λi, 1064.1},AccuracyGoal→4,WorkingPrecision→60],freq4[[1]],G,α][[2]]/
     VectorDiffer2[Λp,0,λi/.FindRoot[kt[λp,λi]-Differ2[λp,0,λi,freq4[[1]],G,α]==0,
     {λi, 1064.1},AccuracyGoal→4,WorkingPrecision→60],freq4[[1]],G,α][[1]]]
     /Degree<0,
   90 +
    ArcTan[VectorDiffer2[λp,0,λi/.FindRoot[kt[λp,λi]-Differ2[λp,0,λi,freq4[[1]],G,α]
    ==0,{λi,1064.1},AccuracyGoal→4,WorkingPrecision→60],freq4[[1]],G,α][[2]]/
     VectorDiffer2[λp,0,λi/.FindRoot[kt[λp,λi]-Differ2[λp,0,λi,freq4[[1]],G,α]==0,
    {λi,1064.1},AccuracyGoal→4,WorkingPrecision→60],freq4[[1]],G,α][[1]]]/Degree,
   90 -
    ArcTan[VectorDiffer2[λp,0,λi/.FindRoot[kt[λp,λi]-Differ2[λp,0,λi,freq4[[1]],G,α]
    ==0,{λi,1064.1},AccuracyGoal→4,WorkingPrecision→60],freq4[[1]],G,α][[2]]/
     VectorDiffer2[λp,0,λi/.FindRoot[kt[λp,λi]-Differ2[λp,0,λi,freq4[[1]],G,α]==0,
    {λi,1064.1},AccuracyGoal→4,WorkingPrecision→60],freq4[[1]],G,α][[1]]]/Degree;
```

freq1' to **freq4'** are the other tarehertz frequencies that satisfy the phase-matching conditions with the same idler propagation angle but utilising the opposite grating vector direction.

```
freq1'={freq1[[1]],3*10^-4/λt[λp,λi/.FindRoot[kt[λp,λi]-Differ2[λp,0,λi,freq1[[1]],G,α]
   ==0,{λi,1064.1},AccuracyGoal→7,WorkingPrecision→60]]};
freq2'={freq2[[1]],3*10^-4/λt[λp,λi/.FindRoot[kt[λp,λi]-Differ2[λp,0,λi,freq2[[1]],G,α]
   ==0,{λi,1064.1},AccuracyGoal→7,WorkingPrecision→60]]};
freq3'={freq3[[1]],3*10^-4/λt[λp,λi/.FindRoot[kt[λp,λi]-Differ2[λp,0,λi,freq3[[1]],G,α]
   ==0,{λi,1064.1},AccuracyGoal→7,WorkingPrecision→60]]};
freq4'={freq4[[1]],3*10^-4/λt[λp,λi/.FindRoot[kt[λp,λi]-Differ2[λp,0,λi,freq4[[1]],G,α]
   ==0,{λi,1064.1},AccuracyGoal→7,WorkingPrecision→60]]};
```

angle1' to **angle4'** are the propagation angles of the alternative terahertz frequencies and are calculated as before.

```
angle1' =
   If[
    ArcTan[VectorDiffer2[λp, 0,λi/.FindRoot[kt[λp,λi]-Differ2[λp,0,λi,freq1'[[1]],G,α]
    ==0,{λi, 1064.1},AccuracyGoal→4,WorkingPrecision→60],freq1'[[1]],G,α][[2]]/
     VectorDiffer2[Λp,0,λi/.FindRoot[kt[λp,λi]-Differ2[λp,0,λi,freq1'[[1]],G,α]==0,
     {λi, 1064.1},AccuracyGoal→4,WorkingPrecision→60],freq1'[[1]],G,α][[1]]
     /Degree<0,
   90 +
    ArcTan[VectorDiffer2[λp,0,λi/.FindRoot[kt[λp,λi]-Differ2[λp,0,λi,freq1'[[1]],G,α]
    ==0,{λi,1064.1},AccuracyGoal→4,WorkingPrecision→60],freq1'[[1]],G,α][[2]]/
     VectorDiffer2[λp,0,λi/.FindRoot[kt[λp,λi]-Differ2[λp,0,λi,freq1'[[1]],G,α]==0,
    {λi,1064.1},AccuracyGoal→4,WorkingPrecision→60],freq1'[[1]],G,α][[1]]]/Degree,
   90 -
    ArcTan[VectorDiffer2[λp,0,λi/.FindRoot[kt[λp,λi]-Differ2[λp,0,λi,freq1'[[1]],G,α]
    ==0,{λi,1064.1},AccuracyGoal→4,WorkingPrecision→60],freq1'[[1]],G,α][[2]]/
     VectorDiffer2[λp,0,λi/.FindRoot[kt[λp,λi]-Differ2[λp,0,λi,freq1'[[1]],G,α]==0,
    {λi,1064.1},AccuracyGoal→4,WorkingPrecision→60],freq1'[[1]],G,α][[1]]]/Degree;
angle2' =
   If[
    ArcTan[VectorDiffer2[λp, 0,λi/.FindRoot[kt[λp,λi]-Differ2[λp,0,λi,freq2'[[1]],G,α]
    ==0,{λi, 1064.1},AccuracyGoal→4,WorkingPrecision→60],freq2'[[1]],G,α][[2]]/
```

```
    VectorDiffer2[Λp,0,λi/.FindRoot[kt[λp,λi]-Differ2[λp,0,λi,freq2'[[1]],G,α]==0,
    {λi, 1064.1},AccuracyGoal→4,WorkingPrecision→60],freq2'[[1]],G,α][[1]]
    /Degree<0,
   90 +
    ArcTan[VectorDiffer2[λp,0,λi/.FindRoot[kt[λp,λi]-Differ2[λp,0,λi,freq2'[[1]],G,α]
    ==0,{λi,1064.1},AccuracyGoal→4,WorkingPrecision→60],freq2'[[1]],G,α][[2]]/
    VectorDiffer2[λp,0,λi/.FindRoot[kt[λp,λi]-Differ2[λp,0,λi,freq2'[[1]],G,α]==0,
    {λi,1064.1},AccuracyGoal→4,WorkingPrecision→60],freq2'[[1]],G,α][[1]]]/Degree,
   90 -
    ArcTan[VectorDiffer2[λp,0,λi/.FindRoot[kt[λp,λi]-Differ2[λp,0,λi,freq2'[[1]],G,α]
    ==0,{λi,1064.1},AccuracyGoal→4,WorkingPrecision→60],freq2'[[1]],G,α][[2]]/
    VectorDiffer2[λp,0,λi/.FindRoot[kt[λp,λi]-Differ2[λp,0,λi,freq2'[[1]],G,α]==0,
    {λi,1064.1},AccuracyGoal→4,WorkingPrecision→60],freq2'[[1]],G,α][[1]]]/Degree;
angle3' =
   If[
    ArcTan[VectorDiffer1[λp, 0,λi/.FindRoot[kt[λp,λi]-Differ1[λp,0,λi,freq3"[[1]],G,α]
    ==0,{λi,
1064.1},AccuracyGoal→4,WorkingPrecision→60],freq3"[[1]],G,α][[2]]/
    VectorDiffer1[Λp,0,λi/.FindRoot[kt[λp,λi]-Differ1[λp,0,λi,freq3'[[1]],G,α]==0,
    {λi, 1064.1},AccuracyGoal→4,WorkingPrecision→60],freq3'[[1]],G,α][[1]]]
    /Degree<0,
   90 +
    ArcTan[VectorDiffer1[λp,0,λi/.FindRoot[kt[λp,λi]-Differ1[λp,0,λi,freq3'[[1]],G,α]
    ==0,{λi,1064.1},AccuracyGoal→4,WorkingPrecision→60],freq3'[[1]],G,α][[2]]/
    VectorDiffer1[λp,0,λi/.FindRoot[kt[λp,λi]-Differ1[λp,0,λi,freq3'[[1]],G,α]==0,
    {λi,1064.1},AccuracyGoal→4,WorkingPrecision→60],freq3'[[1]],G,α][[1]]]/Degree,
   90 -
    ArcTan[VectorDiffer1[λp,0,λi/.FindRoot[kt[λp,λi]-Differ1[λp,0,λi,freq3'[[1]],G,α]
    ==0,{λi,1064.1},AccuracyGoal→4,WorkingPrecision→60],freq3'[[1]],G,α][[2]]/
    VectorDiffer1[λp,0,λi/.FindRoot[kt[λp,λi]-Differ1[λp,0,λi,freq3'[[1]],G,α]==0,
    {λi,1064.1},AccuracyGoal→4,WorkingPrecision→60],freq3'[[1]],G,α][[1]]]/Degree;
angle4' =
   If[
```

```
    ArcTan[VectorDiffer1[λp, 0,λi/.FindRoot[kt[λp,λi]-Differ1[λp,0,λi,freq4'[[1]],G,α]
    ==0,{λi, 1064.1},AccuracyGoal→4,WorkingPrecision→60],freq4'[[1]],G,α][[2]]/
     VectorDiffer1[Λp,0,λi/.FindRoot[kt[λp,λi]-Differ1[λp,0,λi,freq4'[[1]],G,α]==0,
     {λi, 1064.1},AccuracyGoal→4,WorkingPrecision→60],freq4'[[1]],G,α][[1]]]
     /Degree<0,
   90 +
    ArcTan[VectorDiffer1[λp,0,λi/.FindRoot[kt[λp,λi]-Differ1[λp,0,λi,freq4'[[1]],G,α]
    ==0,{λi,1064.1},AccuracyGoal→4,WorkingPrecision→60],freq4'[[1]],G,α][[2]]/
     VectorDiffer1[λp,0,λi/.FindRoot[kt[λp,λi]-Differ1[λp,0,λi,freq4'[[1]],G,α]==0,
    {λi,1064.1},AccuracyGoal→4,WorkingPrecision→60],freq4'[[1]],G,α][[1]]]/Degree,
   90 -
    ArcTan[VectorDiffer1[λp,0,λi/.FindRoot[kt[λp,λi]-Differ1[λp,0,λi,freq4'[[1]],G,α]
    ==0,{λi,1064.1},AccuracyGoal→4,WorkingPrecision→60],freq4'[[1]],G,α][[2]]/
     VectorDiffer1[λp,0,λi/.FindRoot[kt[λp,λi]-Differ1[λp,0,λi,freq4'[[1]],G,α]==0,
    {λi,1064.1},AccuracyGoal→4,WorkingPrecision→60],freq4'[[1]],G,α][[1]]]/Degree;
```

The list called **data** contains the idler propagation angle, terahertz frequency and terahertz propagation angle of each solution. This data is presented in a table in the output of the program. The points labelled with a ' are the alternative terahertz frequencies.

```
data = {{"1", freq1[[1]], n, angle1},
   {"1' ", freq1'[[1]], freq1'[[2]], angle1'},
   {"2", freq2[[1]], n, angle2},
   {"2' ", freq2'[[1]], freq2'[[2]], angle2'},
   {"3", freq3[[1]], n, angle3},
   {"3' ", freq3'[[1]], freq3'[[2]], angle3'},
   {"4", freq4[[1]], n, angle4},
   {"4' ", freq4'[[1]], freq4'[[2]], angle4'}};
```

The first element in the output **Grid** is a line plot of the generated terahertz frequencies as a function of the idler angle. This is produced by first constructing

a table of these values using the expressions defined above and by varying the idler angle in the range (-2 to 2)°, in steps of 0.01°.

```
Grid[
{{ListLinePlot[{Table[{ϕ,3*10^-4/λt[λp, λi /.FindRoot[kt[λp, λi] -Differ1[λp,θ],λi,ϕ,G,
  α]==0,{λi, 1064.4}, AccuracyGoal→7, WorkingPrecision→60]]}, {ϕ, -2,2, 0.01}],
Table[{ϕ,3*10^-4/λt[1064.4, λi /. FindRoot[kt[1064.4, λi]- Differ2[λp,0,λi,ϕ,G,α]==0,
  {λi,1064.4},AccuracyGoal→7,WorkingPrecision→60]]},{ϕ,-2,2, 0.01}]},Frame→
   True,Axes→None,PlotStyle→{{Blue, Thickness[0.00125]}, {Red,Thickness
  [0.005]}}, Joined→True,
FrameLabel→{"Angle between idler and pump (°)","THz frequency"},
FrameStyle→Directive[FontFamily→"Calibri", FontSize→11],
PlotLegend→{Style["Grating vector in +ve direction", 10, FontFamily→"Calibri"],
  Style["Grating vector in -ve direction", 10, FontFamily→"Calibri"]},
LegendShadow→None, LegendSpacing→0.0, LegendTextSpace→4, LegendSize
  →{0.5, 0.2}, LegendPosition→{-0.2, 0.3},
PlotLabel→"Tuning range of THz as a function of pump-idler separation",
   LabelStyle→Directive[Bold, FontFamily→"Calibri"], PlotRange→All,
GridLines→{{{-0.1, Dotted}, {-0.2, Dotted}, {-0.3,Dotted}, {-0.4, Dotted}, {-0.5,
Dashed}, {-0.6,Dotted}, {-0.7, Dotted}, {-0.8, Dotted}, {-0.9, Dotted}, {-1,
Dashed}, {-1.1, Dotted}, {-1.2, Dotted}, {-1.3, Dotted}, {-1.4, Dotted}, {-1.5,
Dashed}, {-1.6, Dotted}, {-1.7, Dotted}, {-1.8, Dotted}, {-1.9, Dotted}, {-2,
Dashed}, {0, Dashed}, {0.1, Dotted}, {0.2, Dotted}, {0.3, Dotted}, {0.4, Dotted},
{0.5, Dashed}, {0.6, Dotted}, {0.7, Dotted}, {0.8, Dotted}, {0.9, Dotted}, {1,
Dashed}, {1.1, Dotted}, {1.2, Dotted}, {1.3, Dotted}, {1.4, Dotted}, {1.5,
Dashed}, {1.6, Dotted}, {1.7, Dotted}, {1.8, Dotted}, {1.9, Dotted}, {2, Dashed},
{2.1, Dotted}}, {{0, Dashed}, {1, Dashed}, {2, Dashed}, {3, Dashed}, {4,
Dashed}, {n, {Orange, Thick}}}}, ImageSize→{700, 500},
```

The **Epilog** term is used to draw labelled points on the graph at each of the possible solutions, for reference to the data in the table.

```
Epilog→{{PointSize[Large], Red, Point[freq1], Text[StyleForm[DisplayForm["1"],
```

FontFamily→ “Helvetica”, FontSize→9, FontWeight→Bold], freq1 + {0, 0.2}]},
{PointSize[Large], Red, Point[freq1’], Text[StyleForm[DisplayForm[“1’ ”],
FontFamily→“Helvetica”, FontSize→9, FontWeight→Bold], freq1’ + {0, 0.2}]},
{PointSize[Large], Purple, Point[freq2], Text[StyleForm[DisplayForm[“2”],
FontFamily→“Helvetica”, FontSize→9, FontWeight→Bold], freq2 + {0, 0.2}]},
{PointSize[Large], Purple, Point[freq2’], Text[StyleForm[DisplayForm[“2’ ”],
FontFamily→“Helvetica”, FontSize→9, FontWeight→Bold], freq2’ + {0, 0.2}]},
{PointSize[Large], Blue, Point[freq3], Text[StyleForm[DisplayForm[“3”],
FontFamily→“Helvetica”, FontSize→9, FontWeight→Bold], freq3 + {0, 0.2}]},
{PointSize[Large], Blue, Point[freq3’], Text[StyleForm[DisplayForm[“3’ ”],
FontFamily→“Helvetica”, FontSize→9, FontWeight→Bold], freq3’ + {0, 0.2}]},
{PointSize[Large], Black, Point[freq4], Text[StyleForm[DisplayForm[“4”],
FontFamily→“Helvetica”, FontSize→9, FontWeight→Bold], freq4 + {0, 0.2}]},
{PointSize[Large], Black, Point[freq4’], Text[StyleForm[DisplayForm[“4’ ”],
FontFamily→“Helvetica”, FontSize→9, FontWeight→Bold], freq4’ + {0, 0.2}]},

This section of code produces the data table containing the numerical data describing the solutions. These can be compared easily to establish which folution is likely to be generated the most effectively.

Text@Grid[Prepend[data, {“Solution”, “P→I separation (°)”, “THz frequency”, “Exit angle (°)”}],
Background→{None, {Lighter[Yellow, 0.9], {White, Lighter[Blend[{Blue, Green}], 0.8]}}},
Dividers→{{Darker[Gray, 0.6], {Lighter[Gray, 0.5]}, Darker[Gray, 0.6]}, {Darker[Gray, 0.6], Darker[Gray, 0.6], {False}, Darker[Gray, 0.6]}},
Alignment→{{Center, Center, Center, Center}}, ItemSize→{{4, 9, 8, 6}}, Frame→Darker[Gray, 0.6], ItemStyle→Directive[FontSize→12, FontFamily→“Helvetica”],
Spacings→{Automatic, 0.8}]},

The final element in the output **Grid** is a line plot of the terahertz angle as a

function of the idler angle. This is produced by first constructing a table of these values using the expressions defined above and by varying the idler angle in the range (-2 to 2)°, in steps of 0.01°.

```
{ListLinePlot[
 {Table[
  {ϕ,
   If[
    ArcTan[VectorDiffer1[λp,θ, λi /. FindRoot[kt[λp, λi] - Differ1[λp, θ, λi, ϕ, G, α]
      == 0, {λi, 1064.4}, AccuracyGoal→4, WorkingPrecision→60], ϕ, G,
     α][[2]]/VectorDiffer1[λp, θ, λi /. FindRoot[kt[λp, λi] - Differ1[λp, θ, λi, ϕ, G,
     α] == 0, {λi, 1064.4}, AccuracyGoal→4, WorkingPrecision→60], ϕ, G,
      α][[1]]]/Degree <0,
    90 + ArcTan[VectorDiffer1[λp,θ, λi /. FindRoot[kt[λp, λi] - Differ1[λp, θ, λi, ϕ,
     G, α] == 0, {λi, 1064.4}, AccuracyGoal→4, WorkingPrecision→60], ϕ, G,
     α][[2]]/VectorDiffer1[λp, θ, λi /. FindRoot[kt[λp, λi] - Differ1[λp, θ, λi, ϕ, G,
      α] == 0, {λi, 1064.4}, AccuracyGoal→4, WorkingPrecision→60], ϕ, G,
      α][[1]]]/Degree,
    90 - ArcTan[VectorDiffer1[λp, θ, λi /. FindRoot[kt[λp, λi] - Differ1[λp, θ, λi, ϕ,
     G, α] == 0, {λi, 1064.4}, AccuracyGoal→4, WorkingPrecision→60], ϕ, G,
     α][[2]]/VectorDiffer1[λp, θ, λi /. FindRoot[kt[λp, λi] - Differ1[λp, θ, λi, ϕ, G,
      α]== 0, {λi, 1064.4}, AccuracyGoal→4, WorkingPrecision→60], ϕ, G,
      α][[1]]]/Degree]}, {ϕ, -2, 2.1, 0.01}],
Table[
  {ϕ,
   If[
    ArcTan[VectorDiffer2[λp,θ, λi /. FindRoot[kt[λp, λi] - Differ2[λp, θ, λi, ϕ, G, α]
      == 0, {λi, 1064.4}, AccuracyGoal→4, WorkingPrecision→60], ϕ, G,
     α][[2]]/VectorDiffer2[λp, θ, λi /. FindRoot[kt[λp, λi] - Differ2[λp, θ, λi, ϕ, G,
     α] == 0, {λi, 1064.4}, AccuracyGoal→4, WorkingPrecision→60], ϕ, G,
      α][[1]]]/Degree <0,
    90 + ArcTan[VectorDiffer2[λp,θ, λi /. FindRoot[kt[λp, λi] - Differ2[λp, θ, λi, ϕ,
     G, α] == 0, {λi, 1064.4}, AccuracyGoal→4, WorkingPrecision→60], ϕ, G,
```

```
α][[2]]/VectorDiffer2[λp, θ, λi /. FindRoot[kt[λp, λi] - Differ2[λp, θ, λi, ϕ, G,
α] == 0, {λi, 1064.4}, AccuracyGoal→4, WorkingPrecision→60], ϕ, G,
α][[1]]]/Degree,
90 - ArcTan[VectorDiffer2[λp, θ, λi /. FindRoot[kt[λp, λi] - Differ2[λp, θ, λi, ϕ,
G, α] == 0, {λi, 1064.4}, AccuracyGoal→4, WorkingPrecision→60], ϕ, G,
α][[2]]/VectorDiffer2[λp, θ, λi /. FindRoot[kt[λp, λi] - Differ2[λp, θ, λi, ϕ, G,
α]== 0, {λi, 1064.4}, AccuracyGoal→4, WorkingPrecision→60], ϕ, G,
α][[1]]]/Degree]}, {ϕ, -2, 2.1, 0.01}]} Frame→True, Axes→None,
PlotStyle→{{Blue, Thickness[0.00125]}, {Red, Thickness[0.005]}}, Joined→True,
FrameLabel→{"Angle between pump and idler (°)", "Angle of THz to PPLN:Si
interface (°)"}, FrameStyle→Directive[FontFamily→"Calibri", FontSize→11],
PlotLegend→{Style["Grating vector in +ve direction", 10, FontFamily→"Calibri"],
Style["Grating vector in -ve direction", 10, FontFamily→"Calibri"]},
LegendShadow→None, LegendSpacing→0.0, LegendTextSpace→4, PlotLabel
→"Angle of THz to PPLN:Si interface as a function of pump-idler separation",
LegendSize→{0.5, 0.2}, LegendPosition→{0.2, 0.3}, LabelStyle→Directive[Bold,
FontFamily→"Calibri"], PlotRange→All,
Epilog→{{Text[StyleForm[DisplayForm["Critical angle"], FontFamily→"Helvetica",
FontSize→9, FontWeight→Bold], {1, θcrit[n]}]}, {PointSize[Large], Red,
Point[{freq1[[1]], angle1}], Text[StyleForm[DisplayForm["1"], FontFamily→
"Helvetica", FontSize→9, FontWeight→Bold], {freq1[[1]], angle1} + {0, -3}]},
{PointSize[Large], Red, Point[{freq1'[[1]], angle1'}], Text[StyleForm
[DisplayForm["1'"], FontFamily→"Helvetica", FontSize→9], {freq1'[[1]], angle1'}
+ {0, -3}]}, {PointSize[Large], Purple, Point[{freq2[[1]], angle2}],
Text[StyleForm[DisplayForm["2"], FontFamily→"Helvetica", FontSize→9,
FontWeight→Bold], {freq2[[1]], angle2} + {0, -3}]}, {PointSize[Large], Purple,
Point[{freq2'[[1]], angle2'}], Text[StyleForm[DisplayForm["2'"],
FontFamily→"Helvetica", FontSize→9, FontWeight→Bold], {freq2'[[1]], angle2'}
+ {0, -3}]}, {PointSize[Large], Blue, Point[{freq3[[1]], angle3}],
Text[StyleForm[DisplayForm["3"], FontFamily→"Helvetica", FontSize→9,
FontWeight→Bold], {freq3[[1]], angle3} + {0, -3}]}, {PointSize[Large], Blue,
Point[{freq3'[[1]], angle3'}], Text[StyleForm[DisplayForm["3'"],
FontFamily→"Helvetica", FontSize→9, FontWeight→Bold], {freq3'[[1]], angle3'}
```

+ {0,3}]}, {PointSize[Large], Black, Point[{freq4[[1]], angle4}],
Text[StyleForm[DisplayForm["4"], FontFamily→"Helvetica", FontSize→9,
FontWeight→Bold], {freq4[[1]], angle4} + {0, -3}]}, {PointSize[Large], Black,
Point[{freq4'[[1]], angle4'}], Text[StyleForm[DisplayForm["4'"],
FontFamily→"Helvetica", FontSize→9, FontWeight→Bold], {freq4'[[1]], angle4'}
+ {0, -3}]}},
GridLines→{{{-0.1, Dotted}, {-0.2, Dotted}, {-0.3,Dotted}, {-0.4, Dotted}, {-0.5, Dashed}, {-0.6,Dotted}, {-0.7, Dotted}, {-0.8, Dotted}, {-0.9, Dotted}, {-1, Dashed}, {-1.1, Dotted}, {-1.2, Dotted}, {-1.3, Dotted}, {-1.4, Dotted}, {-1.5, Dashed}, {-1.6, Dotted}, {-1.7, Dotted}, {-1.8, Dotted}, {-1.9, Dotted}, {-2, Dashed}, {0, Dashed}, {0.1, Dotted}, {0.2, Dotted}, {0.3, Dotted}, {0.4, Dotted}, {0.5, Dashed}, {0.6, Dotted}, {0.7, Dotted}, {0.8, Dotted}, {0.9, Dotted}, {1, Dashed}, {1.1, Dotted}, {1.2, Dotted}, {1.3, Dotted}, {1.4, Dotted}, {1.5, Dashed}, {1.6, Dotted}, {1.7, Dotted}, {1.8, Dotted}, {1.9, Dotted}, {2, Dashed}, {2.1, Dotted}}, {{-60, Dashed}, {-50, Dashed}, {-40, Dashed}, {-30, Dashed}, {-20, Dashed}, {-10, Dashed},{0, Dashed}, {10, Dashed}, {20, Dashed}, {30, Dashed}, {40, Dashed}, {50, Dashed}, {60, Dashed}, {70, Dashed}, {80, Dashed}, {[θcritn], Orange}}}, ImageSize→{700, 500}]}}, Spacings→1],
{{n, 1, "THz frequency"}, 1, InputField, FieldSize→4}, {{λp, 1064.4, "Pump frequency"}, 1064.4, InputField, FieldSize→4}, {{θ, 0, "Pump angle"}, 0, InputField, FieldSize→4}, {{G, 86784, "Grating vector magnitude"}, 86784, InputField, FieldSize→4}, {{α, 86.5, "Grating vector angle"}, 86.5, InputField, FieldSize→4}, {{s, -2, "Starting point to look for root for sol. 2"}, 0, InputField, FieldSize→4}, {{p, -2, "Starting point to look for root for sol. 4"}, 0, InputField, FieldSize→4}]